

Deciphering molecular interactions in presynaptic dense
projection formation in *C. elegans*

Lewis A. Cockram

Degree awarded by

Oxford Brookes University

Thesis submitted in partial fulfilment of the requirements for the
award of Doctor of Philosophy

September 2023

Acknowledgements

First of all, I need to thank my supervisors Maike and Isabel for their help and support throughout the project. With the Covid-19 pandemic this has perhaps been the strangest few years of my life, but your contributions have helped to push me in the right direction and steered me through any difficulties that I faced.

I'd also like to thank the McGregor lab for being so welcoming and making me feel like part of the group even though my research subjects had considerably fewer legs than any of yours. It's been a pleasure to work alongside you. I also want to thank Tom O'Brien and André Brown from Imperial College London for your help conducting behavioural assays and guidance with the analysis of data. Also thank you to Flavia for keeping the TEM (just about) working as it continually threatened to scupper my work.

Next, I want to thank my friends. You won't realise it, but you've provided a much-needed escape in times of stress, even if it was just to have a game of football.

Finally, to my parents, for all of your support and encouragement, I thank you. Without you I wouldn't have developed my love for the natural world, and I definitely wouldn't have made it this far.

Abstract

Neurons are unique in their capacity to build complex systems of information transfer, which comes as a product of their ability to communicate with one another. Neuronal communication occurs at biological structures known as synapses the majority of which are chemical. Chemical synapses comprise a presynaptic neuron, which releases molecular messengers such as neurotransmitters, and a postsynaptic cell, which receives these messages and respond appropriately. To perform its specific role the presynapse utilises a distinct set of proteins at a site known as the active zone, which dictates the location and timing of neurotransmitter release. These active zone functions are thought to revolve around a central protein scaffold, which is visible under electron microscopy as a structure known as the dense projection. While several of the proteins localised to these structures are known, the removal of individual components typically has limited effect on the formation of the presynaptic active zone scaffold/ dense projection. This has made it difficult to determine the function of the structure in neurotransmission. One of the only proteins which notably affects active zone scaffold formation is Liprin- α /SYD-2. In the nematode worm *Caenorhabditis elegans* the loss of SYD-2 causes fewer dense projections to form along motor neurons; the remaining structures are also smaller and have reduced ultrastructural complexity. As dense projections continue to form in the absence of SYD-2, however; there must be some degree of functional redundancy with other active zone proteins.

This thesis explores the combined contribution of the known major active zone organiser SYD-2 (Liprin- α), and the more recently characterised active zone proteins HLB-1 (Liprin- β) and CLA-1, in the formation of a functional presynaptic active zone scaffold in *Caenorhabditis elegans*. Both single mutant strains, and double and triple

mutant strains carrying a *syd-2* null mutation combined with *h1b-1* and *cla-1* mutations were generated and investigated using a combination of approaches. These included confocal imaging of active zone components, locomotor behaviour assays, pharmacological assessment of neurotransmitter release and electron microscopy of the presynaptic ultrastructure. My results indicate that CLA-1 acts downstream of SYD-2 in the formation of the presynaptic active zone scaffold, whereas HLB-1 is not involved in the formation of the structure. Both CLA-1 and HLB-1 do have roles in managing the subsynaptic localisation of synaptic vesicles, however. CLA-1 maintains a subset of synaptic vesicles proximal to the dense projection and supports their docking at the presynaptic plasma membrane. HLB-1 meanwhile appears to act as a negative regulator of SYD-2 in synaptic vesicle docking. Loss of these proteins and their respective functions also modulates crawling locomotion. Therefore, while HLB-1 and CLA-1 can be eliminated as proteins which work independently of SYD-2 or compensate for SYD-2 loss in active zone scaffold/ dense projection formation, this thesis provides new evidence for the respective roles of HLB-1 and CLA-1 at the presynaptic active zone.

Contents

1 General Introduction	14
1.1 Synaptic vesicles and the SV Cycle	17
1.1.1 Formation of synaptic vesicles	17
1.1.2 Docking, Priming and Fusion at the AZ	20
1.1.3 Endocytosis	22
1.2 The active zone scaffold	25
1.2.1 Dense projections	27
1.3 <i>C. elegans</i> as a model organism	35
1.3.1 <i>C. elegans</i> neuromuscular biology	39
1.4 Potential organisers of the <i>C. elegans</i> AZ	42
1.4.1 SYD-2	45
1.4.2 HLB-1	48
1.4.3 CLA-1	52

2. Investigating the role of SYD-2, HLB-1 and CLA-1 in the localisation of core active zone and synaptic vesicle components **56**

2.1 Results 61

2.1.1 Loss of SYD-2 reduces UNC-10 recruitment to synaptic sites but the additional removal of CLA-1 and HLB-1 does not amplify this phenotype 62

2.1.2 SV recruitment to synaptic sites is mediated primarily by SYD-2 although HLB-1 may play an independent role 66

2.2 Discussion 70

2.2.1 SYD-2 remains the primary AZ scaffold organiser 70

2.2.2 HLB-1 and SYD-2 independently contribute to SV recruitment but do not account for all recruited SVs 73

3 Assessing neuromuscular functionality in the absence of SYD-2, HLB-1 and CLA-1 **76**

3.1 Results 79

3.1.1 Regular crawling locomotion is strongly disrupted by the loss of SYD-2 although this is modulated by the additional removal of CLA-1 79

3.1.2 Loss of HLB-1 and CLA-1 does not enhance *syd-2* mutant swimming defects 92

3.1.3 Loss of SYD-2 does not affect aldicarb sensitivity, but loss of HLB-1 amplifies <i>cla-1(ok2285)</i> mutant resistance in the <i>cla-1; hlb-1 syd-2</i> triple mutant	98
3.3 Discussion	102
3.3.1 SYD-2 is necessary for normal locomotion patterns but is not integral to basal locomotion	102
3.3.2 SYD-2 loss disrupts crawling locomotor patterns	103
3.3.3 SYD-2 maintains consistent, sustained swimming locomotion	106
3.3.4 HLB-1 opposes SYD-2-driven crawling behaviour	109
3.3.5 CLA-1 modulates crawling locomotion	110
3.3.6 The loss of HLB-1 further disrupts cholinergic signalling in <i>cla-1</i> mutants	113
4 Examining presynaptic ultrastructure in the absence of SYD-2, HLB-1 and CLA-1	115
4.1 Results	122
4.1.1 Dense projection formation and synaptic structure is disrupted in <i>syd-2(ok217)</i> -containing mutants	122
4.1.2 Dense projection size is similarly reduced in <i>syd-2</i> and <i>cla-1</i> mutants but is not additive in double mutants.	127

4.1.3 The loss of SYD-2, CLA-1 and HLB-1 has differing effects on synaptic vesicle localisation at the presynaptic active zone	129
4.1.4 Reduced dense core vesicle recruitment to synaptic sites indicate a transport defect beyond those affecting SVs	143
4.2 Discussion	146
4.2.1 SYD-2 organises the dense projection	146
4.2.2 SYD-2 manages SV localisation at the presynapse	148
4.2.3 CLA-1 contributes to dense projection morphology through the same pathway as SYD-2	150
4.2.4 CLA-1 tethers SVs proximal to the dense projection	152
4.2.5 HLB-1 is a regulator of SYD-2 mediated synaptic vesicle docking	155
5 General Discussion	159
5.1 CLA-1 and HLB-1 do not contribute to active zone scaffold formation independent of SYD-2 but do influence synaptic vesicle localisation at cholinergic neuromuscular junctions	159
5.2 What are the other AZ proteins involved dense projection formation?	163
5.3 Thinking of the AZ as more than a simple scaffold	167

5.4 Does AZ scaffold assembly, maintenance and function differ between synapses?	169
6 Methods	172
6.1 Strains and reagents	172
6.2 <i>C. elegans</i> strains and maintenance	183
6.3 Confocal fluorescence imaging	184
6.4 <i>C. elegans</i> crawling motion tracking and analysis in Tierpsy Tracker (performed by collaborator Tom O'Brien)	186
6.5 Swimming assays and Tierpsy Tracker Software	188
6.6 Aldicarb assays	189
6.7 HPF and freeze substitution	190
6.8 Production of Formvar-coated grids	192
6.9 Ultramicrotomy and transmission electron microscopy	192
6.10 Serial section reconstruction	193
6.11 Vesicle distribution analysis	193
6.12 Statistical analysis	194

7 References	197
---------------------	------------

Appendix 1	231
-------------------	------------

Figures

Figure 1.1. A typical chemical synapse consisting of a presynaptic terminal, postsynaptic cell and the separating synaptic cleft.....	15
Figure 1.2. The transport and processing of SVs from the golgi apparatus at cell body to the presynapse	19
Figure 1.3. SNARE mediated SV fusion and neurotransmitter release.	22
Figure 1.4. The synaptic vesicle cycle.....	24
Figure 1.5. Appearance of dense projections in electron micrographs among different species.	31
Figure 1.6. Overview of the main features of the <i>C. elegans</i> nervous system.....	38
Figure 1.7. Schematic of the innervation patterns found within the <i>C. elegans</i> nerve cords.	41
Figure 1.8. Overview of the known protein composition of the AZ cytomatrix in <i>C. elegans</i> and the protein interactions held therein.	45
Figure 1.9. Schematic of the gene structure of <i>syd-2</i> and the structure of the protein product.....	46
Figure 1.10. Schematic of the gene structure of <i>h1b-1</i> and the structure of the protein product.....	49

Figure 1.11. Conservation of residues between <i>Mus musculus</i> and <i>Caenorhabditis elegans</i> liprins	51
Figure 1.12. Schematic of the gene structure of <i>cla-1</i> and the structure of the protein product	53
Figure 2.1. Localisation of UNC-10 within the presynaptic dense projection as demonstrated by immuno-electron microscopy (ImmunoEM) analysis.....	60
Figure 2.2. Dorsal nerve cord profile of wild-type <i>C. elegans</i> expressing UNC-10::GFP	62
Figure 2.3. <i>syd-2(ok217)</i> modulates the total level of UNC-10:GFP at cholinergic motor neuron synapses but not the number of sites to which it is recruited	63
Figure 2.4. <i>syd-2(ok217)</i> causes a reduction in SNB-1:GFP recruitment to sites of synaptic release	66
Figure 3.1. SYD-2 loss promotes directed crawling locomotion	81
Figure 3.2. SYD-2 loss promotes greater exploration of the worm's environment....	84
Figure 3.3. <i>syd-2</i> mutants display enhanced speed in both forward and backward directions.....	86
Figure 3.4. Body curvature is reduced in <i>syd-2</i> mutants	88
Figure 3.5. Minor axis length is enhanced in <i>syd-2</i> mutants.....	90
Figure 3.6. SYD-2 loss causes defective swimming which is not exacerbated by additional loss of HLB-1 and CLA-1.	93
Figure 3.7. <i>syd-2</i> mutants show greater variability in their swimming dynamics	95
Figure 3.8. Mutants carrying a <i>syd-2</i> mutation express a prolonged curling phenotype.	97
Figure 3.9. The <i>syd-2(ok217)</i> mutant allele promotes periods of quiescence during extended swimming sessions.....	98

Figure 3.10. <i>h1b-1(ok725)</i> enhances inherent aldicarb resistance in <i>cla-1(ok2285)</i> mutants, whereas <i>syd 2(ok217)</i> does not increase aldicarb resistance.	101
Figure 4.1. Schematic illustration of how cholinergic and GABAergic neuromuscular junctions (NMJs) appear under electron microscopy accompanied by electron micrographs.	118
Figure 4.2. 5µm reconstruction of cholinergic motor neuron axons from 50nm serial sections of a wild-type dorsal nerve cord.	123
Figure 4.3. 5µm reconstruction of cholinergic motor neuron axons from 50nm serial sections of a <i>syd-2(ok217)</i> single mutant dorsal nerve cord	124
Figure 4.4. 5µm reconstruction of cholinergic motor neuron axons from 50nm serial sections of a <i>cla-1(ok2285); h1b-1(ok725) syd-2(ok217)</i> triple mutant dorsal nerve cord	125
Figure 4.5. Dense projection size is reduced in mutants with the <i>syd-2(ok217)</i> allele.	128
Figure 4.6. Fewer SVs are present <i>syd-2</i> mutant synapses.	131
Figure 4.7. Presynaptic terminal size is reduced across <i>cla-1(ok2285)</i> mutants....	133
Figure 4.8. Docked and undocked vesicle localisation is differentially affected in <i>syd-2</i> single, double and triple mutants	135
Figure 4.9. Undocked SVs are reduced in strains carrying a <i>syd-2</i> mutation regardless of their distance from the dense projection.	137
Figure 4.10. Analysis of docked SV distribution around the dense projection reveals that <i>syd-2</i> single mutants only display consistent mild reductions in docked SVs whereas they are consistently increased in <i>h1b-1(ok725)</i> single mutants.	141
Figure 4.11. Dense core vesicle recruitment is diminished in <i>syd-2</i> mutants suggesting defective transport to synaptic sites	144

Figure 5.1. Summary of findings relating to the interactions of SYD-2, CLA-1 and HLB-1 at the presynaptic active zone.....	161
Figure 6.1. Schematic diagram of the experimental design for the crawling assays.	187
Figure 6.2. Pipeline for electron microscopy from high-pressure freezing of specimens to generation of electron micrographs.....	191

Tables

Table 6.1. <i>C. elegans</i> strains used throughout the thesis.....	172
Table 6.2. Bacterial strains used throughout the thesis.....	176
Table 6.3. Primers used throughout the thesis.....	176
Table 6.4. Reagents used throughout the thesis.....	178
Table 6.5. Solutions used throughout the thesis.	181

1 General Introduction

Nervous systems are a feature of all metazoans outside of Porifera (sponges), Placozoa and two specific groups of highly reduced parasites (Myxozoa and Dicyemida), playing pivotal roles in many diverse functions throughout the lifetime of these organisms. While the origin of nervous systems remains a divisive topic it is broadly believed that they first emerged in radially symmetrical organisms, initially as simple nerve nets (Arendt, 2021).

The prevailing principle behind the effectiveness and success of nervous systems, and therefore their evolutionary longevity, are their capacity for intercellular communication. This mechanism is central to allowing synergism between spatially disparate cellular units to perform complex tasks. For example, the sensory detection of a threat in the external environment is converted into a flight response by activating muscle cells to flee to safety. In neurons the contact points that govern this signal transmission are synapses (Foster and Sherrington, 1897).

Two forms of synapses are present in the nervous system, electrical and chemical, the latter being the more common of the two forms and the focus of this thesis. Chemical synapses have three essential components, a presynaptic terminal, a synaptic cleft, and a postsynaptic cell (Peter and Palay, 1996). An electrical signal generated in a presynaptic neuron is propagated towards the site of synaptic transmission to facilitate the release of neurotransmitters, the chemical signal, into the synaptic cleft. The neurotransmitters diffuse across the synaptic cleft, an extracellular region, and then binds to receptors on the postsynaptic cell triggering an appropriate intracellular response. These synapses are likely derived from paracrine secretory

epithelial cells transitioning from participating in volume transmission to the extracellular environment to targeted neuropeptide, and later neurotransmitter, release on to target cells. Analogous structures have been identified in synapseless sponges. 'Neuroid' cells enriched expression of homologues of presynapse-associated genes wrap around and signal to choanocyte feeding cells which demonstrate complementary 'postsynapse' gene expression (Musser et al, 2021).

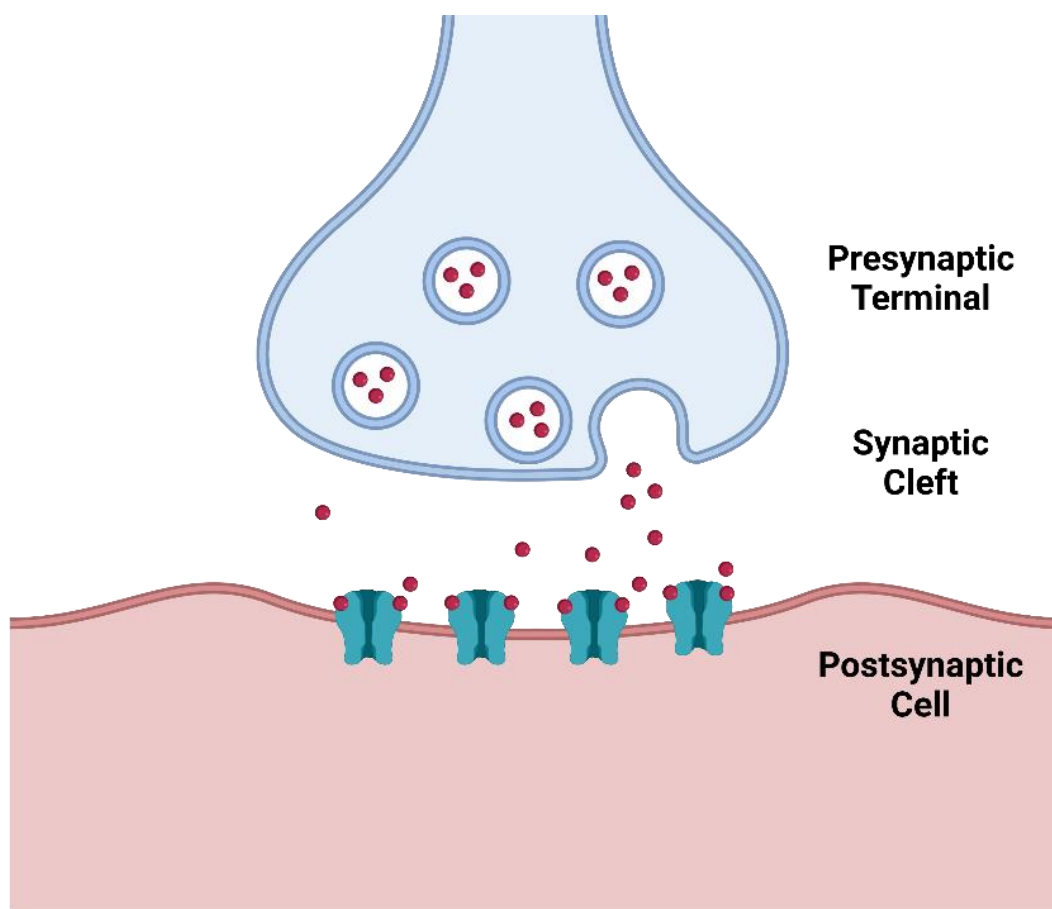


Figure 1.1. A typical chemical synapse consisting of a presynaptic terminal, postsynaptic cell and the separating synaptic cleft. An electrical stimulus triggers SV fusion with the presynaptic plasma membrane. Neurotransmitters are released into the synaptic cleft and bind to postsynaptic receptors. This initiates a postsynaptic response such as depolarisation, hyperpolarisation or the enlistment of secondary messengers in signal transduction. Created with "BioRender.com"

Neural networks require precise spatiotemporal co-ordination to function efficiently and give rise to the appropriate behaviour (Wojcik and Brose, 2007). Therefore, it is critical to ensure that the release of neurotransmitter is tightly regulated. This is achieved through the interplay of the proteins in the presynaptic active zone (AZ), the site where synaptic vesicles (SVs) fuse with the presynaptic membrane. The means by which many of these proteins interact to form a functional presynapse remains unclear. This is epitomised by the central AZ scaffold, a highly conserved prominent feature of the presynaptic terminal which is visible in electron micrographs as a “dense projection” (Zhai and Bellen, 2004; Ackermann et al, 2015), but one which we only have limited understanding of. Although several AZ scaffold components are known (Yeh et al, 2005; Weimer et al, 2006; Ackermann et al, 2015; Xuan et al, 2017) and many of these are essential for SV localisation and fusion at the presynapse (Richmond et al, 1999; Koushika et al, 2001; Stigloher et al, 2011; Xuan et al, 2017), whether the dense projection structure holds any significance beyond concentrating these proteins in a single location is unclear.

Changes in the architecture of the dense projection, including the loss of putative SV docking bays (Kittelmann et al, 2013), have been suggested to affect the dynamics of neurotransmission including synaptic strength. This indicates that the morphology of the AZ scaffold and not just its proteins components may have functional relevance at the AZ through interactions with SVs. Understanding how the AZ scaffold is constructed may therefore help to dissect how the recruitment and fusion of SVs is regulated in time and space.

1.1 Synaptic vesicles and the SV Cycle

An understanding of SVs is crucial to appreciate the importance of the AZ and its associated structures. SVs are the fundamental hallmark of chemical synapses. These small, highly abundant neuronal organelles with a proteinaceous phospholipid membrane act as a receptacle for neurotransmitter molecules and facilitates their release into the synaptic cleft. Enclosing neurotransmitters into these mobile subcellular compartments serves several important purposes. Firstly, it allows the manipulation of numerous neurotransmitter molecules simultaneously, allowing them to be precisely localised, a process which would be virtually impossible by simple diffusion of free neurotransmitter molecules. Additionally, it allows the amount of neurotransmitter that can be released under stimulation, and hence the strength of the transmitted signal, to be tightly controlled by adjusting the number of SVs available to fuse.

1.1.1 Formation of synaptic vesicles

Precursor SVs are initially formed through budding from the Golgi apparatus at the cell body before undergoing anterograde transport through association with the Kinesin family motor proteins, such as KIF-1A/UNC-104, which move along microtubules (Hall and Hedgecock, 1991). This active transport is likely to take place alongside presynaptic AZ proteins (Wu et al, 2013). Once a cargo precursor vesicle reaches its presynaptic destination it then disembarks from the microtubule motor protein. The process through which this occurs remains poorly understood. Recent work indicates that microtubule GTP plus ends are enriched at axonal presynaptic sites, and that this

promotes the detachment of KIF-1A motors from microtubules (Guedes-Dias et al, 2019). Such events could act as a delivery mechanism to presynaptic sites, however a means of retaining precursor vesicles would also be required. In *C. elegans*, a specific set of proteins referred to as the core synapse stability (CSS) system, consisting of Liprin- α /SYD-2, SAD-1, SYD-1 and STR-1, support the retention of synaptic vesicles at synaptic sites and prevents their clearance by the retrograde Dynein motor protein (Edwards et al, 2015; Edwards et al, 2018). The CSS system proteins may also assist in the initial stabilisation of precursor vesicles at synaptic sites. Maturation of these precursor vesicles into fusion-competent vesicles occurs by adjusting the composition of proteins in the SV membrane through fusion with either the plasma membrane or synaptic endosomes and then reforming as a fusion-competent SV (Rizzoli, 2014).

At this stage the newly formed mature synaptic vesicle can enter the SV cycle (reviewed in Sudhof, 2004; Rizzoli, 2014; Chanaday et al, 2019), which allows the materials making up the SVs to be continually recycled in a locally controlled process (detailed in 1.113, Figure 1.2). This ensures that sufficient SVs remain available at the AZ without having to continually traffic large volumes of precursors from the cell body. The mature vesicles are first filled with neurotransmitter through a two-step process. Vesicles undergo acidification whereby protons are pumped into the SV lumen by the membrane-bound vATPase, these protons are then exchanged for neurotransmitter through the relevant neurotransmitter transporter (e.g, VACHT for acetyl choline and VMAT for monoamine neurotransmitters) (Parsons et al, 1993). The filled vesicles are typically integrated into the “reserve pool”, which manifests as a cloud of SVs away from release sites at the AZ plasma membrane. SVs are sequestered there, waiting to be recruited to the plasma membrane and release their neurotransmitter load.

These vesicles are held together by links made of synapsin which immobilise them until they are required for release (Hirokawa et al, 1989; Takei et al,1995; Zhang and Augustine, 2021).

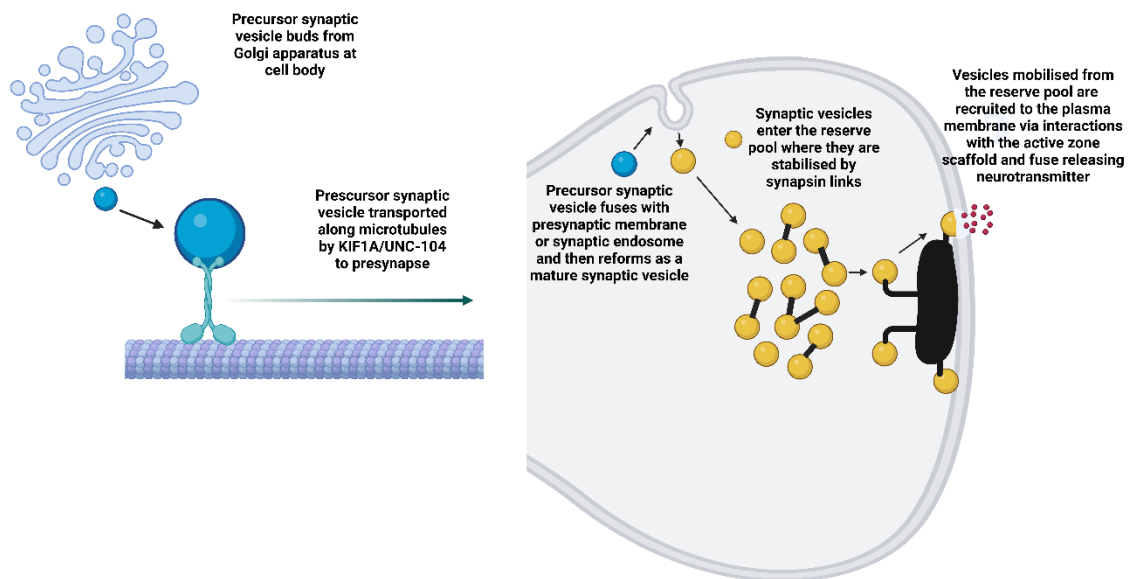


Figure 1.2. The transport and processing of SVs from the golgi apparatus at the cell body to the presynapse. Precursor SVs which have budded from the Golgi apparatus are transported to the presynapse by Kinesin-family motor proteins. The precursor proteins then fuse with either the plasma membrane or a synaptic endosome to reform as a fusion competent vesicle which is then filled with neurotransmitter. Fusion competent vesicles are sequestered in the reserve pool until recruited to the plasma membrane which is thought to be mediated by interactions with AZ scaffold proteins in a process known as tethering. Once docked and primed the vesicles then fuse. Created with “BioRender.com”

1.1.2 Docking, Priming and Fusion at the active zone

Neurotransmitters are released into the synaptic cleft through the fusion of SVs with the AZ plasma membrane at specific release sites. The SVs first localise to the plasma membrane in a process known as docking. In this process SVs are directed towards PIP2 (phosphatidylinositol 4,5-bisphosphate)-enriched regions of the presynaptic plasma membrane in part by Synaptotagmin (Syt) localised at the SV membrane, which then forms a spacer between the SV and the plasma membrane in the shape of a ring (Zhu et al, 2022).

Docked SVs are prepared for fusion by interacting with SNARE (soluble N-ethylmaleimide sensitive fusion protein (NSF) attachment receptor) complex proteins that are located in the SV membrane as well as the AZ plasma membrane. This process is termed priming. Synaptobrevin, the vesicular SNARE, binds other SNARE proteins situated in the AZ plasma membrane, specifically Syntaxin and SNAP-25 (Figure 1.3). Together the SNARE proteins form a stable partially coiled complex through the interaction of amphipathic helices in their SNARE motifs (Fasshauer et al, 1998). SNAP-25 donates two helices, whereas Synaptobrevin and Syntaxin each provide one, forming a 4-helical bundle. This process is supported by the AZ scaffold protein UNC-13 which transitions Syntaxin into an open conformation to facilitate its involvement in complex formation (Richmond et al, 2001; Yang et al, 2015). These complexes may be further stabilised by the SV-localised calcium sensor, Synaptotagmin in association with Complexin (Ramakrishnan et al, 2020).

Fusion itself is initiated upon the influx of calcium through AZ localised voltage-gated calcium channels (VGCCs) once an electrical stimulus reaches the synapse. These

VGCCs are localised to dedicated neurotransmitter release sites via AZ scaffold proteins including RIMB-1 and UNC-10 (Kushibiki et al, 2019; Krout et al, 2023). The increased calcium concentration is thought to trigger a conformational change in the vesicular membrane calcium sensor Synaptotagmin dissolving its homomeric ring structure and weakening its interaction with the SNARE complex (Courtney et al, 2019, Zhu et al, 2022). This allows the SNARE complex helices to transition from a loose partial coil to a tighter full coil, producing a “zipper” effect that generates enough energy for the vesicular and plasma membranes to be pulled together overcoming the charge repulsion between the two (Gao et al, 2012). The opening of a fusion pore through the destabilisation of the hydrophilic surfaces allows neurotransmitter to exit into the synaptic cleft and interact with postsynaptic receptors (Figure 1.3).

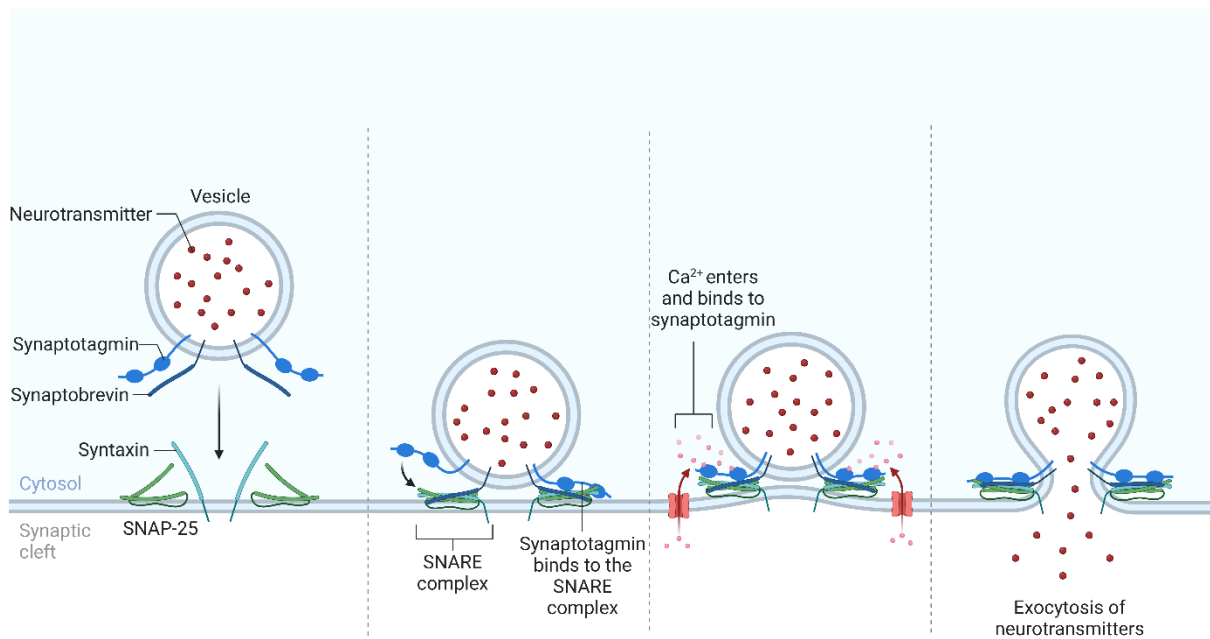


Figure 1.3. SNARE mediated SV fusion and neurotransmitter release. SVs are brought to the plasma membrane where the SV transmembrane protein Synaptobrevin interacts with fellow SNARE proteins Syntaxin and SNAP-25 in the plasma membrane to form a partially coiled SNARE complex. This complex is stabilised by the SV membrane protein Synaptotagmin, at this stage the vesicle has become 'primed'. Calcium influx into the presynapse caused by electrical stimulation weakens the stabilising influence of Synaptotagmin and permits SV fusion through a zipping mechanism of the SNARE complex dragging the SV membrane and plasma membrane together. A fusion pore is formed, and neurotransmitter released into the synaptic cleft. Reprinted from "Ca²⁺-triggered Vesicle Fusion and Exocytosis of Neurotransmitters", by BioRender.com (2023).

1.1.3 Endocytosis

To maintain SV presence at the presynapse without having to continually transport new vesicles; SVs and their membrane proteins are recycled through endocytosis (Figure 1.4). In this process, SV membrane which has fused with the presynaptic plasma membrane during neurotransmitter release is retrieved alongside SV

membrane proteins. The most common form of endocytosis is clathrin-mediated endocytosis (CME). The membrane patch is first targeted by amphipathic helices from co-factors, such as amphiphysin and endophilin, which induce membrane curvature (Rizzoli, 2014). The curved region is then coated with clathrin, forming clathrin-coated pits which gradually become more spherical. This creates a 'neck' between the nascent vesicle and the plasma membrane, which is severed by the GTPase dynamin, releasing the newly formed vesicle. The recycled vesicle can then be refilled with neurotransmitter. In response to high levels of exocytosis clathrin independent activity-dependent bulk endocytosis (ADBE) is also utilised, where invaginations of the plasma membrane form large cisternae from which multiple new synaptic vesicles can be formed (Figure 1.4) (Clayton and Cousin, 2009). In recent years a new, faster method of endocytosis has also been described, which may also support the high rates of exocytotic release found at synapses. Ultrafast endocytosis is clathrin-independent but like CME supports the endocytosis of single SVs. Ultrafast endocytosis is much quicker, however, recovering vesicle membrane within 100ms (Watanabe et al, 2013; Watanabe et al, 2017). CME meanwhile requires 30-120s due to the requirement for adaptor proteins and clathrin triskelia which must be activated and recruited to the site of endocytosis. This time lag likely means that CME is likely insufficient to support high rates of exocytosis.

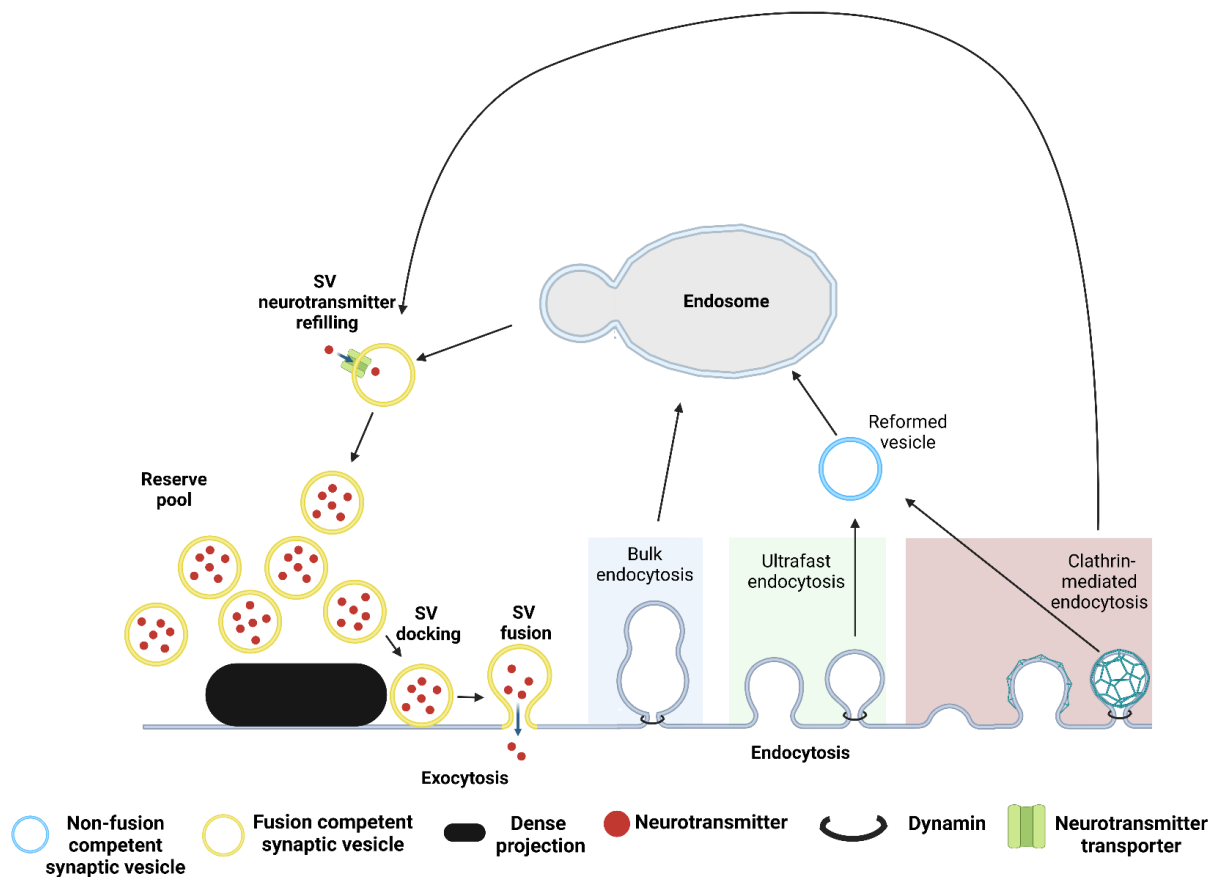


Figure 1.4. The synaptic vesicle cycle. Following SV fusion synaptic vesicle membrane components and proteins fused into the presynaptic plasma membrane are recovered to form new SVs in a process known as endocytosis. Endocytosis can take different forms depending upon the specific neuron and its state of activity. These are either clathrin-mediated endocytosis (CME), ultrafast endocytosis or bulk endocytosis. CME and ultrafast endocytosis initially form new vesicles which typically fuse with a synaptic endosome. Bulk endocytosis meanwhile typically invaginates enough membrane to form its own endosome. From the endosome, fusion competent vesicles are produced which are then filled with neurotransmitter and re-enter the reserve pool. CME can bypass fusion and remodelling at an endosome. Created with Biorender.com.

SVs are the most important entities of chemical neurotransmission in that they provide a mechanism through which neurotransmission can be controlled. Their transport,

recruitment, release, and recycling therefore must be tightly regulated, all these processes are closely linked to the central AZ protein scaffold.

1.2 The active zone scaffold

The AZ scaffold refers to a structure situated immediately adjacent to the presynaptic plasma membrane in the centre of the AZ. The central AZ scaffold is one of the earliest features to develop at a burgeoning synapse following specification of a presynaptic site (Patel and Shen, 2006; Fouquet et al, 2009) and is composed of several key facilitators of SV release.

Studies among different bilaterian species have shown that a core set of five evolutionarily conserved proteins are consistently integrated into the AZ scaffold, namely Liprin- α , RIM (RAB-3 interacting molecule), RIM-BP (RIM binding protein), ELKS and MUNC-13 family proteins. More recently a functionally homologous group of scaffold proteins has also become more prominent, namely Bassoon/Piccolo (vertebrates) (tom Dieck et al, 1998; Fenster et al, 2000), Fife (*Drosophila*) (Bruckner et al, 2012; Bruckner et al, 2017), and Clarinet (*C. elegans*) (Xuan et al, 2017).

The active zone scaffold proteins form multiple interactions, both with each other and a multitude of other presynaptic proteins, including those coating the outer SV membrane. RIM and Bassoon/Piccolo-family proteins have both been implicated in the SV docking process. Bassoon and Piccolo are thought to sequester SVs from the cytoplasm and shuttle them close to the plasma membrane near to docking sites (Cases-Langhoff et al, 1996; Mukherjee et al, 2010), where they are in part retained

by RIM proteins (Richmond et al, 1999; Lichter et al, 2022). MUNC-13 meanwhile is a key designator of the sites of SV release (Weimer et al, 2006; Reddy-Alla et al, 2017), while also being the primary promoter of SNARE complex formation through manipulation of Syntaxin conformation (Sassa et al, 1999; Yang et al, 2015). MUNC-13 is therefore vital to SV priming and release. In many species the loss of RIM or MUNC-13 proteins strongly reduces SV release probability at synapses due to a lack of fusion-competent SVs at the presynaptic membrane (Augustin et al, 1999; Richmond et al, 1999; Koushika et al, 2001; Schoch et al, 2002).

The broad interactome of AZ scaffold proteins means that not only are they able to ensure functional synaptic release but they may be capable of fine-tuning it. One mechanism through which they are suggested to achieve this is the regulation of calcium channel localisation at the plasma membrane. Both RIM and RIM-BP have mutually redundant roles in calcium channel recruitment to the plasma membrane (Kubishiki et al, 2019). Due to the paramount importance of calcium to SV fusion and neurotransmitter release, changes in calcium channel expression have the potential to alter neurotransmitter release probability and can therefore modify the strength of synaptic connections (Catterall and Few, 2008).

While the AZ scaffold is clearly vital to presynaptic function, much about how the structure forms and remains as a complex is unclear. While Liprin- α seems to typically be the first scaffold component arriving at a new presynaptic site and appears to organise the initial AZ scaffold (Fouquet et al, 2009), the mechanisms through which other components are integrated into a functional complex are unclear. One way we can begin to unravel this is by using electron microscopy to interrogate how the loss of individual proteins change the AZ scaffold architecture. This is possible due to the

presence of an electron-dense correlate of the AZ scaffold at presynaptic sites known as the dense projection.

1.2.1 Dense projections

At the presynaptic AZ, the core of the AZ scaffold can be visualised with electron microscopy (EM) as an electron-dense structure projecting into the cytoplasm from the plasma membrane. These structures, often referred to as dense projections, are conserved across bilateria and have been identified in multiple ecdysozoan, spiralian and deuterostome species. Electron-dense material has also been found lining photoreceptor presynaptic membranes in cnidarians, suggesting that dense projections are ancient structures which may even predate the bilaterian common ancestor (Gray et al, 2009). Despite evolutionary conserved core components like Liprin- α , RIM, RIM-BP, ELKS, (M)UNC-13 and Piccolo/Bassoon family proteins, there is striking morphological diversity in dense projection structure between species and synapse types.

In vertebrates, considerable variation in dense projection morphology can be observed across different types of synapses. Early electron microscopy studies using ethanolic phosphotungstic acid staining in examination of central synapses, such as those of the mammalian parietal cortex, revealed dense projections as a grid of almost pyramidal densities with SVs docking in the gaps between them (Aghajanian and Bloom, 1967; Dresbach et al, 2001). Later approaches using high-pressure freezing and freeze substitution for sample preparation paired with electron tomography found less electron-dense material at the presynaptic plasma membrane although this was

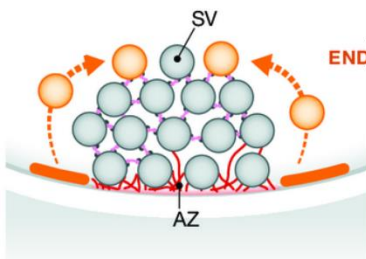
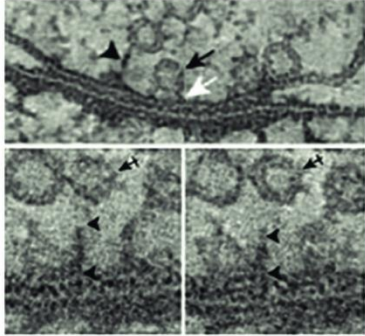
accompanied by filaments extending out into the cytoplasm, contacting synaptic vesicles (Figure 1.5A) (Siskou et al, 2007). RIM1 α appears to be involved in the formation of these tethers (Fernández-Busnadiego et al, 2013). Neuromuscular junctions (NMJ), where neurons innervate muscle cells, may be somewhat more complex and expansive. At the NMJ of the northern leopard frog (*Rana pipiens*), the dense projection has been likened to a sail-like structure with a 'beam'-like density running along the plasma membrane with 'masts' extending ~75nm into the cytoplasm at regular intervals (Figure 1.5B). From these 'beams' and 'masts' protrude numerous additional dense structures including 'booms', 'spars' and 'ribs' which contact docked SVs, and 'topmasts' which appear to tether undocked SVs to the structure (Harlow et al, 2001; Szule et al, 2012). These structures are thought to act as a means of recruiting and docking SVs to the presynaptic plasma membrane. Whether specific scaffold proteins correspond to these structures is unclear, although due to its association with SV docking RIM is hypothesised to be located within the 'ribs', 'spars' or 'booms' whereas Piccolo and Bassoon may form part of the mast or topmasts to recruit SVs from the reserve pool (Szule et al, 2012). Mammalian NMJs appear to conform to a similar shape although they have not been examined to the same extent. The greatest active zone scaffold complexity is found within sensory synapses. Vertebrate retinal photoreceptors, cochlear inner hair cells and electroreceptors found in fish have been shown to have very long dense projections, termed ribbons, which extend a considerable distance into the cytoplasm and are thought to act as a conveyor belt continually transporting SVs to release sites (Figure 1.5C) (Sejnowski and Yodlowski, 1982; Rao-Mirotnik et al, 1995; Dick et al, 2003). These ribbon synapses are formed of two electron-dense portions. The first is a presynaptic density which abuts the presynaptic plasma membrane next to which SVs dock on either side.

This is known as the arciform density at retinal photoreceptors. The second is the synaptic ribbon itself which attaches to the presynaptic/ arciform density and protrudes into the cytoplasm. The ribbon is a product of the RIBEYE/CTBP2 protein (Maxeiner et al, 2016), which is specific to sensory synapses in vertebrates. Interestingly, proteomic analysis has indicated that beyond RIBEYE/CTBP2 the composition of sensory presynapses is very similar to that of central synapses with active zone scaffold proteins Liprin- α 2, RIMBP2, ELKS1, ELKS2, Piccolo and Bassoon all being identified from affinity purified synaptic ribbons (Kantardzhieva et al, 2012). Later studies have also confirmed the presence of RIM2 at photoreceptor ribbon synapses (Jung et al, 2015; Löhner et al, 2017). Considering that the morphological differences between dense projections at different synapses are likely to be reflective of varying functional requirements this suggests that active zone scaffold proteins are incredibly versatile in terms of constructing subcellular complexes and supporting their functions.

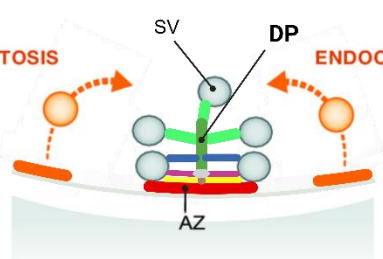
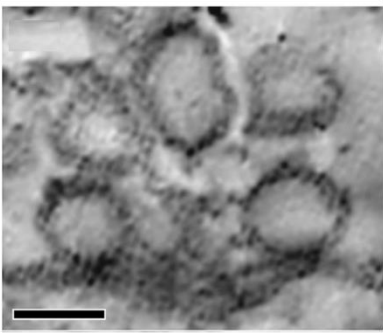
Invertebrates appear to have less variability in dense projection morphology at different synapses in individuals, however, there is still considerable diversity between different species. While in *Drosophila melanogaster* dense projections at both central and peripheral synapses form as a distinct T-bar structure advancing into the cytoplasm (Figure 1.5D) (Wagh et al, 2006), dense projections of the *C. elegans* nervous system remain closer in proximity to the plasma membrane (Figure 1.5E). Similar structures to the *Drosophila melanogaster* T-bar have been identified in a variety of other arthropods including other insects (Ribi, 1981; Newman and Duce, 1983; Tolbert et al, 1983) and crustaceans (Govind et al, 1980). The *Drosophila* T-bar shape is tightly linked to its ELKS homologue, Bruchpilot (BRP) which also acts as a tether for SVs and recruits Ca²⁺ channels. Proper arrangement of BRP at the active

zone is supported by RIM-BP which also provides a means of shuttling SVs to the plasma membrane.

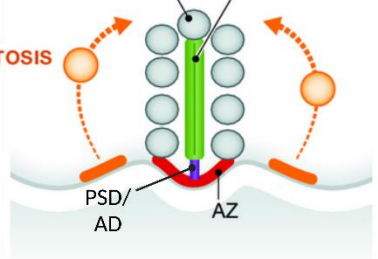
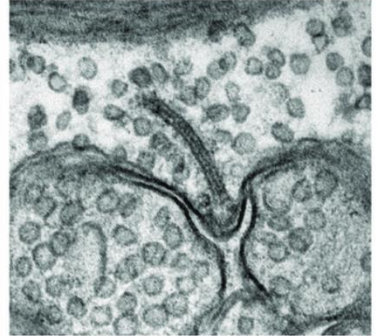
A CENTRAL SYNAPSE
Vertebrate



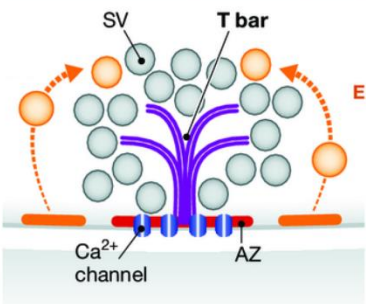
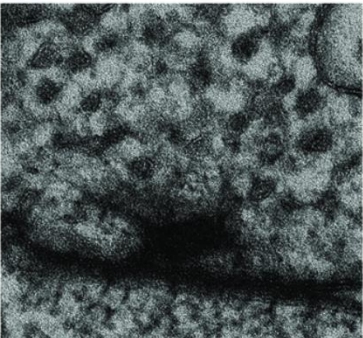
B NEUROMUSCULAR JUNCTION
Vertebrate



C RIBBON SYNAPSE
Vertebrate photoreceptor cell
ribbon synapse



D T-BAR STRUCTURE
Neuromuscular junction (NMJ)
D.melanogaster



E DENSE PROJECTIONS
Neuromuscular junction (NMJ)
C.elegans

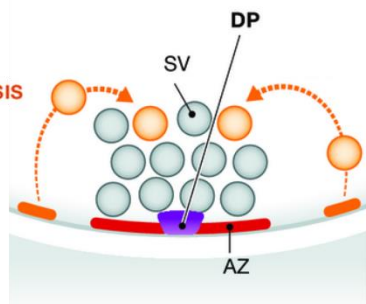
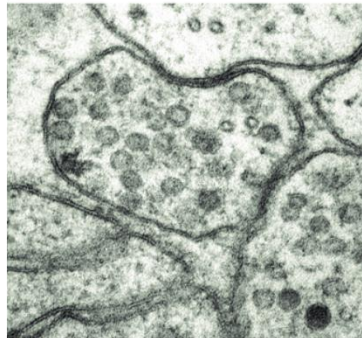


Figure 1.5. Appearance of dense projections in electron micrographs among different species.

For each type of dense projection morphology a schematic representation is shown below. **A.** Dense projection of mammalian central synapses from high-pressure freezing (HPF) and freeze substitution preparation. **B.** Morphology of the northern leopard frog (*Rana pipiens*) NMJ dense projection. Independent regions of the dense projection structure are indicated as described in Szule et al, 2012 with mast (dark green), topmasts (light green), ribs (yellow), spars (pink) and booms (blue). **C.** Ribbon synapse dense projection structure found at highly active vertebrate sensory synapses. **D.** Morphology of the *Drosophila melanogaster* T-bar as found at the NMJ. **E.** Typical *C. elegans* dense projection. Electron micrograph shows a *C. elegans* NMJ. A, C, D and E reprinted with permission from Ackermann F, Waites CL, Garner CC. Presynaptic active zones in invertebrates and vertebrates. EMBO Rep. 2015. doi: 10.15252/embr.201540434. B Micrograph reprinted with permission from Szule JA, Harlow ML, Jung JH, et al. Regulation of synaptic vesicle docking by different classes of macromolecules in active zone material. PLoS One. 2012;7(3):e33333. doi:10.1371/journal.pone.0033333. Created with Biorender.com.

Historically the *C. elegans* dense projection had been suggested to lack complexity, however, contemporary approaches to EM have helped to shed light on previously hidden features of the structures. Techniques such as electron tomography, which provides high resolution detail of the structures in three dimensions, and high-pressure freezing with subsequent freeze substitution, which better preserves protein interactions and structural morphology, have been at the forefront of this (Hall and Rice, 2015). Filamentous strands have been observed emanating from the centre of the dense projection into the cytoplasm (Stigloher et al, 2011), much like those at vertebrate central synapses, and are believed to be involved in the recruitment of SVs (Hallermann and Silver, 2013). In addition to the discovery of filaments, 3D reconstructions of *C. elegans* AZs have revealed a branching ultrastructure with

putative SV docking bays (Kittelmann et al, 2013). This complex architecture appears to be in part maintained by SYD-2/Liprin- α and UNC-10/RIM (Stigloher et al, 2011; Kittelmann et al, 2013).

Despite our improving grasp of the complexity of the AZ scaffold ultrastructure the identity of the full complement of proteins which contribute to the formation and stability of the structure remains contentious as no single protein among the archetypal active zone scaffold proteins appears to be critical to the formation of the structure. As discussed, α -liprins (Wyszynski et al, 2002; Yeh et al, 2005), RIM (Weimer et al, 2006), RIM-binding proteins (RBP) (Liu et al, 2011), (M)UNC13 (Weimer et al, 2006), CAST/ELKS (Ohtsuka et al, 2002; Fouquet et al, 2009) and Piccolo/Aczonin family proteins (tom Dieck et al, 1998; Xuan et al, 2017) have all been demonstrated to localise to the AZ either within or in close proximity to the AZ scaffold. While there have been relatively few studies exploring the effects of genetic disruption of these proteins on dense projection formation, the removal of SYD-2/Liprin- α , RIM/UNC-10, ELKS, RBP or CLA-1/Fife in invertebrates does not prevent the formation of presynaptic dense projections and often have limited effects (Koushika et al, 2001; Krout et al, 2023), although the resulting structures can be reduced in size and complexity (Kaufmann et al, 2002; Kittelmann et al, 2013; Xuan et al, 2017; Krout et al, 2023). The resistance of the dense projection to disruption is likely a consequence of the complexity of the AZ protein milieu, which may have mechanisms to compensate for the loss of single proteins. Indeed, only in one model organism, *Drosophila melanogaster*, has the functional deletion of one of these proteins, namely the ELKS homologue BRP been demonstrated to drastically reduce the dense projection structure. This also results in greatly reduced evoked junctional currents at larval NMJs (Kittel et al, 2006). In most examined species ELKS family proteins lack

a clear role in dense projection formation, however BRP is notably unusual. BRP possesses an elongated C-terminal region which extends into the cytoplasm providing the recognisable T-bar shape of the *Drosophila* dense projection. The protein also possesses multiple key interaction sites with other active zone proteins including calcium channels, Liprin- α and RIM-BP which are critical to T-bar structure and function. Together these adaptations appear to have allowed BRP to take up a central role in *Drosophila* active zone scaffold formation. While the dense projection at *brp* mutant synapses is clearly reduced in size and frequency, however; electron-dense material is not completely eradicated from the presynaptic site.

Altogether, this suggests that full disruption of the dense projection requires the simultaneous removal of several AZ proteins. Using this as an investigative approach would allow us to understand the most important components of the structure by determining the minimal components that need to be removed to eliminate the structure. This would also help us to understand whether there are specific proteins directing the formation or stability of the structure or if there is redundancy between the AZ proteins.

Investigating this concept in higher organisms such as vertebrates is often complicated by the presence of multiple paralogues of AZ scaffold proteins. In mammalian systems for instance four different genes encode Liprin- α proteins, two encode RIM-family proteins and two encode ELKS proteins. Although these paralogous proteins can differ slightly in sequence, they possess considerable structural similarity and can in some instances functionally compensate each other (Han et al, 2015). The invertebrate *C. elegans* meanwhile, only possess a single gene encoding any of the AZ scaffold proteins, and unlike many other organisms remains

consistently viable upon the removal of any of them. This makes *C. elegans* an incredibly valuable model organism for exploring the function of the AZ scaffold/dense projection and the role individual proteins play in its formation.

1.3 *C. elegans* as a model organism

Caenorhabditis elegans is a free-living, soil dwelling transparent nematode found ubiquitously around the world. Research using this organism was initiated by Sydney Brenner in the mid-1960s and it is now perhaps the most well understood multicellular organism (Brenner, 1974). *C. elegans* are very small reaching an adult length of 1mm-1.5mm and a diameter of 65µm. They feed upon bacteria, in laboratory environments this typically consists of a specific *Escherichia coli* strain (OP50) which is seeded upon agar plates. The worms typically consist of self-fertile hermaphrodite populations which allows easy maintenance of viable homozygous mutant strains. Males can arise spontaneously through chromosomal non-disjunction at a rate of 1 in 1000 and can be used for genetic crossing. Their life cycle is also incredibly rapid, taking approximately 3.5 days from egg fertilisation to becoming a fertile adult. Altogether this makes *C. elegans* easy to maintain in large numbers.

Alongside the ease of its maintenance, the organism also has numerous biological advantages. It was the first multicellular organism to have its entire genome sequenced and annotated (*C. elegans* Sequencing Consortium, 1998), consequently this has seen the production of a large suite of genetic tools to manipulate gene expression. Alongside mutagenesis screens, CRISPR-Cas9 is now routinely used to make custom edits to the genome (Kim et al, 2022). Despite a lack of obvious

redundancy among the majority of *C. elegans* proteins most homozygous null mutations are viable in the worms. Together this is incredibly useful for clarifying the functional significance of specific genes and proteins. Additionally, genetic crossing allows the combination of several mutant backgrounds. As the majority of *C. elegans* proteins are also highly conserved and possess strong structural and functional similarities, the organism is an excellent model for understanding the function of protein families in health and disease.

Exploring the effects of null mutations in *C. elegans* is aided by the overall simplicity of the organism. All wild-type adult hermaphrodites are composed of exactly 959 somatic cells which derive from invariant lineages. This results in remarkable uniformity between individuals with the location of any specific cell being highly predictable. The trajectory of neurites and their synaptic targets are similarly consistent and has facilitated the publishing of the full *C. elegans* connectome which has detailed the shape and synaptic connections of all 302 neurons within the adult hermaphrodite (White et al, 1986; Cook et al, 2019). To date this remains the only existing full connectome of any adult animal and is an incredibly valuable resource for neurobiological research.

With only 302 total neurons in the *C. elegans* adult hermaphrodite (387 in the male), the *C. elegans* nervous system is small, but is easily the most complex tissue within the organism, being composed of 37% of the animal's somatic cells and containing 118 distinct neuronal classes. The three major features of the nervous system are the nerve ring and the ventral and dorsal nerve cords, most neurons can be found within one of these three structures (Figure 1.6A). The nerve ring is a tight bundle of axons containing processes from more than half of the total *C. elegans* neurons. Nerve ring

interneurons integrate information from other neurons including sensory cues from gustation and olfaction to direct animal behaviour. The ventral and dorsal nerve cords meanwhile, are primarily involved in facilitating locomotion through the formation of neuromuscular junctions with body wall muscle. The nerve cords are composed of cholinergic and GABAergic motor neurons, which form *en passant* synapses along their axons with muscle arms which extend into the nerve cords from the body wall muscle (Figure 1.6B).

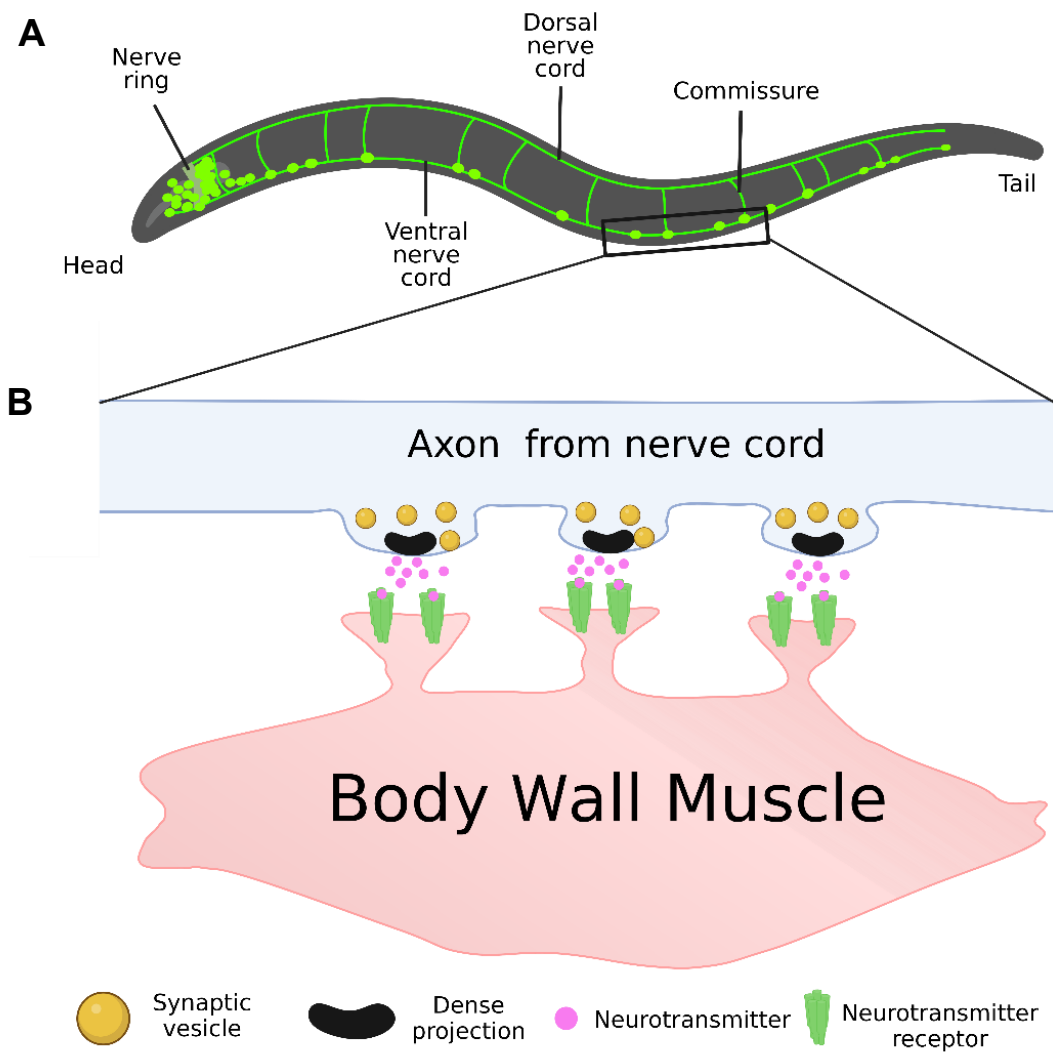


Figure 1.6. Overview of the main features of the *C. elegans* nervous system. **A.** Simplified representation of the *C. elegans* nervous system visualising the nerve ring and the dorsal and ventral nerve cords with the commissures connecting them. **B.** Representation of the *en passant* neuromuscular junctions formed between a nerve cord axon and the muscle arms of body wall muscle.

Created with Biorender.com

The nervous system of *C. elegans*, while primitive compared to that of vertebrates, and even other invertebrates such as *Drosophila*, is still capable of giving rise to complex behaviours. *C. elegans* is amenable to classical conditioning through which they demonstrate positive and negative taxis to desirable and noxious stimuli

respectively (Rahmani and Chew, 2021). The ability to adapt behaviour requires a level of plasticity within neuronal circuits and, much like in higher organisms, *C. elegans* can modulate the strength of its synaptic connections through the modification of synaptic proteins, modulation of synaptic protein expression or signalling with neuropeptides (Bozorgmehr et al, 2013; Hawk et al, 2018; Cuentas-Condori and Miller, 2020).

On the surface *C. elegans* is a biologically simple organism, having a small genome with little redundancy and a very small nervous system. Despite these limitations it is still capable of generating intracellular structures which are analogous to those found in more complex organisms such as presynaptic dense projections. Together this makes *C. elegans* a useful model for identifying the proteins fundamental to these complexes. This is particularly relevant for the nervous system which in higher organisms can vary greatly between individuals but remains incredibly consistent in *C. elegans*. These properties make *C. elegans* both a versatile and robust model in which to study the nervous system.

1.3.1 *C. elegans* neuromuscular biology

Of the 302 neurons within *C. elegans*, 113 innervate muscles. The majority (75) of these innervate the 95 body wall muscle cells which direct gross body movement in both forward and backward directions which typically take the form of a sinuous wave on a solid surface. While these motor neurons collectively span both the ventral and dorsal nerve cords their somas all reside within the ventral nerve cord.

C. elegans motor neurons innervating the body wall muscle can be divided into 5 major classes: A, B, D, VC and AS (Zhen and Samuel, 2015). The A, B and D, which represent the main muscle innervating classes in the nerve cords, are further subdivided depending upon whether they synapse with the dorsal or ventral body wall muscles (Figure 1.7). This gives rise to the ventrally innervating VA, VB and VD and the dorsally innervating DA, DB and DD neuron classes. The A- and B-type motor neurons are both cholinergic and provide excitatory input to the muscle. The A subclass contribute specifically to backwards locomotion whereas the B subclass drive forward locomotion. The D subclass meanwhile is GABAergic and instead deliver an inhibitory signal.

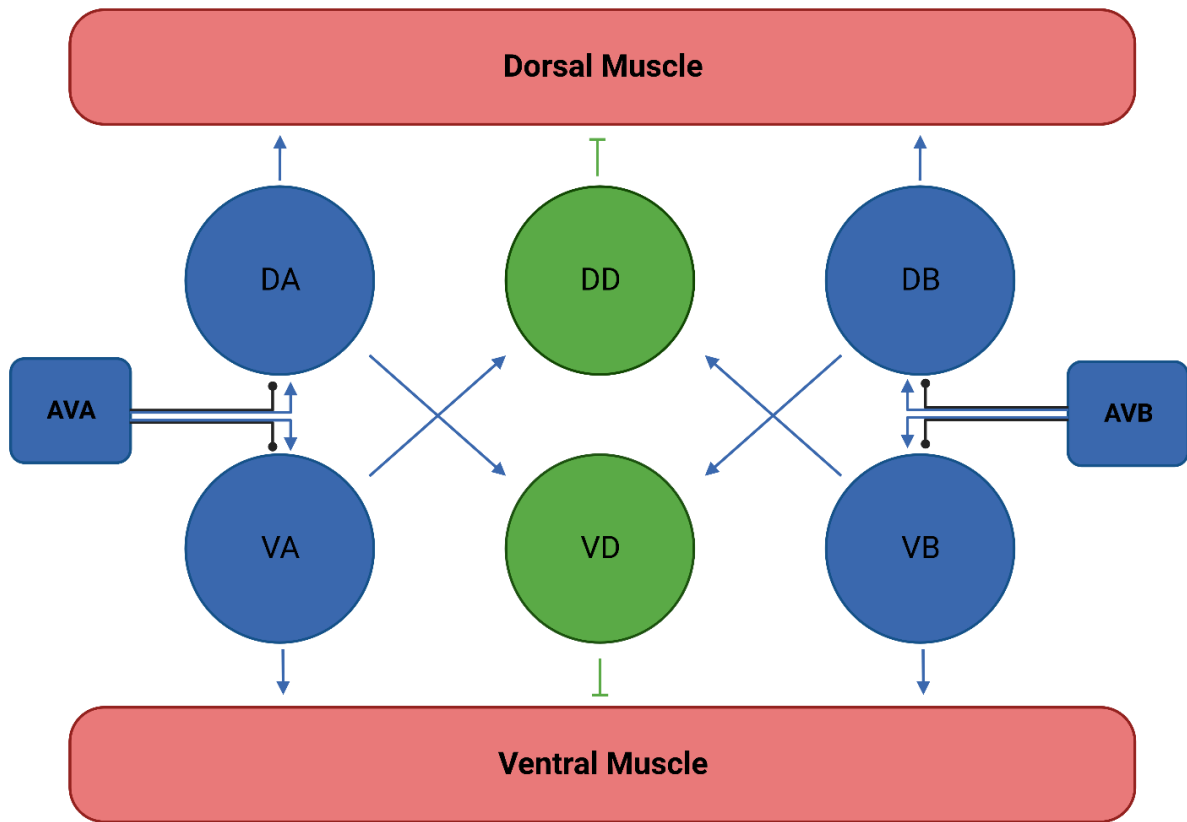


Figure 1.7. Schematic of the innervation patterns found within the *C. elegans* nerve cords. Circles are motor neurons; squares are command interneurons. Blue is cholinergic, green is GABAergic. Lines indicate synaptic connections with arrow tips indicating excitatory neurotransmission, flat ends are inhibitory, circular ends on a back line are electrical gap junction synapses. Created with Biorender.com.

The 22 dorsally innervating motor neurons send their axons across commissures to the dorsal nerve cord from the ventral nerve cord to form synapses (Zhen and Samuel, 2015). The interconnectivity of the two cords via these commissures is exploited to provide contralateral regulation of locomotion. DA and DB motor neurons stimulate inhibitory VD neurons, whereas VA and VB motor neurons stimulate inhibitory DD neurons. This means that as muscle on one side of the worm is instructed to contract

the opposite side is relaxed. This adversarial signalling is thought to maintain the wave-like locomotion of *C. elegans*.

The neuromuscular junctions which form between the motor neurons and body wall muscle are an excellent model for examining synapse formation and function. Neuromuscular junctions in each *C. elegans* nerve cord are highly structured and can be approximately reduced to an iterative pattern of 3 muscle pairs being innervated by 6 motor neurons which repeats 6 times (Haspel and O'Donovan, 2011; Haspel and O'Donovan, 2012). This results in regular, evenly spaced synapses which make them ideal for investigations into abnormal synapse formation using fluorescence microscopy techniques. Additionally, as the activity of these synapses drive locomotion, assessment of *C. elegans* movement can provide an indication of synaptic function.

1.4 Potential organisers of the *C. elegans* AZ

In *C. elegans* the formation of the AZ is initiated soon after the designation of a synaptic site. The mechanisms underlying synaptic specification are not fully understood at all synaptic sites, although some important insights have been made. In the hermaphrodite specific neuron (HSN) the interaction between the postsynaptic SYG-2 and the presynaptic SYG-1, immunoglobulin superfamily transmembrane proteins with large extracellular domains which span the synaptic cleft, have been shown to designate new synaptic sites (Shen et al, 2004). Other proteins possessing extracellular domains such as neurexin and netrin have also been implicated (Nelson and Colón-Ramos, 2013; Kurshan et al, 2018; Philbrook et al, 2018). These direct

trans-synaptic interactions are thought to trigger recruitment of NAB-1, which in turn recruits early AZ proteins SYD-1 and SYD-2 (Patel et al, 2006).

The arrival of SYD-2, the homologue of Liprin- α , signals the beginning of AZ scaffold formation. Other AZ scaffold proteins are then recruited to the site including UNC-10/RIM, RIMB-1/RIM-BP, ELKS-1 and CLA-1 as well as SVs (Figure 1.8). SYD-2 appears to be critical in the recruitment of these other components. Previous studies have shown that the loss of SYD-2 interferes with SV recruitment and the organisation of other AZ components, particularly UNC-10, ELKS-1, RIMB-1 and CLA-1 (Deken et al, 2005; Xuan et al, 2017; Oh et al, 2021). These active zone scaffold proteins have themselves been suggested to contribute to the recruitment and localisation of other active zone proteins, although this is contested across some studies (Koushika et al, 2001; Deken et al, 2005; Xuan et al, 2017) and their effects are dwarfed by that of *syd-2* mutants (Oh et al, 2021).

Based on these observations SYD-2 has been interpreted as the major organiser of the presynaptic AZ scaffold. In line with this the elimination of SYD-2 has been linked to a reduction in the size and complexity of dense projections (Stigloher et al, 2011; Kittelmann et al, 2013). This is likely linked to changes in presynaptic molecular composition and active zone scaffold construction caused by defective active zone protein recruitment. It is notable that there is a reduction in the prevalence of filamentous tethers in *syd-2* mutants which are associated with UNC-10, a protein recruited by SYD-2. Other changes to dense projection morphology such as reduced incidence of docking bays, may also be associated with changes in protein recruitment however as we currently know little regarding the subsynaptic localisation of many active zone scaffold proteins in *C. elegans*, or whether additional active zone can

replace diminished core scaffold components, it is difficult to infer the associations between recruitment and morphology.

The disruption caused by SYD-2 loss at the presynaptic active zone culminates in less effective neurotransmission with reduced evoked amplitudes, reduced frequency of miniature events and enhanced depression during extended stimulation trains (Kittelmann et al, 2013). Despite this, synaptic connections are still formed although both the number of AZ sites and SVs recruited to these sites are reduced (Kittelmann et al, 2013).

The continued capacity to form synapses in these null mutants suggests that other factors exist that are vital to AZ formation and stabilisation and perhaps even compensate for the loss of SYD-2. The aim of this thesis is to explore AZ proteins which may work alongside SYD-2 to form a functional AZ scaffold in *C. elegans*. For this, two proteins were chosen for examination alongside SYD-2, which are thought to localise to the active zone and interact with active zone scaffold components but have thus far undergone only limited study: CLA-1 and HLB-1. Throughout this thesis I have examined the effects exerted upon AZ formation, dense projection morphology and synaptic function, in terms of neurotransmission and locomotor behaviour, by the simultaneous loss of these three proteins in double and triple mutant strains.

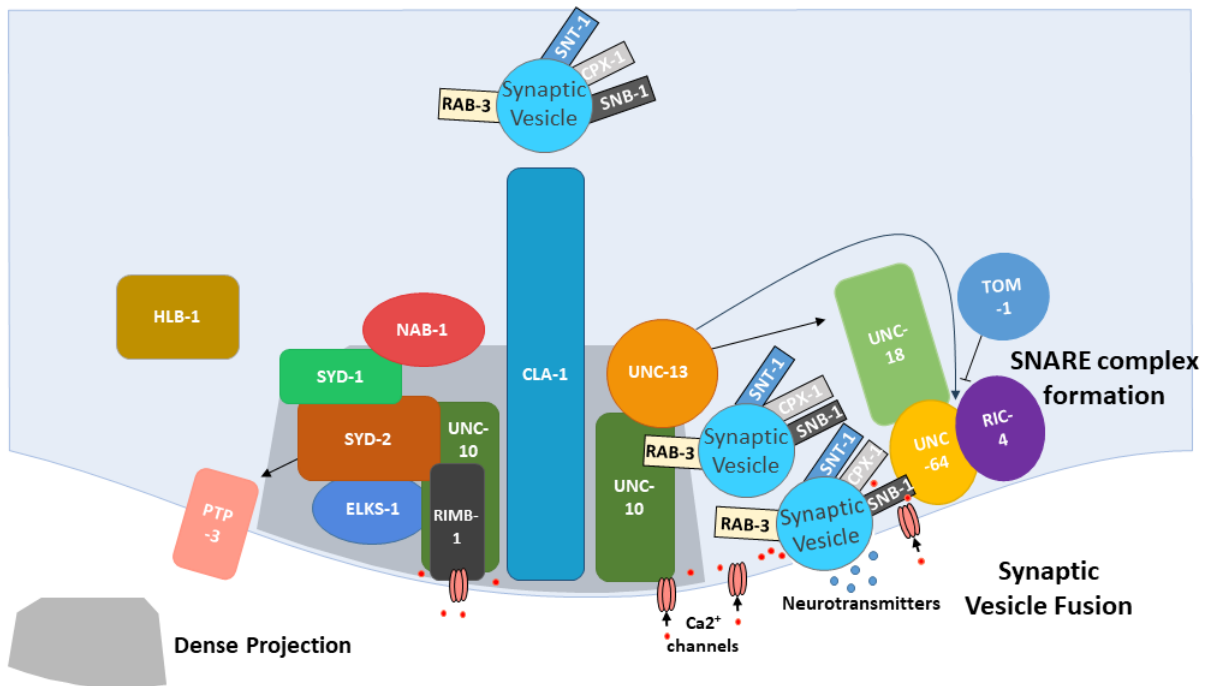


Figure 1.8. Overview of the known protein composition of the AZ cytomatrix in *C. elegans* and the protein interactions held therein. Published interactions of note between individual active zone scaffold proteins (shown within the dense projection), synaptic vesicle proteins and other active zone proteins are indicated by overlapping proteins or arrows. The SNARE complex (UNC-64, RIC-4 and SNB-1) is a three-part interaction involving all three proteins.

1.4.1 SYD-2

SYD-2 is the lone *C. elegans* homologue of Liprin- α . The protein was first identified through sequence similarity searches of the mammalian Liprin- α sequence in *C. elegans* databases (Serra-Pagès et al, 1998). The protein is 1139 amino acids long with an evolutionarily conserved domain structure which can be divided into two regions: the N-terminal coiled-coil region which extends along the first half of the

protein (AA 1-514), and the three C-terminal SAM (sterile alpha motif) domains, also referred to as the liprin homology domain (LHD), spanning the last quarter of the protein (AA864-1107) (Figure 1.9). These two regions are divided by a region of intrinsic disorder.

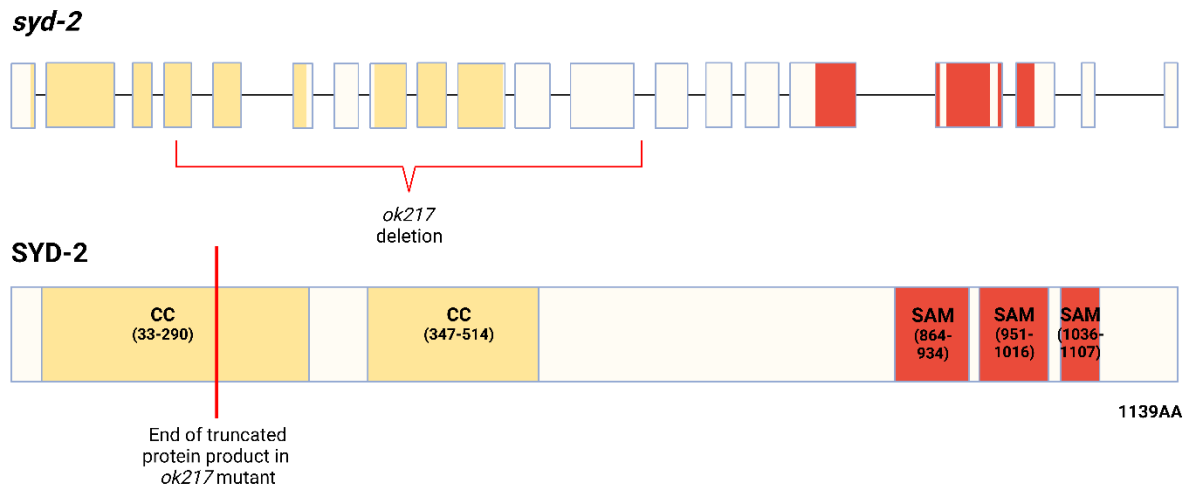


Figure 1.9. Schematic of the gene structure of *syd-2* (top) and the structure of the protein product (bottom). Exons are coloured to correspond with the domains of the protein encoded by them. The region affected by the *ok217* deletion and its effect on the protein product are as shown.

Created with Biorender.com.

SYD-2 plays several major roles in facilitating the formation of the AZ scaffold. It is involved in the active transport of SV precursors from the soma to synaptic sites along microtubules. This is achieved through its role as an adaptor protein for UNC-104 (Wagner et al, 2009), the homologue of the Kinesin-3 motor protein KIF1A. SYD-2 binds UNC-104 through both its N-terminal coiled-coil domains and C-terminal SAM domains and promotes the anterograde movement of the motor protein which transports several AZ proteins to the presynapse, including CLA-1, UNC-10, ELKS-1,

as well as SYD-2 itself (Xuan et al, 2017; Oliver et al, 2022). SYD-2 is also important for these transported proteins to disembark once they arrive at a synaptic site. SYD-2, SYD-1, SAD-1 and the recently identified Sentryn form the core synapse stability (CSS) system which retains the transported components at the synaptic site (Edwards et al, 2018).

The role SYD-2 plays in shaping the AZ scaffold itself is greatly influenced by its ability to form interactions with several other important proteins that participate in the structure. The N-terminal coiled coil regions of SYD-2 can interact with both ELKS-1 and UNC-10 (Deken et al, 2005). This region is also critical for SYD-2 to oligomerise with itself which may permit the creation of larger and more complex scaffolds. It is notable that docking bays for SVs observed in *C. elegans* wild-type dense projections are diminished and the overall size of the structure is reduced in loss of function *syd-2* mutants (Kittelmann et al, 2013). Conversely, a *syd-2* gain of function mutant, which has been demonstrated to promote oligomerisation of SYD-2 over dimerization (Liang et al, 2021), has been shown to produce much larger dense projections with additional bay-like structures (Kittelmann et al, 2013). Although C-terminal SAM domains are not known to interact directly with other AZ scaffold proteins they do mediate interactions with the LAR receptor protein tyrosine kinase-homologue PTP-3 (Serra-Pagès et al, 1998, Ackley et al, 2005) and RSY-1 (Patel and Shen, 2009), which are positive and negative regulators of AZ formation respectively.

For the purposes of this thesis, a SYD-2 null mutant was used as a sensitised background to understand whether the loss of other potential AZ scaffold components enhance its inherent defects. The *syd-2(ok217)* allele causes a 2184bp deletion

generating a premature stop codon creating a 200AA product (Figure 1.9) which appears to undergo degradation (Wagner et al, 2009).

1.4.2 HLB-1

HLB-1 is the single *C. elegans* homologue of Liprin- β and was originally identified alongside SYD-2 as the only other Liprin family molecule of the organism (Serra-Pagès et al, 1998). Liprin- α and Liprin- β proteins are predicted to have derived from an ancestral gene through a gene duplication event (Serra-Pagès et al, 1998), hence HLB-1 and SYD-2 possess ~23% identity between each other. Like other liprin proteins HLB-1 has a C-terminal liprin homology domain composed of three individual SAM domains (Figure 1.10). Unlike SYD-2, however, the HLB-1 SAM domains are not capable of interacting with the LAR receptor PTP-3 (Serra-Pagès et al, 1998). The HLB-1 N-terminus lacks a clearly defined structural organisation.

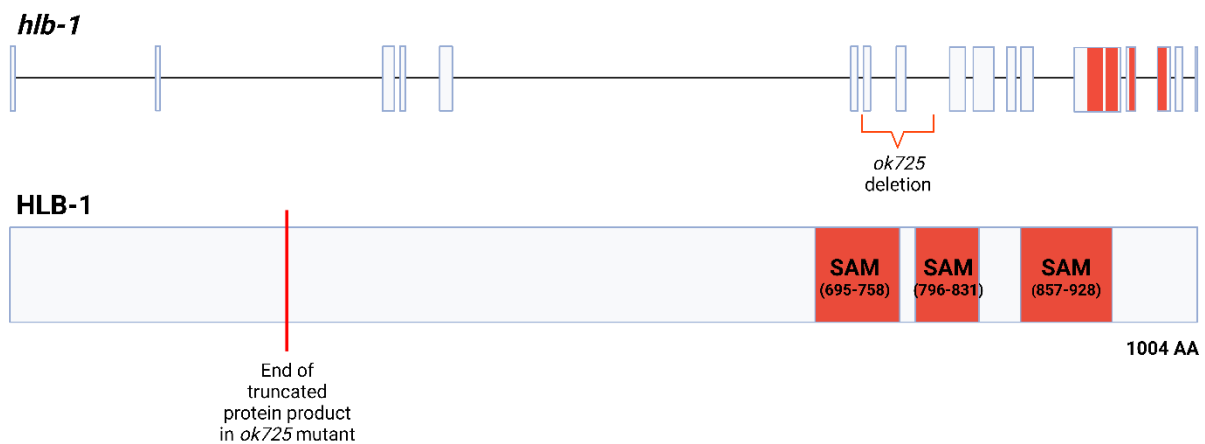


Figure 1.10. Schematic of the gene structure of *hlb-1* (top) and the structure of the protein product (bottom). Exons are coloured to correspond with the domains of the protein encoded by them. The region affected by the *ok725* deletion and its effect on the protein product are as shown. Created with Biorender.com.

Although the existence of HLB-1 has been known for some time its function is not well characterised. In *C. elegans*, the loss of HLB-1 has been found to reduce SV recruitment to AZ sites and reduce overall cholinergic neurotransmission based on increased aldicarb resistance (Wang and Wang, 2009; Rosenhahn et al, 2022). Reduced pharyngeal pumping rates have also been observed in these mutants (Wang and Wang, 2009; Rosenhahn et al, 2022). While this suggests the possibility that the protein has some role in ensuring regular presynaptic function, the mechanisms it acts through are entirely unknown.

In *Drosophila* the loss of Liprin- β causes a reduction in NMJ size, intriguingly this is further reduced when combined with Liprin- α (Astigarraga et al, 2010). The reduction in the double mutant is also greater than that of the Liprin- α single mutant.

Aside from the associations with synaptic function one of the most compelling reasons for investigating HLB-1 is that it may have a biologically relevant interaction with SYD-2. In both mammals and *Drosophila melanogaster* Liprin- α and Liprin- β proteins have been shown to interact through their respective C-terminal SAM domains (Serra-Pagès et al, 1998; Astigarraga et al, 2010; Wei et al, 2011). Many of the key residues likely to be involved in this interaction, such as those with opposing electrostatic charges, appear to be conserved in the *C. elegans* homologues SYD-2 and HLB-1 (Figure 1.11). An interaction between SYD-2 and HLB-1 could therefore be important for integrating HLB-1 into the AZ, limiting SYD-2s interactions with other regulatory factors or structural proteins.

only 234aa in length (Wang and Wang, 2009) (Figure 1.10). This small product lacks any clearly defined domains and is therefore unlikely to be functional.

1.4.3 CLA-1

CLA-1 was recently identified through a forward genetic screen for genes involved in SV recruitment in the serotonergic neuron NSM (Xuan et al, 2017). Further investigations showed the protein had much broader implications for presynaptic function throughout the nervous system. CLA-1 has no obvious single homologue in other organisms although its C-terminal C2 and PDZ domains have sequence similarity to complementary domains in RIM1 and Piccolo/Aczonin (Xuan et al, 2017)

The protein exists as two short (~1000AA), two medium (~3000aa) and two long (~9000aa) isoforms that only differ in the presence or absence of a short C-terminal sequence (Figure 1.12). All isoforms share a C2 and PDZ C-terminal domain which has been shown to localise to the AZ where these domains likely interact with other AZ proteins.

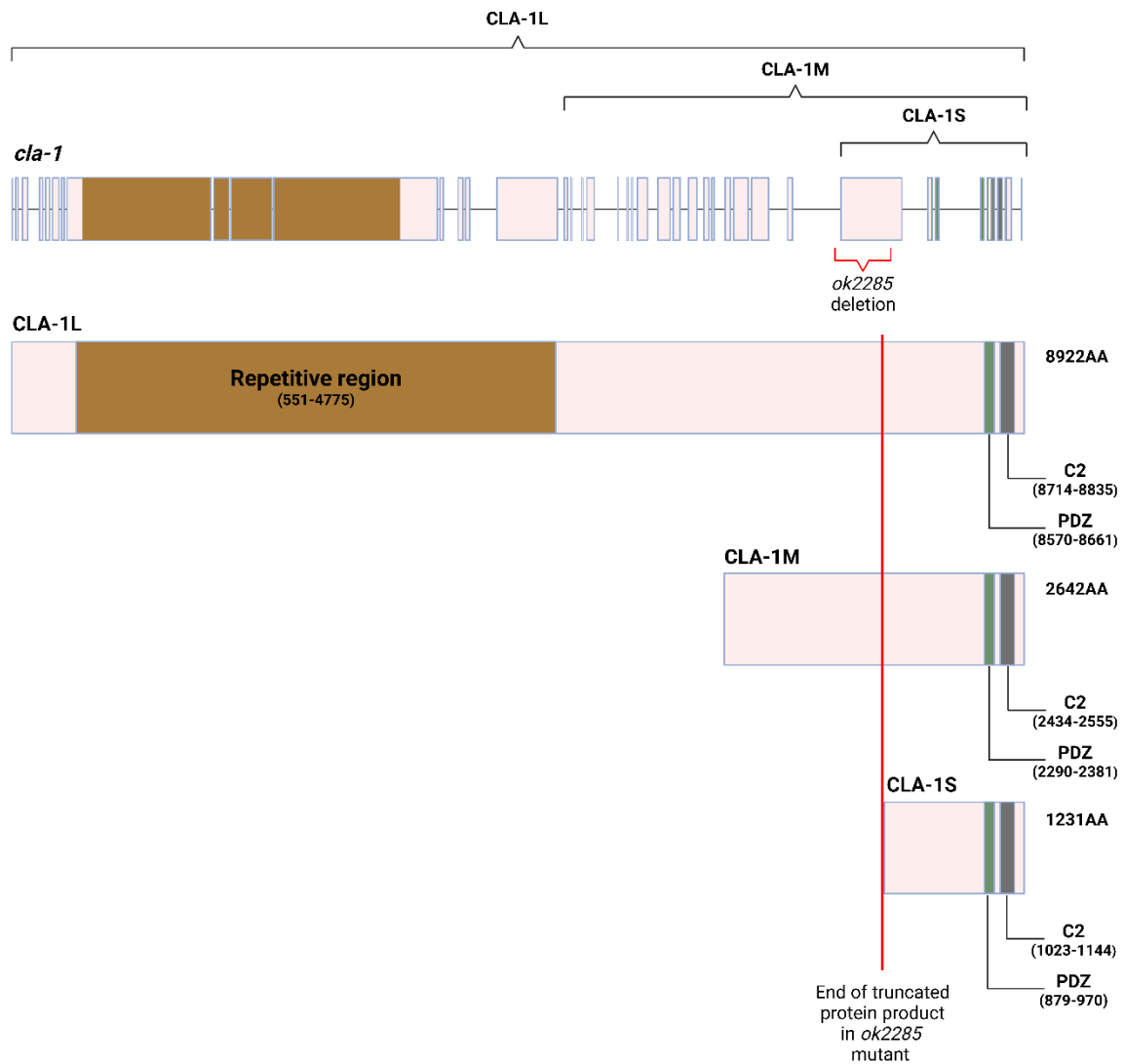


Figure 1.12. Schematic of the gene structure of *cla-1* (top) and the structure of the protein product (bottom). Exons are coloured to correspond with the domains of the protein encoded by them. The region affected by the *ok2285* deletion and its effect on the protein product are as shown.

Created with Biorender.com

The longest isoforms (CLA-1L) express an additional 4000aa long repetitive region at their N-terminus predicted to consist of random coils interspersed with α -helices. This

elongated region is thought to be reflective of a distinct function for these isoforms. Fluorescent tagging of the N-terminus of CLA-1L isoforms demonstrated that it extends out into the cytoplasm away from the AZ (Xuan et al, 2017). This may be important for procuring SVs at synapses undergoing prolonged stimulation. Recently published studies have indicated that these extended N-terminal regions may also contribute to endocytosis and degradation of unrequired synaptic components (Xuan et al, 2023).

The shorter isoforms are thought to be critical in tethering SVs to the AZ scaffold. This would be analogous to the putative roles of Bassoon and Piccolo at the mammalian synapse (Cases-Langhoff et al, 1996; Mukherjee et al, 2010). This was supported by electron microscopical analysis of *cla-1* null mutants which display fewer SVs at synaptic sites. Electrophysiological studies appear to further confirm this with stimulation trains inducing synaptic depression in mutant animals (Xuan et al, 2017).

The complete loss of CLA-1 from the dense projection has previously been shown to significantly reduce the length of the dense projection which suggests a function as AZ scaffold component or at least in its development (Xuan et al, 2017; Krout et al, 2023). This makes CLA-1 an intriguing candidate protein as a contributor to AZ formation in parallel or with SYD-2.

Throughout this thesis *cla-1* mutant worms carried the *cla-1(ok2285)* allele. This allele introduces a 2410bp deletion causing a frameshift and a subsequent premature stop codon. This deletion affects all CLA-1 isoforms removing the C-terminal C2 and PDZ domains which are likely to be important for their stabilisation at the AZ. Due to these

being the only domains shared by all isoforms these mutants have previously been predicted as functionally null (Xuan et al, 2017).

2. Investigating the role of SYD-2, HLB-1 and CLA-1 in the localisation of core active zone and synaptic vesicle components

The *C. elegans* active zone (AZ) scaffold sits at the centre of the presynapse. The prominent position of the structure at the synapse reflects its important role in controlling neurotransmission. The AZ scaffold acts as a focal point in the recruitment of synaptic vesicles (SVs), with several scaffold components involved in maintaining SV proximity to release sites and regulating their capacity to fuse with the plasma membrane and release neurotransmitter. Despite its implied functional importance, the pathways underpinning the formation of the AZ scaffold, including its full protein composition, organising elements, and stabilising factors are not fully understood.

Formation of the AZ scaffold occurs shortly after the designation of a presynaptic site by the recognition of a post-synaptic partner via transmembrane protein interactions. This initiates an intracellular cascade recruiting new proteins to the site. Among these is SYD-2, which is the best understood organiser of the *C. elegans* AZ scaffold (Dai et al, 2006; Kittelmann et al, 2013) and is a component of the structure itself (Yeh et al, 2005). SYD-2 homologues, Liprin- α family proteins, also play similar roles in other species (Kaufmann et al, 2002; Xie et al, 2021).

SYD-2 is important for the localisation of other scaffold components including UNC-10 (Deken et al, 2005; Oh et al, 2021), ELKS-1 (Oh et al, 2021), CLA-1 (Xuan et al, 2017), RIMB-1 (Oh et al, 2021) and UNC-2 calcium channels (Oh et al, 2021) as well as SVs (Zhen and Jin, 1999; Kittelmann et al, 2013). Electron microscopy has also

demonstrated that its loss results in a significant reduction in the size and complexity of the presynaptic AZ dense projection (Kittelmann et al, 2013). While this suggests a clear role for SYD-2 in AZ scaffold formation the observed reduction in dense projection size is mild, with dense projection length only reduced by a third (Kittelmann et al, 2013). Therefore, SYD-2 does not appear to be either the lone organiser or single core component of the AZ scaffold complex. The broader roles of SYD-2 in promoting anterograde transport of other AZ scaffold components and SVs via the Kinesin-3 motor protein UNC-104/KIF1A (Shin et al, 2003; Wagner et al, 2009), and the disengagement of these cargoes (Edwards et al, 2015) also adds complexity in determining SYD-2's role in AZ scaffold formation. The reduced availability of various synaptic components in animals lacking SYD-2 is likely to contribute to the reduced dense projection size of *syd-2* mutants. Of the other *C. elegans* AZ components only CLA-1 and RIMB-1 are currently known to contribute to dense projection size, however (Xuan et al, 2017; Krout et al; 2023). It is possible that redundancy among the AZ scaffold proteins compensate for the loss of single proteins from the structure.

To disentangle the contribution of SYD-2 and other AZ proteins in the formation of the AZ scaffold several proteins may need to be removed concurrently. This approach may be the path to observing greater disruption to the structure although it may require looking beyond the traditional AZ proteins such as UNC-10, ELKS-1 and RIMB-1. HLB-1 and CLA-1 are two such proteins which may support SYD-2 in the formation of the AZ scaffold.

Like SYD-2, loss of HLB-1 has been shown to disrupt SV recruitment to synaptic sites. HLB-1 is the homologue of Liprin- β , which has been shown to interact with Liprin- α in other species (Astigarraga et al, 2010; Wei et al, 2011). Liprin- α and Liprin- β also share

a number of structural similarities particularly in their C-terminal SAM domains (Wei et al, 2011). CLA-1, meanwhile is thought to localise to the AZ scaffold, based on fluorescence co-localisation studies and reduced dense projection size in mutants (Xuan et al, 2017). CLA-1 possesses a C-terminal PDZ domain which localises to the AZ (Xuan et al, 2017). PDZ domains are often a key feature of biological scaffold complexes (Zhang and Wang, 2003) and could be similarly important for AZ scaffold integrity. *cla-1* mutants also display reduced SV recruitment to specific synaptic sites (Xuan et al, 2017). I set out to examine whether CLA-1 and HLB-1 contribute to AZ formation alongside SYD-2 using a fluorescence imaging approach. Specifically, the distribution of fluorescence-tagged synaptic proteins in cholinergic motor neurons was assessed when *hlb-1* and *cla-1* mutations were added to the *syd-2* mutant background to see if AZ disruption is enhanced.

Cholinergic motor neuron synapses of the *C. elegans* dorsal and ventral nerve cords have a unique “pearls on a string” localisation pattern. Due to the transparency of *C. elegans* these synapses can be visualised *in vivo* by fluorescence tagging of synaptic proteins, this is also an effective means of identifying disrupted synapse formation. I used strains expressing GFP-tagged UNC-10 (the *C. elegans* homologue of RIM) and SNB-1 (the *C. elegans* homologue of Synaptobrevin) under the cholinergic neuron specific promoter *unc-129* to examine the state of the synaptic landscape when CLA-1 and HLB-1 is lost alongside SYD-2.

In these investigations GFP-tagged UNC-10 protein was used as a proxy for the distribution of AZ scaffolds. UNC-10 is one of the few proteins known to form part of the central AZ scaffold (Figure 2.1) (Weimer et al, 2006) and forms filamentous tethers which maintain SV proximity to release sites (Stigloher et al, 2011). UNC-10/RIM is

highly conserved with homologues performing similar synaptic roles found across all bilateria, as well as more basal porifera and placozoa (Piekut et al, 2020). UNC-10 forms interactions with many of the other proteins situated at the presynaptic site including ELKS-1 (Deken et al, 2005), SYD-2 (Schoch et al, 2002), RIMB-1 (Wang et al, 2000), RAB-3 (Wang et 1997, Koushika et al, 2001) and UNC-13 (Liu et al, 2019). The interaction with UNC-13 is particularly important in facilitating the release of neurotransmitters (Liu et al, 2019). This multitude of interactions makes UNC-10 a strong indicator of the formation of an AZ scaffold.

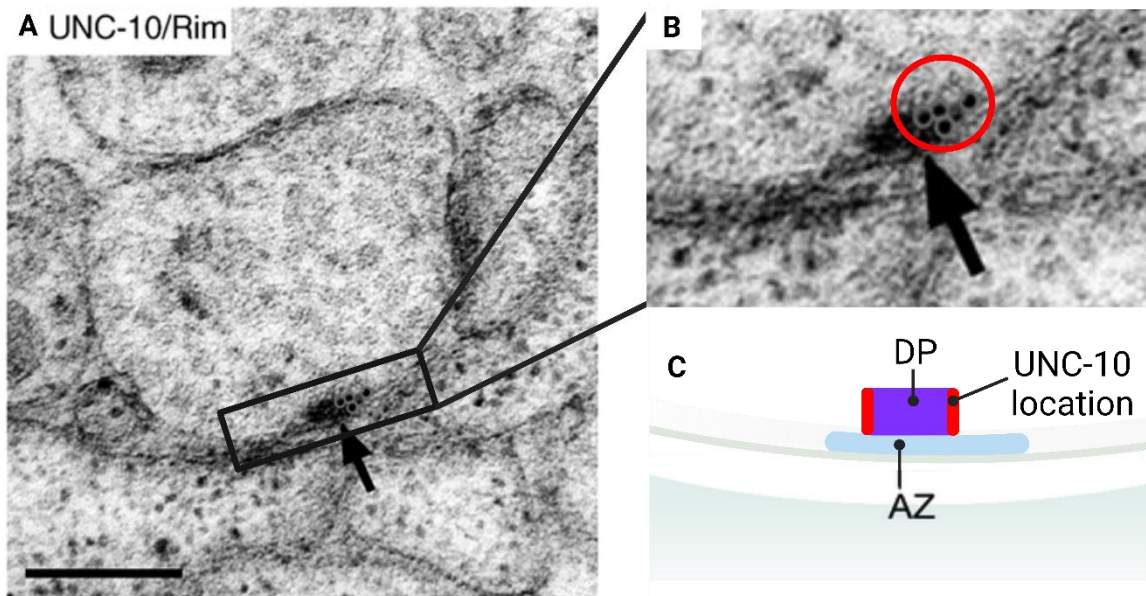


Figure 2.1. Localisation of UNC-10 within the presynaptic dense projection as demonstrated by immuno-electron microscopy (ImmunoEM) analysis. **A.** Electron micrograph of a neuromuscular junction in *C. elegans*. Arrow points to the presynaptic dense projection. **B.** Expansion of the boxed area in A. The red circle surrounds the immunogold particles (black with a grey halo) indicating the localisation of UNC-10 within the dense projection. **C.** A schematic showing the relative position of UNC-10 (Red) within the dense projection based on the immunoEM findings. **A** and **B** reprinted with permission from Weimer RM, Gracheva EO, Meyrignac O, et al. UNC-13 and UNC-10/rim localize synaptic vesicles to specific membrane domains. *JNeurosci*. 2006. doi: 10.1523/JNEUROSCI.2350-06.2006. Copyright 2006 Society for Neuroscience. **C** created with Biorender.com.

GFP-tagged SNB-1, an SV transmembrane protein (Figure 1.8), was used as a marker to assess SV recruitment to synaptic sites. SVs, as the carriers of neurotransmitter, are integral for synapses to perform neurotransmission. Therefore, their localisation to synapses is an indicator of functional synapse formation. Additionally, as AZ scaffold formation and SV recruitment can be regulated independently, it is important to

examine these features separately to appreciate how synaptic formation differs in mutant genotypes.

The SV marker SNB-1, a homologue of Synaptobrevin, is conserved across all metazoans (Göhde et al, 2021) and is critical to SV fusion and subsequent neurotransmitter release. Approximately 70 copies of SNB-1 typically localise to the membrane of a mature SV (Takamori et al, 2006). Their most important role occurs once the SVs are docked at the synaptic membrane. Here it forms part of the SNARE complex along with UNC-64(Syntaxin) and RIC-4 (SNAP25) by donating a helix within its structure facilitating membrane fusion (Söllner et al, 1993a, Söllner et al, 1993b, Poirier et al, 1998). The stable association of this protein with SVs makes them ideal to understand the localisation of SVs within neurons and hence can be indicative of reduced capacity for neurotransmission.

Investigating UNC-10 and SNB-1 to assess of AZ scaffold and SV localisation respectively, which are the two predominant features of a correctly assembled presynaptic terminal, provides a robust insight into the combined effect of *syd-2(ok217)*, *h1b-1(ok725)* and *cla-1(ok2285)* loss of function mutations.

2.1 Results

Three features of the dorsal nerve cord were assessed with fluorescence confocal microscopy: 1) discrete puncta count, 2) total fluorescence intensity and 3) total fluorescence area. The number of discrete puncta formed by a fluorescence-tagged AZ protein in nerve cord profiles is indicative of the number of synapses present

(Figure 2.2). By specifically analysing UNC-10 and SNB-1 I examined the AZ scaffold and SV cloud respectively. Analysis of the total fluorescence intensity and total fluorescence area demonstrate how much of the tagged AZ protein is recruited to the nerve cord and changes in synapse size or patterns of localisation within the nerve cord, respectively. Together these measures provide valuable insight into the transport and localisation of AZ proteins in the mutant background.

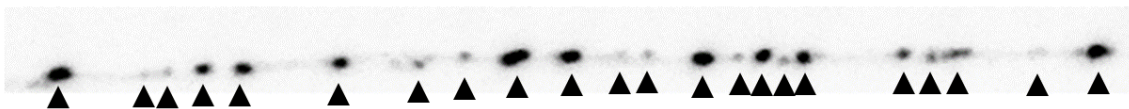


Figure 2.2. Dorsal nerve cord profile of wild-type *C. elegans* expressing UNC-10::GFP. Arrowheads indicate discrete puncta which were counted in analysis.

2.1.1 Loss of SYD-2 reduces UNC-10 recruitment to synaptic sites but the additional removal of CLA-1 and HLB-1 does not amplify this phenotype

In wild-type *C. elegans*, UNC-10::GFP formed the typical “pearls on a string” pattern reflecting normal synaptic localisation (Figure 2.3A). The number of discrete UNC-10::GFP puncta was not significantly reduced in any of the mutant conditions compared to wild-type (Figure 2.3B), suggesting that the ability to form synaptic sites is not disrupted by the loss of SYD-2, HLB-1 or CLA-1.

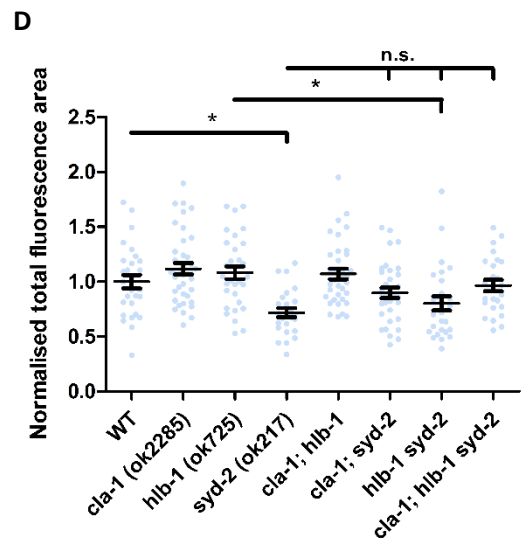
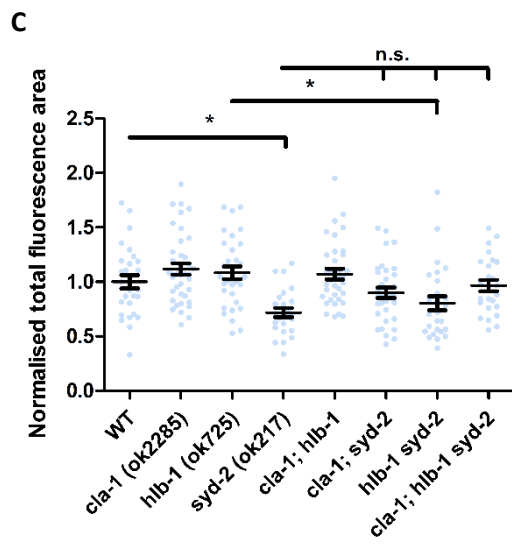
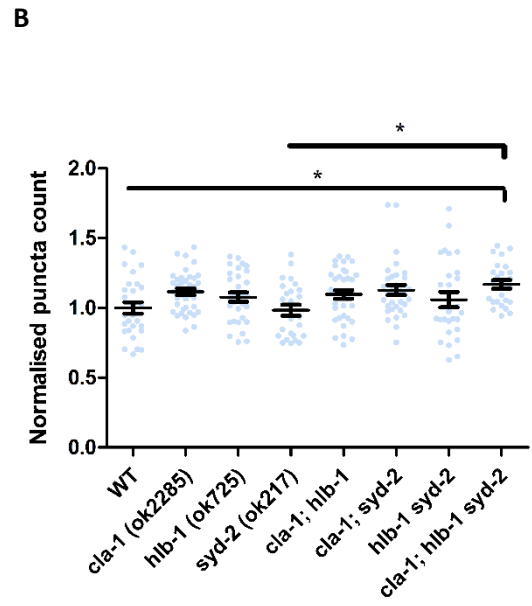
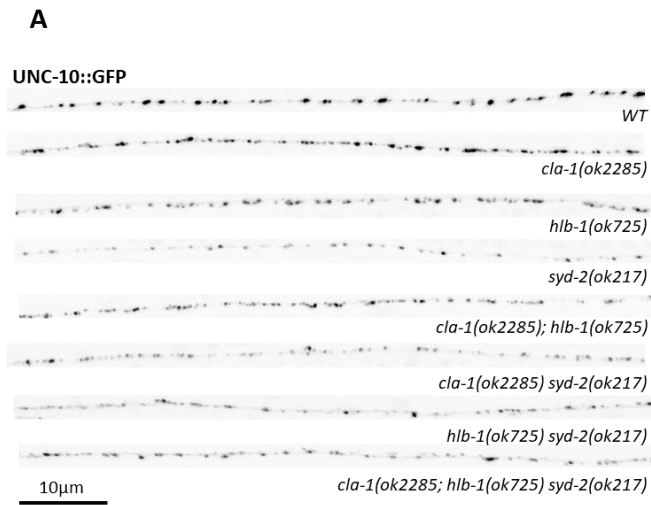


Figure 2.3. *syd-2(ok217)* modulates the total level of UNC-10:GFP at cholinergic motor neuron synapses but not the number of sites to which it is recruited. **A.** Maximum intensity projection images of UNC-10::GFP fluorescence expression in the posterior dorsal nerve cord. **B.** Mean puncta count per 100µm nerve cord, normalised to the WT mean. Discrete puncta count was determined by automated identification of distinct intensity point maxima, where pixel intensity was suitably enriched compared to the surrounding pixels (examples of discrete puncta are indicated by arrows in Figure. 2.2). **C.** Mean total fluorescence area per 100µm of nerve cord following subtraction of background fluorescence, normalised to the WT mean. The total fluorescence area was significantly reduced in *syd-2(ok217)* single mutants compared to WT (*syd-2* 0.72±0.21, WT 1.00±0.33). **D.** Mean total fluorescence per 100µm nerve cord normalised to the WT mean. Both the *syd-2(ok217)* single and the *h1b-1 syd-2* double mutants were significantly reduced compared to wild-type (*syd-2* 0.57±0.23, *h1b-1 syd-2* 0.61±0.31 Vs WT 1.00±0.41). Bars in the data show mean±SEM. Pairwise comparisons for significance testing used Dunn's test for multiple comparisons following Kruskal-Wallis test for variance. Pairwise comparisons were made between wild-type and all other conditions, between single mutants and double mutants which shared mutations, and between the triple mutant and all single and double mutants. Pairwise comparisons are shown by lines with ticks indicating mutants being compared to the condition at the unticked left-hand end. *p<0.05 corrected for multiple comparisons. n.s. - not significant. N-values are as follows: WT=28, *cla-1*=39, *h1b-1*=31, *syd-2*=25, *cla-1;h1b-1*=36, *cla-1;syd-2*=33, *h1b-1 syd-2*=27, *cla-1; h1b-1 syd-2*=25. Post-hoc power calculations can be found in Appendix 1.

The *syd-2* loss of function mutation caused a significant reduction in UNC-10::GFP fluorescence intensity and area in nerve cords compared to the wild-type (Figure 2.3C and 2.2D), indicating defective UNC-10 recruitment to synaptic sites. This is consistent with previous observations in *syd-2* mutants demonstrating reduced UNC-10 recruitment (Oh et al, 2021). Together with the lack of change in puncta number, this suggests that in the absence of SYD-2 both AZ scaffold formation and UNC-10 recruitment persists although the latter is diminished.

The loss of CLA-1 and HLB-1 had no effect on UNC-10::GFP fluorescence either in single mutants or together as the *cla-1; hlb-1* double mutant. Therefore, neither protein appears to play a central role in UNC-10 recruitment. The lack of effect on UNC-10 recruitment in the *hlb-1* mutant background is consistent with previous findings from immunostaining (Wang and Wang, 2009). The introduction of *hlb-1* or *cla-1* mutations in the *syd-2* mutant background also failed to enhance its synaptic defects. This suggests that neither HLB-1 or CLA-1 provide compensatory UNC-10 recruitment and AZ scaffold formation in the absence of SYD-2.

Despite carrying three strong loss of function alleles for AZ proteins, the *cla-1; hlb-1 syd-2* triple mutant was not phenotypically worse than the *syd-2* single mutant in any of the examined features. Curiously, the triple mutant displayed significantly increased puncta count compared to the *syd-2* single mutant and even the wild-type. Non-significant increases in both total fluorescence and total area were also observed compared to *syd-2* single mutants. This may be a consequence of broad disruption to the presynaptic AZ initiating compensatory pathways which upregulate the formation of AZ scaffolds to preserve synaptic function. It has been suggested that the expression of abnormal mRNA, such as that produced from deletions within coding regions can promote the upregulation of other genes which can provide compensatory effects. For example, mutations which cause the premature termination of Actin-encoding *act-5* causes the upregulation of another Actin-encoding gene, *act-3* which can then compensate (Seroby et al, 2020). Whether such an effect is in operation here is unclear. It may be that other proteins able to maintain UNC-10 recruitment are integrated into the active zone in the absence of HLB-1 and CLA-1. To identify which proteins are responsible for this response, mutagenesis suppressor screens for the compensated UNC-10::GFP expression phenotype would be required.

2.1.2 SV recruitment to synaptic sites is mediated primarily by SYD-2 although HLB-1 may play an independent role

I next examined SV recruitment at presynaptic sites represented by GFP-tagged SNB-1 puncta along the nerve cord (Figure 2.4A). These puncta were more diffuse than those of UNC-10::GFP due to SVs localising to synapses as expansive clouds, with vesicles also capable of transferring between different synaptic sites.

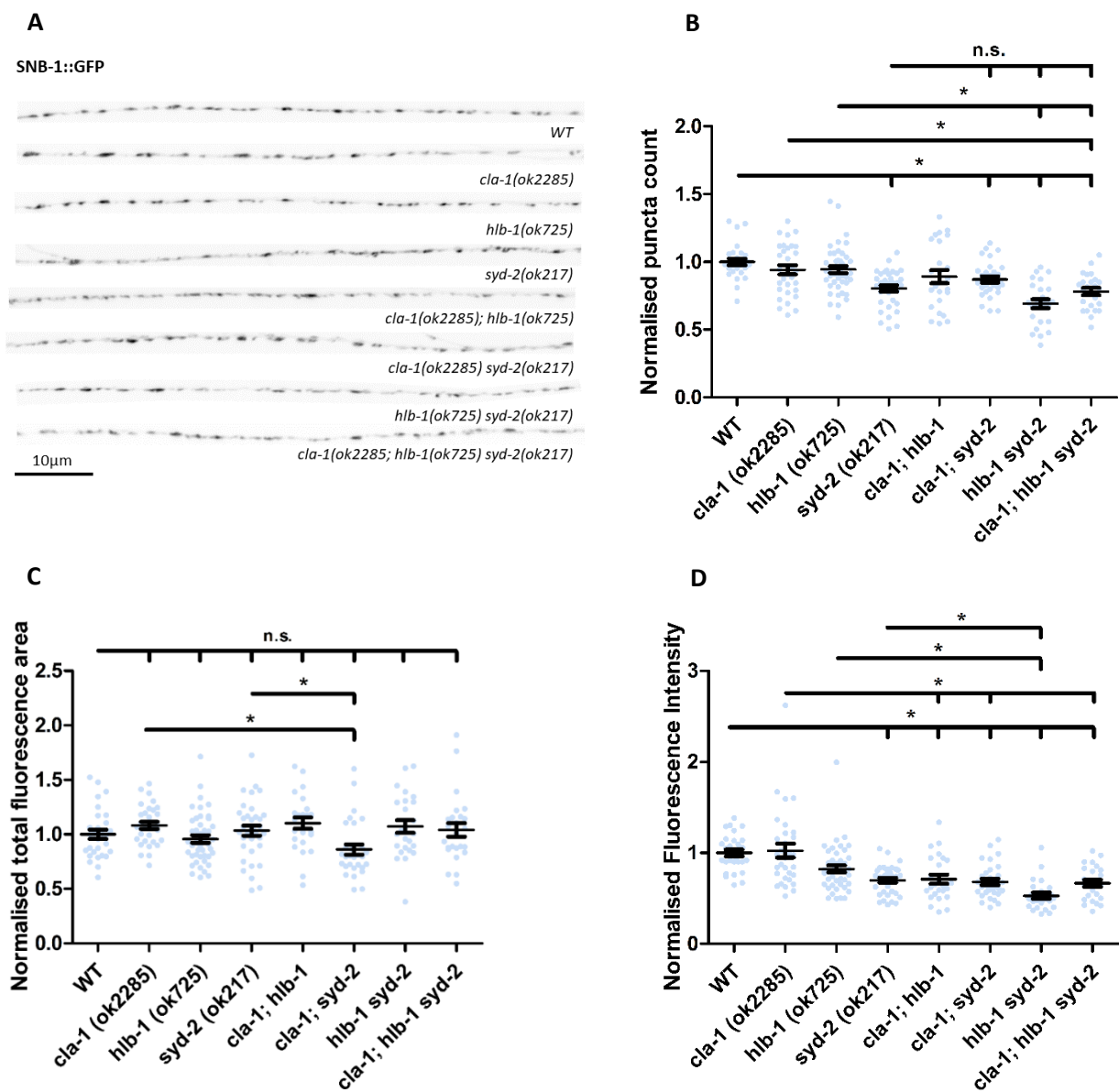


Figure 2.4. *syd-2(ok217)* causes a reduction in SNB-1::GFP recruitment to sites of synaptic release. **A.** Maximum intensity projection images of SNB-1::GFP fluorescence expression in the posterior dorsal nerve cord for each genetic condition. **B.** Mean puncta count per 100µm nerve cord, normalised to the WT mean. Discrete puncta count was determined by automated identification of distinct intensity point maxima, where pixel intensity was suitably enriched compared to the surrounding pixels (examples of discrete puncta are indicated by arrows in Figure. 2.2). All *syd-2(ok217)* containing mutants were significantly different from WT but not each other (*syd-2*-0.80±0.14, *h1b-1 syd-2*-0.69±0.16, *cla-1;syd-2*-0.87±0.13, *cla-1;h1b-1 syd-2* – 0.78±0.13 Vs WT – 1.00±0.13, p<0.05). **C.** Mean total fluorescence area for imaged nerve cords normalised to the WT mean. The total fluorescence area was not significantly different from the WT in any of the mutant strains. *cla-1(ok2285); syd-2(ok217)* double mutants showed a significant reduction compared to *cla-1(ok2285)* and *syd-2(ok217)* single mutants (*cla-1;syd-2*-0.86±0.26 Vs *cla-1* 1.08±0.18, *syd-2* 1.04±0.27). **D.** Mean total fluorescence, normalised to the wild-type mean. Again, all *syd-2(ok217)*-containing mutants were significantly different from WT (*syd-2*-0.70±0.16, *h1b-1 syd-2*-0.53±0.17, *cla-1;syd-2*-0.68±0.19, *cla-1;h1b-1 syd-2* – 0.67±0.19 Vs WT – 1.00±0.20). Bars in the data show mean±SEM. Pairwise comparisons for significance testing used Dunn's test for multiple comparisons following Kruskal-Wallis test for variance. Pairwise comparisons were made between wild-type and all other conditions, between single mutants and double mutants which shared mutations, and between the triple mutant and all single and double mutants. Pairwise comparisons are shown by lines with ticks indicating mutants being compared to the condition at the unticked left-hand end. *p<0.05 corrected for multiple comparisons. n.s. - not significant. N-values are as follows: WT=29, *cla-1*=31, *h1b-1*=44, *syd-2*=35, *cla-1;h1b-1*=25, *cla-1;syd-2*=30, *h1b-1 syd-2*=25, *cla-1; h1b-1 syd-2*=25. Post-hoc power calculations can be found in Appendix 1.

The number of discrete puncta was significantly reduced in all *syd-2(ok217)*-containing mutants. This is indicative of reduced SV recruitment to synaptic sites. As the number of UNC-10::GFP puncta was unchanged in these strains (Figure 2.4B), this suggests that some synaptic sites may be unable to recruit SVs. *syd-2(ok217)* mutants also

displayed significantly reduced SNB-1::GFP fluorescence intensity throughout their nerve cords (Figure 2.4D) confirming defective SV recruitment. Despite the reduction in SNB-1::GFP puncta the total fluorescence area was unchanged in *syd-2* mutants compared to wild-type. This indicates a more diffuse localisation pattern of SNB-1::GFP in the absence of SYD-2 and again suggests that SVs are improperly sequestered at the presynapse.

In the *h1b-1* single mutant SNB-1::GFP total fluorescence intensity was notably reduced, although this did not reach significance. The *h1b-1(ok725)* null allele has previously been associated with decreased SNB-1::GFP recruitment at GABAergic motor neuron synapses (Wang and Wang, 2009). HLB-1 may contribute to SV recruitment at excitatory synapses as well. *cla-1; h1b-1* and *h1b-1 syd-2* double mutants both had significantly reduced SNB-1::GFP intensity compared to *cla-1* and *syd-2* single mutants respectively. This provides further support for HLB-1 supporting SV recruitment. The additive effect contributed by the *h1b-1* mutant allele in the *syd-2* mutant background also suggests that HLB-1 is involved in the recruitment of SVs independent of SYD-2.

The loss of HLB-1 had no effect on either SNB-1::GFP puncta number or total fluorescence area despite its noted effect on total intensity, however. Therefore HLB-1 may only provide a supporting role at synaptic sites already capable of recruiting SVs. This contrasts with SYD-2 which likely affects SV recruitment to synaptic sites more broadly through its contributions to SV transport and capture as well as its role in recruiting other AZ proteins (Wagner et al, 2009; Edwards et al, 2015; Oh et al, 2021).

The *cla-1* single mutant was indistinguishable from WT and when combined with the *syd-2(ok217)* mutation it also failed to reduce either puncta number or total fluorescence beyond that observed in *syd-2* single mutants. This suggests that CLA-1 does not have an independent role in SV recruitment and furthermore does not fulfil a compensatory role in SV recruitment in the absence of SYD-2. SV clustering at cholinergic motor neuron synaptic regions has previously been shown to be unchanged in *cla-1* mutants with confocal microscopy, although this was paired with a reduction in puncta (Xuan et al, 2017). This latter effect could be due to Xuan et al's use of a more expansive mutation affecting the CLA-1 C-terminus more broadly than that used here.

The *cla-1; hlb-1 syd-2* triple mutant was comparable with the *syd-2* single mutant in terms of SNB-1::GFP puncta number, fluorescence area and intensity. Considering the observation that the loss of HLB-1 reduces SNB-1::GFP intensity the lack of difference between the *syd-2* single mutant and the triple mutant is somewhat surprising. This may be due to an unknown compensatory mechanism triggered by the loss of several AZ proteins simultaneously, such as that suggested for the UNC-10::GFP expression patterns in *cla-1; hlb-1 syd-2* triple mutants.

Overall, the results of the fluorescence confocal analysis point to SYD-2 as the most important protein in the formation of presynaptic sites, playing important roles in AZ scaffold protein recruitment, scaffold formation and SV localisation. While CLA-1 does not appear to contribute to AZ formation, HLB-1 might support SV recruitment through a SYD-2-independent pathway.

2.2 Discussion

In this chapter I used a fluorescence imaging approach to determine whether the additional loss of CLA-1 and HLB-1 in the *syd-2* mutant background enhanced defects in AZ scaffold formation and SV recruitment to synaptic sites. SYD-2/Liprin- α is considered one of the main drivers of AZ scaffold formation and SV recruitment. These processes are still able to occur in its absence however, although they are disrupted. This implies that either other proteins assist SYD-2 function, or there exist proteins which can compensate for the loss of SYD-2.

My results suggest that neither CLA-1 nor HLB-1 contribute to the decision to form an AZ scaffold at a synaptic site either autonomously or in the *syd-2* mutant background. HLB-1 does contribute to SV recruitment at synaptic sites independent of SYD-2 function; however, SV recruitment persists even in *h1b-1 syd-2* double mutants. This suggests that there are further proteins required for both AZ scaffold formation and SV recruitment.

2.2.1 SYD-2 remains the primary AZ scaffold organiser

Loss of SYD-2 from the presynapse has a multitude of effects upon the presynaptic AZ. Its removal depletes other AZ scaffold proteins such as UNC-10, RIMB-1 and ELKS-1 from presynaptic sites (Oh et al, 2021). This culminates in reduced AZ scaffold size and complexity when visualised as a dense projection, although the structure is not eliminated (Kittelmann et al, 2013). The finding that the additional removal of CLA-1 or HLB-1 does not further decrease UNC-10 expression in cholinergic motor

neurons suggests that these proteins are not responsible for preserving AZ scaffold formation.

In the case of CLA-1 this is somewhat unsurprising as CLA-1 expression has been shown to be greatly reduced in *syd-2* mutants (Xuan et al, 2017). Therefore, there may be little difference in the amount of CLA-1 present at *syd-2* single and *cla-1; syd-2* double mutant synapses. As *cla-1* single mutants also had no effect on UNC-10 recruitment however it seems that CLA-1's role in AZ scaffold formation is limited regardless. The lack of effect in the single mutant is curious as CLA-1 has been implicated in the recruitment of SYD-2 previously (Xuan et al, 2017). As relatively strong SYD-2 expression persists in the absence of CLA-1 this may be enough to maintain regular synaptic organisation. It should also be noted that Xuan et al used a different *cla-1* mutant allele (*wy1048*) which affected the C-terminal region of the protein more broadly therefore it is possible that SYD-2 recruitment in my analysis is identical to the wild-type. Indeed, it is notable that in this previous study a reduction in SV-associated puncta was observed in *cla-1(wy1048)* mutants, something which was not observed here in *cla-1(ok2285)* mutants. Confocal analysis could be used in future to compare SYD-2 expression and broader presynaptic active zone defects in *cla-1(ok2285)* and *cla-1 (wy1048)* mutants.

Although the Liprin- β homologue, HLB-1, is a likely interactor with SYD-2, based on interactions between homologues in mammalian and *Drosophila* models (Serra-Pagès et al, 1998; Astigarraga et al, 2010), HLB-1 had no effects upon UNC-10 expression. This is consistent with previous findings in *h1b-1* single mutants (Wang and Wang, 2009). It also reflected findings in *Drosophila melanogaster* where loss of the HLB-1 homologue, Liprin- β , retains wild-type-like distribution of AZ scaffolds when Bruchpilot

is used as a marker (Astigarraga et al, 2010). This suggests that the SYD-2-HLB-1 interaction is unlikely to be critical to AZ scaffold formation.

Altogether this suggests that neither HLB-1 or CLA-1 act alongside SYD-2 in forming and stabilising the AZ scaffold. Therefore, other proteins will need to be examined in future to better understand this process. NRX-1, the homologue of neurexin, has recently emerged as an interesting candidate protein. *nrx-1* null mutants produce fewer synaptic sites, based on CLA-1 distribution, and also have reduced neurotransmission (Kurshan, 2018). The close relationship of SYD-1 and NRX-1 in *Drosophila melanogaster* suggests that NRX-1 may work upstream of SYD-2, however (Owald et al, 2012).

New developments for investigating protein interactomes such as the AZ, hold promise in uncovering interesting new candidates as well. Recently a turbID proximity labelling approach paired with mass spectrometry was used to identify proteins interacting with ELKS-1 *in vivo* (Artan et al, 2021). This both confirmed expected interactions at the presynaptic AZ and revealed new protein candidates. Investigation of these candidates alongside others from similar proteomic approaches should expand our knowledge of other AZ organisers.

Although the formation of AZ scaffolds was not observably disrupted in *h1b-1* and *cla-1* mutants it is important to note that only a single AZ scaffold marker was used in this study, UNC-10. While UNC-10 is incredibly important to AZ scaffold function due to its roles in bringing SVs to release sites (Stigloher et al, 2011) and facilitating SV fusion (Koushika et al, 2001; Kushibiki et al, 2019) its loss does not affect the size of the dense projection itself. This means that formulating complete conclusions regarding

active zone scaffold formation based on UNC-10 alone is difficult. Additionally, it is worth considering whether changes in the distribution of other AZ scaffold proteins may occur even if the number of scaffolds formed do not. While ELKS-1 and RIMB-1 are, to our knowledge, less functionally important than UNC-10 in facilitating SV release, disruption to their recruitment to the AZ scaffold could affect its integrity and functionality due to the many interactions they form with other proteins (Dai et al, 2006; Koushibiki et al, 2019; Artan et al, 2021). Indeed, the loss of RIMB-1 has recently been associated with a reduction in dense projection size (Krout et al, 2023). Additionally, examination of factors strongly implicated in neurotransmitter release such as CaV2 calcium channels (UNC-2) and UNC-13L would also be beneficial in understanding how neurotransmission may be altered. These analyses which can be carried out by the same methods employed here would further improve our understanding of SYD-2, CLA-1, and HLB-1's collective relationship to the AZ scaffold.

2.2.2 HLB-1 and SYD-2 independently contribute to SV recruitment but do not account for all recruited SVs

SV availability is a major limiting factor for neurotransmission as SVs are fundamental for neurotransmitter release into the synaptic cleft. *syd-2* mutants have previously been shown to recruit fewer SVs to synaptic sites resulting in reduced synaptic transmission (Zhen and Jin, 1999; Kittelmann et al, 2013). I found that the loss of HLB-1 also elicited a trend towards reduced SV recruitment to synaptic sites in both wild-type and *syd-2* mutant backgrounds. This suggests that HLB-1 may support SV recruitment to the synapse independently of SYD-2.

SYD-2 has a multitude of roles at the presynapse which collectively contribute to the recruitment of SVs. SYD-2 promotes the activity of UNC-104 which transports SVs to the presynapse (Wagner et al, 2009; Muniesh et al, 2020) and also contributes to the CSS complex which captures and stabilises SVs at synaptic sites (Edwards et al, 2018). Similarly, SYD-2 is also involved in the transport, capture and integration of numerous AZ proteins into the presynapse which directly interact with SVs; for example, UNC-10 (Gracheva et al, 2008; Oh et al, 2021). Disrupted organisation of the presynapse is likely why we see less SV recruitment to distinct synaptic sites.

Unlike SYD-2, HLB-1 loss only reduced total SV recruitment and not the number of synaptic sites at which they were present. This, combined with its lack of effect on UNC-10 recruitment suggests that HLB-1's function at the presynapse is specifically directed towards SV localisation and retention, rather than as a presynaptic organiser.

At this stage it is difficult to interpret the precise role of HLB-1 in SV recruitment. The protein could be involved in a variety of functions including transport, endocytosis, SV recycling or direct binding and retention of SVs at synaptic sites. More directed fluorescence confocal microscopy examinations of *hlb-1* mutants may be useful in determining which processes HLB-1 contributes to. Transport could be assessed through examination of UNC-104 mobility through live particle displacement analysis (Wagner et al, 2009). Investigations into endocytosis meanwhile could utilise synapto-pHluorin, a luminal synaptic vesicle protein-fused tag which becomes fluorescent when exposed to the neutral pH of the extracellular environment and is quenched following endocytosis and acidification of the SVs they are repackaged into. The rate of fluorescence quenching following release is proportional to the rate of endocytosis (Kavalali and Jorgenson, 2014).

While *h1b-1 syd-2* double mutants did display the greatest reduction in SV recruitment, this was not enough to eliminate all SVs from synaptic sites. This means that there must be additional proteins ensuring their localisation at the presynapse. Disrupted SV recruitment has been demonstrated in mutants for numerous AZ associated proteins including RIMB-1 (Jánosi et al, 2021), UNC-10 (Koushika et al, 2001), NRX-1 (Kurshan et al, 2018), PTP-3 (Ackley et al, 2005), SAD-1 (Crump et al, 2001; Kim et al, 2008) and SYD-1 (Hallam et al, 2002). Considering that SVs are integral to synaptic transmission it makes sense for many proteins to contribute to their recruitment so that there is redundancy in the case of loss of function mutations. Therefore, to eliminate SV recruitment from synapses a multitude of proteins would likely have to be removed.

Altogether this chapter provided an overview of the cholinergic presynaptic AZ landscape in SYD-2, HLB-1 and CLA-1 double and triple mutants by looking at the two most prominent, and arguably most important synaptic features, the AZ scaffold and SVs. HLB-1 and CLA-1 exerted only limited further effect upon the defects inherent within *syd-2* single mutants. Therefore, these proteins appear much less important in the recruitment of SVs and the formation of AZ scaffolds. Furthermore, there must be other proteins contributing to these functions in the absence of SYD-2. This does not preclude HLB-1 and CLA-1 from being important for synaptic function, however, whether this is through the loss of SVs as observed in *h1b-1* mutants or an alternative pathway.

3 Assessing neuromuscular functionality in the absence of SYD-2, HLB-1 and CLA-1

Fluorescence confocal microscopy established that synaptic vesicles (SVs) and active zone (AZ) scaffold components are diminished in *syd-2(ok217)* mutants, but this effect is not significantly enhanced upon the addition of *cla-1(ok2285)* and *hlb-1(ok725)* mutations. While the observed effects are interesting to consider they only provide a snapshot of the AZ landscape. As neurotransmission is not only influenced by the abundance of synaptic components but also their subcellular assembly it is pivotal to assess the functional impact of the investigated mutations at synapses. Although electrophysiological methods remain the gold-standard to examine neurotransmission at the cellular and molecular level, these assays are complex and require technical expertise and setups (Goodman et al, 2012). Alternatively, examination of *C. elegans* locomotion can provide an insight into neuromuscular deficiencies which are often rooted in abnormal motor neuron signalling using simpler experimental strategies. While such behavioural analyses lack the ability to assess the fine details of release dynamics at the neuromuscular junction, electrophysiology being able to examine amplitude of postsynaptic currents and frequency of spontaneous release alongside readily-releasable pool size, it does allow the effects of neuromuscular outputs to be considered across the whole animal rather than being confined to a single point of muscle as reference.

C. elegans locomotion can take different forms depending on the environment in which it is studied. While crawling on agar, the medium on which laboratory worms are typically cultured, the worms move in a sinuous wave pattern and are capable of both

forward and backward directionality. When in liquid the locomotor pattern of worms alters dramatically with both a higher frequency and wavelength (Fang-Yen et al, 2010), appearing to repeatedly create a C-shaped bend on one side and then immediately transitioning to the other (Figure 3.6A). While these movements seem to differ greatly, they are unlikely to be the product of different neuromuscular inputs. Studies that slowly increase the viscosity of the liquid media in which a worm is placed, suggest that these changes are a product of the modulation of the regular crawling gait (Korta et al, 2007; Boyle et al, 2011). This modulation is thought to be a reflex to sharp increases in mechanical resistance between low viscosity liquid media and a firm solid substrate such as agar. The view that swimming (also known as thrashing) and crawling actions are closely related is supported by calcium imaging studies examining nerve cord motor neurons which demonstrate shared dynamics in motor neuron activity and body curvature in each form of locomotion (Butler et al, 2015).

C. elegans locomotion is built upon the innervation of muscle cells by motor neurons which provide excitatory and inhibitory inputs to the muscle facilitating contraction and relaxation respectively (Figure 1.7). Forward and backward crawling locomotion is driven by distinct cholinergic motor neuron sets, which provide the excitatory input to body wall muscle. Whereas forward movement requires innervation by the posteriorly projecting B-type motor neurons, backwards locomotion requires innervation by anteriorly projecting A-type motor neurons (Zhen and Samuel, 2015). These motor neurons are stimulated by specific premotor interneurons via gap junctions, AVA stimulating A-type neurons and AVB stimulating B-type neurons.

D-type GABAergic motor neurons also provide direct inhibitory input to the body wall muscle but provide a more modulatory function. The inhibitory neurotransmission

elicited by these neurons appears to subtly maintain balance between dorsal and ventral bending, indeed ablation of VD and DD motor neurons produces a bias in body bends towards the ventral and dorsal directions respectively (Donnelly et al, 2013). This is likely reflective of their role in counterbalancing local contraction and relaxation on opposite sides of the body. Additionally, *unc-25* null mutants, which do not express GABA decarboxylase and therefore fail to produce the GABA neurotransmitter, are still capable of forward movement although this is slowed with animals displaying slight hypercontraction (Donnelly et al, 2013). This emphasises excitatory cholinergic inputs as the main drivers of directed *C. elegans* locomotion with inhibitory GABAergic inputs being more modulatory.

Cholinergic motor inputs are also vital to propagating *C. elegans*' characteristic wave-like crawling pattern. Recently, both A-type and B-type motor neurons have been shown to exhibit intrinsic calcium oscillations (Fouad et al, 2018; Gao et al, 2018; Xu et al, 2018). In A-type motor neurons, this oscillatory signalling is particularly strong and is even capable of generating rhythmic reversals, albeit slow, in animals where the A-type neurons experience no synaptic input (Gao et al, 2018). Although B-type motor neurons do not display the same level of autonomy they are required for maintaining a rhythmic sinuous waveform during forward locomotion (Fouad et al, 2018).

In this chapter I investigated how locomotion was affected in the *syd-2(ok217)* mutant and whether the additional loss of CLA-1 and HLB-1 modified this. As effective neurotransmission at the neuromuscular junction is critical to maintaining locomotion, defects in presynaptic AZ scaffold formation and SV recruitment would be expected to manifest as defective locomotion. Additionally, as confocal analysis in the previous

chapter was focused on cholinergic synapses, which drives locomotion, these assays would link the molecular observations to synaptic function.

Both crawling and swimming locomotion was examined in synaptic mutants to understand their capability in their default state and during higher intensity locomotion, respectively. The types of movement (forward, backward, paused), speed and posture (body curvature and minor axis size) while crawling were all assessed to gauge their locomotor behaviour. Swimming meanwhile focused on the thrashing capacity of the worms and the regularity of body bending. To better appreciate the interplay between the observed locomotor defects and cholinergic neurotransmission, aldicarb paralysis assays were employed to assess acetylcholine release.

3.1 Results

3.1.1 Regular crawling locomotion is strongly disrupted by the loss of SYD-2 although this is modulated by the additional removal of CLA-1

Wild-type *C. elegans* navigates its environment by crawling in a sinuous wave-like motion and are typically highly active. To assess locomotion in synaptic mutants I worked in collaboration with the Behavioural Phenomics Research Group at Imperial College London to employ a video-based worm tracking approach. Recordings of *C. elegans* crawling locomotion followed a specific experimental design. An initial five-minute recording of the worms was taken before entering a six-minute window with interspersed blue light pulses at 60, 160 and 260 seconds. Following the six-minute stimulation period a further five-minute recording was then taken. Under blue light

C. elegans demonstrate an aversive escape response meaning that upon stimulus worms initiate high-speed locomotion (Ward et al, 2008). During the blue light stimulus window, the worms should be more active therefore this window was primarily used for analysis.

I found that all mutants expressing the *syd-2(ok217)* allele were significantly less likely to be found in a paused state than wild-type worms, but more likely to be moving backward (Figure 3.1A & C). *syd-2* single mutants also displayed an increased propensity to forward locomotion compared to wild-type although this effect was mostly diminished in double and triple mutants (Figure 3.1B). As *h1b-1* and *cla-1* single mutants were both less likely to engage in forward locomotion this may counteract the increased forward locomotion caused by the *syd-2* mutation.

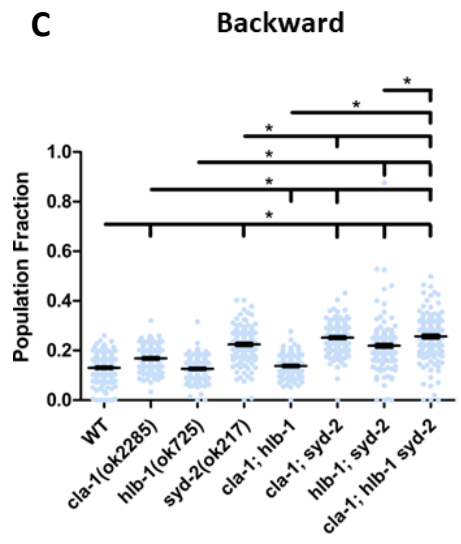
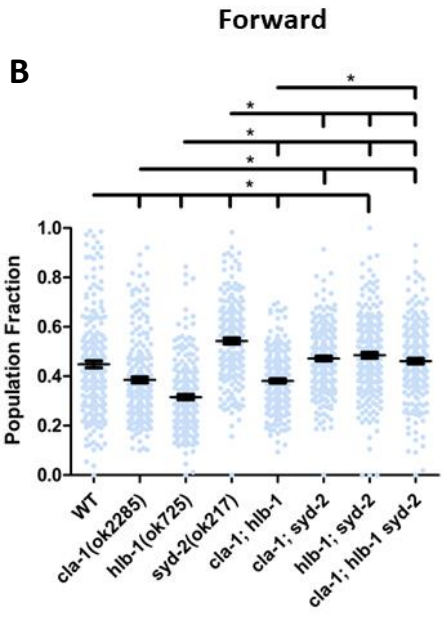
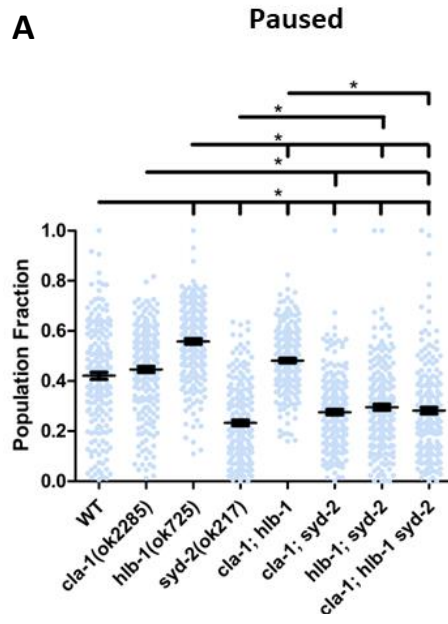


Figure 3.1. SYD-2 loss promotes directed crawling locomotion. Comparisons of the fraction of worms found to be paused (A), or in forward (B) or backward (C) locomotion over the course of crawling observations. As these motion modes cover all potential motion states a worm can occupy throughout the course of observations the sum of the paused forward and backward fraction for each strain is equal to 1. Bars in the data show mean±SEM. Pairwise comparisons for significance testing used Dunn's test for multiple comparisons following Kruskal-Wallis test for variance. Pairwise comparisons were made between wild-type and all other conditions, between single mutants and double mutants which shared mutations, and between the triple mutant and all single and double mutants. Pairwise comparisons are shown by lines with ticks indicating mutants being compared to the condition at the unticked left-hand end. *p<0.05 corrected for multiple comparisons. n.s. - not significant. N-values are as follows: *WT*=216, *cla-1*=216, *h1b-1*=208, *syd-2*=205, *cla-1;h1b-1*=209, *cla-1;syd-2*=211, *h1b-1 syd-2*=213, *cla-1; h1b-1 syd-2*=205. Post-hoc power calculations can be found in Appendix 1.

The observed upregulation of locomotion in *syd-2* mutants differs from previous characterisations of the strain being sluggish but capable of fast movement when stimulated. This previous observation is likely to derive from mixed adult populations where older adults may have inhibited locomotion due to accumulation of eggs due to defective egg laying (Taru and Jin, 2011). In my experiments only young adult worms were used to minimise this effect.

Interestingly, *syd-2* single mutants and both *cla-1; syd-2* and *h1b1 syd-2* double mutants were found to explore a significantly larger region of their environment. This is reflective of the observed increase in locomotor activity (Figure 3.2B). The *cla-1; h1b-1 syd-2* triple mutant was not significantly different from the wild-type, however. This again suggests counteracting effects of the *h1b-1* and *cla-1* mutations against the *syd-2* allele. *h1b-1* single mutants specifically showed a significant reduction in path

coverage compared to wild-type, likely reflecting their increased tendency to pause. The observed counteractions of the different mutations suggest they influence independent molecular systems or circuits, each eliciting different behavioural effects.

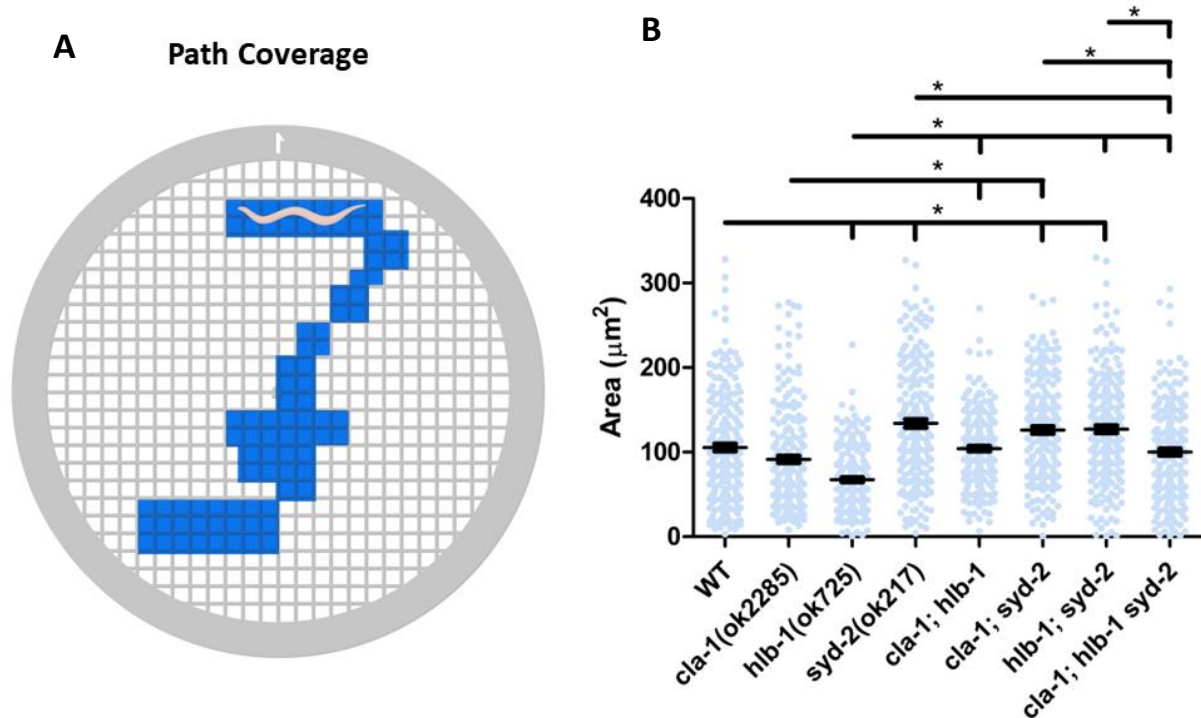


Figure 3.2. SYD-2 loss promotes greater exploration of the worm's environment. **A.** Path coverage is determined by dividing the well area into equally sized grids and then summing the area of the grids visited by the worms. In the diagram the grids highlighted in blue represent the regions visited by the worm. **B.** Comparisons of the path coverage exhibited by the different strains over the course of observations. Bars in the data show mean \pm SEM. Pairwise comparisons for significance testing used Dunn's test for multiple comparisons following Kruskal-Wallis test for variance. Pairwise comparisons were made between wild-type and all other conditions, between single mutants and double mutants which shared mutations, and between the triple mutant and all single and double mutants. Pairwise comparisons are shown by lines with ticks indicating mutants being compared to the condition at the unticked left-hand end. * $p < 0.05$ corrected for multiple comparisons. n.s. - not significant. N-values are as follows: *WT*=216, *cla-1*=216, *hlb-1*=208, *syd-2*=205, *cla-1; hlb-1*=209, *cla-1; syd-2*=211, *hlb-1 syd-2*=213, *cla-1; hlb-1 syd-2*=205. Post-hoc power calculations can be found in Appendix 1. A was created with BioRender.com

While analysis of locomotor patterns tells us that *syd-2* mutants engage in greater directional movement and cover a larger area of their environment, this is not necessarily indicative of a change in neuromuscular function. Several pathways outside of the motor circuit, including those that detect the presence of food or influence the decision to remain in place or to move and explore the environment may also be affected by the loss of SYD-2 from the presynapse (Iwanir et al, 2016; Scheer and Bargmann, 2023). To investigate changes which are more reflective of altered neuromuscular signalling I examined two specific features of *C. elegans* movement, speed and body posture.

All *syd-2(ok217)*-carrying mutants displayed increased speed in backward locomotion compared to the wild-type to a similar extent (Figure 3.3A). In forward locomotion the *cla-1; hlb-1 syd-2* triple mutant was the only *syd-2* mutant not to demonstrate increased speed (Figure 3.3B). *syd-2* single mutants were the fastest of all the strains in the forward direction with *cla-1; syd-2* and *hlb-1 syd-2* double mutants displaying modest increases in speed by comparison. As *cla-1* and *hlb-1* single mutants both had significantly decreased speed in forward locomotion this again suggests that the *cla-1* and *hlb-1* mutations may act in opposition to *syd-2* in the promotion of movement.

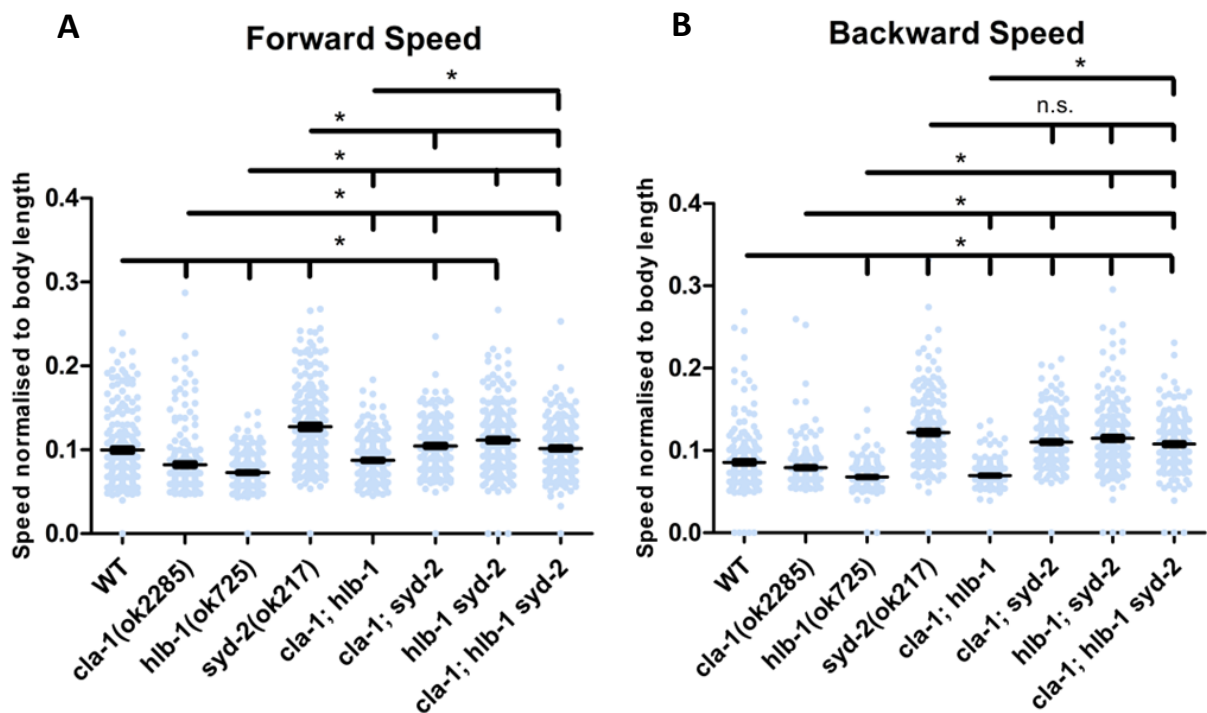


Figure 3.3. *syd-2* mutants display enhanced speed in both forward and backward directions. Mean crawling speed of *C. elegans* in forward (A) and backward (B) locomotion. Bars in the data show mean \pm SEM. Pairwise comparisons for significance testing used Dunn's test for multiple comparisons following Kruskal-Wallis test for variance. Pairwise comparisons were made between wild-type and all other conditions, between single mutants and double mutants which shared mutations, and between the triple mutant and all single and double mutants. Pairwise comparisons are shown by lines with ticks indicating mutants being compared to the condition at the unticked left-hand end. * $p < 0.05$ corrected for multiple comparisons. n.s. - not significant. N-values are as follows: *WT*=216, *cla-1*=216, *hlb-1*=208, *syd-2*=205, *cla-1; hlb-1*=209, *cla-1; syd-2*=211, *hlb-1 syd-2*=213, *cla-1; hlb-1 syd-2*=205. Post-hoc power calculations can be found in Appendix 1.

The increased speed of the *syd-2* mutant worms suggests that there may be some change in neuromuscular function, which increases the efficiency of directional

movement. The sinuous wave locomotor pattern of wild-type *C. elegans* is typically very consistent during forward and backward movement. Changes to this pattern are potential indicators of altered neuromuscular signalling which can manifest through changes to internal calcium oscillations in motor neurons or disrupted input to body wall muscle. To investigate this, I examined the curvature of the regions designated as the “neck”, “midbody” and “hips” (Figure 3.4A).

Curvature was most reduced in *syd-2* single mutants for all regions of the body during both forward and backward locomotion (Figure 3.4B-D). In all cases apart from “neck” curvature during backward locomotion, *syd-2*-carrying double and triple mutants had significantly reduced curvature compared to wild-type, although these reductions were again modest compared to the single *syd-2* mutant. In this case it is more difficult to interpret this as an adversarial effect between *syd-2* and the *cla-1* and *h1b-1* mutations. Curvature was unaffected in *h1b-1* single mutants and in *cla-1* single mutants it was significantly reduced compared to wild-type, although to a lesser degree than *syd-2* single mutants.

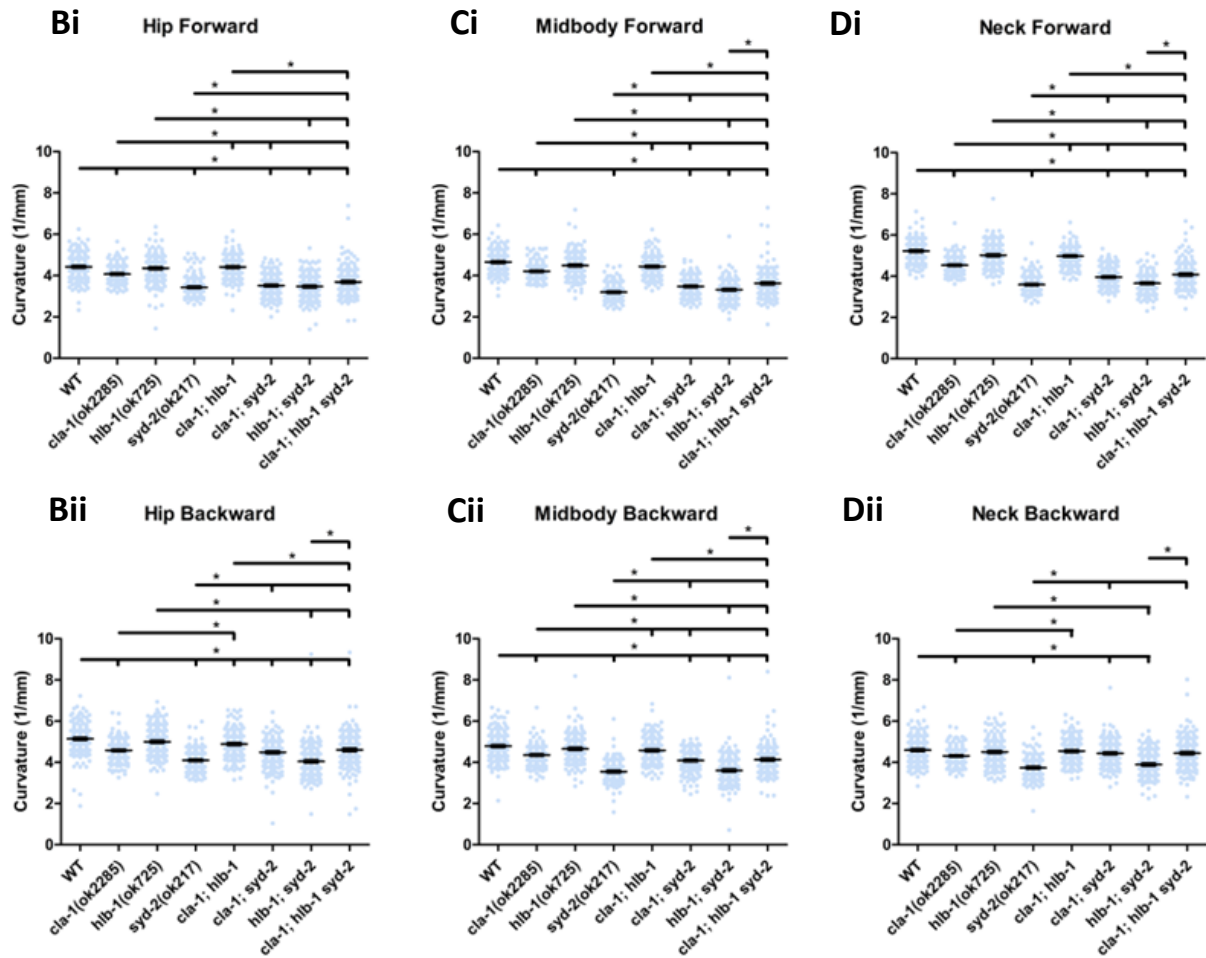
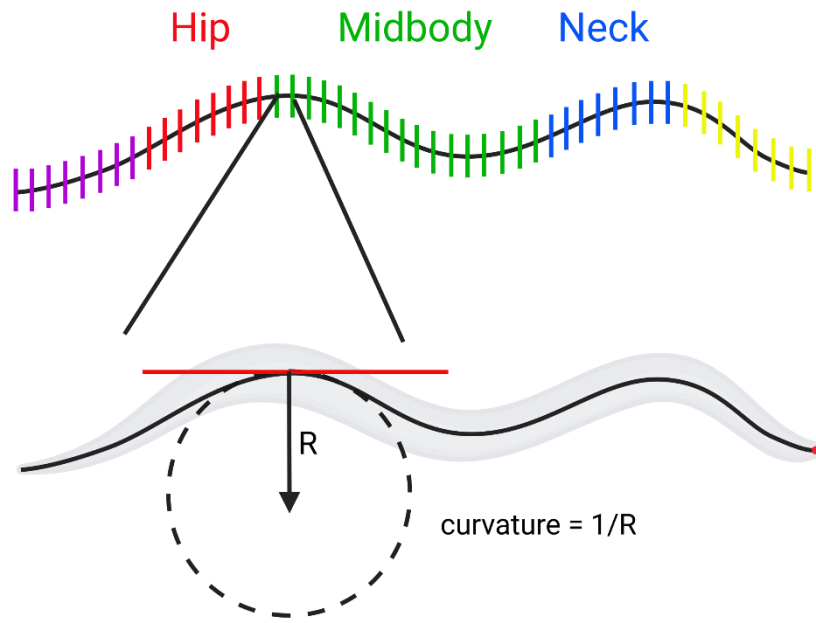
A

Figure 3.4. Body curvature is reduced in *syd-2* mutants. **A.** Body segments such as “hip”, “midbody” and “neck” are specified by breaking down the *C. elegans* skeleton (the midline through the centre of the worm) into 50 equally spaced segments and labelling the body region based on the number of the segment from anterior to posterior (e.g. 9-16 is the neck, 17-33 is the midbody, 34-41 is the hip). Curvature for each body region is determined by taking the mean of all curvature measurements between each segment within each body region. Curvature is determined by finding the radius of the circle which best fits the curve (mm) and dividing 1 by this radius. Curvature was compared between each strain for each body region (**B-D**) in both forward (**i**) and backward (**ii**) crawling locomotion. Bars in the data show mean±SEM. Pairwise comparisons for significance testing used Dunn’s test for multiple comparisons following Kruskal-Wallis test for variance. Pairwise comparisons were made between wild-type and all other conditions, between single mutants and double mutants which shared mutations, and between the triple mutant and all single and double mutants. Pairwise comparisons are shown by lines with ticks indicating mutants being compared to the condition at the unticked left-hand end. *p<0.05 corrected for multiple comparisons. N-values for forward measurements (**Bi, Ci, Di**) are *WT*=215, *cla-1*=216, *h1b-1*=207, *syd-2*=204, *cla-1;h1b-1*=209, *cla-1;syd-2*=210, *h1b-1 syd-2*=210, *cla-1; h1b-1 syd-2*=204. N-values for backward measurements (**Bii, Cii, Dii**) are *WT*=211, *cla-1*=216, *h1b-1*=206, *syd-2*=204, *cla-1;h1b-1*=208, *cla-1;syd-2*=210, *h1b-1 syd-2*=210, *cla-1; h1b-1 syd-2*=202. Post-hoc power calculations can be found in Appendix 1. **A** was created with BioRender.com.

To further investigate postural changes in the *C. elegans* locomotor pattern I also examined the length minor axis length of each strain. The minor axis is the smaller of the two axes when the length and width of a worm’s posture is confined to a bounding box (Figure 3.5A). A change in the length of the minor axis can therefore be indicative of a change in *C. elegans* crawling waveforms. All mutants with the *syd-2* mutation had increased minor axis length compared to wild-type in both forward and backward motion (Figure 3.5B & C). Interestingly, double and triple mutants carrying the *syd-2* mutation displayed an even greater increase in their minor axis length in at least one

direction suggesting that the additional loss of *h1b-1* and *cla-1* in the *syd-2* mutant background modifies the *C. elegans* crawling gait. This was particularly prevalent in *cla-1; syd-2* double and *cla-1; h1b-1 syd-2* triple mutants which increased minor axis length in both forward and backward crawling. This suggests that the additional loss of CLA-1 may influence crawling posture in the absence of SYD-2.

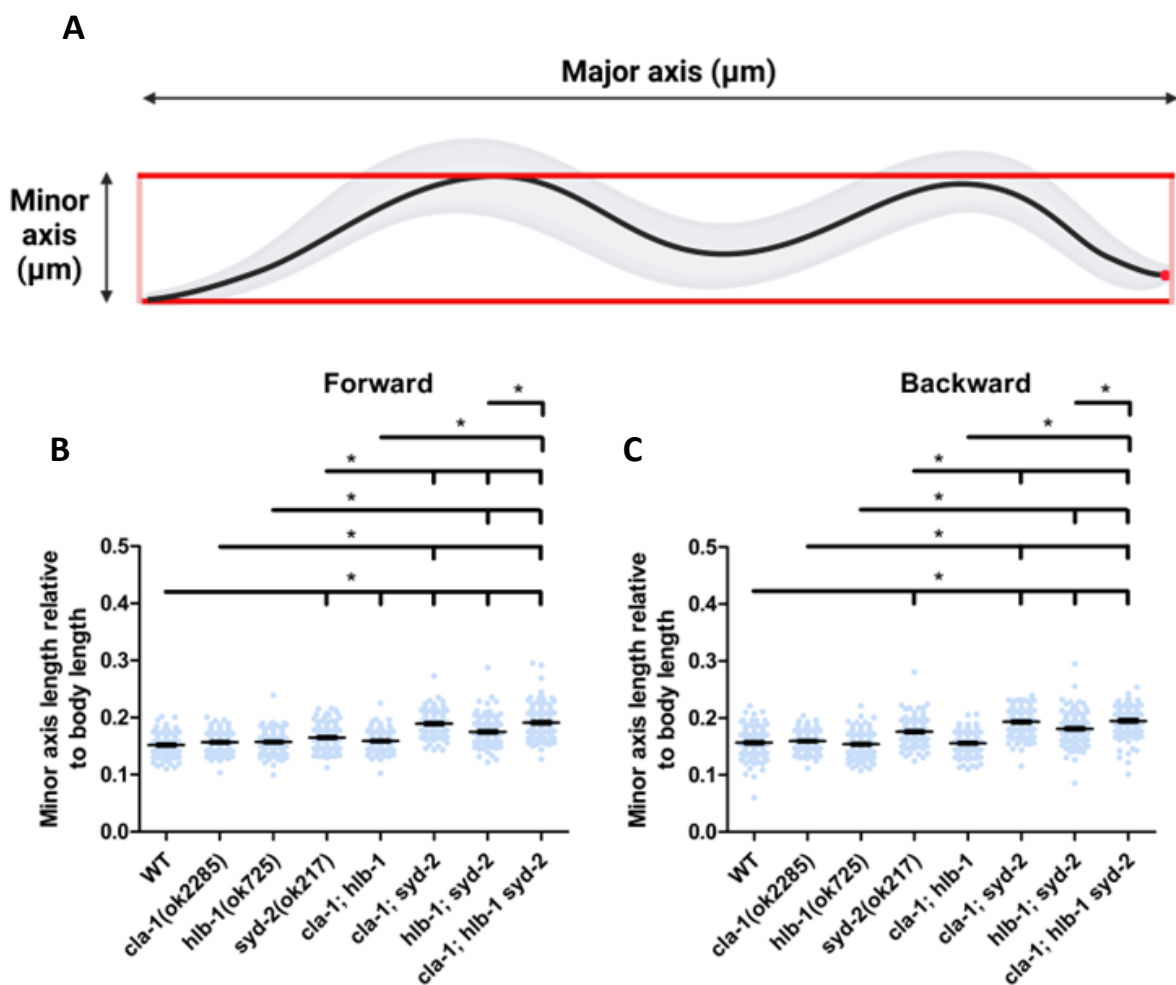


Figure 3.5. Minor axis length is enhanced in *syd-2* mutants. **A.** The minor axis corresponds to the total y-directional space taken up by a worm when confined to a bounding box. This was normalised for the against the total length of each worm and examined in forward (**B**) and backward (**C**) locomotion for each strain. Bars in the data show mean±SEM. Pairwise comparisons for significance testing used Dunn's test for multiple comparisons following Kruskal-Wallis test for variance. Pairwise comparisons were made between wild-type and all other conditions, between single mutants and double mutants which shared mutations, and between the triple mutant and all single and double mutants. Pairwise comparisons are shown by lines with ticks indicating mutants being compared to the condition at the unticked left-hand end. *p<0.05 corrected for multiple comparisons. N-values for forward measurements (**B**) are *WT*=215, *cla-1*=216, *h1b-1*=207, *syd-2*=204, *cla-1;h1b-1*=209, *cla-1;syd-2*=210, *h1b-1 syd-2*=210, *cla-1; h1b-1 syd-2*=204. N-values for backward measurements (**C**) are *WT*=211, *cla-1*=216, *h1b-1*=206, *syd-2*=204, *cla-1;h1b-1*=208, *cla-1;syd-2*=210, *h1b-1 syd-2*=210, *cla-1; h1b-1 syd-2*=202. Post-hoc power calculations can be found in Appendix 1. **A** was created with BioRender.com.

Altogether this appears to suggest that the loss of SYD-2 causes notable changes to *C. elegans* crawling locomotion however, this does not appear to reduce their locomotor capabilities instead modifying behaviour and posture. While additional loss of HLB-1 and CLA-1 further modified locomotion this again does not appear to reduce crawling ability compared to the *syd-2* single mutants. The subtle nature of these adaptations means that their origin may not be the result of defective cholinergic neurotransmission at the NMJ. Defective neurotransmission from rhythm generators such as interneuron signalling to motor neurons could also be involved in these behaviours.

3.1.2 Loss of HLB-1 and CLA-1 does not enhance *syd-2* mutant swimming defects

Next, to gain further insights on the effects of the mutations on neuromuscular transmission, I examined *C. elegans* swimming. *C. elegans* swimming is an alternative form of locomotion which occurs when worms are shifted to a low viscosity medium, such as a liquid buffer. While swimming, *C. elegans* continuously produce “C”-shaped bends shifting from one side to the other at a high intensity (Figure 3.6A). This behaviour is highly consistent, with wild-type worms rarely taking prolonged breaks. Previous examinations of *C. elegans* swimming behaviour have likened it to a form of exercise with animals becoming fatigued after extended sessions in liquid with the activity being more energetically demanding than regular crawling (Laranjeiro et al, 2017). Defects in swimming, such as reduced bending rate or reduced stamina can be indicative of insufficient neuromuscular function.

To assess swimming, I began by counting the number of body bends performed by each of the strains within a thirty second timeframe from video recordings. A significant separation was observed between all strains harbouring the *syd-2* mutation and those without (Figure 3.6B). Strains with loss of function mutations for *cla-1* or *h1b-1* and the double mutant *cla-1; h1b-1* were not significantly different from wild-type (Figure 3.6B). In contrast, all *syd-2*-containing mutant strains produced significantly fewer body bends compared to WT while being statistically indistinguishable from one another (Figure 3.6B). Like in crawling locomotion this strongly suggests a strong *syd-2(ok217)* driven defect.

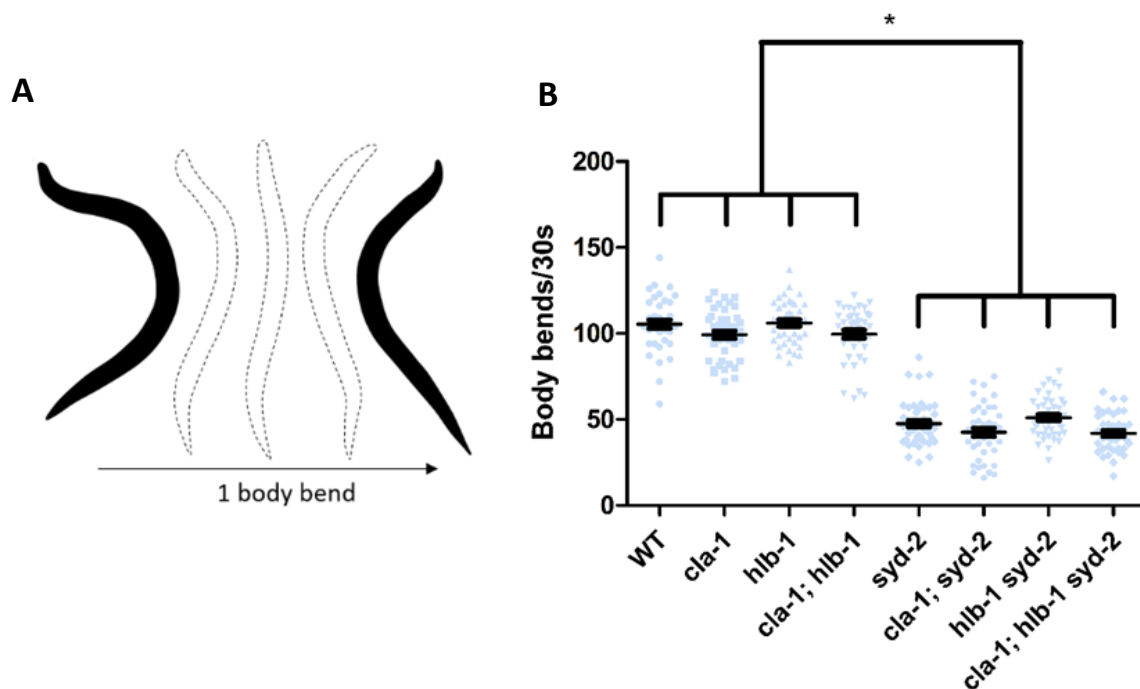


Figure 3.6. SYD-2 loss causes defective swimming which is not exacerbated by additional loss of HLB-1 and CLA-1. **A.** Body bend counts were taken over a 30 second period. A body bend was considered to be a transition from one C-shaped bend to another. **B.** Comparison of the number of body bends performed while swimming over 30 seconds. Bars in the data show mean \pm SEM. Pairwise comparisons for significance testing used Dunn's test for multiple comparisons following Kruskal-Wallis test for variance. Pairwise comparisons were made between wild-type and all other conditions, between single mutants and double mutants which shared mutations, and between the triple mutant and all single and double mutants. Pairwise comparisons are shown by lines with ticks indicating mutants being compared to the condition at the unticked left-hand end. * $p < 0.05$ corrected for multiple comparisons. N-values are as follows: *WT*=40, *cla-1*=44, *hlb-1*=40, *syd-2*=42, *cla-1; hlb-1*=43, *cla-1; syd-2*=40, *hlb-1 syd-2*=42, *cla-1; hlb-1 syd-2*=39. Post-hoc power calculations can be found in Appendix 1.

While midbody bend count is a robust initial measure to compare locomotor capacity, it is also important to understand the dynamics responsible for the observed differences. Using parameters available through the Tierpsy Tracker software (Javer

et al, 2018) the peak midbody curvature and time between peak midbody bends were examined from a subset of the full population of each strain. Peak midbody curvature refers to the most acute midbody curvature achieved by worms during each body bend and is indicative of the degree of muscle contraction (Figure 3.7A), whereas the time between peak bends illustrates their speed in changing posture (Figure 3.7B).

In wild-type *C. elegans*, the peak midbody curvature and time between peak bends remains highly regular during swimming behaviour. *syd-2(ok217)* single mutants and *syd-2*-containing double and triple mutants displayed significantly greater variation in both peak body curvature (Figure 3.7Aii) and time between bends compared to the wild-type (Figure 3.7Bii), suggesting an uncoordinated swimming motion. While the mean time between midbody bends was significantly increased in *syd-2* mutants (Figure 3.7Bi), the mean peak curvature was unchanged (Figure 3.7 Ai) suggesting slower bend transitions were not the result of increased curvature. *cla-1* and *h1b-1* single, and *cla-1; h1b-1* double mutants displayed no significant difference from wild-type in any of the measured parameters, indicative of normal swimming locomotion.

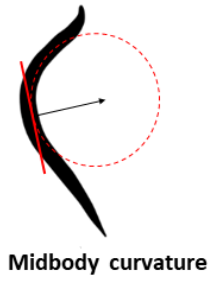
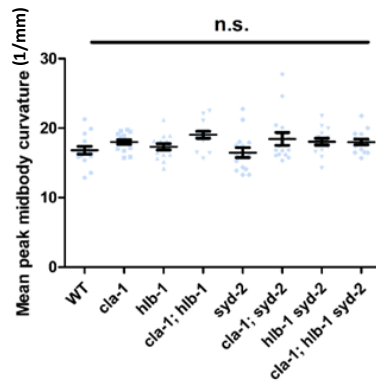
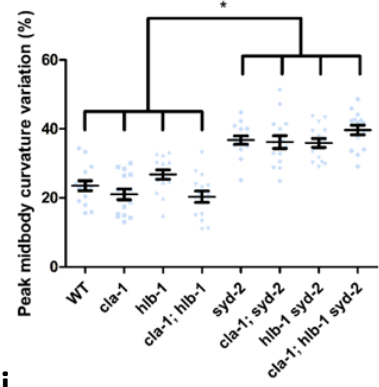
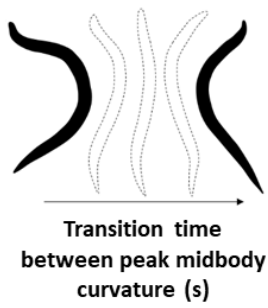
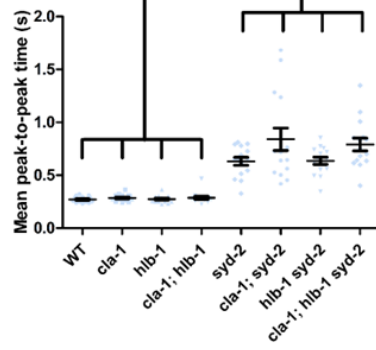
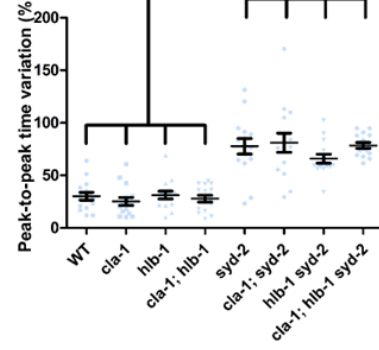
A**i****ii****B****i****ii**

Figure 3.7 *syd-2* mutants show greater variability in their swimming dynamics. **A.** Peak midbody curvature was taken as the maximum curvature achieved during a midbody bend while swimming. Curvature was calculated by taking the mean of all curvature measurements across the midbody segment (**Figure 3.4**) over a 30 second swimming session. Curvature is determined by finding the radius of the circle which best fits the curve (mm) and dividing 1 by this radius. **Ai.** Comparison of midbody curvature across strains. **Aii.** Comparison of the mean variability in midbody bends across strains using the co-efficient of variation. **B.** Time between peak midbody curvature was measured as the time taken to transition from the peak midbody curvature of one body bend to the peak midbody curvature of the next. **Bi.** Comparison of the time between peak midbody curvature of each body bend across strains. **Bii.** Comparison of the mean variability in midbody bends across strains using the co-efficient of variation. For **Aii** pairwise comparisons for significance testing used the Bonferroni test for multiple comparisons following ANOVA test for variance. For **Bi** and **Bii** pairwise comparisons for significance testing used Dunn's test for multiple comparisons following Kruskal-Wallis test for variance. Pairwise comparisons were made between wild-type and all other conditions, between single mutants and double mutants which shared their mutations, and between the triple mutant and all single and double mutants. The bar in **Ai** shows there was no significance found for any of the pairwise comparisons performed. For **Aii**, **Bi** and **Bii** pairwise comparisons are shown by the bars above the data and indicate that there was a consistent significant difference between all strains carrying a *syd-2(ok217)* mutation and those without. * $p < 0.05$ corrected for multiple comparisons. n.s. - not significant. N=15 for all strains. Post-hoc power calculations can be found in Appendix 1.

One of the main causes of the increased variability in both peak midbody curvature and time between midbody bends observed in the *syd-2(ok217)*-containing strains appears to be an increased propensity for curling behaviour. These curling behaviours involve the worms entering a posture of high curvature, often adopting a "6" shape (**Figure 3.8**) and remaining in this conformation for at times several seconds. This

typically occurred multiple times in recordings. Such behaviours were incredibly rare if not entirely absent in mutants without the *syd-2(ok217)* allele.

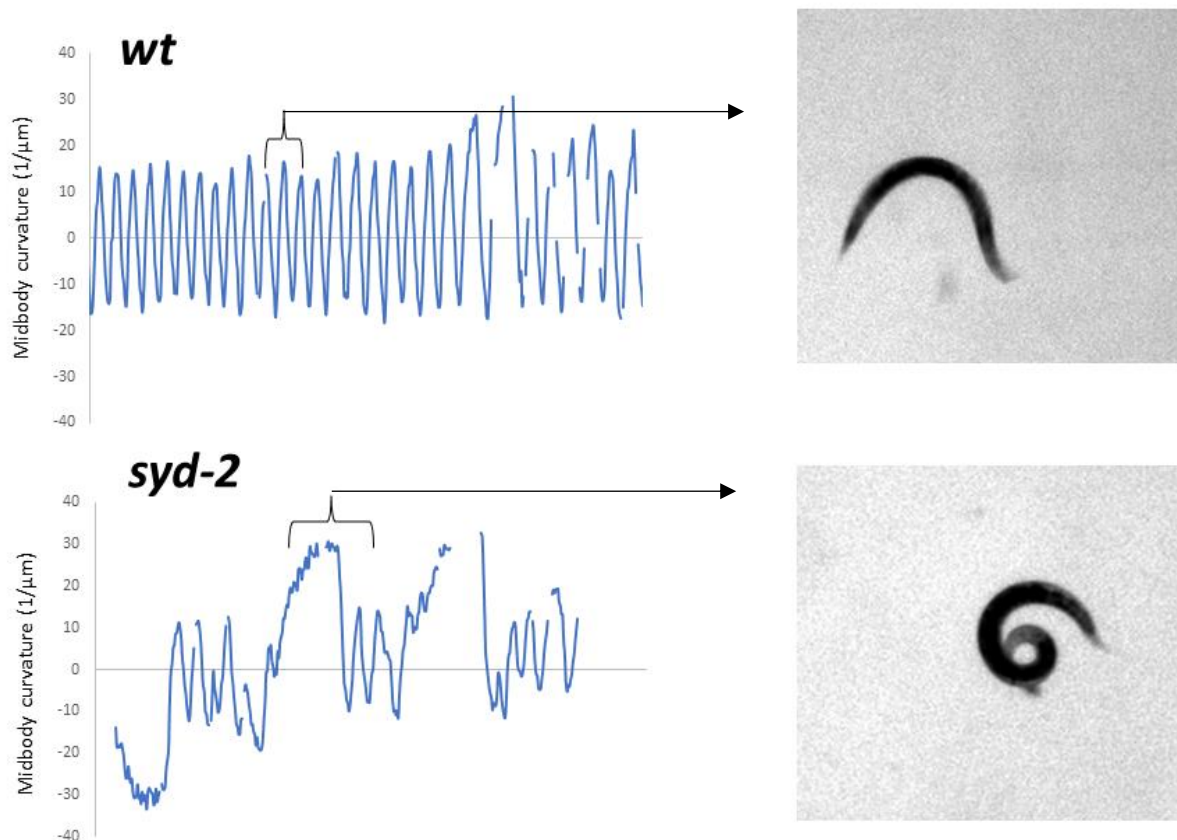


Figure 3.8. Mutants carrying a *syd-2* mutation express a prolonged curling phenotype. A comparison of the typical wild-type swimming pattern and the *syd-2* mutant curling phenotype with an accompanying frame showing the posture adopted by the worm in video recordings.

Interestingly when observed over the course of 15 minutes *syd-2(ok217)*-containing double and triple mutants would often enter a quiescent period where swimming ceased (Figure 3.9). Often the worms would appear paralysed and remain in place until resuming swimming. These quiescent phases often lasted over one minute and may reflect a recovery period following protracted swimming.

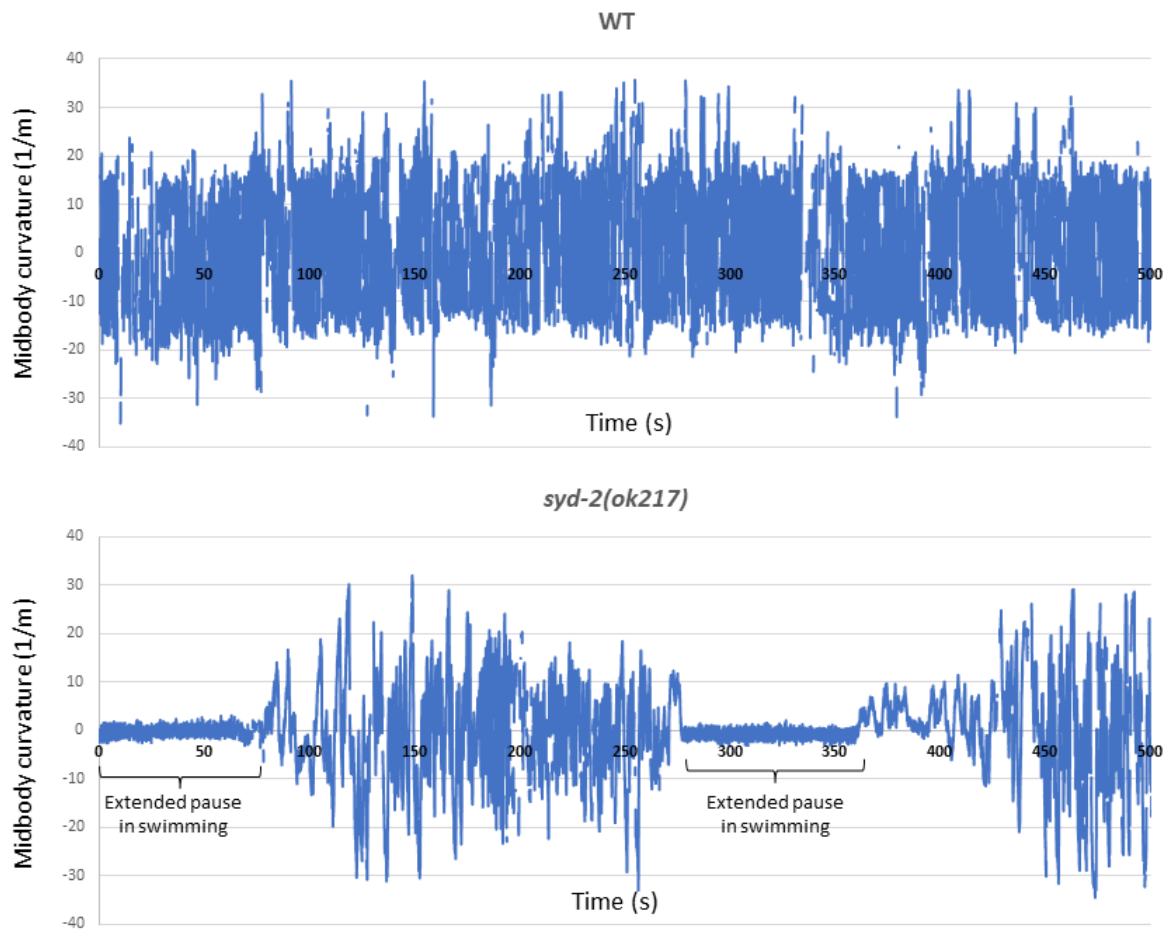


Figure 3.9. The *syd-2(ok217)* mutant allele promotes periods of quiescence during extended swimming sessions. Midbody curvature over time for wild-type and *syd-2(ok217)* single mutant worms over 500 seconds taken as excerpts from 15-minute swimming recordings.

3.1.3 Loss of SYD-2 does not affect aldicarb sensitivity, but loss of HLB-1 amplifies *cla-1(ok2285)* mutant resistance in the *cla-1; hlb-1 syd-2* triple mutant

The observations from locomotion analysis suggested that neuromuscular function is altered in several of the strains investigated. Both swimming and locomotor assays

appear to establish that SYD-2 is a determinant of regular locomotion. The introduction of additional mutations in genes encoding AZ components, in particular *cla-1(ok2285)*, appears to further modulate the crawling gait of the worms as well as their locomotor speed while not exerting any further effect upon swimming. Due to the presynaptic nature of the proteins encoded by the mutant genes both the robust and more subtle effects observed could be a consequence of changes in neurotransmission at the neuromuscular junction. To investigate this further, I characterised the pharmacological properties of cholinergic transmission in *syd-2*, *cla-1* and *h1b-1* single mutants and double and triple mutants combining them.

Acetylcholine acts as one of the primary *C. elegans* neurotransmitters and is the exclusive excitatory neurotransmitter of neuromuscular junctions. Defective acetylcholine release can be easily assayed using the neuropharmacological agent aldicarb. Aldicarb is a neurotoxin which acts as a competitive inhibitor of acetylcholine esterase, an enzyme which breaks down acetylcholine after it has been released into the synaptic cleft. Through this mechanism abnormally high levels of acetylcholine remain at the synapse causing hypercontraction and eventual paralysis. Mutations causing reduced acetylcholine release result in slower build-up of the neurotransmitter and therefore delay paralysis compared to wild-type, conversely increased acetylcholine release accelerates paralysis. In aldicarb assays, worms of each strain were placed on to media containing 0.5mM aldicarb and observed for body paralysis over 5 hours.

Previous examination of *syd-2* mutants using aldicarb assays have suggested that these strains display either mild (Zhen and Jin, 1999; Kittelmann et al, 2013) or no (Wang and Wang, 2009) resistance to aldicarb. As shown in Fig 3.10, aldicarb

sensitivity was unchanged in *syd-2* single mutants compared to wild-type (Figure 3.10). *hlb-1* single mutants were also comparable to wild-type, *hlb-1 syd-2* double mutants meanwhile were slightly more sensitive to aldicarb than wild-type worms but not compared to either *hlb-1* or *syd-2* single mutants. Previous study had found both *hlb-1* single mutants and *hlb-1 syd-2* mutants have increased resistance to aldicarb (Wang and Wang, 2009; Rosenhahn et al, 2022). These contradictory results may be due to differences in experimental design between these previous studies and my own.

cla-1(ok2285) single mutants, meanwhile, demonstrated significant aldicarb resistance (Figure 3.10), agreeing with previous findings (Xuan et al, 2017). *cla-1; syd-2* double mutants were similarly resistant to aldicarb suggesting that the *cla-1* mutant allele also confers defective cholinergic neurotransmission in the *syd-2* mutant background. The lack of effect SYD-2 loss has on aldicarb resistance either independently or in combination with other mutations suggests that SYD-2 has a limited effect on physiological cholinergic neurotransmission. Interestingly this stands in contrast with the reduced evoked release recorded from *syd-2* mutants in electrophysiological assays (Kittelmann et al, 2013), although this could be reflective of the differing sensitivities of the two assays.

Interestingly, a synergistic effect was observed when CLA-1 and HLB-1 were removed together. The presence of the *hlb-1(ok725)* allele in the triple mutant caused a significant increase in resistance compared to the *cla-1(ok2285); syd-2(ok217)* double mutant (Figure 3.10). Although a weaker effect, the *cla-1(ok2285); hlb-1(ok725)* double mutant also appeared to have enhanced aldicarb resistance compared to the *cla-1(ok2285)* single mutant. Together these results suggest that in the absence of

CLA-1, HLB-1 may be able to compensate for the reduction in cholinergic neurotransmission despite not typically being important to the process.

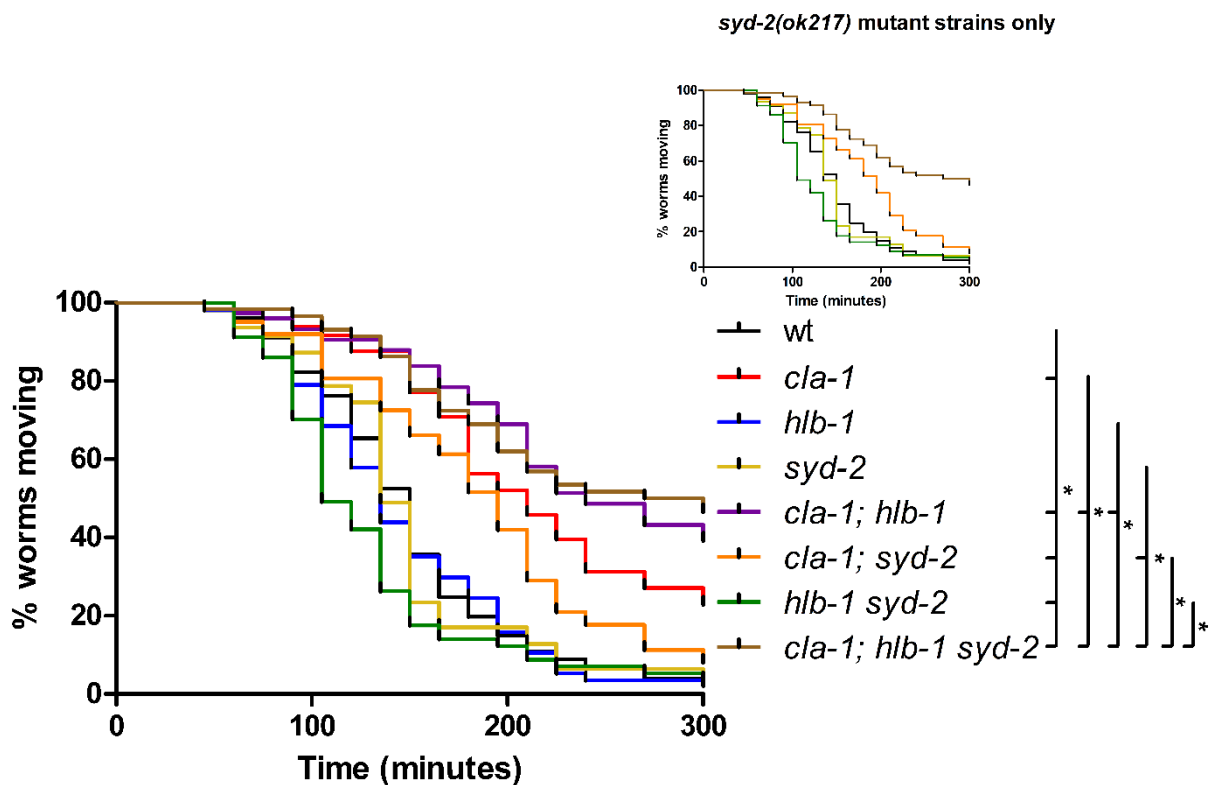


Figure 3.10. *hlb-1(ok725)* enhances inherent aldicarb resistance in *cla-1(ok2285)*, whereas *syd-2(ok217)* does not increase aldicarb resistance. Main graph (bottom-left) depicts aldicarb paralysis survival plots for a concentration of 0.5mM over a 5-hour time course. Results are pooled from 3 separate assays. All *cla-1(ok2285)* mutant conditions displayed greater aldicarb resistance than wild-type, whereas *syd-2(ok217)* and *hlb-1(ok725)* single mutants and the *hlb-1(ok725) syd-2(ok217)* were comparable to wild-type. The triple mutant displayed significantly greater resistance than the *cla-1(ok2285); syd-2(ok217)* double. Inset (top-right) presents the same data but only with mutant strains with the *syd-2(ok217)* allele. Significance testing was performed using pairwise Log-Rank Mantel-Cox tests between wild-type and all other conditions, between single mutants and double mutants which shared their mutations, and between the triple mutant and all single and double mutants. Pairwise comparisons are shown by lines with ticks indicating mutants being compared to the condition at the unticked top end. * $p < 0.05$. Total animals WT=101, *cla-1*=48, *hlb-1*=57, *syd-2*=49, *cla-1; hlb-1*=74, *cla-1; syd-2*=68, *hlb-1 syd-2*=61, *cla-1; hlb-1 syd-2*=65. Post-hoc power calculations are in Appendix 1.

3.3 Discussion

3.3.1 SYD-2 is necessary for normal locomotion patterns but is not integral to basal locomotion

In the previous chapter I confirmed SYD-2's involvement in the recruitment of SVs and UNC-10, part of the AZ scaffold and a key component of SV docking at cholinergic synapses. Muscle contraction is driven by cholinergic neurotransmission from motor neurons, hence disruption to SV recruitment, docking and fusion can affect *C. elegans* locomotion. Loss of function alleles encoding proteins closely involved with the SNARE complex and SV fusion such as UNC-64 (Saifee et al, 1998; Nonet et al, 1998), UNC-13 (Richmond et al, 1999) and UNC-18 (Sassa et al, 1999; Zhu et al, 2020) are almost completely paralysed. The locomotor defects observed in *syd-2* null mutants were considerably less severe with mutant worms being capable of prolonged crawling locomotion, although crawling posture was modified and swimming locomotion was uncoordinated. This suggests that the loss of SYD-2 does not have a strong effect on the localisation or assembly of the machinery involved in SV fusion, such as the SNARE complex, that enable basal locomotion. This may explain why *syd-2* mutants did not exhibit aldicarb resistance in my investigations. The unchanged aldicarb sensitivity was consistent with other aldicarb studies where *syd-2* mutants only display mild to non-existent aldicarb resistance (Zhen and Jin, 1999; Wang and Wang, 2009; Kittelmann et al, 2013).

This does not mean that SYD-2 has no effect on cholinergic signalling, however. Electrophysiological recordings have previously shown that *syd-2* loss of function mutants have reduced evoked excitatory postsynaptic current amplitude at body wall muscle following stimulation of the ventral nerve cord, suggesting that the capacity for

acetylcholine release from motor neurons is reduced (Kittelmann et al, 2013). *syd-2* mutants also display enhanced synaptic depression following extended stimulation trains (Kittelmann et al, 2013). During endogenous cholinergic release however, which is examined in aldicarb assays, loss of SYD-2 at neuromuscular synapses may not have a strong enough effect to clearly influence aldicarb sensitivity.

An additional consideration is whether higher order circuits which modulate motor neuron activity are also affected by the loss of SYD-2. SYD-2 has broad nervous system expression and may influence different synapses asymmetrically. The removal of other AZ proteins has been demonstrated to have variable effects at different synapses. Confocal studies have shown CLA-1 is important for maintaining organised SV recruitment to synaptic regions in PVD mechanosensory neurons and AIY interneurons but not cholinergic and GABAergic motor neurons (Xuan et al, 2017). Such changes could lead to variable effects on neurotransmission at these different synapses. Disruption to higher order synapses could hypothetically mask subtle aldicarb resistance phenotypes by upregulating the frequency of cholinergic neurotransmission at the NMJ.

A combination of subtle or specific cholinergic neurotransmission defects and defective neurotransmission in higher neurons controlling motor neuron activity or behaviour are likely to underlie the locomotor defects of *syd-2* mutants.

3.3.2 SYD-2 loss disrupts crawling locomotor patterns

Although *syd-2* mutants were still capable of consistent crawling locomotion their crawling dynamics deviated from wild-type in several respects. *syd-2* mutants

exhibited a crawling gait with reduced body curvature and moved faster than their wild-type counterparts. The reduced body curvature may itself be responsible for the increase in speed by extending the wavelength of sinuous crawling and therefore increasing the Euclidean distance travelled over time. The reduced body curvature is a consequence of altered input to the muscle cells which could arise directly from changes to the presynaptic release machinery of motor neurons or altered inputs from higher circuits. To differentiate between these mechanisms future studies can examine whether knockdown or knockout of SYD-2 specifically within DA and DB motor neurons phenocopy the curvature effects of whole animal *syd-2* null mutation. DA and DB motor neuron specific overexpression through a rescue construct in *syd-2* null mutants meanwhile would confirm whether SYD-2's contribution to speed and curvature are cell autonomous.

Some other *syd-2* mutant crawling behaviours may have more complex origins arising from defects in multiple upstream networks. During crawling experiments *syd-2* mutants were found to pause less frequently and explored a greater region of the environment. *C. elegans* hermaphrodites primarily explore their environment in search of food, once food is detected the worm slows down and remains within that area (Ben Arous et al, 2009; Calhoun et al, 2014; Oranth et al, 2018). In the crawling experiments a thin layer of food was placed on the agar medium to keep them centralised. Although this could not be confirmed as the bacterial lawn was not visible in recordings, *syd-2* mutants may engage in foraging and area restricted search behaviour less frequently than wild-type worms. This could occur due to defects in relaying food detection information from sensory neurons to the circuits initiating foraging behaviour or defective neurotransmission in those downstream circuits.

C. elegans detects food through the amphid sensilla of the head which act as their primary sense organs. The amphid sensilla consist of cilia from twelve sensory neurons namely ADF, ADL, AFD, ASE, ASG, ASH, ASI, ASJ, ASK, AWA, AWB and AWC (Bargmann et al, 1990). These sensory neuron cilia can sense many stimuli associated with food including odour, taste, oxygen levels and temperature (Bargmann et al, 1993; Mori & Ohshima, 1995; Kaplan, 1996; Chang et al, 2006). To integrate this environmental information into the rest of the nervous system sensory neurons typically have high rates of neurotransmission. In both vertebrates and invertebrates enlarged dense projections are frequently observed at sensory neuron synapses (Ackermann et al, 2015; Okawa et al, 2019) which are thought to assist in the continual replacement of SVs at plasma membrane docking sites following fusion (Becker et al, 2018). SYD-2's role in both promoting AZ scaffold formation and maintaining sustained release could make the protein critical for relaying environmental cues to the rest of the nervous system.

Foraging behaviours in response to food meanwhile are driven by dopaminergic and serotonergic signalling (Sawin et al, 2000; Iwanir et al, 2016; McCloskey, 2017 et al). SYD-2 is known to be required at serotonergic synapses of the HSN motor neuron to initiate normal egg-laying behaviour (Patel et al, 2006). Therefore, defective serotonergic signalling at least is a plausible driver of some of the observed behavioural defects in *syd-2* mutants.

Further behavioural studies will be required to establish if increased exploration in *syd-2* mutants is associated with a failure to induce foraging behaviour. If true, this behaviour and its extensively studied circuitry could provide an excellent setting in which to explore the relationship between SYD-2 expression and both serotonergic and dopaminergic neurotransmission. Many of the specific neurons which drive

dwelling and local search foraging behaviours are well characterised including the dopaminergic ADE and PDE interneurons and the serotonergic interneuron NSM. It is intriguing to consider whether the loss of SYD-2 in any of these neurons specifically would elicit the same locomotor defects as whole germline null mutants.

As the effects of the loss of *syd-2* do not severely hamper crawling locomotion it is important that future studies attempt to isolate how different neurons and circuits are affected by the loss of *syd-2*. This will provide a clearer picture of how individual features of its crawling phenotype arise and from which circuits.

3.3.3 SYD-2 maintains consistent, sustained swimming locomotion

Swimming locomotion was more strongly affected in *syd-2* mutants than crawling locomotion, being clearly uncoordinated compared to wild-type. The most striking feature of *syd-2* mutant locomotion was their tendency to intermittently cease swimming. Frequently *syd-2* mutants would curl to some degree before reinitiating thrashing. Additionally, over longer observations *syd-2* mutants would enter a quiescent state during which worms would adopt a straight, rigid body position at their posterior end with a curve leading towards the head. Neither of these behaviours were observed in wild-type, *cla-1* or *h1b-1* single mutants or the *cla-1; h1b-1* double mutant.

Coiling behaviour, which is similar to the curling I observed, is frequently observed in moderate to severe synaptic mutants such as the *unc-10* null mutant (Gracheva et al, 2008; Chen et al, 2021). This normally occurs during crawling, something that is not observed in the *syd-2* mutants. The intermittent nature of curling during *syd-2* mutant swimming is therefore curious. It could be the consequence of a relatively mild

neurotransmission defect which only manifests during swimming due to the greater intensity of activity. One possibility is that repeated high intensity fusion events driving frequent body bending depletes the number of SVs available for release. This would be consistent with the enhanced synaptic depression exhibited by *syd-2* mutants following repetitive stimulation in electrophysiological studies (Kittelmann et al, 2013). As *C. elegans* swimming has previously been described as analogous to a form of exercise (Laranjeiro et al, 2017) enhanced muscle fatigue cannot be ruled out as an explanation particularly as SYD-2 is known to be expressed at postsynaptic body wall muscle (Serra-Pagès et al, 1998).

It is also interesting to note that several of the *syd-2* mutant phenotypes overlap with behaviours seen in defective dopaminergic signalling. Knockdown of UNC-64 specifically in dopaminergic neurons, severely compromising dopaminergic release, reduces body bending while swimming (Lanzo et al, 2018). Meanwhile, a recent paper has proposed that coiling during crawling can result from diminished dopaminergic signalling (Chen et al, 2021). A finding which is supported by the dopaminergic neuron specific toxin MPTP eliciting coiling behaviour in *C. elegans* (Braungart et al, 2004). Quiescent periods observed between bouts of swimming, such as that observed in *syd-2* mutants, have also been associated with dopaminergic signalling. These prolonged periods of inactivity are likely to be a premature form of “exercise induced quiescence” a phenomenon which in wild-type worms is normally observed after a period of approximately 90 minutes of continuous swimming (Ghosh and Emmons, 2008). *grk-2* mutants display a similar phenotype to *syd-2* mutants which is believed to initiate quiescence through a pathway dependent upon dopaminergic and neuropeptide signalling to premotor interneurons (Xu et al, 2021). Given both crawling (as discussed in 3.3.2) and swimming locomotion defects in *syd-2* mutants are

potentially associated with dopaminergic signalling it may be pertinent to investigate whether SYD-2 loss in these circuits specifically drives the observed behaviours. Some interesting first steps would be to examine whether the loss of SYD-2 selectively in dopaminergic circuits through targeted gene knockout or knockdown could elicit the same curling and quiescent behaviours during swimming. Conversely the efficacy of rescuing *syd-2* mutant behavioural phenotypes through overexpression of wild-type SYD-2 in dopaminergic neurons will also need to be examined. These investigations would confirm if dopaminergic neurotransmission requires SYD-2 to support normal swimming behaviour. If so, to investigate dopaminergic neurotransmission calcium imaging approaches will need to be used as dopaminergic interneurons are typically not accessible for electrophysiology. Techniques have been developed allowing optogenetic constructs and calcium indicators to be targeted to specific cells. This approach would require a dopaminergic neuron to be stimulated by optogenetics and the postsynaptic target neurons examined for calcium transients (Guo et al, 2009). Developments have also been made recently to perform calcium imaging in freely moving worms which could be useful to assess endogenous neurotransmission (Shiple et al, 2014; Nguyen et al, 2016).

If swimming-specific curling and quiescence derive from the loss of one AZ protein broadly expressed across synapses it is perhaps surprising that these defects have not been observed in other presynaptic mutants. This may simply be the result of SYD-2 loss having a more modest effect than mutants that greatly affect neurotransmission and eradicate a normal swimming motion such as those for *unc-13* (Richmond et al, 1999; Moseley-Allred et al, 2022), but a more severe effect than those which are mostly dispensable for neurotransmission and retain regular swimming locomotion such as those for *elks-1* (Oh et al, 2021).

3.3.4 HLB-1 opposes SYD-2-driven crawling behaviour

Compared to *syd-2* mutants, *hlb-1* mutants typically have a weaker effect on locomotion. Loss of HLB-1 had no observable effect on swimming phenotype. *hlb-1* single mutants had an identical swimming phenotype to wild-type worms whereas *hlb-1 syd-2* double mutants were indistinguishable from *syd-2* single mutants. HLB-1 did modify crawling behaviour, however. *hlb-1* mutants pause more often and engage in less forward directed locomotion than wild-type worms, consequently covering a smaller proportion of their environment. They were also much slower than their wild-type counterparts.

Curiously despite HLB-1 loss broadly affecting crawling in a manner which stood in opposition to the effects of SYD-2 loss, in *hlb-1 syd-2* double mutants speed and path coverage were unchanged compared to *syd-2* single mutants. Frequency of forward or paused motion in *hlb-1 syd-2* double mutants was also much more like *syd-2* single mutants than *hlb-1* single mutants. This suggests that the effects of HLB-1 loss are somewhat dependent upon the presence of SYD-2. As coordination of locomotion requires many different neuronal circuits it is difficult to differentiate whether this effect is a consequence of the proteins affecting different neurons within the same circuit (e.g., loss of HLB-1 in a neuron requiring HLB-1 for neurotransmission signalling to a neuron requiring SYD-2 would have no effect if SYD-2 was not present) or interactions between the proteins within the same neuron.

Within individual neurons, HLB-1 function could be dependent upon SYD-2 either as a recruiter or as a target for inhibition neither of which are necessarily mutually exclusive. The latter is an appealing proposition considering the two proteins are likely to bind each other based on data from homologues (Serra-Pagès et al, 1998;

Astigaraga et al, 2010; Wei et al, 2011). This interaction prevents Liprin- α (the mammalian SYD-2 homologue) from binding its presynaptic receptor LAR (Wei et al, 2011; Xie et al, 2021) which is thought to contribute to presynaptic assembly (Yim et al, 2013; Han et al, 2020). Confocal assays exploring HLB-1's localisation, and yeast-2 hybrid or coimmunoprecipitation assays examining HLB-1 and SYD-2's interactions will be useful to differentiate these mechanisms.

Interestingly like SYD-2, HLB-1 loss has no effect on cholinergic signalling in aldicarb assays. This suggests neither protein's effects are driven by changes in strength at the cholinergic neuromuscular junction. Therefore, genetic interaction between the proteins may occur above the level of the NMJ. Like in *syd-2* mutants, loss of HLB-1 affects pausing and exploratory behaviour, which are associated with foraging behaviours driven by dopaminergic and serotonergic signalling (as discussed in 3.3.3). It is interesting to consider whether the loss of HLB-1 specifically in dopaminergic or serotonergic neurons would phenocopy the effects on pausing and exploratory behaviour seen in non-specific *h1b-1* single mutants. It would also be tempting to explore whether the additional loss of *syd-2* in these neurons mask these effects.

3.3.5 CLA-1 modulates crawling locomotion

The relationship between CLA-1 and locomotion is more difficult to determine. Like HLB-1, CLA-1 loss did not affect swimming locomotion. Although CLA-1 loss does have a limited effect on some aspects of crawling locomotion these did not adhere to the broadly oppositional effects of *h1b-1* and *syd-2* single mutants (as discussed in 3.3.4). Like *h1b-1* mutants, *cla-1* mutants moved forward less frequently and more slowly than wild-type worms. However, like *syd-2* mutants, backward motion was more

frequent, and curvature was decreased across body regions. In most cases though, loss of CLA-1 had a weaker effect than loss of HLB-1 or SYD-2.

CLA-1 has broad nervous system expression therefore loss of CLA-1 function throughout an entire worm has the potential to disrupt a multitude of synaptic connections across different neurons. Recently CLA-1 has been shown to have broad synaptic involvements including the recruitment of both RIMB-1, which promotes calcium channel localisation near release sites, and UNC-13 (Krout et al, 2023). As the recruitment of calcium channels and the formation of the SNARE complex, facilitated by UNC-13, enhance release probability CLA-1 is likely to affect neurotransmission. The effects that CLA-1 loss has upon synapses is not necessarily uniform, however. Confocal studies have previously shown that *cla-1* mutants affect SV recruitment more strongly in PVD sensory neurons and AIY interneurons compared to GABAergic or cholinergic motor neurons (Xuan et al, 2017). As many different synaptic connections throughout the *C. elegans* nervous system influence locomotor behaviour the broad and non-uniform effects on neurotransmission caused by the loss of CLA-1 are likely to generate their unique behavioural repertoire. As *syd-2* and *h1b-1* mutants may also have variable effects across synapses this could explain some of the more surprising effects in double and triple mutants. This includes curvature, where *cla-1; syd-2* double mutants regularly exhibited an intermediate curvature phenotype between the *cla-1* and *syd-2* single mutants despite both single mutants having reduced curvature compared to wild-type.

Interestingly, *cla-1* mutants were the only single mutant examined to have reduced aldicarb sensitivity, suggesting there is reduced cholinergic neurotransmission at the NMJ. Although notable compared to *h1b-1* and *syd-2* mutants the effect on aldicarb resistance may actually be fairly weak, however. Aldicarb still induced paralysis in

~80% of *cla-1* mutant worms over the course of the assay, whereas previous assays examining mutants with strong effects on neurotransmission such as *unc-10(md1117)* exhibit almost no paralysis over longer time periods under higher concentrations of aldicarb (Koushika et al, 2001). The idea that CLA-1 only mildly influences cholinergic neurotransmission is also supported by the lack of change in evoked release in previous electrophysiology assays (Xuan et al, 2017). CLA-1 loss may induce a modest modulatory effect on cholinergic neurotransmission which could affect locomotion, although it should be noted that defects in the signalling of higher order synapses can also affect aldicarb resistance. *cat-2*, *dop-2* and *dop-3* mutants, all of which specifically contribute to dopaminergic signalling, exhibit increased aldicarb resistance (Suo and Ishiura et al, 2013). Due to CLA-1 also being expressed in interneurons a similar scenario is also possible here.

This emphasises the need for future investigations of locomotion in synaptic mutants to be targeted to specific neuronal subtypes and, where possible and relevant, specific neurons. While my analysis has revealed that there are locomotor consequences to the loss of CLA-1 the interconnectivity and non-linear signalling of the neurons involved in locomotion makes interpretation of the origin of these effects difficult. Targeting *cla-1* mutations to cholinergic synapses, or preferably the cholinergic DA and DB motor neurons innervating body wall muscle, would allow the locomotor effects at neuromuscular junctions to be more precisely determined. Advances in mutagenesis techniques are making targeting of neuronal subtypes, and even single neurons, more viable in *C. elegans*. Such approaches can also be tied to calcium imaging assays allowing the visualisation of synaptic activity at the neuromuscular junction. Applying these approaches to CLA-1, SYD-2 and HLB-1 in both cholinergic and other synapses involved in locomotion in future will help us to identify the precise

contributions of AZ proteins to synaptic function and neuronal pathways to locomotion. Utilising a similar approach to aldicarb assays could also be incredibly useful to isolate the effects of the loss of AZ proteins on endogenous cholinergic release specifically at the neuromuscular junction.

3.3.6 The loss of HLB-1 further disrupts cholinergic signalling in *cla-1* mutants

In aldicarb assays the loss of HLB-1 in mutants carrying the *cla-1(ok2285)* allele further enhanced aldicarb resistance. As *h1b-1* single mutants displayed no resistance to aldicarb, this seems to suggest that HLB-1's contribution to cholinergic neurotransmission at the NMJ may be enhanced when CLA-1 is also lost.

Previous reports have suggested that HLB-1 loss promotes aldicarb resistance (Wang and Wang, 2009; Rosenhahn et al, 2022). The contrary results between my own experiments and these previous studies may be due to differing experimental designs. Wang and Wang et al defined paralysis in aldicarb assays as the absence of both body movement and continuous pharyngeal pumping. While both types of movement are dependent upon cholinergic neurotransmission, they are believed to have very different mechanisms of control, pharyngeal pumping also being dependent upon both intrinsic myogenic rhythmicity (Trojanowski et al, 2016) and non-cholinergic neurotransmitters (Niacaris and Avery, 2003; Tsalick et al, 2003; Lee et al, 2020). Therefore, pharyngeal pumping could be affected by aldicarb treatment differently to the body wall muscle and extend the time to paralysis (Izquierdo et al, 2022). Rosenhahn et al meanwhile used a mutant which excised all exons from *h1b-1*, meaning that it produced no protein product, unlike the 234AA long product theoretically produced following the *h1b-1(ok725)* deletion, which could indicate that

the N-terminal region encoded by the *h1b-1(ok725)* mutant supports cholinergic release. Their experiments used only a very low concentration of aldicarb (1-10µm), however, examining the fraction of sedentary worms rather than complete paralysis. Such a phenotype could also be present in *h1b-1(ok725)* mutant worms and may represent reduced neurotransmission in circuits controlling the decision to move which feed into the NMJs which could have greater dependence on HLB-1 than the NMJs themselves. Therefore, it is currently difficult to tell what effect HLB-1 has on cholinergic neurotransmission and under what circumstances.

While the function of HLB-1 in regulating neurotransmitter release is still unclear, its loss may enhance the defects in SV recruitment in the *cla-1* mutants as suggested by the findings of my confocal microscopy studies. As discussed previously, aldicarb resistance can be affected at synapses above the neuromuscular junction, therefore, it will be important to establish whether this effect emanates from the neuromuscular junction itself. This could be achieved through specific knockdown or knockout of *h1b-1* and *cla-1* in cholinergic DA and DB neurons independently and together to examine if the synergistic effect of the proteins is maintained in aldicarb assays. If so, further research will be required to explore whether the proteins have a redundant function in cholinergic neurotransmission.

4 Examining presynaptic ultrastructure in the absence of SYD-2, HLB-1 and CLA-1

In the previous chapters I used confocal microscopy and functional assays to understand the collective contributions of SYD-2, CLA-1 and HLB-1 to synaptic formation and neurotransmission. While these approaches can give an overview of how these proteins function together, they lack the resolution to interpret the molecular contributions of SYD-2, HLB-1 and CLA-1 at individual presynaptic sites. Exploration of the combined role of these proteins at the level of a single synapse and their effect on the presynaptic active zone (AZ) ultrastructure requires the resolution of electron microscopy (EM).

EM was first used to visualise neurons in the 1950s giving the first glimpse of synaptic vesicles (SVs) and the synaptic cleft (Pease, 1953; Palay, 1955; Sotelo, 2020). This tool has continued to be influential in neurobiology allowing visualisation of synaptic connections and neuropathological features such as misfolded protein plaques (Han et al, 2017; Yang et al, 2022) and neurofibrillary tangles (Ruben et al, 1993; Tatsumi et al, 2014). EM has been crucial to establish the connectomes of nervous systems including the entire *C. elegans* connectome (White et al, 1986; Cook et al, 2019), which remains the only complete connectome for any adult organism, and more recently larval connectomes of *Ciona intestinalis* (Ryan et al, 2016), *Platynereis dumerilii* (Verasztó et al, 2020) and the *Drosophila melanogaster* larval brain (Winding et al, 2023).

While the advent of EM was revolutionary for the field of neurobiology, the relevance of the observed structures to living organisms was historically the subject of some scrutiny. Early chemical fixation methods involved processing of specimens at room temperature with some samples requiring dissection to permit adequate infiltration of fixatives (Epstein et al, 1974; White et al, 1976). These preparation methods often distorted cellular membranes and organelles. The introduction of high-pressure freezing and freeze substitution techniques have been ground-breaking in the examination of biological samples under EM. The freezing of biological samples in liquid media, such as whole *C. elegans*, with liquid nitrogen results in immediate cryofixation of the specimen whereas the high-pressure environment prevents tissue damage by freezing the sample in vitreous ice (Rostaing et al, 2004). The sample is then gradually brought towards higher temperatures while being submersed in fixatives. During this process water in the sample is exchanged for the fixative, in a process known as freeze substitution, which preserves the sample's native morphology.

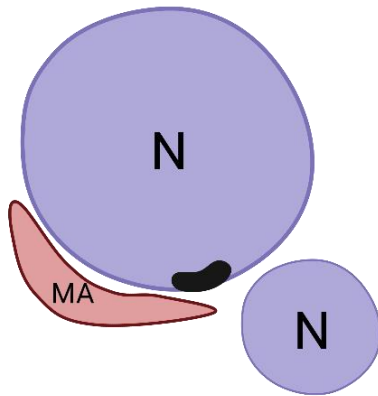
This approach has allowed a more precise assessment of the size and spatial organisation of subcellular structures. For example, the presynaptic dense projection, which is analogous to the AZ scaffold, had previously been found to be increased in size following the loss of the scaffold protein SYD-2 when fixed at room temperature (Zhen and Jin, 1999), however; with high-pressure freezing the structure was instead found to be reduced in size (Kittelmann et al, 2013). Distances measured between structures are also likely to be truer to the living biological systems.

In *C. elegans*, neuromuscular junctions (NMJs) arise along the dorsal and ventral nerve cords where they innervate body wall muscle (Chapter 1 – Figure 1.7). These

connections underlie *C. elegans* locomotion as discussed and investigated in Chapter 3. Imaging of serial sections through the cords shows synapses appear in extended swellings of the motor neuron axonal plasma membrane also known as synaptic boutons. Within these boutons, sites of presynaptic neurotransmitter release (synaptic sites) are defined by the presence of a central dense projection. SVs, 30-50nm diameter spherical compartments carrying neurotransmitters, are typically found clustered around the dense projection.

Both excitatory cholinergic motor neurons and inhibitory GABAergic motor neurons form NMJs with the body wall muscles. These two forms of NMJ can be visually distinguished by their postsynaptic targets (Figure 4.1). GABAergic NMJs have only muscles as a postsynaptic partner whereas cholinergic NMJs innervate both muscle and other neurons. The postsynaptic neurons are typically GABAergic motor neurons which are stimulated to provide inhibitory input to the body wall muscle on the opposite side of the body (Figure 1.7).

Cholinergic NMJ



GABAergic NMJ

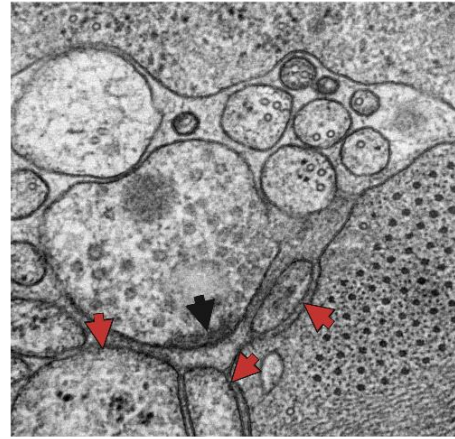
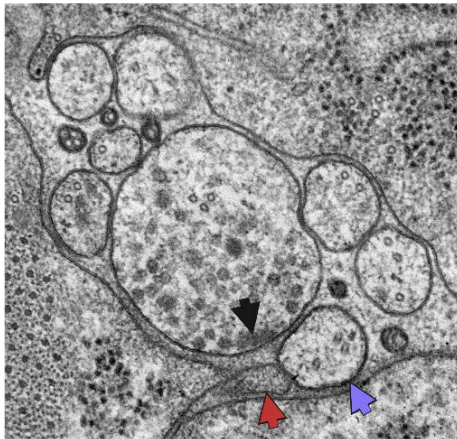
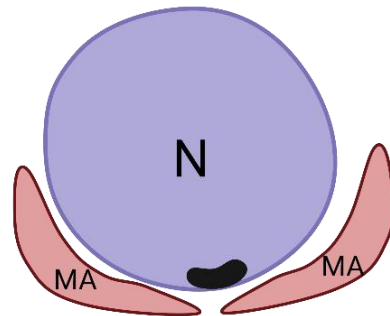


Figure 4.1. Schematic illustration of how cholinergic and GABAergic neuromuscular junctions (NMJs) appear under electron microscopy accompanied by electron micrographs. Cholinergic NMJs are defined by dense projections facing towards both neurons (N) and muscle arms (MA) as postsynaptic targets, whereas GABAergic NMJ dense projections only face towards muscle arms which serve as their postsynaptic targets. In the accompanying electron micrographs arrow heads indicate the dense projection (black), postsynaptic muscle arms (red) and postsynaptic neurons (purple). Created with Biorender.com

While neurotransmission in cholinergic and GABAergic synapses is broadly governed by the same presynaptic proteins the mechanisms through which they are regulated appear to differ. Mutations in AZ proteins such as RIMB-1 (Jánosi et al, 2021) and UNC-13 (Li et al, 2019) have previously been shown to have differential effects on neurotransmitter release at cholinergic and GABAergic NMJs. It has also been suggested that *C. elegans* GABAergic motor neurons may possess a calcium independent form of tonic release not present in the cholinergic subtype (Liu et al, 2018). Therefore, GABAergic and cholinergic motor neurons require independent analysis.

The advances made in EM sample preparation have greatly furthered our understanding of the neuromuscular junction presynapse and its most important features. TEM combined with tomographic imaging have allowed detailed analysis of dense projection structure revealing the presence of tethers which contact SVs to maintain their proximity to the structure (Stigloher et al, 2011; Kittelmann et al, 2013). They have also allowed us to gauge the importance of AZ proteins to the docking of SVs (Weimer et al, 2003; Weimer et al, 2006; Hammarlund et al, 2007; Hobson et al, 2011; Jánosi et al, 2021), and the location of putative release sites (Weimer et al, 2006).

Previous work has established SYD-2 as a major organiser of the *C. elegans* dense projection. Loss of SYD-2 reduces the frequency, size, and complexity of dense projections (Kittelmann et al, 2013). There are at least two mechanisms through which SYD-2 contributes to the formation of dense projections. The first is through SYD-2's role in the recruitment of other AZ proteins including UNC-10, ELKS-1, RIMB-1, and CLA-1 (Zhen and Jin, 1999; Kittelmann et al, 2013; Xuan et al, 2017; Oh et al, 2021).

These proteins reach the presynapse as cargo of the Kinesin-3 motor proteins UNC-104 (Oliver et al, 2022), to which SYD-2 binds to promote anterograde movement towards presynaptic sites (Wagner et al, 2009). While much remains unknown regarding how AZ scaffold proteins are attached to UNC-104 as cargo, a long-standing hypothesis is that they are first packaged into transport vesicles at the Golgi apparatus (Shapira et al, 2003). SYD-2 also contributes to the capture of both SVs and DCVs at presynaptic sites through its participation in the CSS (Core synapse stability) complex alongside SYD-1 and SAD-1 (Edwards et al, 2015; Morrison et al, 2018). SYD-2 could therefore also contribute to the capture of these transport vesicles. The second mechanism through which SYD-2 may affect AZ scaffold formation is by moulding its morphology and integrity, by managing the integration of other proteins into the scaffold. This would be a more direct role utilising SYD-2's localisation within the dense projection (Yeh et al, 2005) and ability to interact with other scaffold proteins such as UNC-10 (Schoch et al, 2002) and ELKS-1 (Dai et al, 2006). The removal of intrinsically disordered regions (IDRs) from SYD-2, which contribute to interactions with other AZ scaffold proteins to form phase condensates, has been shown to alter synaptic ultrastructure previously (McDonald et al, 2020). A *syd-2* gain of function mutant has also been shown to enhance dense projection size (Kittelmann et al, 2013). A recent study using the mammalian SYD-2 homologue Liprin- α suggested this mutation enhances the ability of SYD-2 to oligomerise, altering how ELKS-2 (the ELKS-1 homologue) and RIM (the UNC-10 homologue) integrate into the AZ complexes (Liang et al, 2021). The idea that SYD-2 shapes AZ scaffold morphology would provide an explanation for the reduced complexity of AZ scaffolds previously described in *syd-2* mutants which lack putative SV docking bay structures (Kittelmann et al, 2013). Despite these impairments *syd-2* mutants are still capable of forming

dense projections. This suggests that there are other proteins involved in promoting dense projection formation potentially through redundancy between proteins or compensatory mechanisms.

Loss of other, well characterised AZ scaffold proteins such as UNC-10 and ELKS-1 do not have an observable effect on dense projection size (Koushika et al, 2001; Kittelmann et al, 2013). This suggests that we may need to look beyond the classical *C. elegans* presynaptic proteins to discover other dense projection organisers. The recently discovered protein CLA-1 was previously shown to contribute to the formation of fully sized dense projections (Xuan et al, 2017). HLB-1 may also be capable of compensating for SYD-2 loss due to their similar C-terminal Liprin homology domains.

I examined whether the addition of deleterious mutations for *cla-1* or *h1b-1* would enhance the disruption to dense projection formation and the broader presynaptic ultrastructure present in *syd-2* null mutants. To correlate my findings to the fluorescence and behavioural examinations I restricted my analysis to cholinergic synapses. I measured the frequency of synapses along the dorsal nerve cord, size of dense projections at cholinergic neuromuscular junctions and the distribution of the SVs within the presynaptic bouton to understand how CLA-1, HLB-1 and SYD-2 loss affects AZ ultrastructure and function.

4.1 Results

4.1.1 Dense projection formation and synaptic structure is disrupted in *syd-2(ok217)*-containing mutants

The synaptic structure of cholinergic motor neurons was first examined through the reconstruction of 5µm of the dorsal nerve cord from 50nm serial sections of the wild-type, *syd-2* single mutant and *cla-1; hlb-1 syd-2* triple mutant strains (Figure 4.2, 4.3 & 4.4). The *cla-1; hlb-1 syd-2* triple mutant was specifically reconstructed to examine the ultrastructure when CLA-1, HLB-1 and SYD-2 were removed together. Additionally, as the *cla-1; hlb-1 syd-2* triple mutant displayed the greatest resistance to aldicarb it was interesting to examine if reduced cholinergic transmission could be related to a change in synapse distribution. Reconstructions were made of three cholinergic motor neurons which displayed clear synapses indicated by the presence of a dense projection (Figure 4.2, 4.3 and 4.4).

N2 (wildtype)

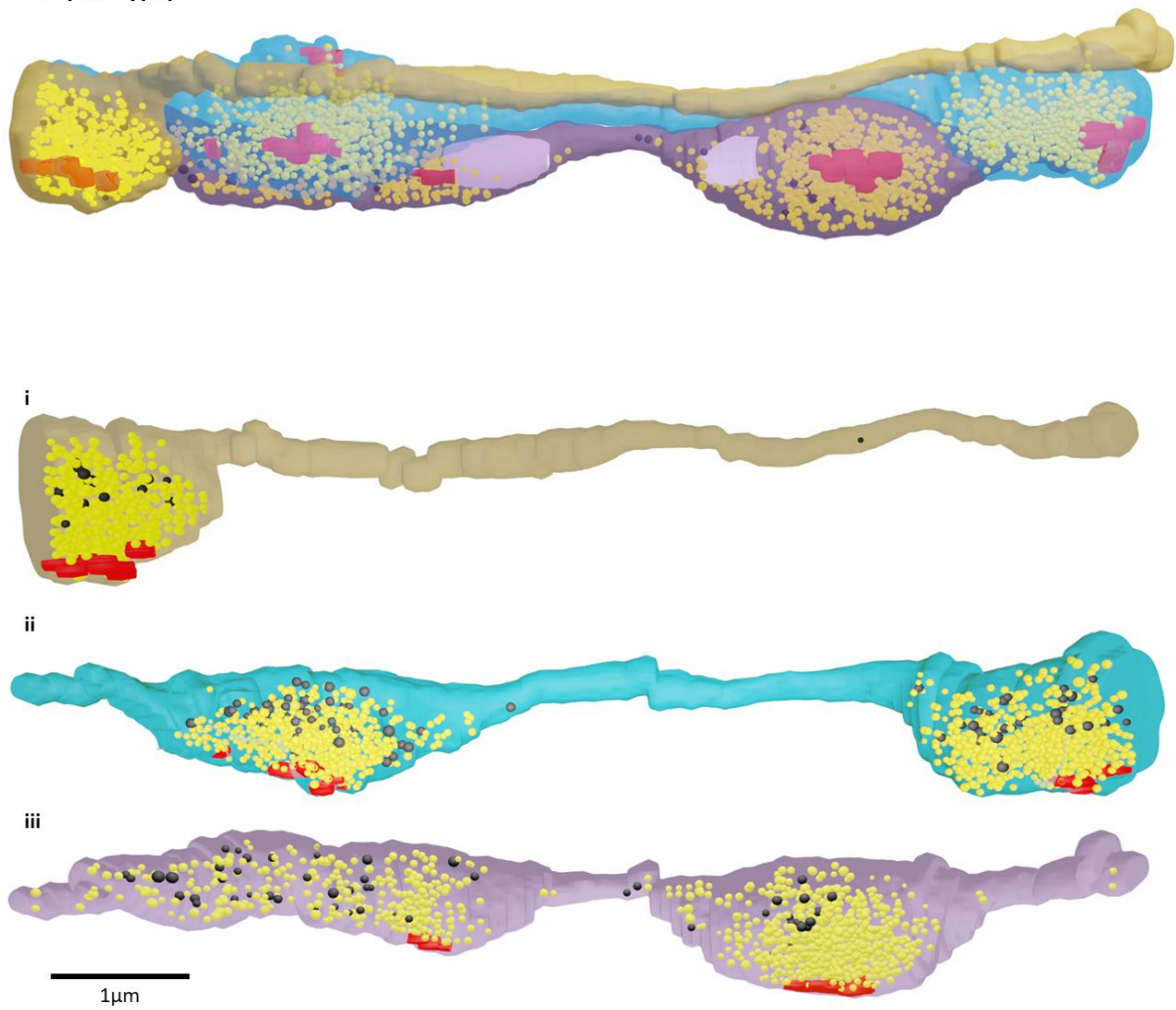


Figure 4.2. 5μm reconstruction of cholinergic motor neuron axons from 50nm serial sections of a wild-type dorsal nerve cord. Full reconstruction of cholinergic motor neuron axons as they appear in the cord (top). i, ii, iii. Individual motor neuron axons. Red - dense projections, yellow - SVs, Black – dense core vesicles. Mitochondria (only in the reconstruction showing all cords) are shown in white.

syd-2(ok217)

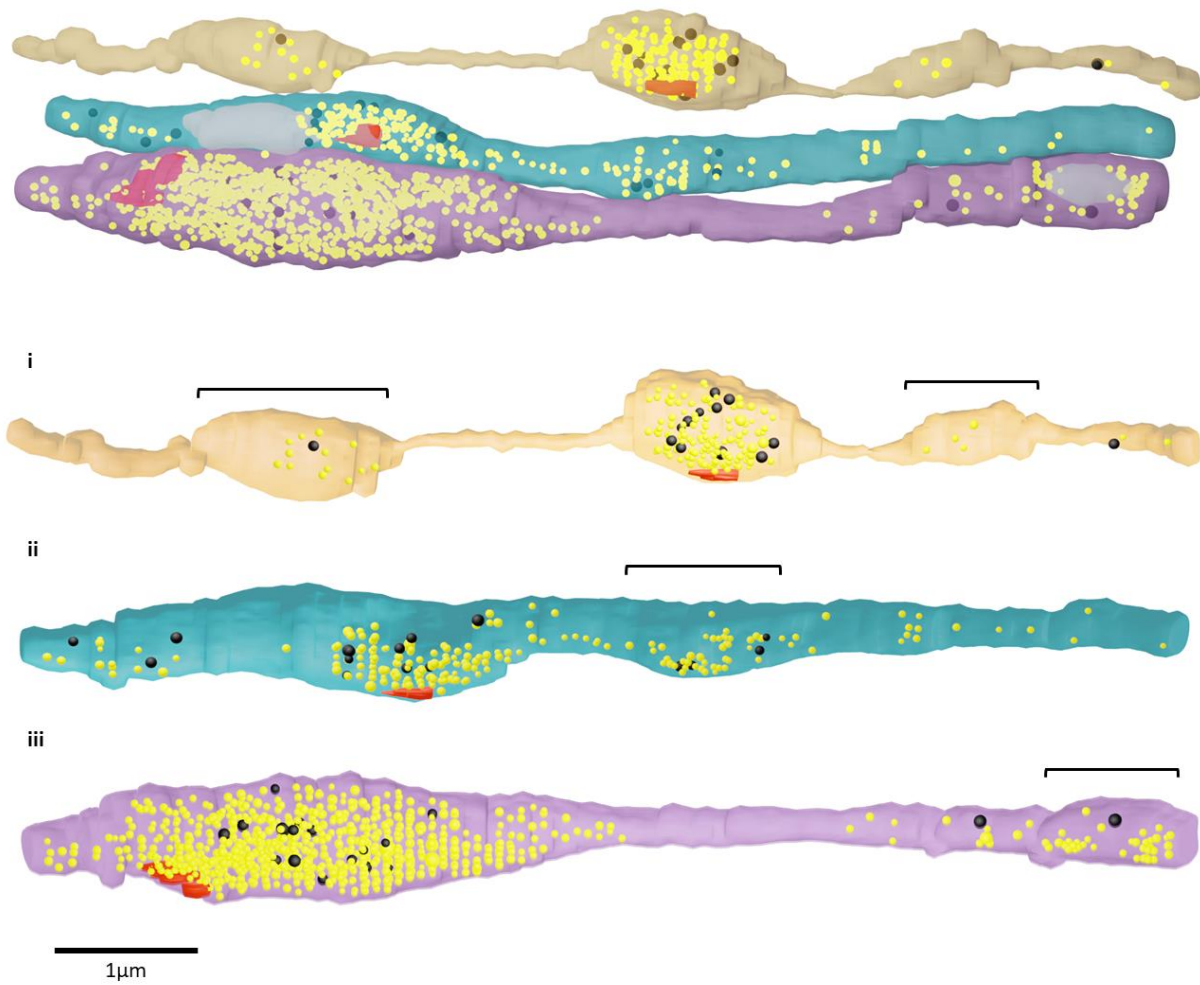


Figure 4.3. 5µm reconstruction of cholinergic motor neuron axons from 50nm serial sections of a *syd-2(ok217)* single mutant dorsal nerve cord. Full reconstruction of cholinergic motor neuron axons as they appear in the cord (top). **i, ii, iii.** Individual motor neuron axons with bouton-like asynaptic structures marked by bracketed lines. Red - dense projections, yellow - SVs, Black – dense core vesicles. Mitochondria (only in the reconstruction showing all cords) are shown in white.

cla-1(ok2285); hlb-1(ok725) syd-2(ok217)

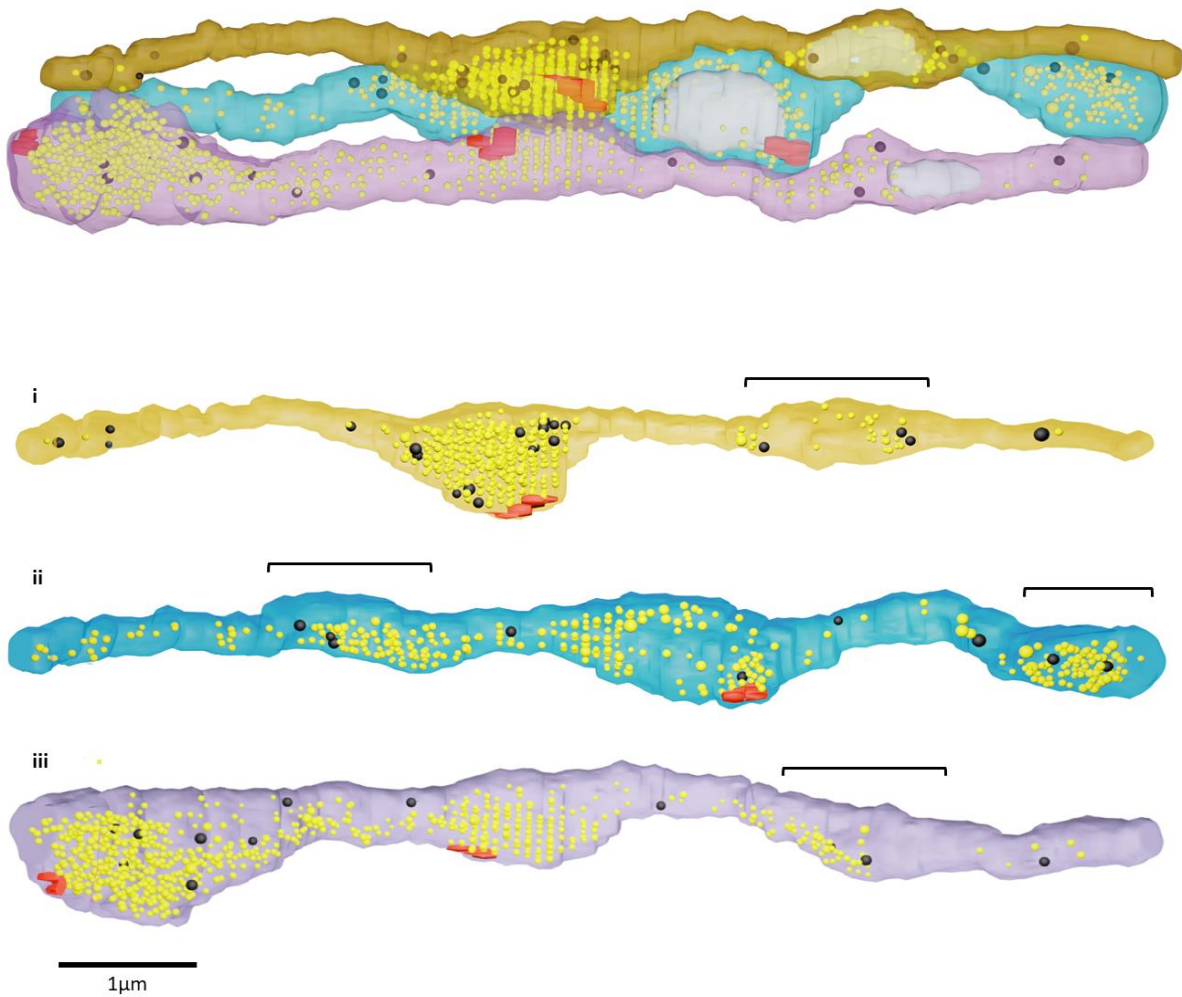


Figure 4.4. 5 μm reconstruction of cholinergic motor neuron axons from 50nm serial sections of a *cla-1(ok2285); hlb-1(ok725) syd-2(ok217)* triple mutant dorsal nerve cord. Full reconstruction of cholinergic motor neuron axons as they appear in the cord (top). i, ii, iii. Individual motor neuron axons with bouton-like asynaptic structures lacking mitochondria marked by bracketed lines. Red - dense projections, yellow - SVs, Black – dense core vesicles. Mitochondria (only in the reconstruction showing all cords) are shown in white.

A similar number of axons displayed synapses in wild-type (3), *syd-2* single (3) and *cla-1; hlb-1 syd-2* (4) triple mutants along the 5µm of nerve cord examined. The frequency of synaptic sites, indicated by the presence of dense projections, was reduced in the *syd-2* single mutant compared to the other strains (6 in the wild-type and 5 in the *cla-1; hlb-1 syd-2* triple mutant versus 3 in the *syd-2* single mutant). SYD-2 loss has previously been found to cause reduced synapse formation (Kittelmann et al, 2013), consistent with its role in recruiting AZ scaffold components (Oh et al, 2021). This differs from the wild-type-like distribution of UNC-10 puncta observed in *syd-2* single mutants with confocal analysis, however (Chapter 2 – Figure 2.3). This could result from UNC-10 being deposited at additional sites which lack the ability to form dense projections due to an absence of other essential components.

The increased synaptic frequency in the *cla-1; hlb-1 syd-2* triple mutant compared with the *syd-2* single mutant meanwhile is consistent with the findings of the confocal analysis for UNC-10 (Chapter 2 – Figure 2.3). As only a relatively short length of the nerve cord in single worms was used for this analysis, however; conclusions on synapse frequency should be treated with caution.

Intriguingly in both the *syd-2* single and the *cla-1; hlb-1 syd-2* triple mutant there was an increase in the number of SVs localised outside of synaptic sites compared to the wild-type where SVs were almost exclusively sequestered at synaptic boutons. This is indicative of inefficient SV recruitment and localisation and is consistent with the role of SYD-2 in SV transport and their retention at synaptic sites (Wagner et al, 2009). This validates earlier confocal results indicating diffuse SV localisation in the nerve cord of these mutants (Chapter 2 - Figure 2.3).

Many of the SVs found at asynaptic sites were found in bouton-like structures lacking a dense projection (Figure 4.3 and 4.4). These structures were only found in the *syd-2* single and *cla-1; hlb-1 syd-2* triple mutant. These structures could be “protosynapses” which fail to form dense projections or otherwise the result of misdirected cytoskeletal modification.

4.1.2 Dense projection size is similarly reduced in *syd-2* and *cla-1* mutants but is not additive in double mutants

To understand how the loss of CLA-1 and HLB-1 alongside SYD-2 influenced defects at the single synapse, ultrastructure had to be explored in greater detail in double and triple mutants. As a reduction in the number of dense projections was seen in the dorsal nerve cord reconstructions of *syd-2* single mutants, I first examined whether the size of the dense projections was also altered.

Cumulative dense projection area was calculated by summing the area of the visible dense projection in each of the sections that it appeared in (Figure 4.5A). Cumulative dense projection area was significantly reduced in the *syd-2* single mutant compared to the wild-type (Figure 4.5B). This is consistent with previous work demonstrating a reduction in dense projection size in *syd-2* mutant strains (Kittelmann et al, 2013) and, similarly to the reduced synaptic frequency observed in nerve cord reconstructions, could be the result of less efficient recruitment of other AZ scaffold proteins such as UNC-10/RIM and ELKS-1 (Deken et al, 2005; Oh et al, 2021). Additionally, I found that *cla-1* mutants also displayed reduced cumulative dense projection area compared to

wild-type worms consistent with previous findings of reduced dense projection size in *cla-1* mutants (Xuan et al, 2017; Krout et al, 2023).

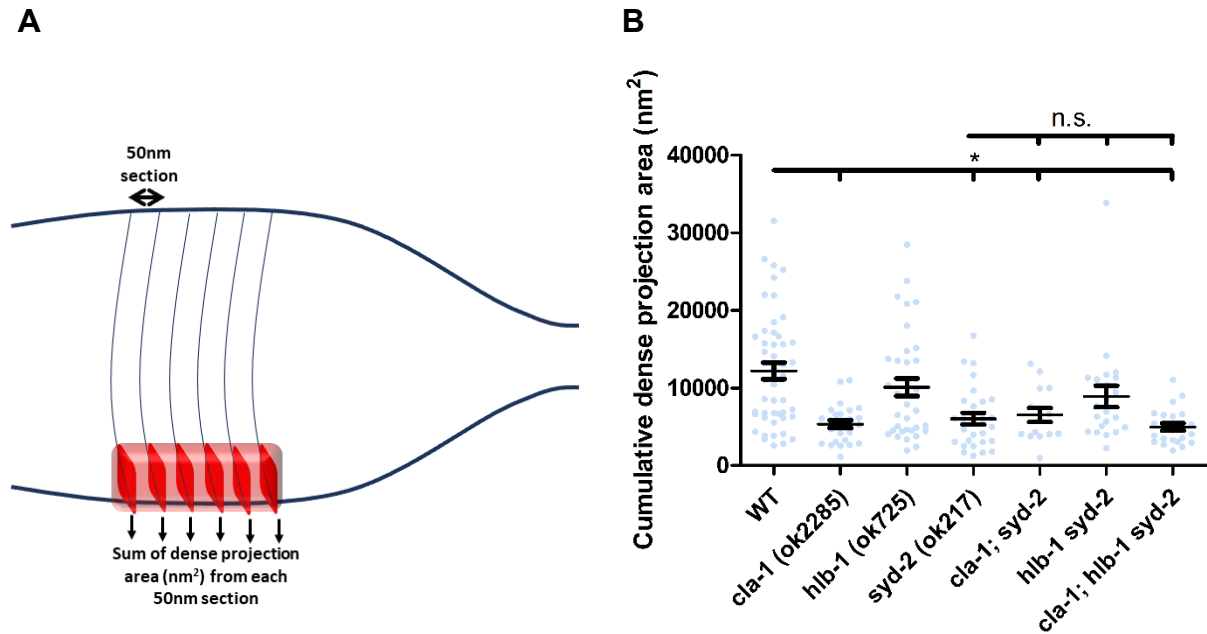


Figure 4.5. Dense projection size is reduced in mutants with the *syd-2(ok217)* allele. **A.** The method to determine cumulative dense projection area by summing the area of the dense projection as it appeared in each section. **B.** Cumulative dense projection area for each synapse. Bars in the data show mean \pm SEM. Pairwise comparisons for significance testing used Dunn's test for multiple comparisons following Kruskal-Wallis test for variance. Pairwise comparisons were made between wild-type and all other conditions, between single mutants and double mutants which shared mutations, and between the triple mutant and all single and double mutants. Pairwise comparisons are shown by lines with ticks indicating mutants being compared to the condition at the unticked left-hand end. * $p < 0.05$ corrected for multiple comparisons. n.s. - not significant. Number of animals used are as follows: *WT*=4, *cla-1*=3, *hlb-1*=2, *syd-2*=3, *cla-1; syd-2*=1, *hlb-1 syd-2*=2; *cla-1; hlb-1 syd-2*=4. Post-hoc power calculations can be found in Appendix 1.

No significant difference was found between the *syd-2* single mutant and double and triple mutants carrying the *syd-2* mutant allele suggesting that the *hlb-1* and *cla-1*

mutant alleles did not enhance the dense projection structural defects of the *syd-2* mutant background. As the *cla-1* and *syd-2* single mutants and the *cla-1; syd-2* double mutant all had similarly reduced cumulative dense projection area it appears that CLA-1 and SYD-2 are likely to act within the same pathway to promote dense projection size. CLA-1 and SYD-2 have previously been shown to reciprocally recruit each other to synaptic sites, with SYD-2 being shown as the dominant partner (Xuan et al, 2017).

4.1.3 The loss of SYD-2, CLA-1 and HLB-1 has differing effects on synaptic vesicle localisation at the presynaptic active zone

Several components of the dense projection are major facilitators of neurotransmitter release from the synapse. They primarily achieve this by directing SV localisation and interacting with other important AZ proteins. SYD-2 supports SV transport to synaptic sites and helps to retain them there (Wagner et al, 2009; Edwards et al, 2015), while others such as UNC-13 promote their ability to dock at, and fuse with, the plasma membrane (Richmond et al, 1999; Weimer et al, 2006). UNC-10 contributes to both processes (Koushika et al, 2001; Liu et al, 2019). The loss of CLA-1 and HLB-1 alongside SYD-2 could enhance defects in SV recruitment and release. CLA-1 has previously been shown to contribute to SV retention at the synapse in EM analysis. HLB-1 meanwhile appeared to have a role in synaptic localisation of SVs in the confocal analysis of the previous chapter (Chapter 2 - Figure 2.3). Therefore, I turned my attention to SV recruitment and localisation in each of the strains.

To compare the number of SVs localised to synaptic sites in each strain I examined all 50nm sections of a synapse containing a dense projection and one either side. The total number of SVs counted across the synapse was then divided by the total number of sections to give an average SV count independent of synapse length.

The total number of SVs per section in *syd-2* single, *cla-1*; *syd-2* double and *cla-1*; *h1b-1 syd-2* triple mutants was significantly reduced compared to the wild-type strain (Figure 4.6). This suggests defective SV recruitment or at least a failure of SV retention, which has previously been reported upon the loss of SYD-2 (Kittelmann et al, 2013). This also complements my earlier observations from the nerve cord reconstructions where *syd-2* mutant strains displayed increased numbers of SVs outside of synaptic sites (Figure 4.3). *cla-1* mutants have also previously been shown to have moderately reduced numbers of SVs at cholinergic motor neuron synapses in EM analysis (Xuan et al, 2017; Krout et al, 2023). I found that *cla-1* mutants trended towards having fewer SVs at synapses in my results however this effect was not additive with the *syd-2* mutation. This may again be indicative of CLA-1 acting downstream of SYD-2.

Interestingly the *h1b-1 syd-2* double mutant showed a trend of increased SV localisation compared to *syd-2* single mutants. This appears to conflict with both my previous confocal results (Chapter 2, Figure 2.3) and confocal analysis from a previous study where reduced SV recruitment was found (Wang and Wang, 2009). As the *h1b-1* single mutant also displayed a mild non-significant increase in SV recruitment compared to the wild-type it is possible that the loss of HLB-1 counteracts the *syd-2* mutant defects.

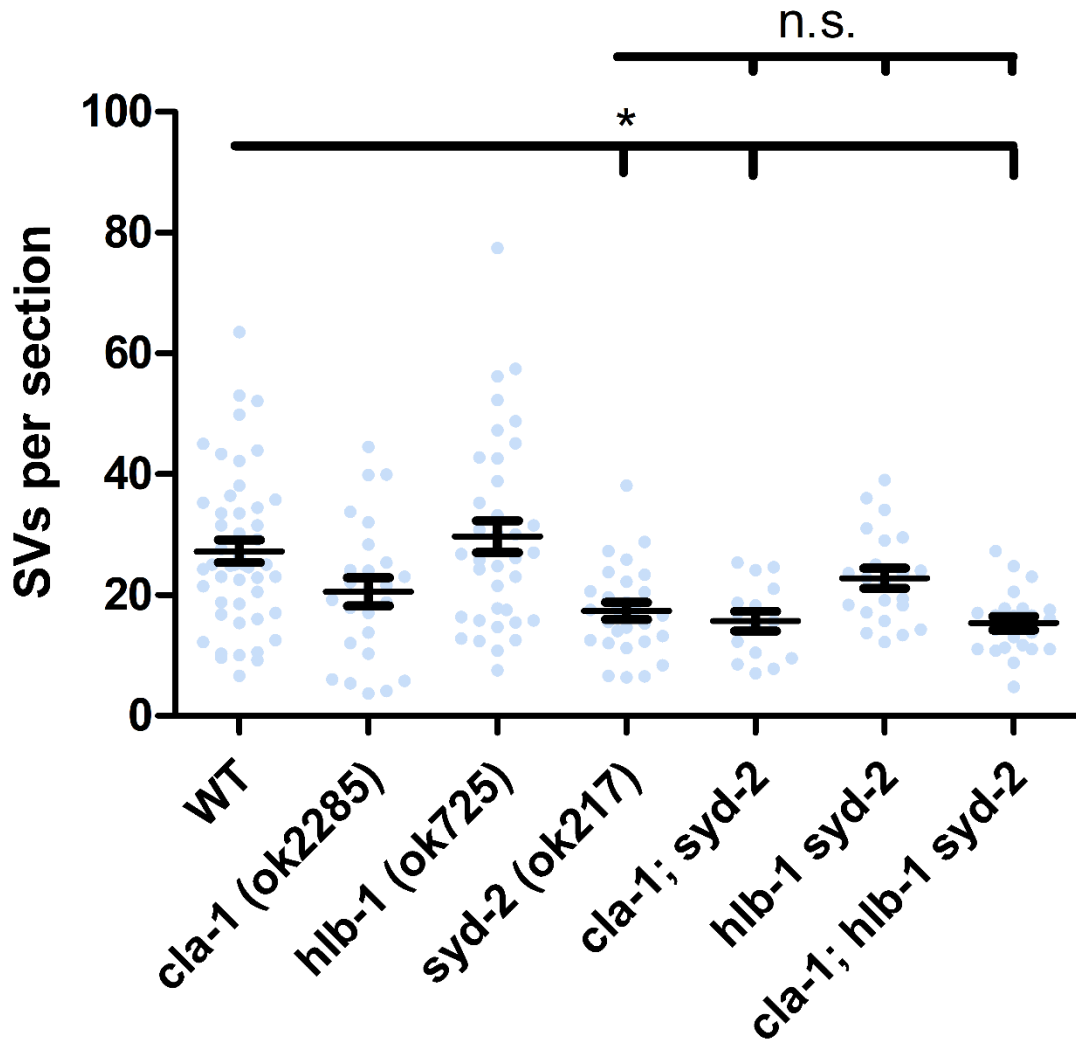


Figure 4.6. Fewer SVs are present *syd-2* mutant synapses. Mean total SVs per section for each synapse. Bars in the data show mean \pm SEM. Pairwise comparisons for significance testing used Dunn's test for multiple comparisons following Kruskal-Wallis test for variance. Pairwise comparisons were made between wild-type and all other conditions, between single mutants and double mutants which shared mutations, and between the triple mutant and all single and double mutants. Pairwise comparisons are shown by lines with ticks indicating mutants being compared to the condition at the unticked left-hand end. * $p < 0.05$ corrected for multiple comparisons. n.s. - not significant. Animals used are as follows: *WT*=4, *cla-1*=3, *hlb-1*=2, *syd-2*=3, *cla-1; syd-2*=1, *hlb-1 syd-2*=2; *cla-1; hlb-1 syd-2*=4. Post-hoc power calculations can be found in Appendix 1.

The number of vesicles localised to synaptic sites could additionally be restricted by reduced synaptic bouton size. Therefore, I examined the size of the synaptic terminals in the synaptic cross sections in which SVs were counted. The maximum synaptic terminal area of each synapse was reduced in all mutants but only reached significance in *cla-1* single, *cla-1; syd-2* double and *cla-1; hlb-1 syd-2* triple mutants compared to wild-type (Figure 4.7). *syd-2* single mutants which had a similar number of SVs at terminals compared to *cla-1; syd-2* double and *cla-1; hlb-1 syd-2* triple mutants typically had larger terminals than these mutants, however. This suggests that there is not a simple relationship between synaptic terminal size and synaptic SV recruitment. My results do suggest that CLA-1 may be involved in maintaining synaptic bouton size, however.

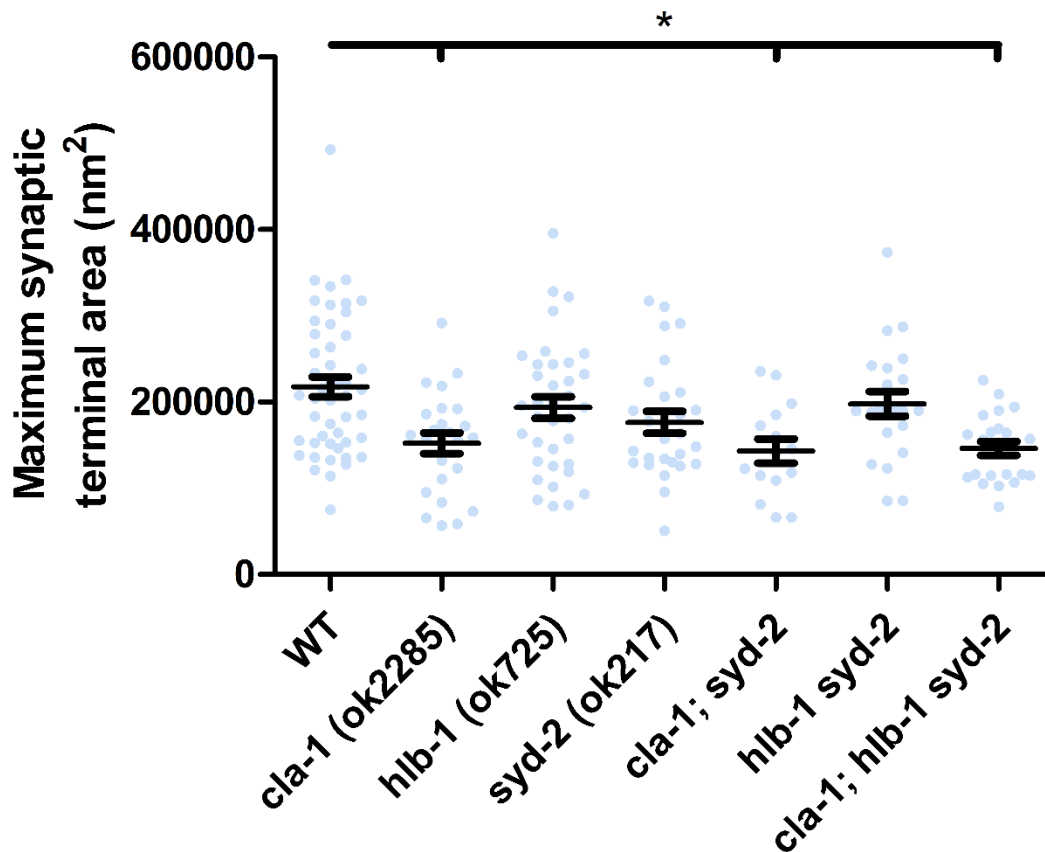


Figure 4.7. Presynaptic terminal size is reduced across *cla-1(ok2285)* mutants. Mean of the largest synaptic terminal area found within a section for each synapse. Bars in the data show mean \pm SEM. Pairwise comparisons for significance testing used Dunn's test for multiple comparisons following Kruskal-Wallis test for variance. Pairwise comparisons were made between wild-type and all other conditions, between single mutants and double mutants which shared mutations, and between the triple mutant and all single and double mutants. Pairwise comparisons are shown by lines with ticks indicating mutants being compared to the condition at the unticked left-hand end. * $p < 0.05$ corrected for multiple comparisons. n.s. - not significant. Animals used are as follows: *WT*=4, *cla-1*=3, *hlb-1*=2, *syd-2*=3, *cla-1; syd-2*=1, *hlb-1 syd-2*=2; *cla-1; hlb-1 syd-2*=4. Post-hoc power calculations can be found in Appendix 1.

Although recruitment of SVs to the presynapse is important, their ability to support neurotransmission is dependent upon their subsynaptic position. Docked vesicles in contact with the plasma membrane are the main contributors of the readily releasable pool (Kaeser and Regehr, 2017). These vesicles await a stimulus which triggers their fusion with the plasma membrane so that they can release their neurotransmitter load. Undocked SVs which are located away from the plasma membrane meanwhile are retained to support extended patterns of release and form the reserve pool. These vesicles typically take the place of docked vesicles following fusion, a process which is thought to be mediated by the AZ scaffold proteins UNC-10 (Stigloher et al, 2011) and CLA-1 (Xuan et al, 2017). I used the SynapsEM programme (Watanabe et al, 2020) to count undocked and docked SVs for each mutant (Figure 4.8).

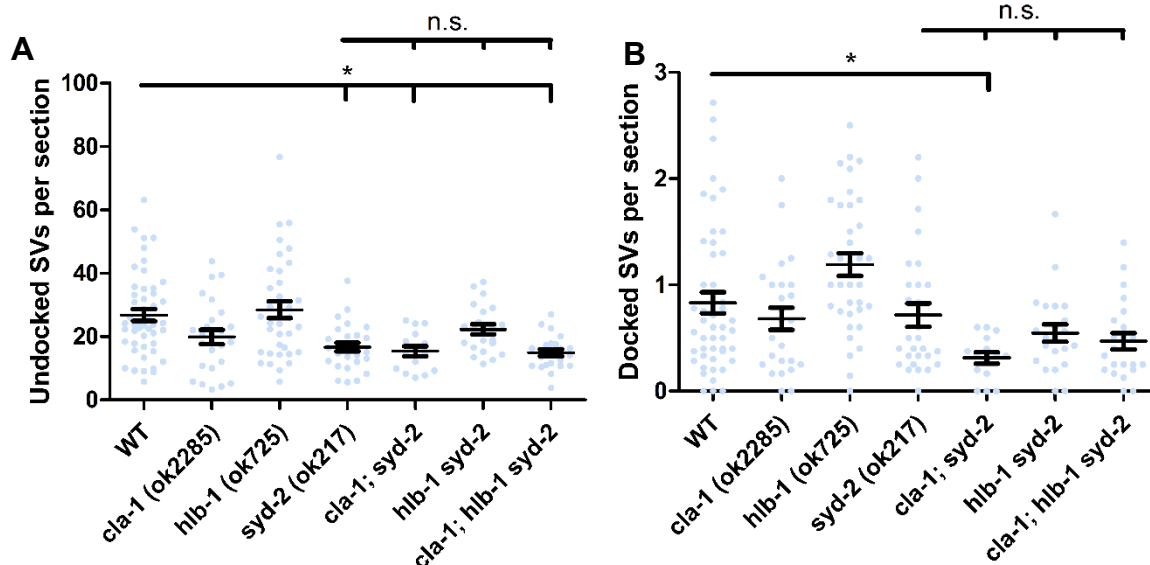


Figure 4.8. Docked and undocked vesicle localisation is differentially affected in *syd-2* single, double and triple mutants. **A.** Mean undocked SVs per section in each synapse. **B.** Mean docked SVs per section in each synapse. Bars in the data show mean±SEM. Pairwise comparisons for significance testing used Dunn's test for multiple comparisons following Kruskal-Wallis test for variance. Pairwise comparisons were made between wild-type and all other conditions, between single mutants and double mutants which shared mutations, and between the triple mutant and all single and double mutants. Pairwise comparisons are shown by lines with ticks indicating mutants being compared to the condition at the unticked left-hand end. * $p < 0.05$ corrected for multiple comparisons. n.s. - not significant. Animals used are as follows: *WT*=4, *cla-1*=3, *hlb-1*=2, *syd-2*=3, *cla-1; syd-2*=1, *hlb-1; syd-2*=2, *cla-1; hlb-1; syd-2*=4. Post-hoc power calculations can be found in Appendix 1.

Like the analysis of all SVs (Figure 4.6), *syd-2* single mutants, *cla-1; syd-2* double and *cla-1; hlb-1; syd-2* triple mutants displayed significantly reduced numbers of undocked vesicles compared to the wild-type.

It is also important to consider the distribution of the undocked vesicles around the dense projection. As these vesicles contribute to the reserve pool which replaces

docked vesicles during periods of extended neurotransmitter release, a subset of vesicles should remain in reasonable proximity to release sites which are localised around the dense projection. To test if the loss of CLA-1, HLB-1 or SYD-2 affected the distribution of undocked vesicles around the dense projection I used the SynapseEM programme (Watanabe et al, 2020) to calculate the minimum distance between each undocked SV and the dense projection at each synapse and subsequently separate them into 99nm bins (Figure 4.9A). This was performed for each synapse in all sections where a dense projection was present and one additional section either side with SV-to-dense projection distance calculated in three-dimensions across sections.

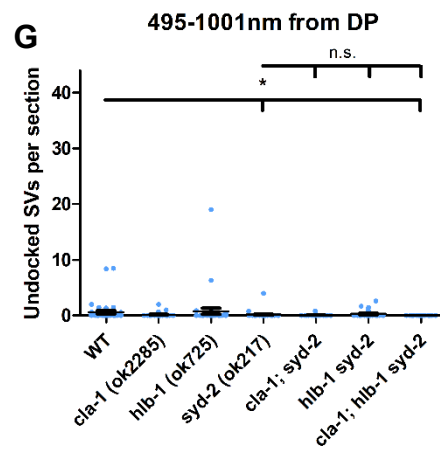
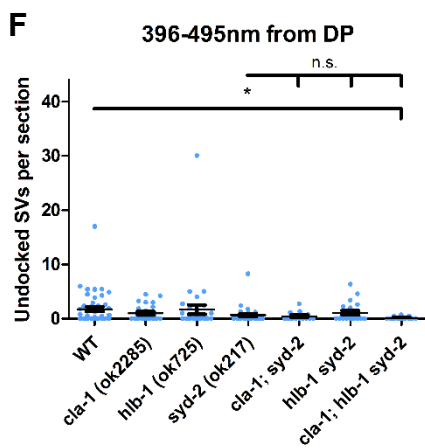
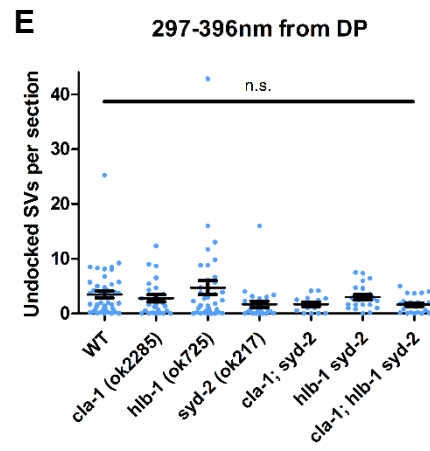
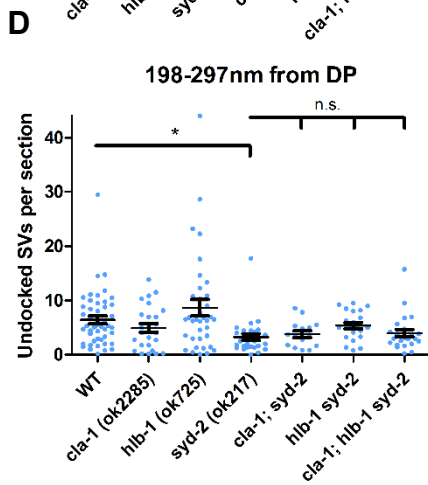
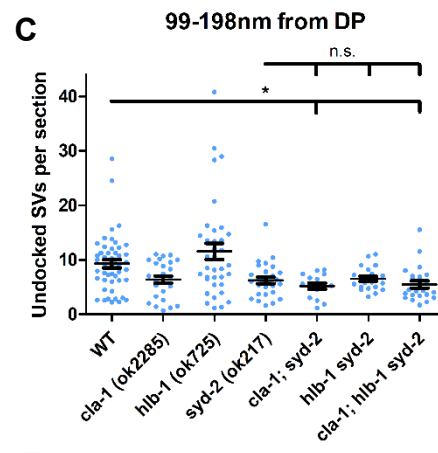
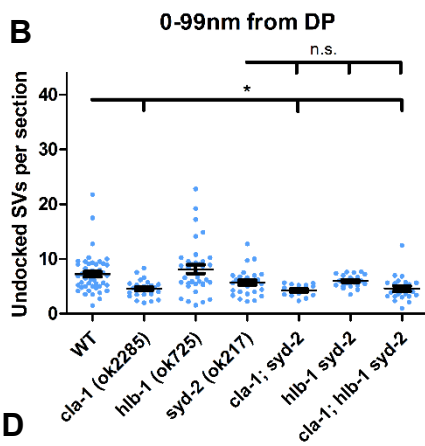
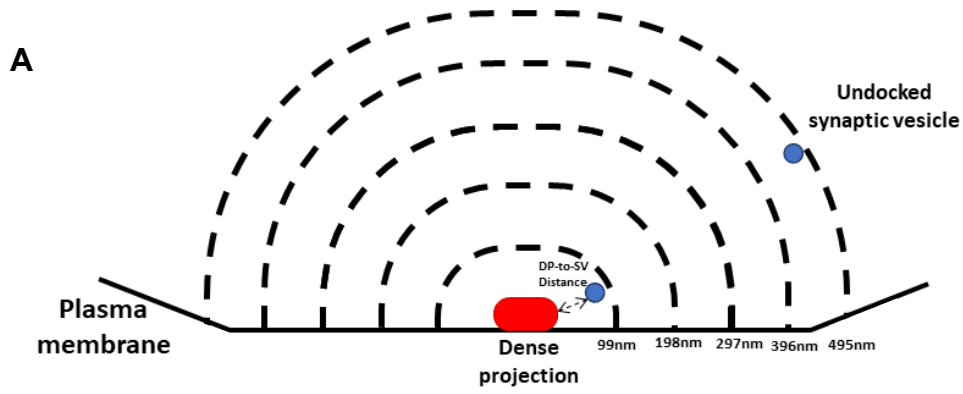


Figure 4.9. Undocked SVs are reduced in strains carrying a *syd-2* mutation regardless of their distance from the dense projection. A. Schematic of SV distribution analysis showing how the 99nm bins were arranged with respect to dense projection. Example undocked SVs are shown in blue. Total undocked vesicles section averaged by the number of sections (all sections with the dense projection plus an additional section either side) for each synapse. Undocked SV distributions are shown for each 99nm bin from the dense projection: 0-99nm (including vesicles contacting the dense projection (DP) (**B**), 99-198nm (**C**), 198-297nm (**D**), 297-396nm (**E**), 396-495nm (**F**) and all SVs from 495nm to the maximum measurement distance of 1001nm (**G**). Bars in the data show mean±SEM. Pairwise comparisons for significance testing used Dunn's test for multiple comparisons following Kruskal-Wallis test for variance. Pairwise comparisons were made between wild-type and all other conditions, between single mutants and double mutants which shared mutations, and between the triple mutant and all single and double mutants. Pairwise comparisons are shown by lines with ticks indicating mutants being compared to the condition at the unticked left-hand end. * $p < 0.05$ corrected for multiple comparisons. n.s. - not significant. The bar in **E** shows there was no significance found for any of the pairwise comparisons performed. Animals used are as follows: *WT*=4, *cla-1*=3, *h1b-1*=2, *syd-2*=3, *cla-1; syd-2*=1, *h1b-1 syd-2*=2; *cla-1; h1b-1 syd-2*=4. Post-hoc power calculations can be found in Appendix 1.

Across all bins *syd-2* mutants had fewer undocked SVs at synaptic sites compared to the wild-type, although this only reached significance at 199-297nm from the DP (Figure 4.9 B-G). The inability to populate the regions closest to the dense projection to wild-type levels could affect the replenishment of the readily-releasable pool following SV fusion, as there may be insufficient SVs to replace those which have fused with the plasma membrane. Electrophysiological studies have previously demonstrated long-term depression during extended stimulus trains for *syd-2* single mutants (Kittelmann et al, 2013). Notably, *cla-1* single mutants also had significantly fewer undocked vesicles proximal (0-99nm) to the dense projection (Figure 4.9B) and,

like *syd-2* mutants, have been shown to exhibit enhanced depression under repetitive stimulation (Xuan et al, 2017). *cla-1; syd-2* double mutants and *cla-1; hlb-1 syd-2* triple mutants also had reduced SVs across the bins especially within 198nm of the dense projection compared to the wild-type (Figure 4.9 B-C). This suggests that these mutants harbour the properties of both the *cla-1* and *syd-2* single mutants.

While not significant, *hlb-1* mutants consistently had more vesicles than wild-types across bins suggesting not just an increase in overall vesicles but a higher density of SVs around the DP.

The critical step in facilitating neurotransmitter release is the docking of SVs to the AZ plasma membrane. Docked SVs interact with SNARE complex proteins entering a primed state (Goda, 1997; Sauvola and Littleton, 2021) after which they are capable of fusion and neurotransmitter release once an appropriate stimulus reaches the synapse. The number of docked vesicles was only significantly changed in *cla-1; syd-2* mutants where they were greatly reduced (Figure 4.8). This supports the notion that loss of CLA-1 enhances SV localisation defects in the *syd-2* mutant background.

In contrast, *hlb-1* single mutants trended towards increased recruitment of docked vesicles compared to the wild-type, although this did not reach significance (Figure 4.8). This suggests that HLB-1 may have a role in negatively regulating SV docking at the synapse. This effect did not occur in *hlb-1 syd-2* mutants, when compared *syd-2* single mutants, however. Therefore, the proposed regulatory role of HLB-1 may be dependent on the presence of SYD-2.

Although SV docking is vital to neurotransmitter release, the efficiency of release is modulated by their proximity to calcium channels (Grauel et al, 2016; Gratz et al, 2019;

Dolphin, 2021). Many of the calcium channels within the AZ are located around the dense projection where they are recruited by scaffold proteins such as RIMB-1 (Kushibiki et al, 2019; Krout et al, 2023). Dense projection components such as UNC-10 and UNC-13 are also mediators of SNARE complex activity which is pivotal to SV fusion (Richmond, 2001; Liu et al, 2019). Therefore, it is important to maintain docked SVs proximal to the dense projection. I therefore measured the minimum distance between each docked vesicle and the dense projection and accordingly separated them into bins of 33nm to give a mean per synapse (Figure 4.10A).

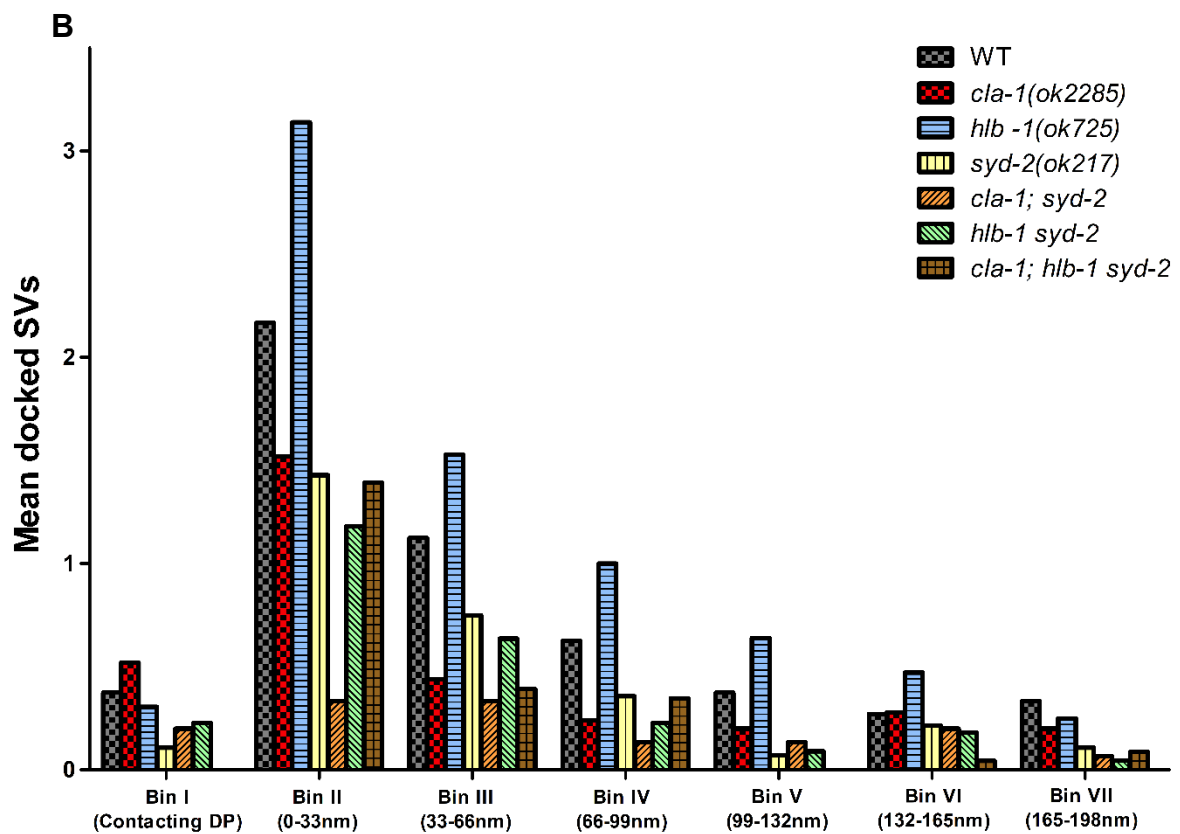
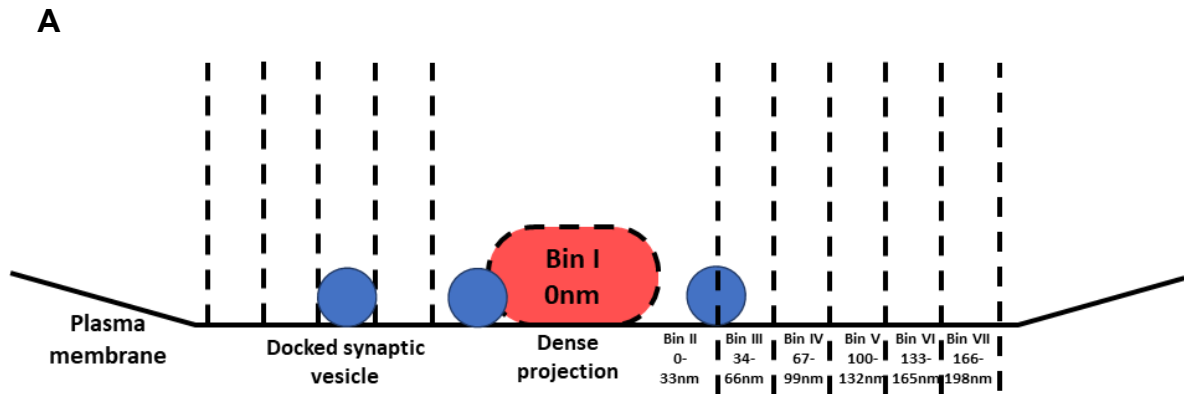


Figure 4.10. Analysis of docked SV distribution around the dense projection reveals that *syd-2* single mutants only display consistent mild reductions in docked SVs whereas they are consistently increased in *h1b-1(ok725)* single mutants. A. Schematic of SV distribution analysis showing how the 33nm bins were arranged with respect to dense projection. Example docked SVs are shown in blue. Vesicles contacting the dense projection would be counted in the first bin (0nm). B. Mean docked SVs within 33nm bins of the dense projection across the profiles for each strain. Animals used are as follows: *WT*=4, *cla-1*=2, *h1b-1*=2, *syd-2*=3, *cla-1; h1b-1* *syd-2*=4.

In all strains the greatest number of docked vesicles were found in bin II, within 33nm of the dense projection but not making direct contact (Figure 4.10B). This was similar to results from previous studies (Watanabe et al, 2020; Jánosi et al, 2021)

In all bins, *cla-1* and *syd-2* single, double and triple mutant strains were reduced compared to the wild-type suggesting a uniform reduction in SV docking regardless of the distance from the dense projection. The reduction in docked SVs across the first four bins (up to 99nm from the dense projection) in these mutants is particularly notable as UNC-10 and UNC-13, proteins which are thought to define the SV release sites have previously been found to localise up to 100nm from the lateral edges of the dense projection (Weimer et al, 2006). Reduced SV docking in this region could reduce the efficiency of neurotransmission. Interestingly, *cla-1; syd-2* double mutants demonstrated the greatest reduction in docked vesicles within 99nm of the dense projection and may represent an additive effect caused by the concurrent absence of CLA-1 and SYD-2.

Across five of the seven bins (spanning >0nm-165nm from the dense projection) *h1b-1* single mutants displayed the greatest number of docked vesicles consistent with the

increased number of docked vesicles previously observed (Figure 4.8B). This suggests that HLB-1 promotes SV docking indiscriminate of the distance from the dense projection. This effect was again not observed in *h1b-1 syd-2* double mutants when compared to the *syd-2* mutant background suggesting epistasis.

4.1.4 Reduced dense core vesicle recruitment to synaptic sites indicate a transport defect beyond those affecting SVs

The number of vesicles recruited to synaptic sites was markedly reduced in mutants carrying the *syd-2(ok217)* allele (Figure 4.6). A potential explanation for this is a deficiency in transport to the synaptic sites. SYD-2 is a known co-factor of the molecular motor UNC-104, which transports numerous components to presynaptic sites including SV precursors (Hall and Hedgecock, 1991) and AZ scaffold proteins. Such a mechanism may also contribute to the reduced dense projection size.

UNC-104 is also involved in transporting other synaptic components including neuropeptide carrying dense core vesicles (DCVs) (Morrison et al, 2018) and mitochondria (Barmaver and Wagner, 2023). Neuropeptidergic DCVs are enriched at synaptic sites albeit in smaller numbers than SVs and do not cluster around the presynaptic AZ. Like SVs, DCVs are also captured at synaptic sites by the CSS (core synapse stability) complex which consists of SYD-2, SYD-1, SAD-1 and Sentryn (Morrison et al, 2018; Edwards et al, 2018).

As SYD-2 is believed to play important roles in the trafficking of DCVs (Goodwin and Juo, 2013; Morrison et al, 2018) I examined the presence of DCVs at synapses in

each mutant strain. By doing this I aimed to assess whether the addition of *cla-1* and *h1b-1* mutations enhanced DCV recruitment defects in the *syd-2* mutant sensitised background. DCVs were counted from all sections of a synapse containing a dense projection and one section either side and then averaged based on the number of sections.

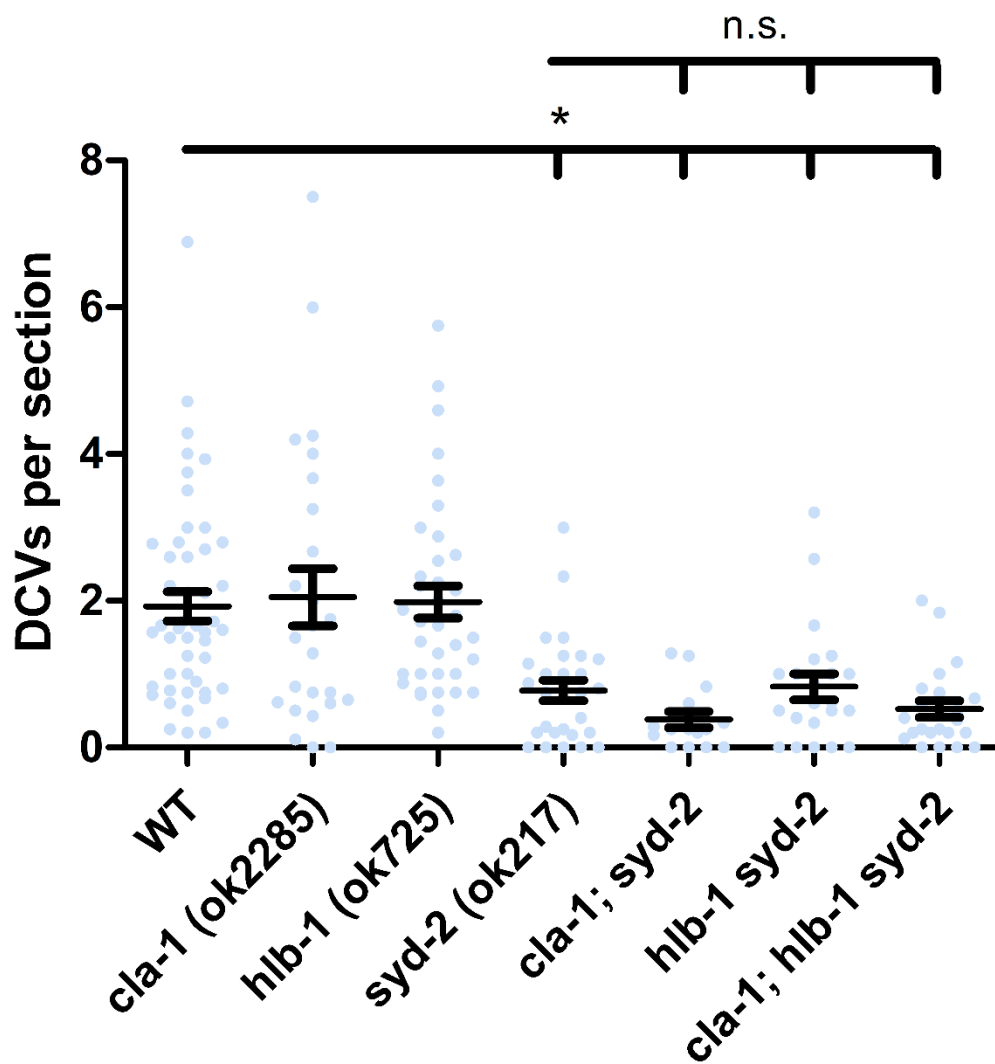


Figure 4.11. Dense core vesicle recruitment is diminished in *syd-2* mutants suggesting defective transport to synaptic sites. Mean total DCVs per section at each synapse. Bars in the data show mean±SEM. Pairwise comparisons for significance testing used Dunn's test for multiple comparisons following Kruskal-Wallis test for variance. Pairwise comparisons were made between wild-type and all other conditions, between single mutants and double mutants which shared mutations, and between the triple mutant and all single and double mutants. Pairwise comparisons are shown by lines with ticks indicating mutants being compared to the condition at the unticked left-hand end. *p<0.05 corrected for multiple comparisons. n.s. - not significant. Animals used are as follows: *WT*=4, *cla-1*=3, *hlb-1*=2, *syd-2*=3, *cla-1; syd-2*=1, *hlb-1 syd-2*=2; *cla-1; hlb-1 syd-2*=4. Post-hoc power calculations can be found in Appendix 1.

The total number of DCVs per section were significantly reduced in all strains carrying a *syd-2* mutation confirming that the loss of SYD-2 reduces DCV recruitment to synaptic boutons (Figure 4.11). The addition of the *hlb-1* and *cla-1* mutant alleles had no significant further effect in the *syd-2* mutant background. This suggests that neither HLB-1 or CLA-1 support the recruitment of DCVs to synaptic regions. Furthermore, as neither protein was shown to be involved in SV recruitment in my EM analysis, this suggests that unlike SYD-2 these proteins do not appear to be important for the promotion of UNC-104 motor protein anterograde movement. My data supports SYD-2 being a main driver of SV and DCV recruitment among the proteins examined providing further credence to its reported roles in both capture, as part of the CSS system, and anterograde transport, as an adaptor of UNC-104, of presynaptic cargo.

4.2 Discussion

In this chapter I used electron microscopy to investigate the presynaptic ultrastructural defects caused by the loss of CLA-1 and HLB-1 in comparison to the loss of SYD-2 and to understand whether they cause additional defects in the *syd-2* mutant background. While I was able to confirm that the loss of SYD-2 reduces the size of the dense projection and the total number of SVs localised at the presynapse, neither the *cla-1* or *hlb-1* mutant alleles added to these effects despite dense projection size being reduced in *cla-1* single mutants. I found that both CLA-1 and HLB-1 are involved in directing the subcellular localisation of SVs. CLA-1 retains a subset of undocked SVs close to the dense projection and supports SYD-2 in the docking of SVs. Meanwhile, HLB-1 regulates SV docking but only in the presence of SYD-2. This indicates that CLA-1 and HLB-1 have roles in managing the presynaptic AZ ultrastructure although some of their functions may be downstream of SYD-2.

4.2.1 SYD-2 organises the dense projection

During synaptogenesis initial AZ assembly is an incredibly rapid process (Lipton et al, 2018). Maturation of these synaptic sites occurs over a longer period during which further components of the AZ scaffold, SVs and VGCCs are recruited to presynaptic sites (Fouquet et al, 2009; Lipton et al, 2018). SYD-2/Liprin- α is one of the first proteins to arrive at nascent synapses (Fouquet et al, 2009), thought to be recruited by proteins which designate synaptic sites including SYG-1 (Patel et al, 2006) and NRX-1 (Owald et al, 2012). SYD-2/Liprin- α is believed to be one of the major proteins guiding the

development of the presynapse including the formation of the AZ scaffold (Kittelmann et al, 2013).

My findings confirmed that the loss of SYD-2 reduced the frequency of dense projections at cholinergic neuromuscular junctions (Kittelmann et al, 2013), although my earlier confocal microscopy analysis of UNC-10 fluorescence puncta did not detect this defect. This could be due to the single synapse resolution afforded by electron microscopy or UNC-10 being clustered at other sites without fully formed mature AZ scaffolds (dense projections). Abnormal UNC-10 clustering in *syd-2* mutants could also explain why there were similar numbers of dense projections in wild-type and triple mutant nerve cords despite there being increased UNC-10 puncta in the latter in my confocal analysis. ImmunoEM or correlative light EM (CLEM) approaches which provide a means of examining the location of proteins relative to the structures in electron micrographs would be useful to identify regions of UNC-10 expression away from dense projections. Such sites could coincide with boutons present in both *syd-2* single and *cla-1; hlb-1 syd-2* triple mutants that contained SVs but no dense projections. These boutons were reminiscent of *Drosophila melanogaster* 'ghost boutons' at neuromuscular junctions which are thought to be immature synapses lacking full functionality and both presynaptic and postsynaptic structures (Ataman et al, 2006; Menon et al, 2013). While ghost boutons are rarely found in wild-type *Drosophila* they appear more regularly in *dnrx* mutants (encoding the *Drosophila* Neurexin homologue) which are known to have presynaptic defects (Guangming et al, 2020). Interestingly DNRX is thought to stabilise early AZ scaffolds formed by DSYD-1 and DLiprin- α (the *Drosophila* homologue of SYD-2) (Owald et al, 2012). The boutons I observed may similarly be due to failed dense projection formation in the absence of SYD-2. The cell autonomy of this process could be confirmed if cholinergic

“ghost boutons” are eliminated by cholinergic motor neuron specific expression of SYD-2 through a rescue construct in *syd-2* mutants. This would need to be followed up with investigations into the link between SYD-2 and bouton formation to understand whether SYD-2 just facilitates maturation of these boutons or regulates bouton formation.

Dense projection size was also reduced in *syd-2* mutants mirroring previous observations in both *C. elegans* (Kittelman et al, 2013) and *Drosophila* (Kaufmann et al, 2002). This further supports the assertion that SYD-2 is important for the structure’s formation. SYD-2 contributes to the formation of dense projections through its role in the recruitment of other AZ proteins and by affecting how these other AZ proteins are integrated into dense projections (Wagner et al, 2009; Kittelman et al, 2013; Liang et al, 2021). The changes the loss of SYD-2 causes to dense projection morphology is likely to change the way that the structure interacts with SVs affecting their localisation at synaptic sites by eliminating tethers and disrupting docking sites. Such changes have been indicated by electron tomography studies (Stigloher et al, 2011; Kittelman et al, 2013).

4.2.2 SYD-2 manages SV localisation at the presynapse

The ability to dock and fuse SVs at the presynaptic plasma membrane is a major determinant of synaptic strength. The dense projection/AZ scaffold is thought to maintain release sites and ensure SV availability. Total SVs were reduced at *syd-2* mutant synapses consistent with a previous study (Kittelman et al, 2013). Although I did not find a reduction in the total number of docked SVs, there were consistently

fewer docked vesicles in regions up to 198nm away from dense projections, as has been found previously (Kittelmann et al, 2013). As SYD-2 is not known to bind directly to SVs it seems likely that it affects SV docking through its role in forming and stabilising the dense projection in particular the recruitment and arrangement of other proteins within the structure. In both my confocal analysis and previous studies, UNC-10 recruitment has been shown to be reduced in *syd-2* mutants (Oh et al, 2021). Past analysis has shown UNC-10 to be crucial for SV docking (Weimer et al, 2006; Stigloher et al, 2011). In line with this UNC-10 localises to the lateral edges of the dense projection and approximately 100nm beyond where most SV docking takes place (Weimer et al, 2006). Therefore, UNC-10 could be important in the formation of putative SV docking bays in the dense projection (Kittelmann et al, 2013). Electron tomographic study examining the fine ultrastructure of dense projections in *unc-10* mutants, particularly in the longitudinal plane, would help to verify this.

While SYD-2 is clearly important for typical dense projection formation and its loss from synapses disrupts function there are several open questions. Are the effects of the loss of SYD-2 driven by the disorganisation of specific AZ scaffold proteins recruited and integrated into the structure by SYD-2? Additionally, as I still observed residual dense projections in the absence of SYD-2, are there other proteins important for maintaining the stability and functionality of these scaffolds? My investigations into CLA-1 and HLB-1 provide some insight into these questions.

4.2.3 CLA-1 contributes to dense projection morphology through the same pathway as SYD-2

In agreement with previous studies, I found that *cla-1* loss of function mutants had reduced dense projection size (Xuan et al, 2017; Krout et al, 2023). In my investigations I used a deletion which was much smaller than that used in these previous studies and was more focussed towards regions encoding for the C-terminal PDZ and C2 domains. PDZ and C2 domains with similar sequences are also present in CLA-1's assumed interspecies functional homologues Piccolo (vertebrates) and Fife (*Drosophila*). The observation that deletion of these regions reduces dense projection size strengthens the hypothesis that CLA-1's AZ localisation and role in the dense projection are dependent upon its PDZ and C2 domains. PDZ domains are important to the integrity of other biological complexes (Ranganathan and Ross, 1997; Zhang and Wang, 2003; Erlendsson et al, 2019) and likely facilitate interactions with other AZ proteins. We currently know little of the interactions CLA-1 forms with other AZ scaffold proteins and further experiments such as yeast two hybrid and coimmunoprecipitation approaches will be required to identify the CLA-1 interactome. ELKS-1, for instance, exhibits a PDZ binding domain at its C-terminus which could represent an important interaction site for CLA-1 to maintain dense projection stability. Future studies removing either the PDZ or C2 domain specifically will be useful to determine the minimal CLA-1 C-terminal region required for typical dense projection formation. While the PDZ is the more obvious domain to influence scaffold formation, C2 domains are associated with membrane binding to define subcellular localisation and can bind with regions of PDZ and SH3 domains among others (Rizo and Südhof, 1998). Hence the CLA-1 C2 domain may have its own contribution to dense projection structure.

Although SYD-2 and CLA-1 loss caused similar reductions in dense projection size double mutants combining these deleterious alleles had no greater effect. This indicates that CLA-1 and SYD-2 act within the same pathway in dense projection formation. A previous confocal study has shown that there is reciprocal recruitment between CLA-1 and SYD-2, although CLA-1 recruitment by SYD-2 is much stronger (Xuan et al, 2017). This places SYD-2 primarily upstream of CLA-1 and consequently raises the question of whether reduced CLA-1 recruitment could be a main driver of the reduction in dense projection size seen in *syd-2* mutants. Rescue experiments using CLA-1 overexpression in *syd-2* mutants to try to restore dense projection size would be an interesting next step to investigate this. This would depend on enough CLA-1 being able to reach the synapse and integrate into the dense projection in the absence of SYD-2, however.

There may be additional proteins acting downstream of CLA-1 in dense projection formation as well. Recent studies have shown that both SYD-2 and CLA-1 are important for the localisation of RIMB-1 at the presynapse (Oh et al, 2021; Krout et al, 2023). Interestingly, RIMB-1 loss has also been found to reduce dense projection size (Krout et al, 2023). SYD-2, CLA-1 and RIMB-1 could therefore all sit in the same pathway influencing dense projection morphology. If RIMB-1 were the end point of such a pathway *rimb-1; cla-1; syd-2* triple mutants would have an identical dense projection size to *syd-2* and *cla-1* single mutants and the *cla-1; syd-2* double mutant under EM analysis. Examining this will be useful to confirm whether RIMB-1 is the main driver of gross dense projection size, works alongside CLA-1 to maintain DP size or is just one of potentially several downstream effector proteins. CLA-1 is also involved in the localisation of UNC-13 at synaptic sites (Krout et al, 2023), although it remains unknown whether UNC-13 plays a role in dense projection morphology.

4.2.4 CLA-1 tethers SVs proximal to the dense projection

Although CLA-1 loss affected gross dense projection morphology it is important to ask how this translates into functional effects such as the reduced cholinergic neurotransmission observed in the previous chapter. The most likely mechanism would be through disruption of presynaptic SV localisation and docking.

CLA-1 loss did not reduce total SV docking. Previous studies have contrarily shown SV docking is increased (Xuan et al, 2017) and decreased (Krout et al, 2023) at cholinergic neuromuscular junctions in *cla-1* mutants. I did find that *cla-1; syd-2* double mutants affected SV docking more strongly than either mutation alone, however; suggesting that CLA-1 and SYD-2 collectively contribute to the process. This effect was especially prevalent within 99nm of the dense projection where UNC-10 and UNC-13 are thought to define docking and release sites (Weimer et al, 2006). *cla-1* single mutants displayed a mild but consistent reduction in SV docking within 99nm of the dense projection. CLA-1 may support SV docking specifically in the vicinity of the dense projection. SYD-2 meanwhile could have a broader effect on SV docking extending outside of these regions supported by its functions in SV transport and capture at synapses (Wagner et al, 2009; Edwards et al, 2015).

My results also support CLA-1 being important for maintaining undocked SVs proximal to the dense projection (within 99nm). This is likely to reflect the proposed model of the CLA-1 long isoform extending out into the cytoplasm to tether SVs from the reserve pool (Xuan et al, 2017). This tethering is suggested to support neurotransmission during periods of prolonged high frequency release by providing vesicles to dock at vacated release sites (Xuan et al, 2017). As my results support a role for CLA-1 in both tethering and docking under unstimulated conditions CLA-1 could support

physiological release as well. There remains a gap in our knowledge regarding the steps between SV tethering at the dense projection and docking at the plasma membrane. CLA-1 and its multiple isoforms, which are likely to perform different functions, may support the transfer of the tethered SVs to release sites at the plasma membrane as well. Recent investigations explored the functions of individual CLA-1 isoforms through the deletion of the short isoform specific promoter or N-terminal regions of the long isoform. This was not able to confirm specific roles for the short or long isoforms of CLA-1 at the NMJ, however (Krout et al, 2023). It is possible that variations between expression profiles of individual isoforms may change the precise role of CLA-1 within different neurons and hence its importance to their synapses. While single-cell RNA sequencing in *C. elegans* has been valuable in revealing the expression profiles of genes in each of the 302 hermaphrodite neurons (Taylor et al, 2021) the distribution of specific isoforms within them is not currently known although ongoing work is seeking to clarify this for specific cell types (Barrett et al, 2022). This will be valuable to determining whether there is flexibility to how synapses utilise multiple isoform proteins such as CLA-1.

Further investigations using “Flash and Freeze” EM sample preparations could shed further light on how CLA-1 contributes to SV docking. “Flash and freeze” involves the use of optogenetics to stimulate neurotransmission in worms before they undergo high pressure freezing (Watanabe, 2016). Transitioning between these stages quickly allows the presynapse to be observed in the aftermath of SV fusion and release, however; introducing a delay between the stimulation and freezing can allow dynamics of SV docking to be investigated. If docking of new SVs is prolonged in *cla-1* mutants following stimulation this would be indicative of defective SV docking. This would also be interesting to explore in *syd-2* mutants and *cla-1; syd-2* double mutants to

understand the role of SYD-2 in the dynamics of docking and whether there are additive effects between the two mutants.

There is an additional consideration that needs to be made regarding the reduction in undocked SVs near the dense projection in *cla-1* mutants. These vesicles, although undocked, may still be part of the readily releasable pool and participate in SV fusion following a stimulus. Traditionally only docked vesicles have been considered part of the readily releasable pool, however some studies have suggested that this definition is overly simplistic (Rizzoli and Betz, 2004; Kaeser and Rehr, 2017). The idea that there is a reduction in the number of vesicles available for release in *cla-1* mutants could provide an explanation for their increased aldicarb resistance in the previous chapter. It may be useful to examine the size of the readily releasable pool in *cla-1* mutants using electrophysiology by assessing the synaptic charge evoked by hypertonic sucrose (Rosenmunds and Stevens, 1996). Comparing these results against those in WT and *syd-2* single and *cla-1; syd-2* double mutants will help to determine whether there is a reduction in the extended functional readily releasable pool, beyond just docked vesicles, and whether there are additive effects between *syd-2* and *cla-1* mutants. This would also provide a vital link to cholinergic NMJ function.

Overall, my results suggest that the recruitment of CLA-1 by SYD-2 is a determinant of gross dense projection morphology and stability. Despite SYD-2 being a strong recruiter of CLA-1 in confocal studies (Xuan et al, 2017), I suggest that even in reduced quantities CLA-1 supports SV docking close to the dense projection by extending tethers into the cytoplasm to capture SVs which are later trafficked to the plasma membrane to dock. More work is still required to confirm this though. Much remains unclear regarding the roles of the different CLA-1 isoforms. Specific removal of these

isoforms through targeted deletions of isoform specific regions or promoters will allow us to better appreciate which are required for dense projection formation and which are required for docking. Additionally, it is critical that we understand CLA-1's genetic and molecular interactions with other AZ proteins so we can grasp how it associates with the AZ scaffold.

4.2.5 HLB-1 is a regulator of SYD-2 mediated synaptic vesicle docking

Despite first being identified alongside SYD-2 (Serra-Pagès et al, 1998), there have been few investigations into the contributions of HLB-1 to the presynaptic AZ. In this chapter I have conducted the first ultrastructural analysis of *hlb-1* mutant synapses using electron microscopy.

Loss of HLB-1 had no clear effect on dense projection morphology at cholinergic neuromuscular junctions in the presence or absence of SYD-2, suggesting HLB-1 does not contribute to dense projection formation or stability. HLB-1 and SYD-2 both have a C-terminal domain structure consisting of three tandem SAM domains, which is also known as the Liprin homology domain (LHD), and shares sequence similarity. The SYD-2 Liprin homology domain interacts with PTP-3 (Serra-Pagès et al, 1998), RSY-1 (Patel and Shen, 2009), UNC-104 (Wagner et al, 2009) although it is unclear whether these interactions contribute to dense projection formation. As HLB-1 is dispensable in maintaining typical dense projection morphology and provides no compensation for the loss of SYD-2 in dense projection formation this could indicate that the SYD-2 LHD is less important in dense projection formation than the SYD-2 N-terminus. This is consistent with what we already know about the SYD-2 N-terminus which facilitates SYD-2 oligomerisation (Chia et al, 2013; Liang et al, 2021) and

houses interaction sites with UNC-10 (Schoch et al, 2002), ELKS-1 (Dai et al, 2006) and UNC-104 (Wagner et al, 2009). Further studies of dense projection morphology in truncated *syd-2* mutants lacking the LHD will be required to confirm that the N-terminus is sufficient for the structure's formation.

Loss of function mutants of the *Drosophila* HLB-1 homologue DLiprin- β have been associated with a reduction in synaptic bouton formation at NMJs and consequently a reduction in the number of AZs (Astigarraga et al, 2010). HLB-1 could therefore still affect the frequency of dense projections if not the morphology. Liprin- β /HLB-1 proteins form several interactions at the presynapse which may contribute to complex formation at the presynapse. Mammalian Liprin- β has previously been shown to homodimerise via its N-terminal domain and heterodimerise with Liprin- α proteins via its C-terminus (Serra-Pagès et al, 1998; Astigarraga et al, 2010). The Liprin- α /Liprin- β heterodimer has also been shown to interact with the presynaptic CASK complex (Wei et al, 2011). Liprin- α /Liprin- β heterodimers may also regulate Liprin- α 's interactions with other proteins. One such example is LAR, the *C. elegans* homologue of PTP-3, which is involved in shaping the AZ (Ackley et al, 2005). The associations of Liprin- β proteins with complex formation at the synapse indicates that HLB-1 could have an involvement in the initial stages of dense projection formation. To test if HLB-1 loss affects the frequency of dense projection formation in *C. elegans* serial reconstructions will need to be examined in *h1b-1* mutants in future studies.

The idea that HLB-1 regulates SYD-2's interactions with other proteins may also serve as an explanation for the observed increases in SV docking in *h1b-1* single mutants. A consistent increase in SV docking was found up to 165nm from, but not contacting, the dense projection in *h1b-1* single mutants. HLB-1 loss in a *syd-2* sensitised background did not enhance SV docking, however. This suggests that HLB-1's

function in SV docking is dependent on the presence of SYD-2. HLB-1, like many other AZ proteins, may be recruited by SYD-2 to synaptic sites. Confocal imaging analysis could be used to assess whether HLB-1 localisation at the presynapse is affected in the *syd-2* mutant background in future studies. Alternatively, as discussed previously, heterodimerisation of HLB-1 and SYD-2 could disrupt the latter's interactions with other proteins. Liprin- β binding of Liprin- α is mutually exclusive of Liprin- α binding LAR (Xie et al, 2020). As a major ligand of LAR, Liprin- α is thought to contribute to many of the functions of LAR receptors. The *C. elegans* LAR homologue PTP-3 organises UNC-10 at the presynapse (Ackley et al, 2005). Disruption of the SYD-2/PTP-3 interaction may affect regular docking by interfering with UNC-10 localisation.

As so little is known regarding HLB-1's interactions with other AZ proteins or even its localisation patterns within the presynapse, many more investigations will be required to understand how HLB-1 regulates SV docking. It is unclear whether HLB-1's regulation of SV docking is fulfilled at the presynapse itself. ImmunoEM would be a useful approach to investigate HLB-1's subcellular localisation and understand if it acts within the central dense projection structure, at its periphery or elsewhere. Additionally, it would be pertinent to investigate whether HLB-1 forms interactions with other AZ proteins. While the potential HLB-1-SYD-2 interaction is a good starting point, it has not been confirmed in *C. elegans*. There may also be direct interactions with other AZ proteins such as ELKS-1 and UNC-10 which have not previously been investigated. *In vitro* yeast two-hybrid screens examining whether HLB-1 forms interactions with a panel of AZ proteins could be incredibly informative of the HLB-1 presynaptic interactome. To examine whether any identified interactions also occur in *C. elegans* cholinergic motor neurons *in vivo* genetically targeted fluorescence resonance energy transfer (FRET) and biomolecular fluorescence complementation (BiFC) constructs

can be used to confirm their proximity (Hiatt et al, 2008; Wagner et al, 2009). The roles of such candidate proteins alongside HLB-1 could consequently be investigated in double mutants through EM analysis as *h1b-1 syd-2* double mutants were examined here.

Altogether my results suggest that although HLB-1 is not involved in the maintenance of the AZ scaffold it appears to regulate SV docking. If we are to determine how HLB-1 performs this function many more investigations, as described in this discussion, are required.

5 General Discussion

5.1 CLA-1 and HLB-1 do not contribute to active zone scaffold formation independent of SYD-2 but do influence synaptic vesicle localisation at cholinergic neuromuscular junctions

The overall goal of this thesis was to explore whether CLA-1 and HLB-1 support SYD-2 in the organisation of the presynaptic active zone (AZ) scaffold at the *C. elegans* cholinergic neuromuscular junction.

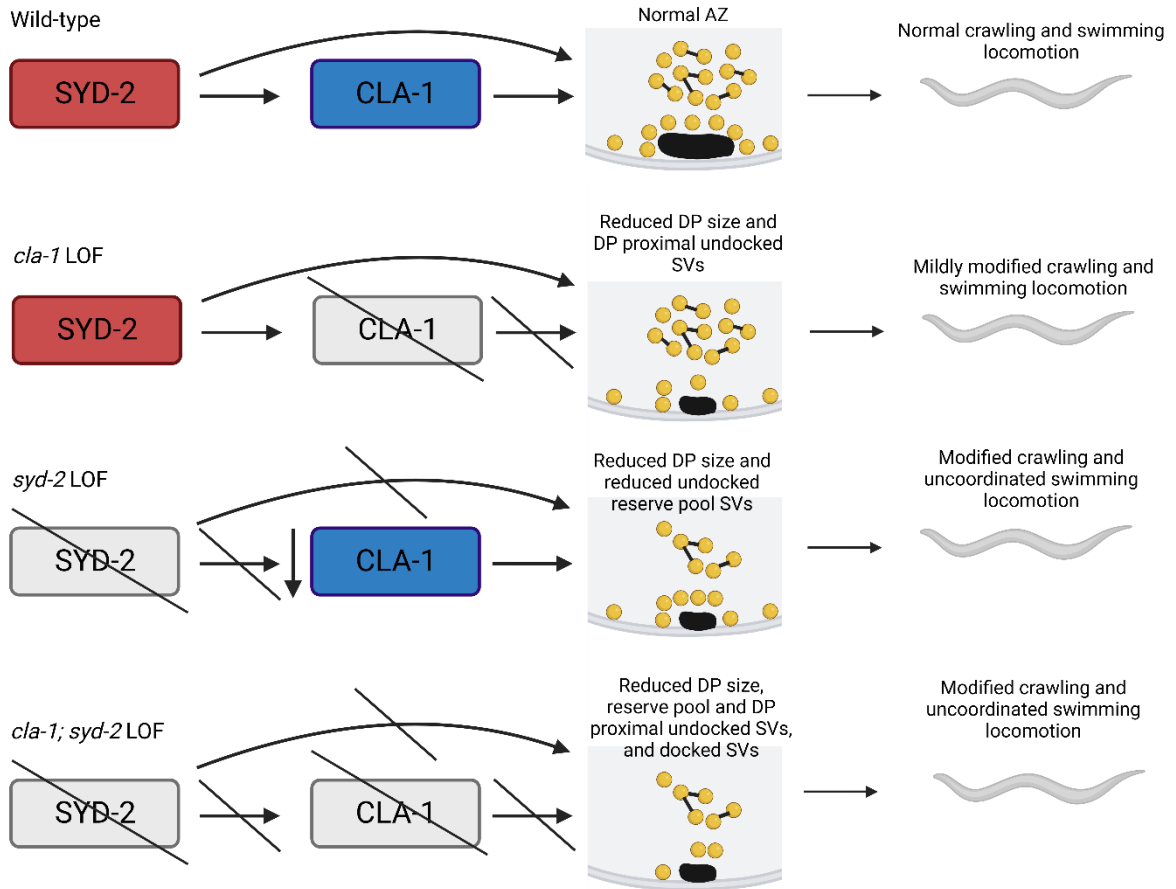
My data confirms many of SYD-2's suggested roles as a major organiser of the presynaptic AZ scaffold at the neuromuscular junction. By examining active zone structure through a combination of fluorescence confocal microscopy and electron microscopy approaches I have been able to show that SYD-2 is important for the recruitment of UNC-10 to the synaptic region, the localisation of synaptic vesicles (SVs) and DCVs (dense core vesicles) to synaptic sites and the formation of a full-sized dense projection. While aldicarb assays were unable to confirm defective cholinergic neurotransmission as has been found through electrophysiology approaches previously (Kittelmann et al, 2013), the altered locomotion visualised in *syd-2* mutant worms indicates that the loss of SYD-2 interrupts typical synaptic communication.

The retained capacity for presynaptic dense projection formation and synaptic functionality in the absence of SYD-2 raises questions regarding which other proteins assist SYD-2 in its roles at the presynaptic AZ, and whether they can compensate for its loss. My analyses of the effects of CLA-1 and HLB-1 loss in a *syd-2* mutant background shows they do not drive the formation of residual dense projection

structures, however both proteins still have roles in maintaining the AZ ultrastructure. Based on my findings, I propose that CLA-1 is one of the main downstream effectors of SYD-2 in determining dense projection size (Figure 5.1A). This fits with previous findings which described SYD-2 as a major recruiter of CLA-1, and CLA-1 as a determinant of dense projection length (Xuan et al, 2017). As several defects found in *syd-2* single mutants throughout experiments were not reflected in *cla-1* single mutants, such as those in UNC-10 and SV recruitment and swimming locomotion it appears clear that SYD-2's synaptic defects are not just linked to a reduction in the size of the dense projection (Figure 5.1A). Closer examination of the fine dense projection architecture through electron tomography will be required to clarify whether SYD-2 and CLA-1 loss affect subtler ultrastructural features such as filamentous tethers and SV docking bays similarly, however.

I also suggest that CLA-1 supports retention of SVs proximal to the dense projection and SV docking independent of SYD-2. Additionally, CLA-1 appears to be capable of fulfilling these roles in the absence of SYD-2 when it is believed to have a greatly reduced molecular concentration at the synapse (Figure 5.1A). Therefore, while relatively large volumes of CLA-1 are required to maintain dense projection size only small amounts are needed to perform its roles in SV retention. Altogether, this generates a model where SYD-2 is involved in the structuring of the entire presynaptic area whereas CLA-1's roles are restricted to the dense projection and the synaptic vesicles in the immediate vicinity (Figure 5.1B).

A



B

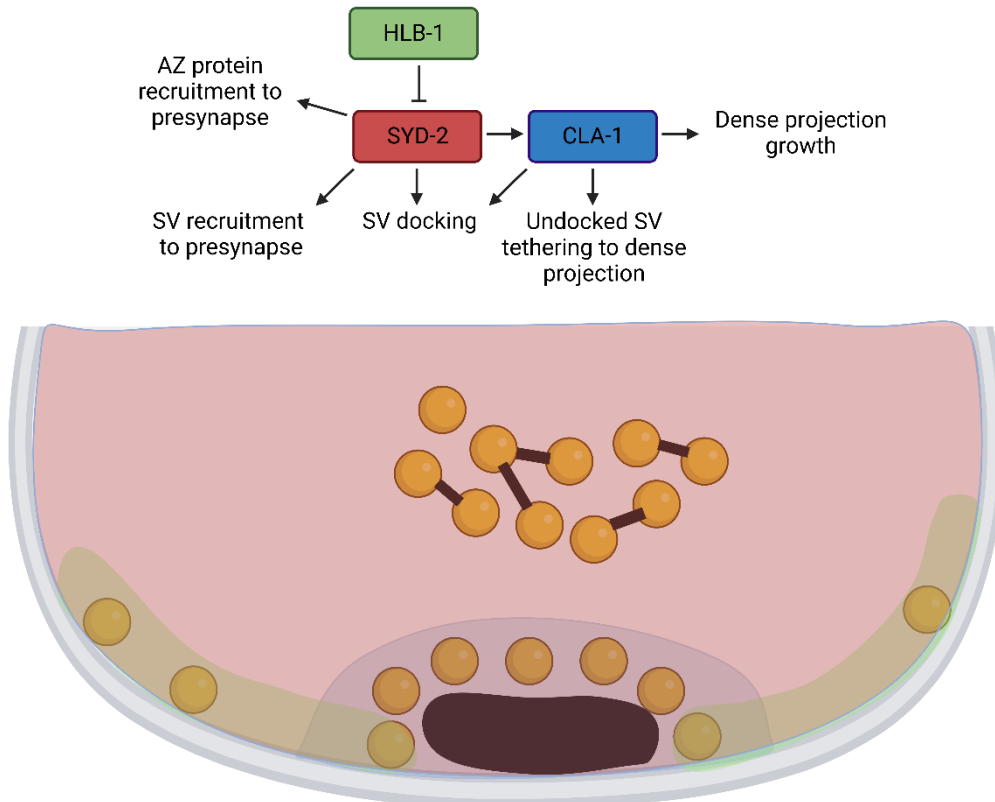


Figure 5.1. Summary of findings relating to the interactions of SYD-2, CLA-1 and HLB-1 at the presynaptic active zone. **A.** Details of the interactions between CLA-1 and SYD-2 and how this links to presynaptic ultrastructure and locomotor phenotypes in wild-type and *cla-1* and *syd-2* mutant *C. elegans*. **B.** Proposed interactions and functions of CLA-1, HLB-1 and SYD-2 at the presynapse. Top shows an interaction map of the proteins and their presynaptic functions. HLB-1 and SYD-2 regulate SV docking through an antagonistic interaction between the two proteins. SYD-2 promotes CLA-1 recruitment promoting dense projection growth. CLA-1 and SYD-2 also have independent functions. Bottom illustrates the proposed regions of the presynaptic active zone affected by SYD-2 (Red), CLA-1 (Blue) and HLB-1 (Green) based on their presynaptic functions. SYD-2 has broad roles across the presynapse, whereas CLA-1 function is restricted to the dense projection and its immediate proximity. HLB-1 may work antagonistically to SYD-2 to regulate SV docking at the presynaptic plasma membrane. Created with Biorender.com.

The role of HLB-1 is less clear; however, it may act as a negative regulator of SYD-2 in SV docking (Figure 5.1B), likely through binding SYD-2 and hindering interactions with other proteins. This antagonism of HLB-1 towards SYD-2 appears to also transfer to specific aspects of crawling locomotion such as crawling speed. Although earlier confocal analysis pointed towards HLB-1 being involved in total SV recruitment to the synaptic region this was not borne out in electron microscopy analysis of specific synapses. Therefore, for the purposes of this thesis I leave HLB-1's role restricted to regulating docking at the plasma membrane (Figure 5.1B).

My results indicate that while CLA-1 and HLB-1 are not involved in active zone scaffold/ dense projection generation in the absence of SYD-2 they are still impactful presynaptic active zone proteins and require greater consideration in our growing model of this subcellular compartment. To fully interpret my findings, however; broader examinations with greater scope will be required to understand whether their roles are consistent across other synapses or have differing levels of potency which could

explain some of the complexity in locomotion analyses. Meanwhile long-range serial constructions, across several samples would also be useful to confirm SV distribution patterns visualised using confocal fluorescence in the context of electron microscopy.

There remains an obvious open question, however. What are the proteins supporting residual active zone scaffold/dense projection formation when SYD-2 is removed from the presynapse?

5.2 What are the other AZ proteins involved in dense projection formation?

Although there are many proteins known to be localised to the AZ and believed to participate in the AZ scaffold our understanding of the proteins integral to this structure is incomplete. The core AZ scaffold proteins are typically identified as SYD-2, UNC-10, RIMB-1, ELKS-1, UNC-13 and CLA-1. Some of these proteins, such as ELKS-1, have no discernible role in the typical formation of dense projections however (Kittelmann et al, 2013). Based on previous studies RIMB-1 and NRX-1 may also contribute to dense projection morphology, however, like CLA-1, there is evidence that these proteins act within the same pathway as SYD-2 (Owald et al, 2012; Krout et al, 2023).

A common interpretation of why the loss of individual AZ scaffold proteins only have mild effects on dense projection structure is that they have high levels of redundancy, hence strong compensation mechanisms allow residual dense projection formation. In my analysis I removed SYD-2, CLA-1, and HLB-1 together to test the resilience of the structure although the effect was no greater than losing SYD-2 alone. There may be merits to removing many if not all the core AZ scaffold proteins at the same time provided viability can be maintained. Considering the significance placed upon SYD-2,

UNC-10, ELKS-1, RIMB-1, UNC-13 and CLA-1 it seems plausible that the removal of all of these proteins simultaneously could eliminate electron-dense material from the presynapse. If this were to be confirmed in future studies this would grant us an avenue to investigate the minimal requirements for forming presynaptic dense projections *in vivo*. This would complement ongoing *in vitro* studies examining how rudimentary AZ scaffolds can be constructed from AZ proteins using phase separation (Wu et al, 2019; Wu et al, 2021) (discussed in 5.3).

If we are to fully grasp the functional significance of the AZ structure itself a more sophisticated approach may be required. This would involve dissecting the specific protein domains which facilitate the formation of dense projections and removing or replacing these regions so that they cannot form the complex while retaining the regions critical for their localisation and other presynaptic functions. Many AZ proteins may need to interact with either other copies of themselves or other AZ proteins to perform their functions, however. The mammalian homologue of UNC-13, MUNC-13, forms nanoclusters at the presynapse which must be at least hexameric to effectively dock SVs (Li et al, 2021).

On the other hand, we may only be scratching the surface regarding the proteins involved in AZ scaffold formation. There may be AZ scaffold proteins which have not yet been identified, these may include transient proteins which play roles in assembly early on but are less important in the mature structure or even proteins which are competent to replace the core AZ scaffold proteins in the structure when they are removed but are typically less involved with the structure. New proteomic methodologies have been critical in identifying the molecular components of biological complexes. These most commonly involve proximity labelling of proteins of interest and closely associated proteins, capture of these molecules with an appropriate ligand

and then analysis with paired liquid chromatography and mass spectrometry (LC-MS) to identify the components (Bosch, 2021; Zafra and Piniella, 2022). A recent study in *C. elegans* used Turbo-ID, a biotin-based proximity labelling approach, to investigate components of the AZ scaffold (Artan et al, 2021). This focussed on ELKS-1 and was able to confirm known interactions with other presynaptic AZ proteins, including UNC-10 and SYD-2 supporting its validity. Several additional previously unidentified proteins were also uncovered which will be worth future examination designated as C03H5.6, C11E4.6 and H06I04.1. Future proximity labelling approaches examining other AZ scaffold proteins will help us appreciate the most important proteins of the AZ scaffold. Additionally using these approaches in *syd-2* mutants to explore the proteome of residual AZ scaffold structures could help us to understand the redundancy or compensatory mechanisms which are employed when major AZ scaffold proteins are lost.

In the investigation of candidate mutant proteins there have also been incredible technical advances in approaches which could enhance our evaluation of dense projection morphology. Electron microscopy techniques utilising focussed ion beam milling such as FIB-SEM (focussed ion beam scanning electron microscopy) offer enhanced z-axis resolution and improved targeting and reliability of sample preparation compared with ultramicrotomy. Focussed ion beam milling has been used in sample preparation for cryo electron tomography (cryo-ET) techniques (Schaffer et al, 2019; Hylton and Swulius, 2021) which can provide extraordinary resolution for molecular structures (Berger et al, 2023). Applied to dense projections, cryo-ET could enhance interpretation of fine ultrastructural features and, as our understanding of the proteomics of the structure grows, improve our insight into the orientation of scaffold proteins within the structure.

Another class of techniques that have greatly furthered our understanding of protein interactions at the presynaptic AZ has been superresolution microscopy. Techniques such as STORM (stochastic optical reconstruction microscopy) and STED (stimulated emission depletion) have helped us to realise the subsynaptic localisation and orientation of many AZ proteins in relation to other AZ proteins. These techniques have been used elegantly in the investigation of the molecular structure of the *Drosophila* T-bar at synapses. This has been critical in determining the orientation of the primary AZ scaffold protein Bruchpilot (Fouquet et al, 2009; Ehmann et al, 2014), within the T-bar and its spatial relationship with calcium channels (Ehmann et al, 2015) and RBP (Petzoldt et al, 2020). There is an argument that superresolution microscopy methods of examining subsynaptic localisation of proteins has been underutilised in *C. elegans*, although this is in part due to the common use of antibodies and chemical dyes which are impeded by the relative impermeability of the animal's cuticle. A developing method in *C. elegans* which could provide an alternative means of investigating the spatial distribution of presynaptic AZ proteins is expansion microscopy (Yu et al, 2020). This method expands the space between proteins or biomolecules isotropically within the sample itself allowing the spatial relationship of proteins to be resolved within the diffraction limits of conventional light microscopy and has recently been validated at the presynapse (Yu et al, 2020).

While exploration of the composition and morphology of the AZ scaffold is incredibly important, we should be careful of oversimplifying the structure as static and inflexible with only simple protein interactions underlying its construction. New biophysical studies are challenging our understanding of the dense projection/AZ scaffold. These studies suggest that it is a much more fluid structure than once thought with the ability to alter its morphology and composition (Liang et al, 2021).

5.3 Thinking of the AZ as more than a simple scaffold

In recent years the idea of the AZ scaffold as a phase condensate has gained considerable traction. Liquid-liquid phase separation (LLPS) describes the process of one liquid remaining concentrated within another without mixing. This is best exemplified by oil droplets in water which form due to the hydrophobic properties of oil. Forming phase condensates would enable the AZ scaffold to maintain a high concentration of specific proteins in one place without them diffusing away. Establishing itself as a condensate would also allow the structure to be more selective about the proteins it interacts with.

Combinations of mammalian Liprin- α and ELKS (Liang et al, 2021) and RIM and RIM-BP (Wu et al, 2019; Wu et al, 2021) have been demonstrated to form co-phase condensates *in vitro*. The latter of these has also been found to be capable of clustering calcium channels at synthetic plasma membranes and attracting SVs to its external surface analogous to a form of tethering (Wu et al, 2021). AZ scaffolds are not likely to exist as a single condensate, however. The dense projection as we see it may actually be an amalgamation of multiple phase condensates attached at specific contact points. Indeed *in vitro* different condensates have been shown to be capable of existing alongside each other without coacervating (Wu et al, 2021). This would allow separate functions of the dense projection to occur independently without the interference of irrelevant proteins.

Something that has not been investigated so far is the relationship between phase condensation and dense projection formation and morphology. Phase separation is typically driven by the intrinsically disordered regions (IDRs) of proteins which lack defined domain structure and are enriched in the presynaptic AZ proteome

(Lautenschläger, 2022). There is evidence that removing IDR domains interferes with the phase condensation of SYD-2 and ELKS-1 (McDonald et al, 2020). *C. elegans* expressing SYD-2 lacking specific IDRs recruit and dock SVs less effectively (McDonald et al, 2020). The effect of these mutations on dense projection frequency and morphology has not yet been investigated although the structures do still form. Other than SYD-2 and ELKS-1 it is unknown whether any other *C. elegans* AZ scaffold proteins form phase condensates although it seems likely. It is entirely plausible that CLA-1 or even HLB-1 also participate in phase condensates as they both contain IDRs. It is interesting to consider whether the total removal of phase condensation relevant IDRs within the core AZ scaffold proteins could eliminate dense projections or whether there are proteins which could fill their place from the broader AZ. If the former is true then this would provide a platform for investigating the precise function of the AZ scaffold.

Part of the reason why the phase separation hypothesis is so interesting is its presentation of the AZ scaffold as a flexible structure susceptible to change. Phase condensates can alter their composition through the addition of new molecules such as crowding agents (André et al, 2023) or changes to environmental conditions such as pH (Adame-Arana et al, 2020). Therefore, depolarisation of synaptic terminals and subsequent calcium influx could affect the structure's morphology and function.

One of the ideas not explored in this thesis is synaptic plasticity. This describes the idea of a synapse being able to change its levels of activity to suit the requirements of information transfer. The simplest way to achieve this is by adjusting receptor expression at the postsynapse or release probability at the presynapse. It has been suggested previously that changes in the protein composition of the presynapse accompany long term depression (periods of reduced presynaptic release) and

potentiation (periods of enhanced release) and recent studies in *Drosophila* have confirmed that changes in the subsynaptic arrangement of AZ proteins accompany this. Properties such as the size of AZs (Goel et al, 2019; Ghelani, 2023) and the clustering of calcium channels and AZ scaffold proteins (Mrestani et al, 2021; Ghelani et al, 2023) have been shown to change when potentiation is induced.

There may be specific AZ proteins that are fundamental for dynamic changes in AZ scaffold structure to occur which could include CLA-1, HLB-1 and SYD-2. It is possible that the proteins involved in AZ scaffold formation and plasticity are not consistent between different synapses in different neurons, however.

5.4 Does AZ scaffold assembly, maintenance and function differ between synapses?

Most investigations into the role of the AZ scaffold in *C. elegans*, including my own, has taken place at cholinergic neuromuscular junctions. There are justifiable reasons for this, these synapses are evenly distributed along the body, easily discernible under both confocal and electron microscopy and represent one of the simplest synapses to functionally assess through electrophysiology. It is arguable that the utility of these synapses experimentally has meant that synapses in sensory and interneurons have been neglected in *C. elegans*. Indeed, there are vanishingly few studies investigating presynaptic ultrastructure in these neurons.

In vertebrates there are clear differences in the presynaptic AZ morphology between central and sensory synapses. Central synapses have very limited electron-dense material, thought to form grids where SVs dock (Pfenninger et al, 1972) whereas

sensory neurons are larger and more specialised utilising a protein unique to these synapses, ctBP2/RIBEYE, to create a ribbon (Maxeiner et al, 2016). As dense projections are primarily thought to exist to support SV replacement at plasma membrane release sites following fusion events it makes sense that these structures would be larger at the highly active sensory synapses. Whether a similar dichotomy is seen between neuromuscular junctions and sensory neurons in *C. elegans* is currently unknown, however enlarged dense projections have previously been found in interneurons (Kittelmann et al, 2013).

What fuels the difference in morphology is unclear. Is there differential expression of specific AZ proteins, are there proteins specific to some synapses but not others like ctBP2/RIBEYE or do some AZ proteins perform different roles at different synapses? CLA-1 has previously been shown to be differentially involved in the recruitment of SVs at cholinergic and GABAergic neuromuscular junctions compared to PVD sensory neurons and the AIY interneuron under fluorescence confocal microscopy (Xuan et al, 2017). My locomotion analysis findings also hint at behaviours controlled by interneurons which utilise dopaminergic and serotonergic neurotransmission being more strongly affected by the loss of specific AZ scaffold proteins like SYD-2, CLA-1 and HLB-1 than the basal locomotion initiated by cholinergic neuromuscular junctions.

If we are to understand the differences in AZ scaffold composition, we will need to refine analyses to compare different neuronal classes (sensory, interneuron, motor neurons), neurons utilising different neurotransmitters (cholinergic, dopaminergic, serotonergic, GABAergic, glutamatergic) and even individual neurons.

An ideal, if ambitious, scenario would be to generate maps of the expression of each AZ scaffold protein across different neurons as well as their subcellular localisation in

relation to each other. Cell specific knockouts or knockdowns of these proteins to explore the ultrastructural consequences with EM and the functional implications with locomotion and calcium imaging assays would also be incredibly informative. The advantage of pursuing such an approach in *C. elegans* is its stereotypical nervous system structure and connectome meaning that individual neurons are traceable. As we also have a strong understanding of the differences in cell specific markers across neurons (the “NeuroPAL” strain which resolves each *C. elegans* hermaphrodite neuron with a specific colour marker is testament to this (Yemini et al, 2021)) our ability target specific neurons with genetic constructs or conditional knockouts is incredibly robust especially with the advent of genetic techniques such as split-cGAL which will allow us to distinguish between neurons even when they share expression of a gene (Wang et al, 2018). These approaches could allow us to have an unprecedented level of understanding of the flexibility of the presynaptic AZ scaffold and begin to understand how its molecular composition and morphology ties to synaptic function.

6 Methods

6.1 Strains and reagents

Table 6.1. *C. elegans* strains used throughout the thesis. Strains not generated in house were obtained from the Caenorhabditis Genetics Centre (CGC) (<https://cgc.umn.edu/>).

Strain name	Allele	Origin
N2(Bristol)	wild-type	CGC
RB1777	<i>cla-1(ok2285)IV</i>	CGC
RB878	<i>h1b-1(ok725)X</i>	CGC
ZM607	<i>syd-2(ok217)X</i>	CGC
MAK2	<i>cla-1(ok2285)IV; syd-2(ok217)X</i>	In house
MAK4/MAK8	<i>h1b-1(ok725) syd-2(ok217)X</i>	In house
MAK6/MAK7	<i>cla-1(ok2285)IV; h1b-1(ok725) syd-2(ok217)X</i>	In house
MAK25	<i>cla-1(ok2285)IV</i> (x3 outcrossed with N2)	In house
MAK20	<i>h1b-1(ok725)X</i> (x3 outcrossed with N2)	In house

MAK32	<i>syd-2(ok217)X</i> (x3 outcrossed with N2)	In house
MAK37	<i>cla-1(ok2285)IV; hlb-1(ok725)X</i> (x3 outcrossed with N2)	In house
MAK29	<i>cla-1(ok2285)IV; syd-2(ok217)X</i> (x3 outcrossed with N2)	In house
MAK21	<i>hlb-1(ok725) syd-2(ok217)X</i> (x3 outcrossed with N2)	In house
MAK24	<i>cla-1(ok2285)IV; hlb-1(ok725) syd-2(ok217)X</i> (x3 outcrossed with N2)	In house
KP5445	nuls165 [<i>myo-2::gfp; punc-129::unc-10-gfp</i>]II	CGC
MAK19	nuls165 [<i>myo-2::gfp; punc-129::unc-10-gfp</i>]II (x3 outcrossed with N2)	In house
MAK35	nuls165 [<i>myo-2::gfp; punc-129::unc-10-gfp</i>]II <i>cla-1(ok2285)IV</i> (x3 outcrossed with N2)	In house
MAK26	nuls165 [<i>myo-2::gfp; punc-129::unc-10-gfp</i>]II <i>hlb-1(ok725)X</i> (x3 outcrossed with N2)	In house
MAK34	nuls165 [<i>myo-2::gfp; punc-129::unc-10-gfp</i>]II <i>syd-2(ok217)X</i> (x3 outcrossed with N2)	In house

MAK38	nuls165 [<i>myo-2::gfp; punc-129::unc-10-gfp</i>] <i>cla-1(ok2285)IV; hlb-1(ok725)X</i> (x3 outcrossed with N2)	In house
MAK23	nuls165 [<i>myo-2::gfp; punc-129::unc-10-gfp</i>] <i>cla-1(ok2285)IV; syd-2(ok217)X</i> (x3 outcrossed with N2)	In house
MAK28	nuls165 [<i>myo-2::gfp; punc-129::unc-10-gfp</i>] <i>hlb-1(ok725) syd-2(ok217)X</i> (x3 outcrossed with N2)	In house
MAK36	nuls165 [<i>myo-2::gfp; punc-129::unc-10-gfp</i>] <i>cla-1(ok2285)IV; hlb-1(ok725) syd-2(ok217)</i> (x3 outcrossed with N2)	In house
KP3814	nulS152[<i>ttx-3::mRFP;punc-129::gfp-snb-1</i>]	CGC
MAK18	nulS152[<i>ttx-3::mRFP;punc-129::gfp-snb-1</i>] (x3 outcrossed with N2)	In house
MAK42	nulS152[<i>ttx-3::mRFP;punc-129::gfp-snb-1</i>] <i>cla-1(ok2285)IV</i> (x3 outcrossed with N2)	In house
MAK27	nulS152[<i>ttx-3::mRFP;punc-129::gfp-snb-1</i>] <i>hlb-1(ok725)X</i> (x3 outcrossed with N2)	In house

MAK33	nulS152[<i>ttx-3::mRFP;punc-129::gfp-snb-1</i>] <i>syd-2(ok217)X</i> (x3 outcrossed with N2)	In house
MAK43	nulS152[<i>ttx-3::mRFP;punc-129::gfp-snb-1</i>] <i>cla-1(ok2285)IV; hlb-1(ok725)X</i> (x3 outcrossed with N2)	In house
MAK39	nulS152[<i>ttx-3::mRFP;punc-129::gfp-snb-1</i>] <i>cla-1(ok2285)IV; syd-2(ok217)X</i> (x3 outcrossed with N2)	In house
MAK40	nulS152[<i>ttx-3::mRFP;punc-129::gfp-snb-1</i>] <i>hlb-1(ok725) syd-2(ok217)X</i> (x3 outcrossed with N2)	In house
MAK31	nulS152[<i>ttx-3::mRFP;punc-129::gfp-snb-1</i>] <i>cla-1(ok2285)IV; hlb-1(ok725) syd-2(ok217)X</i> (x3 outcrossed with N2)	In house

Table 6.2. Bacterial strains used throughout the thesis.

Strain name	description	Origin
OP50-1	Streptomycin resistant <i>E. coli</i> strain	CGC

Table 6.3. Primers used throughout the thesis

Primer name	Sequence	Description
LCP0087	AGCTGAGCACAAAAGGAGATGA	Forward inside primer for the <i>syd-2 (ok217)</i> deletion
LCP0088	AGCCACCTTATTTTCAGTATTTATTGCA	Reverse inside primer for the <i>syd-2 (ok217)</i> deletion
LCP0054	CGAGCATCACAAGGCATTGG	Forward outside primer for the <i>syd-2 (ok217)</i> deletion

LCP0055	CGTAGTCCAAATCTCTAACCATGCG	Reverse outside primer for the <i>syd-2</i> (<i>ok217</i>) deletion
LCP0091	ATCAGTGTTAAGCGAGCAAGTGG	Forward inside primer for the <i>h1b-1</i> (<i>ok725</i>) deletion
LCP0092	CCAGAGAGCACACAGAATGCA	Reverse inside primer for the <i>h1b-1</i> (<i>ok725</i>) deletion
LCP0052	CCTCTTCAGGCTCATTGCGTA	Forward outside primer for the <i>h1b-1</i> (<i>ok725</i>) deletion
LCP0053	GTGCATTCCCTCAGCGTGTTG	Reverse outside primer for the <i>h1b-1</i> (<i>ok725</i>) deletion
LCP0090	TGACTGAATCGGAAATTGAATTGGAAT	Forward inside primer for the <i>cla-1</i> (<i>ok2285</i>) deletion

LCP0089	CTCTGAGCTGGACGACTTCC	Reverse inside primer for the <i>cla-1</i> (<i>ok2285</i>) deletion
LCP0056	AACCTAGTTCTGGGCTGCA	Forward outside primer for the <i>cla-1</i> (<i>ok2285</i>) deletion
LCP0057	AGTTGCATACATCCTTGAGAGAGC	Reverse outside primer for the <i>cla-1</i> (<i>ok2285</i>) deletion

Table 6.4. Reagents used throughout the thesis

Method	Reagent	Supplier
<i>C. elegans</i> maintenance and genetics	Sodium Hypochlorite	Fisher
	NaOH	Sigma
	Proteinase K	Sigma

	Onetaq QUICK-LOAD	NEB
	Verifi	PCR biosystems
Confocal analysis	Agarose	VWR
	NaN ₃	Sigma
	Polybead Microspheres 0.1µm	Generon
Swimming locomotion assays	NUNC Microwell tissue culture treated 96-well plate	Thermofisher Scientific
Aldicarb Assays	Aldicarb	Sigma Aldrich

Electron microscopy sample preparation	45-degree diamond trimming knife	TAAB
	35-degree diamond cutting knife	TAAB
	812 Hard Epoxy Resin	TAAB
	Parafilm	Pechiney Plastic Packaging Company
	Tannic Acid	Sigma Aldrich
	Osmium tetroxide	TAAB
	Copper slot grids	Agar Scientific
	Formvar	TAAB
	3% Lead citrate Reynolds Solution	em-grade.com
	Uranyl acetate	TAAB

Table 6.5. Solutions used throughout the thesis.

Solution	Reagents	Supplier
1M KPO₄ buffer	108.3g/l KH ₂ PO ₄	VWR
	35.6g/l K ₂ HPO ₄	VWR
	H ₂ O to volume	
NGM (nutrient growth medium)	3g/l NaCl	VWR
	17g/l Bacteriological Agar	VWR
	2.5g/l Peptone	VWR
	1ml/l 1M KPO ₄ buffer	See above
	1ml/l 1M CaCl	VWR
	1ml/l 1M MgSO ₄	VWR
	1ml/l 5mg/ml Cholesterol	VWR
	1ml/l 10mg/ml Nystatin	Fisher

M9	3.0g KH ₂ PO ₄	VWR
	6.0g Na ₂ HPO ₄	VWR
	5.0g NaCl	VWR
	1mL 1M MgSO ₄	VWR
	H ₂ O to 1 litre	
S-Buffer	5.85g NaCl	VWR
	1.123g K ₂ HPO ₄	VWR
	5.926g KH ₂ PO ₄	VWR
	H ₂ O to 1 litre	
Freezing solution	70% (V/V) S-buffer	See above
	30% (V/V) Glycerol	VWR

10x PCR buffer	37.25g/l KCl	VWR
	1.975g MgCl ₂	VWR
	100ml/l 1M Tris	Fisher

6.2 *C. elegans* strains and maintenance

All *C. elegans* strains used throughout are detailed in Table 6.1. The N2 Bristol strain was used as the wild-type strain throughout. Strains were cultured on NGM plates containing the antifungal nystatin (12.5mg/ml) seeded with streptomycin resistant OP50 (OP50-1) using previously described standard techniques (Brenner, 1974). Strains were maintained in a 20°C incubator. Where large scale synchronisation of strains was required to gain sizeable populations of young adult worms, high confluence plates with large numbers of eggs were washed with 1.5ml of M9 and treated with 75µl 5% sodium hypochlorite and 50µL of 4M NaOH. After ~15 minutes, bleached worm solutions were centrifuged to obtain a pellet of eggs which was washed with M9 and placed on seeded NGM media plates. After 68-76 hours young adult worms were used for required assays.

Single mutant strains were outcrossed against the wild-type N2 strains. To obtain double and triple mutant strains single functionally null mutants for *syd-2* (allele *ok217*), *h1b-1* (allele *ok725*), and *cla-1* (allele *ok2285*) were mated giving all possible

combinations of the mutant alleles (Table 6.1). The presence of mutations was confirmed by PCR using outside primers spanning the entire deletion and inside primers situated within the deletion (Table 6.3).

Strains carrying a chromosomally integrated construct expressing fluorescent active zone (AZ) proteins under a cholinergic specific promoter *unc-129p* were obtained from the CGC. The fluorescence tagged AZ proteins were SNB-1 (KP3814 - nuls152 [*unc-129p::GFP::snb-1* + *ttx-3p::mRFP*] II) and UNC-10 (KP5445 - nuls165 [*unc-129p::unc-10::GFP* + *myo-2p::GFP*] II). Marker strains were triple outcrossed against the wild-type N2 strains and mated with the outcrossed *syd-2(ok217)*, *h1b-1(ok725)* and *cla-1(ok2285)* mutant strains to produce all single, double, and triple mutant combinations.

6.3 Confocal fluorescence imaging

Sample preparation

A bottle of 5% agarose (w/v) in dH₂O was placed in a beaker of water and heated in a microwave until molten. The molten agarose was mixed by pipetting. Droplets of the molten agarose solution were placed between two clean microscope slides to produce pads of uniform thickness and allowed to cool before use. 5µL of 0.1µm polybead microspheres were placed on the centre of the pad into which 30-50 synchronised young adult worms were transferred. 5µL of 50ng/µL sodium azide (NaN₃) was then placed on top of the worms to anaesthetise them, the slides were moved in a circular

motion on a flat surface to mix the solutions. After ~5 minutes a coverslip was applied to fully immobilise the worms and image them under a confocal microscope.

Confocal imaging

The posterior dorsal nerve cord around the spermatheca was imaged as a Z-stack with a 0.2 μ m interval using a Zeiss LSM800 confocal microscope. This was performed with a 63X/1.4 numerical aperture oil objective lens.

Image analysis

Analysis of confocal images was performed by running them through custom scripts in FIJI ImageJ. 16-bit maximum intensity projections of the imaged dorsal nerve cords were first generated across a 72.44 μ m imaging window.

Puncta counts were performed by counting the “point maxima”. Parameter stringency for “point maxima” identification was decided through comparison to manual puncta counting on an initial subset of wild-type and mutant nerve cords.

Dorsal nerve cord fluorescence was specifically targeted by thresholding a duplicate of the original image to create a mask and then applying this back to the original. The threshold for the mask was determined by thresholding a subset of wild-type and mutant nerve cords and examining how well this adhered to the visible fluorescent signal. Total fluorescence within the dorsal nerve cords were determined based on the fluorescent signal covered by these masks.

See statistical analysis for significance testing and plotting details.

6.4 *C. elegans* crawling motion tracking and analysis in Tierpsy Tracker (performed by collaborator Tom O'Brien)

Motion tracking was performed as detailed previously in Barlow et al, 2022.

Young adult animals were obtained by bleach synchronisation with a diapause imposed at L1. Square-welled 96-well plates to be used for imaging were filled with 200 μ L of low peptone (0.013% Difco Bacto) NGM agar and stored at 4°C prior to use. On the day prior to imaging the plates were placed in a drying cabinet to achieve a uniform target weight, each well of the plates was seeded with 5 μ L of 1:10 diluted OP50 and left at room temperature overnight.

Adult *C. elegans* were washed with M9 and 2-3 worms were dispensed into each well using a COPAS 500 Flow Pilot worm sorter (Union Biometrica). Plates were then left to dry for 1 hour in a 20°C incubator. Once ready for use the plates were taken to the multi-camera tracker for imaging. The tracking experiment was separated into three stages: first, a 5 minute prestimulus recording; second, a six minute stimulus recording with 10 second bluelight pulses at 60, 160 and 260 seconds; finally, a 5 minute post-stimulus recording was also taken (Figure 6.1).

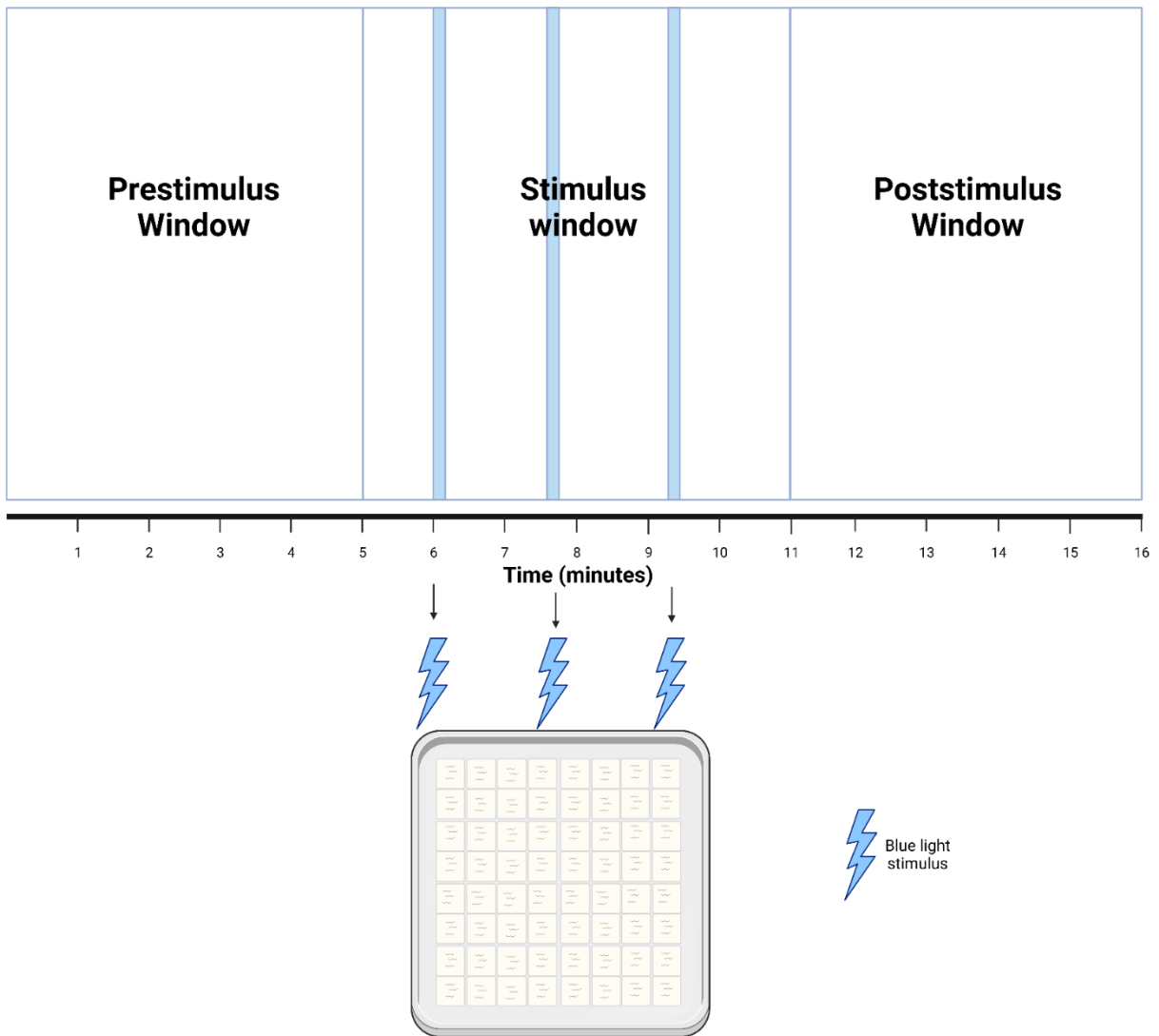


Figure 6.1. Schematic diagram of the experimental design for the crawling assays. Blue lines indicate the time points at which the plates containing crawling worms were exposed to blue light.

Created with Biorender.com

Recordings of the worms were processed using Tierpsy tracker to parameterise behavioural features. This included separation of prestimulus, blue light stimulated and post-stimulus behaviours; examination of features within different motion modes (forwards, backwards and paused); and examination of each worm's behaviour at different percentiles (10%, 50% and 100%). Sample size was defined by each well used in analysis rather than specific worms.

See statistical analysis for details of significance testing and plotting details.

6.5 Swimming assays and Tierpsy Tracker software

Synchronised young adult worms for each strain were first placed on to unseeded NGM media plates and allowed to crawl for 2 minutes to remove excess OP50. Individual worms were then selected and placed into a single well of a 96 well plate containing 50 μ L of M9 buffer. Following a 2-minute acclimation period worms were recorded for 30 seconds using a Zeiss Axiozoom V16 stereoscope at a frame rate of 30fps and a resolution of 1376x1104 pixels.

For analysis, swimming videos were processed through Tierpsy tracker software (v1.4.0, <https://github.com/ver228/tierpsy-tracker/releases>) which allows skeletonisation of the videoed worms. Output "features" files were processed using MatLab (Version R2022a; <https://uk.mathworks.com/>) through a script previously detailed by Deng et al, 2021 (<https://www.eneuro.org/content/eneuro/8/2/ENEURO.0241-20.2020/DC2/embed/inline-supplementary-material-2.zip?download=true>). Extracted

data detailing mean midbody curvature was used to count individual midbody bends. More detailed analysis of the dynamics of body bends including maximum midbody curvature and the time between -maximum body bends was performed by examining the mean midbody curvature for each worm and analysing this alongside its associated timestamp.

Co-efficient of variation to assess the variance within body bend dynamics was performed using the following formula:

$$CV = \frac{s}{\bar{x}} \times 100\%$$

CV = coefficient of variation s = standard deviation \bar{x} = mean

See statistical analysis for details of significance testing and plotting details.

6.6 Aldicarb assays

NGM plates containing 0.5mM aldicarb, and no nystatin, were poured the day prior to the first assay and allowed to set overnight at room temperature. Plates not used for the first day were stored at 4°C for use within one week and were warmed to room temperature overnight before use. Prior to use 20µL of OP50 was placed on each plate and allowed to dry for 30 minutes. ~20 worms of each strain were placed onto each aldicarb plate in such a way that the experimenter was blinded to the identity of

each strain. Each worm was examined for paralysis every 15 minutes for the first 4 hours of the assays and then at 270 and 300 minutes. Paralysis was defined by a lack of movement following 3 head and tail touches with a platinum worm pick and then a subsequent harsh touch to the head.

Significance between strains in aldicarb assays were determined using pairwise Log-Rank Mantel-Cox test comparisons on individual curves derived from survival plots. Significance was defined by an alpha value of $p < 0.05$.

6.7 HPF and freeze substitution

An aluminium planchette with a diameter of 2mm and a depth of 100 μ m was filled with a combination of water and a thick *E. coli* suspension containing 20-30 young adult *C. elegans* (Figure 5.1). The specimen holder was sealed with a second planchette and transferred to the chamber of a BAL-TEC HPM010 for cryofixation. Freeze substitution was performed with an RMC FS8-500 Freeze Substitution System. Worms were initially incubated in 1% tannic acid in acetone at -90 °C for 22h. The specimens were then washed with acetone before incubation in a cocktail of 2% Os₂O₄ during a temperature ramp from -90°C to 4° over 46 hours.

Resin infiltration was performed with increasing concentrations (30%, 50%, 70%, 100%) of 812 hard epoxy resin for several hours at each step and included at least one overnight incubation at 100%. Worms were then embedded in Epon between two Teflon coated glass slides using parafilm strips as a spacer between the slides and allowed to polymerise at 70°C for 24 hours.

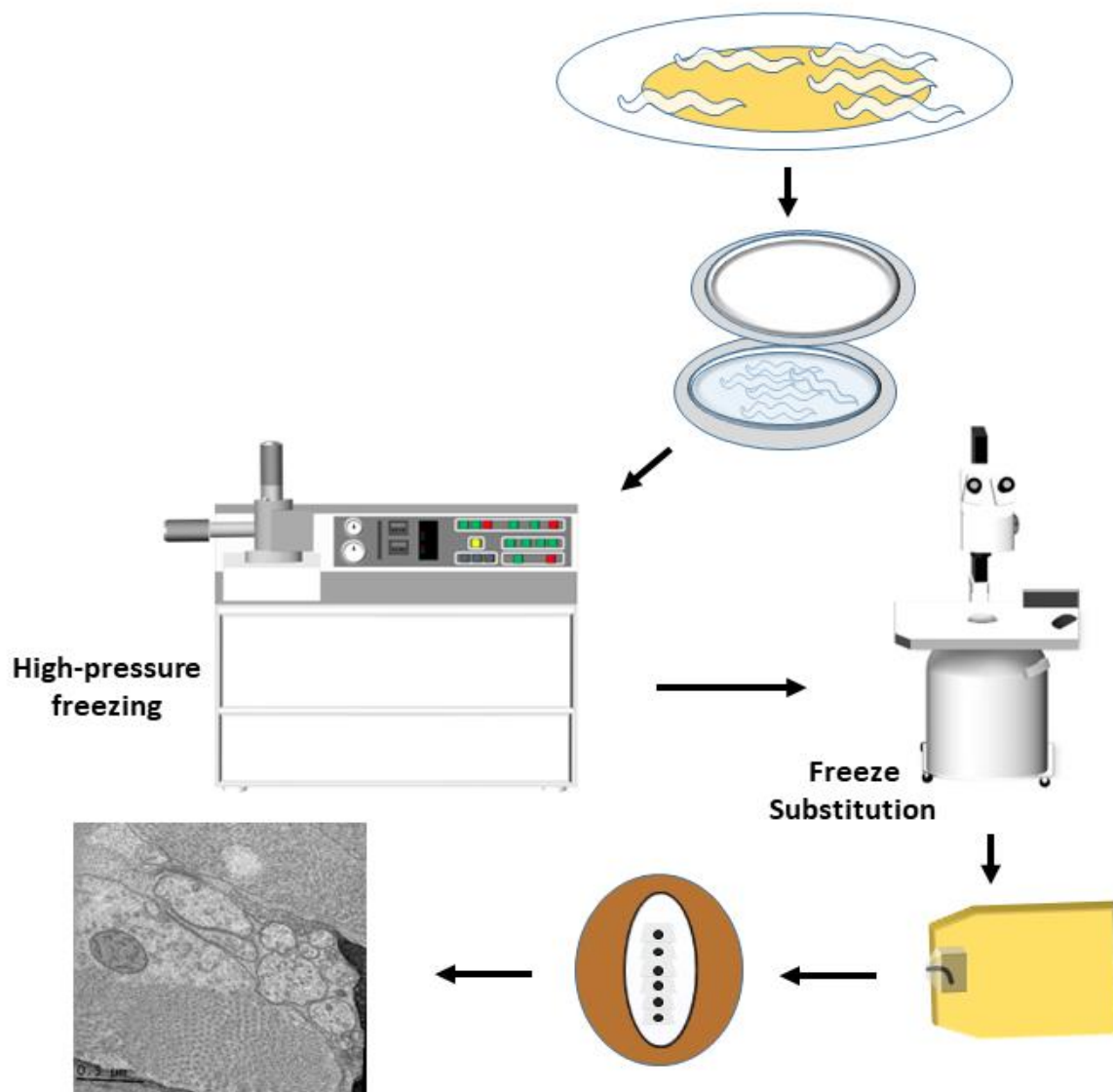


Figure 6.2. Pipeline for electron microscopy from high-pressure freezing of specimens to generation of electron micrographs. Multiple young adult *C. elegans* were transferred with OP50 *E.coli* to a planchette containing water and sealed before undergoing high-pressure freezing. Frozen samples were transferred to a freeze substitution unit to exchange vitreous ice for fixative. Specimens were embedded in resin and underwent ultramicrotomy to generate ultrathin transverse sections of worms which were collected on formvar-coated copper slot grids for imaging using transmission electron microscopy.

6.8 Production of Formvar-coated grids

A 1% Formvar solution was made by dissolving Formvar in water-free chloroform. Clean glass slides were descended into a measuring cylinder containing the 1% formvar solution and then slowly removed to leave a thin, uniform layer of formvar on the slide. The slides were then left to dry. The formvar was detached from the slide by cutting the formvar-coated edges of the slide with a razor blade and then gradually lowering the slide into a 2-litre dish filled with water. Slotted grids (2mmx1mm copper slot grids) were placed on to the floating layer of Formvar (dull side contacting the Formvar). The coated grids were then retrieved using a strip of parafilm.

6.9 Ultramicrotomy and transmission electron microscopy

50 nm ultrathin transverse sections of *C. elegans* for transmission electron microscopy were cut with an RMC Boeckeler Powertome Ultramicrotome. Consecutive sections, forming ribbons, were transferred onto Formvar-coated slot grids (Figure 6.2). Before imaging sections were post-stained, first by placing the grids on to droplets of 5%(w/v) UA with 1% acetic acid in water for 1 hour. The sections were then washed with distilled water and transferred to droplets of 3% lead citrate for 5 minutes in a CO₂ depleted chamber (achieved by surrounding NaOH pellets). Following a further wash in distilled water grids were transferred back to UA droplets for a further 2-minute incubation, to prevent potential lead citrate precipitation, before a final wash in distilled water. Excess water was removed with filter paper.

Micrographs were taken at a JEOL JEM-1400Flash with a GATAN OneView 4K camera with an accelerating voltage of 120kV. Images of nerve cord synapses were taken at 25000X magnification. Cholinergic neurons were distinguished from GABAergic neurons based on their postsynaptic partners (Chapter 4 - Figure 4.1).

6.10 Serial section reconstruction

Electron micrographs were imported into FIJI ImageJ, converted to a stack and then transferred into the trakEM2 module. Sections within each stack were aligned using a least squares alignment. Neurons and dense projections were traced as area lists, whereas synaptic vesicles (SVs) were specified with the circle tool. Reconstructions were rendered in TrakEM2 with a stringency of 5 and then exported to Blender (<http://www.blender.org>) to generate the figures used throughout the thesis.

6.11 Vesicle distribution analysis

Vesicle distribution analysis was performed using a FIJI ImageJ macro developed by Watanabe et al (Watanabe, 2020). Aligned consecutive sections containing a dense projection, as well as one flanking section either side with no dense projection were analysed by an experimenter blinded to the genotype of the profiles. Within each synaptic profile the plasma membrane, dense projection, SVs, dense core vesicles, mitochondria and endosomes were traced, and their positions recorded as region of interest (ROI) data. The ROI data also provided the internal area of the dense

projection and plasma membrane in each section. SVs and dense core vesicles in direct contact with the plasma membrane were marked as docked.

Distances between the dense projection and synaptic and dense core vesicles were calculated by processing the ROI data obtained from FIJI ImageJ through Matlab scripts written by the Watanabe and Jorgenson Labs (Watanabe, 2020). Distance to the dense projection was calculated to the shortest distance between the SV membrane and any point at the edge of the dense projection, for sections without a dense projection the closest point in 3D space in the other sections was used.

See statistical analysis for details of significance testing and plotting details.

6.12 Statistical analysis

Data in figures are primarily displayed as means +/- SEM. Statistical analysis was conducted using GraphPad Prism V5.01 software (GraphPad, Ca, USA). All data, where possible, were assessed for normality via D'agostino-Pearson test for normality. Grouped data in which not all groups conformed to a normal distribution were analysed using a Kruskal Wallis test with post-hoc Dunn's tests for pairwise analysis. Where all groups were normally distributed ANOVA was used for analysis with post-hoc Bonferroni's multiple comparisons test to determine pairwise significance. The alpha value ($P < 0.05$) was adjusted using Bonferroni correction based on the number of pairwise comparisons.

All data was plotted using GraphPad Prism V5.01 software.

Post-hoc power analyses for all experiments except aldicarb studies were performed pairwise adjusting for unequal sample sizes and the number of pairwise comparisons according to Rosner, 2010 (Rosner B. 2010. Fundamentals of Biostatistics. 7th Ed. Brooks/Cole. Page 303 and 304) using the following formula:

$$1 - \beta = \Phi \left(\frac{|\mu_A - \mu_B|}{\sqrt{\sigma_A^2 / n_A + \sigma_B^2 / n_B}} - Z_{1-\alpha/2\tau} \right)$$

A & B indicate the groups (experimental conditions) being compared

μ = mean σ = standard deviation n=group size

1- β =Power α =alpha value τ =number of pairwise comparisons

Φ =standard normal distribution function

Effect size was calculated as Cohen's d using the data from each condition in a pairwise comparison. The formula used was as follows:

$$d = \frac{|\mu_A - \mu_B|}{S_{pooled}}$$

where

$$S_{pooled} = \sqrt{\frac{(n_A - 1)\sigma_A^2 + (n_B - 1)\sigma_B^2}{n_A + n_B - 2}}$$

A & B indicate the groups (experimental conditions) being compared

μ = mean σ = standard deviation n=group size

For aldicarb assays power was calculated for a two sample logrank test using an external calculator using a formula from Schoenfeld, 1981 (Schoenfeld, D. 1981. The asymptotic properties of nonparametric tests for comparing survival distributions. *Biometrika*. 68(1), Page 316-319) and Schoenfeld, 1983 (Schoenfeld, D. A. 1983. Sample-size formula for the proportional-hazards regression model. *Biometrics*. Page 499-503).

The calculator used is available via:

<https://homepage.univie.ac.at/robin.ristl/samplesize.php?test=logrank>

7 References

Ackermann F, Waites CL, Garner CC. Presynaptic active zones in invertebrates and vertebrates. *EMBO Rep.* 2015;16(8):923-38. doi:10.15252/embr.201540434

Ackley BD, Harrington RJ, Hudson ML, et al. The two isoforms of the *Caenorhabditis elegans* leukocyte-common antigen related receptor tyrosine phosphatase PTP-3 function independently in axon guidance and synapse formation. *J Neurosci.* 2005;25(33):7517-7528. doi:10.1523/JNEUROSCI.2010-05.2005

Adame-Arana O, Weber CA, Zaburdaev V, et al. Liquid Phase Separation Controlled by pH. *Biophys J.* 2020;119(8):1590-1605. doi:10.1016/j.bpj.2020.07.044.

Aghajanian GK, Bloom FE. The formation of synaptic junctions in developing rat brain: a quantitative electron microscopic study. *Brain Res.* 1967;6(4):716-27. doi:10.1016/0006-8993(67)90128-x.

André AAM, Yewdall NA, Spruijt E. Crowding-induced phase separation and gelling by co-condensation of PEG in NPM1-rRNA condensates. *Biophys J.* 2023;122(2):397-407. doi:10.1016/j.bpj.2022.12.001.

Arendt D. Elementary nervous systems. *Philos Trans R Soc Lond B Biol Sci.* 2021;376(1821):20200347. doi:10.1098/rstb.2020.0347

Artan M, Barratt S, Flynn SM, et al. Interactome analysis of *Caenorhabditis elegans* synapses by TurboID-based proximity labeling. *J Biol Chem.* 2021;297(3):101094. doi:10.1016/j.jbc.2021.101094

Astigarraga S, Hofmeyer K, Farajian R, et al. Three *Drosophila* liprins interact to control synapse formation. *J Neurosci*. 2010;30(46):15358-15368. doi:10.1523/JNEUROSCI.1862-10.2010

Ataman B, Ashley J, Gorczyca D, et al. Nuclear trafficking of *Drosophila* Frizzled-2 during synapse development requires the PDZ protein dGRIP. *Proc Natl Acad Sci U S A*. 2006;103(20):7841-6. doi:10.1073/pnas.0600387103.

Augustin I, Rosenmund C, Südhof TC, et al. Munc13-1 is essential for fusion competence of glutamatergic synaptic vesicles. *Nature*. 1999;400(6743):457-61. doi:10.1038/22768.

Bargmann CI, Hartweg E, Horvitz HR. Odorant-selective genes and neurons mediate olfaction in *C. elegans*. *Cell*. 1993;74(3):515-27. doi:10.1016/0092-8674(93)80053-h.

Barlow IL, Feriani L, Minga E, et al. Megapixel camera arrays enable high-resolution animal tracking in multiwell plates. *Commun Biol*. 2022;5(1):253. doi:10.1038/s42003-022-03206-1.

Barmaver S, Wagner O. A Sideroflexin/Connexin adaptor ties kinesin-3 to mitochondria in neurons. *Research Square*. 2023. doi:10.21203/rs.3.rs-2953132/v1]

Barrett A, Varol E, Weinreb A, et al. Integrating bulk and single cell RNA-seq refines transcriptomic profiles of specific *C. elegans* neurons. *bioRxiv* 2022:487209; doi:10.1101/2022.04.05.487209

Becker L, Schnee ME, Niwa M, et al. The presynaptic ribbon maintains vesicle populations at the hair cell afferent fiber synapse. *Elife*. 2018;7:e30241. doi:10.7554/eLife.30241.

Berger C, Premaraj N, Ravelli RBG, et al. Cryo-electron tomography on focused ion beam lamellae transforms structural cell biology. *Nat Methods*. 2023;20(4):499-511. doi:10.1038/s41592-023-01783-5.

Ben Arous J, Laffont S, Chatenay D. Molecular and sensory basis of a food related two-state behavior in *C. elegans*. *PLoS One*. 2009;4(10):e7584. doi:10.1371/journal.pone.0007584.

Betz A, Thakur P, Junge HJ, et al. Functional interaction of the active zone proteins Munc13-1 and RIM1 in synaptic vesicle priming. *Neuron*. 2001;30(1):183-196. doi:10.1016/s0896-6273(01)00272-0

Bosch JA, Chen CL, Perrimon N. Proximity-dependent labeling methods for proteomic profiling in living cells: An update. *Wiley Interdiscip Rev Dev Biol*. 2021;10(1):e392. doi:10.1002/wdev.392.

Boyle JH, Berri S, Cohen N. Gait Modulation in *C. elegans*: An Integrated Neuromechanical Model. *Front Comput Neurosci*. 2012;6:10. doi:10.3389/fncom.2012.00010.

Bozorgmehr T, Ardiel EL, McEwan AH, et al. Mechanisms of plasticity in a *Caenorhabditis elegans* mechanosensory circuit. *Front Physiol*. 2013;4:88. doi:10.3389/fphys.2013.00088.

Braungart E, Gerlach M, Riederer P, et al. *Caenorhabditis elegans* MPP+ model of Parkinson's disease for high-throughput drug screenings. *Neurodegener Dis*. 2004;1(4-5):175-83. doi:10.1159/000080983.

Brenner S. The genetics of *Caenorhabditis elegans*. *Genetics*. 1974;77(1):71-94.
doi:10.1093/genetics/77.1.71

Bruckner JJ, Gratz SJ, Slind JK, et al. Fife, a *Drosophila* Piccolo-RIM homolog, promotes active zone organization and neurotransmitter release. *J Neurosci*. 2012;32(48):17048-17058. doi:10.1523/JNEUROSCI.3267-12.2012

Bruckner JJ, Zhan H, Gratz SJ, et al. Fife organizes synaptic vesicles and calcium channels for high-probability neurotransmitter release. *J Cell Biol*. 2017;216(1):231-246. doi:10.1083/jcb.201601098

Butler VJ, Branicky R, Yemini E, et al. A consistent muscle activation strategy underlies crawling and swimming in *Caenorhabditis elegans*. *J R Soc Interface*. 2015;12(102):20140963. doi:10.1098/rsif.2014.0963.

C. elegans Sequencing Consortium. Genome sequence of the nematode *C. elegans*: a platform for investigating biology. *Science*. 1998;282(5396):2012-8. doi:10.1126/science.282.5396.2012.

Calhoun AJ, Chalasani SH, Sharpee TO. Maximally informative foraging by *Caenorhabditis elegans*. *Elife*. 2014;3:e04220. doi:10.7554/eLife.04220.

Cases-Langhoff C, Voss B, Garner AM, et al. Piccolo, a novel 420 kDa protein associated with the presynaptic cytomatrix. *Eur J Cell Biol*. 1996;69(3):214-223.

Catterall WA, Few AP. Calcium channel regulation and presynaptic plasticity. *Neuron*. 2008;59(6):882-901. doi:10.1016/j.neuron.2008.09.005

Chanaday NL, Cousin MA, Milosevic I, et al. The Synaptic Vesicle Cycle Revisited: New Insights into the Modes and Mechanisms. *J Neurosci*. 2019;39(42):8209-8216. doi:10.1523/JNEUROSCI.1158-19.2019

Chang AJ, Chronis N, Karow DS, et al. A distributed chemosensory circuit for oxygen preference in *C. elegans*. *PLoS Biol*. 2006;4(9):e274. doi:10.1371/journal.pbio.0040274.

Chen KS, Menezes K, Rodgers JB, et al. Small molecule inhibitors of α -synuclein oligomers identified by targeting early dopamine-mediated motor impairment in *C. elegans*. *Mol Neurodegener*. 2021;16(1):77. doi:10.1186/s13024-021-00497-6.

Chia PH, Patel MR, Wagner OI, et al. Intramolecular regulation of presynaptic scaffold protein SYD-2/liprin- α . *Mol Cell Neurosci*. 2013;56:76-84. doi:10.1016/j.mcn.2013.03.004.

Clayton EL, Cousin MA. The molecular physiology of activity-dependent bulk endocytosis of synaptic vesicles. *J Neurochem*. 2009;111(4):901-14. doi:10.1111/j.1471-4159.2009.06384.x.

Cook SJ, Jarrell TA, Brittin CA, et al. Whole-animal connectomes of both *Caenorhabditis elegans* sexes. *Nature*. 2019;571(7763):63-71. doi:10.1038/s41586-019-1352-7

Courtney NA, Bao H, Briguglio JS, et al. Synaptotagmin 1 clamps synaptic vesicle fusion in mammalian neurons independent of complexin. *Nat Commun*. 2019;10(1):4076. doi:10.1038/s41467-019-12015-w

Crump JG, Zhen M, Jin Y, et al. The SAD-1 kinase regulates presynaptic vesicle clustering and axon termination. *Neuron*. 2001;29(1):115-29. doi:10.1016/s0896-6273(01)00184-2.

Cuentas-Condori A, Miller 3rd DM. Synaptic remodeling, lessons from *C. elegans*. *J Neurogenet*. 2020;34(3-4):307-322. doi:10.1080/01677063.2020.1802725.

Dai Y, Taru H, Deken SL, et al. SYD-2 Liprin-alpha organizes presynaptic active zone formation through ELKS. *Nat Neurosci*. 2006;9(12):1479-87. doi:10.1038/nn1808.

Deken SL, Vincent R, Hadwiger G, et al. Redundant localization mechanisms of RIM and ELKS in *Caenorhabditis elegans*. *J Neurosci*. 2005;25(25):5975-5983. doi:10.1523/JNEUROSCI.0804-05.2005

Deng L, Denham JE, Arya C, Yuval O, Cohen N, Haspel G. Inhibition Underlies Fast Undulatory Locomotion in *Caenorhabditis elegans*. *eNeuro*. 2021;8(2):ENEURO.0241-20.2020. doi:10.1523/ENEURO.0241-20.2020.

Dick O, tom Dieck S, Altrock WD, et al. The presynaptic active zone protein bassoon is essential for photoreceptor ribbon synapse formation in the retina. *Neuron*. 2003;37(5):775-786. doi:10.1016/s0896-6273(03)00086-2

Dolphin AC. Functions of Presynaptic Voltage-gated Calcium Channels. *Function (Oxf)*. 2021;2(1):zqaa027. doi:10.1093/function/zqaa027.

Donnelly JL, Clark CM, Leifer AM, et al. Monoaminergic orchestration of motor programs in a complex *C. elegans* behavior. *PLoS Biol*. 2013;11(4):e1001529. doi:10.1371/journal.pbio.1001529.

Dresbach T, Torres V, Wittenmayer N, et al. Assembly of active zone precursor vesicles: obligatory trafficking of presynaptic cytomatrix proteins Bassoon and Piccolo via a trans-Golgi compartment. *J Biol Chem.* 2006;281(9):6038-47. doi:10.1074/jbc.M508784200

Edwards RH. The neurotransmitter cycle and quantal size. *Neuron.* 2007;55(6):835-858. doi:10.1016/j.neuron.2007.09.001

Edwards SL, Morrison LM, Manning L, et al. Sentryn Acts with a Subset of Active Zone Proteins To Optimize the Localization of Synaptic Vesicles in *Caenorhabditis elegans*. *Genetics.* 2018;210(3):947-968. doi:10.1534/genetics.118.301466

Edwards SL, Yorks RM, Morrison LM, et al. Synapse-Assembly Proteins Maintain Synaptic Vesicle Cluster Stability and Regulate Synaptic Vesicle Transport in *Caenorhabditis elegans*. *Genetics.* 2015;201(1):91-116. doi:10.1534/genetics.115.177337

Ehmann N, Sauer M, Kittel RJ. Super-resolution microscopy of the synaptic active zone. *Front Cell Neurosci.* 2015;9:7. doi:10.3389/fncel.2015.00007.

Ehmann N, van de Linde S, Alon A, et al. Quantitative super-resolution imaging of Bruchpilot distinguishes active zone states. *Nat Commun.* 2014;5:4650. doi:10.1038/ncomms5650.

Epstein HF, Waterston RH, Brenner S. A mutant affecting the heavy chain of myosin in *Caenorhabditis elegans*. *J Mol Biol.* 1974;90(2):291-300. doi:10.1016/0022-2836(74)90374-x.

Erlendsson S, Thorsen TS, Vauquelin G, et al. Mechanisms of PDZ domain scaffold assembly illuminated by use of supported cell membrane sheets. *Elife*. 2019;8:e39180. doi:10.7554/eLife.39180.

Fang-Yen C, Wyart M, Xie J, et al. Biomechanical analysis of gait adaptation in the nematode *Caenorhabditis elegans*. *Proc Natl Acad Sci U S A*. 2010;107(47):20323-8. doi:10.1073/pnas.1003016107.

Fasshauer D, Sutton RB, Brunger AT, et al. Conserved structural features of the synaptic fusion complex: SNARE proteins reclassified as Q- and R-SNAREs. *Proc Natl Acad Sci U S A*. 1998;95(26):15781-15786. doi:10.1073/pnas.95.26.15781

Fenster SD, Chung WJ, Zhai R, et al. Piccolo, a presynaptic zinc finger protein structurally related to bassoon. *Neuron*. 2000;25(1):203-214. doi:10.1016/s0896-6273(00)80883-1

Foster M, Sherrington CS. *A textbook of physiology, part three: The central nervous system (7th ed.)*, London, MacMillan & Co Ltd; 1897.

Fouad AD, Teng S, Mark JR, et al. Distributed rhythm generators underlie *Caenorhabditis elegans* forward locomotion. *Elife*. 2018;7:e29913. doi:10.7554/eLife.29913.

Fouquet W, Oswald D, Wichmann C, et al. Maturation of active zone assembly by *Drosophila* Bruchpilot. *J Cell Biol*. 2009;186(1):129-145. doi:10.1083/jcb.200812150

Gao S, Guan SA, Fouad AD, et al. Excitatory motor neurons are local oscillators for backward locomotion. *Elife*. 2018;7:e29915. doi:10.7554/eLife.29915.

Gao Y, Zorman S, Gundersen G, et al. Single reconstituted neuronal SNARE complexes zipper in three distinct stages. *Science*. 2012;337(6100):1340-1343. doi:10.1126/science.1224492

Ghelani T, Escher M, Thomas U, et al. Interactive nanocluster compaction of the ELKS scaffold and Cacophony Ca²⁺ channels drives sustained active zone potentiation. *Sci Adv*. 2023;9(7):eade7804. doi:10.1126/sciadv.ade7804.

Ghosh R, Emmons SW. Episodic swimming behavior in the nematode *C. elegans*. *J Exp Biol*. 2008;211(Pt 23):3703-11. doi:10.1242/jeb.023606.

Goda Y. SNAREs and regulated vesicle exocytosis. *Proc Natl Acad Sci U S A*. 1997;94(3):769-72. doi:10.1073/pnas.94.3.769.

Goel P, Dufour Bergeron D, Böhme MA, et al. Homeostatic scaling of active zone scaffolds maintains global synaptic strength. *J Cell Biol*. 2019;218(5):1706-1724. doi:10.1083/jcb.201807165.

Göhde R, Naumann B, Laundon D, et al. Choanoflagellates and the ancestry of neurosecretory vesicles. *Philos Trans R Soc Lond B Biol Sci*. 2021;376(1821):20190759. doi:10.1098/rstb.2019.0759.

Goodman MB, Lindsay TH, Lockery SR, et al. Electrophysiological methods for *Caenorhabditis elegans* neurobiology. *Methods Cell Biol*. 2012;107:409-36. doi:10.1016/B978-0-12-394620-1.00014-X.

Goodwin PR, Juo P. The scaffolding protein SYD-2/Liprin- α regulates the mobility and polarized distribution of dense-core vesicles in *C. elegans* motor neurons. *PLoS One*. 2013;8(1):e54763. doi:10.1371/journal.pone.0054763.

Govind CK, De Rosa RA, Pearce J. Presynaptic dense bars at neuromuscular synapses of the lobster, *homarus americanus*. *Cell Tissue Res.* 1980;207(1):81-8. doi:10.1007/BF00239331.

Gracheva EO, Hadwiger G, Nonet ML, et al. Direct interactions between *C. elegans* RAB-3 and Rim provide a mechanism to target vesicles to the presynaptic density. *Neurosci Lett.* 2008;444(2):137-42. doi:10.1016/j.neulet.2008.08.026.

Gratz SJ, Goel P, Bruckner JJ, et al. Endogenous Tagging Reveals Differential Regulation of Ca²⁺ Channels at Single Active Zones during Presynaptic Homeostatic Potentiation and Depression. *J Neurosci.* 2019;39(13):2416-2429. doi:10.1523/JNEUROSCI.3068-18.2019

Grael MK, Maglione M, Reddy-Alla S, et al. RIM-binding protein 2 regulates release probability by fine-tuning calcium channel localization at murine hippocampal synapses. *Proc Natl Acad Sci U S A.* 2016;113(41):11615-11620. doi:10.1073/pnas.1605256113.

Gray GC, Martin VJ, Satterlie RA. Ultrastructure of the retinal synapses in cubozoans. *Biol Bull.* 2009;217(1):35-49. doi:10.1086/BBLv217n1p35.

Guangming G, Junhua G, Chenchen Z, et al. Neurexin and Neuroligins Maintain the Balance of Ghost and Satellite Boutons at the *Drosophila* Neuromuscular Junction. *Front Neuroanat.* 2020;14:19. doi:10.3389/fnana.2020.00019.

Guedes-Dias P, Nirschl JJ, Abreu N, et al. Kinesin-3 Responds to Local Microtubule Dynamics to Target Synaptic Cargo Delivery to the Presynapse. *Curr Biol.* 2019;29(2):268-282.e8. doi:10.1016/j.cub.2018.11.065.

Guo ZV, Hart AC, Ramanathan S. Optical interrogation of neural circuits in *Caenorhabditis elegans*. *Nat Methods*. 2009;6(12):891-6. doi:10.1038/nmeth.1397.

Hall DH, Hedgecock EM. Kinesin-related gene *unc-104* is required for axonal transport of synaptic vesicles in *C. elegans*. *Cell*. 1991;65(5):837-847. doi:10.1016/0092-8674(91)90391-b

Hall DH, Rice WJ. Electron Tomography Methods for *C. elegans*. *Methods Mol Biol*. 2015;1327:141-158. doi:10.1007/978-1-4939-2842-2_11

Hallam SJ, Goncharov A, McEwen J, et al. SYD-1, a presynaptic protein with PDZ, C2 and rhoGAP-like domains, specifies axon identity in *C. elegans*. *Nat Neurosci*. 2002;5(11):1137-46. doi:10.1038/nn959.

Hallermann S, Silver RA. Sustaining rapid vesicular release at active zones: potential roles for vesicle tethering. *Trends Neurosci*. 2013;36(3):185-194. doi:10.1016/j.tins.2012.10.001

Hammarlund M, Palfreyman MT, Watanabe S, et al. Open syntaxin docks synaptic vesicles. *PLoS Biol*. 2007;5(8):e198. doi:10.1371/journal.pbio.0050198.

Han KA, Kim YJ, Yoon TH, et al. LAR-RPTPs Directly Interact with Neurexins to Coordinate Bidirectional Assembly of Molecular Machineries. *J Neurosci*. 2020;40(44):8438-8462. doi:10.1523/JNEUROSCI.1091-20.2020.

Han S, Kollmer M, Markx D, et al. Amyloid plaque structure and cell surface interactions of β -amyloid fibrils revealed by electron tomography. *Sci Rep*. 2017;7:43577. doi:10.1038/srep43577.

Han Y, Babai N, Kaeser P, et al. RIM1 and RIM2 redundantly determine Ca²⁺ channel density and readily releasable pool size at a large hindbrain synapse. *J Neurophysiol.* 2015;113(1):255-263. doi:10.1152/jn.00488.2014

Harlow ML, Ress D, Stoschek A, et al. The architecture of active zone material at the frog's neuromuscular junction. *Nature.* 2001;409(6819):479-484. doi:10.1038/35054000

Haspel G, O'Donovan MJ. A Perimotor Framework Reveals Functional Segmentation in the Motoneuronal Network Controlling Locomotion in *Caenorhabditis elegans*. *J Neurosci.* 2011;31:14611-14623. doi:10.1523/JNEUROSCI.2186-11.2011.

Haspel G, O'Donovan MJ. A connectivity model for the locomotor network of *Caenorhabditis elegans*. *Worm.* 2012;1(2):125-128. doi:10.4161/worm.19392

Hawk JD, Calvo AC, Liu P, et al. Integration of Plasticity Mechanisms within a Single Sensory Neuron of *C. elegans* Actuates a Memory. *Neuron.* 2018;97(2):356-367.e4. doi:10.1016/j.neuron.2017.12.027.

Hiatt SM, Shyu YJ, Duren HM, et al. Bimolecular fluorescence complementation (BiFC) analysis of protein interactions in *Caenorhabditis elegans*. *Methods.* 2008;45(3):185-91. doi:10.1016/j.ymeth.2008.06.003.

Hirokawa N, Sobue K, Kanda K, et al. The cytoskeletal architecture of the presynaptic terminal and molecular structure of synapsin 1. *J Cell Biol.* 1989;108(1):111-126. doi:10.1083/jcb.108.1.111

Hobson RJ, Liu Q, Watanabe S, et al. Complexin maintains vesicles in the primed state in *C. elegans*. *Curr Biol.* 2011;21(2):106-13. doi:10.1016/j.cub.2010.12.015.

Hylton RK, Swulius MT. Challenges and triumphs in cryo-electron tomography. *iScience*. 2021;24(9):102959. doi:10.1016/j.isci.2021.102959.

Iwanir S, Brown AS, Nagy S, et al. Serotonin promotes exploitation in complex environments by accelerating decision-making. *BMC Biol*. 2016;14:9. doi:10.1186/s12915-016-0232-y.

Jánosi B, Liewald JF, Yu S, et al. RIM and RIM-binding protein localize synaptic CaV2 channels to differentially regulate transmission in neuronal circuits. *bioRxiv*. 2021;429206. doi:https://doi.org/10.1101/2021.02.01.429206

Javer A, Ripoll-Sánchez L, Brown AEX. Powerful and interpretable behavioural features for quantitative phenotyping of *Caenorhabditis elegans*. *Philos Trans R Soc Lond B Biol Sci*. 2018;373(1758):20170375. doi:10.1098/rstb.2017.0375.

Jung S, Oshima-Takago T, Chakrabarti R, et al. Rab3-interacting molecules 2 α and 2 β promote the abundance of voltage-gated CaV1.3 Ca²⁺ channels at hair cell active zones. *Proc Natl Acad Sci U S A*. 2015;112(24):E3141-9. doi:10.1073/pnas.1417207112.

Kaesler PS, Regehr WG. The readily releasable pool of synaptic vesicles. *Curr Opin Neurobiol*. 2017;43:63-70. doi:10.1016/j.conb.2016.12.012.

Kantardzhieva A, Peppi M, Lane WS, et al. Protein composition of immunoprecipitated synaptic ribbons. *J Proteome Res*. 2012;11(2):1163-74. doi:10.1021/pr2008972.

Kaplan JM. Sensory signaling in *Caenorhabditis elegans*. *Curr Opin Neurobiol*. 1996;6(4):494-9. doi:10.1016/s0959-4388(96)80055-9.

Kaufmann N, DeProto J, Ranjan R, et al. Drosophila liprin-alpha and the receptor phosphatase Dlar control synapse morphogenesis. *Neuron*. 2002;34(1):27-38. doi:10.1016/s0896-6273(02)00643-8.

Kavalali ET, Jorgensen EM. Visualizing presynaptic function. *Nat Neurosci*. 2014;17(1):10-6. doi:10.1038/nn.3578.

Kim HM, Hong Y, Chen J. A Decade of CRISPR-Cas Genome Editing in *C. elegans*. *IntJ Mol Sci*. 2022;23(24):15863. doi:10.3390/ijms232415863

Kim, J.S., Lilley, B.N., Zhang, C, et al. A chemical-genetic strategy reveals distinct temporal requirements for SAD-1 kinase in neuronal polarization and synapse formation. *Neural Dev*. 2008;3:23. doi:10.1186/1749-8104-3-23

Kittel RJ, Hallermann S, Thomsen S, et al. Active zone assembly and synaptic release. *Biochem Soc Trans*. 2006;34(Pt 5):939-941. doi:10.1042/BST0340939

Kittelmann M, Hegermann J, Goncharov A, et al. Liprin- α /SYD-2 determines the size of dense projections in presynaptic active zones in *C. elegans*. *J Cell Biol*. 2013;203(5):849-863. doi:10.1083/jcb.201302022

Korta J, Clark DA, Gabel CV, et al. Mechanosensation and mechanical load modulate the locomotory gait of swimming *C. elegans*. *J Exp Biol*. 2007;210(Pt 13):2383-9. doi:10.1242/jeb.004572.

Koushika SP, Richmond JE, Hadwiger G, et al. A post-docking role for active zone protein Rim. *Nat Neurosci*. 2001;4(10):997-1005. doi:10.1038/nn732

Krout M, Oh KH, Xiong A, et al. *C. elegans* Clarinet/CLA-1 recruits RIMB-1/RIM-binding protein and UNC-13 to orchestrate presynaptic neurotransmitter release. *Proc Natl Acad Sci U S A*. 2023;120(21):e2220856120. doi:10.1073/pnas.2220856120.

Kurshan PT, Merrill SA, Dong Y, et al. γ -Neurexin and Frizzled Mediate Parallel Synapse Assembly Pathways Antagonized by Receptor Endocytosis. *Neuron*.2018;100(1):150-166.e4. doi:10.1016/j.neuron.2018.09.007

Kushibiki Y, Suzuki T, Jin Y, et al. RIMB-1/RIM-Binding Protein and UNC-10/RIM Redundantly Regulate Presynaptic Localization of the Voltage-Gated Calcium Channel in *Caenorhabditis elegans*. *J Neurosci*. 2019;39(44):8617-8631. doi:10.1523/JNEUROSCI.0506-19.2019

Kusick GF, Chin M, Raychaudhuri S, et al. Synaptic vesicles transiently dock to refill release sites. *Nat Neurosci*. 2020;23(11):1329-1338. doi:10.1038/s41593-020-00716-1.

Lanzo A, Safratowich BD, Kudumala SR, et al. Silencing of *Syntaxin 1A* in the Dopaminergic Neurons Decreases the Activity of the Dopamine Transporter and Prevents Amphetamine-Induced Behaviors in *C. elegans*. *Front Physiol*. 2018;9:576. doi:10.3389/fphys.2018.00576.

Laranjeiro R, Harinath G, Burke D, et al. Single swim sessions in *C. elegans* induce key features of mammalian exercise. *BMC Biol*. 2017;15(1):30. doi:10.1186/s12915-017-0368-4.

Lautenschläger J. Protein phase separation hotspots at the presynapse. *Open Biol*. 2022;12(2):210334. doi:10.1098/rsob.210334.

Lee KS, Iwanir S, Kopito RB, et al. Serotonin-dependent kinetics of feeding bursts underlie a graded response to food availability in *C. elegans*. *Nat Commun*. 2017;8:14221. doi:10.1038/ncomms14221.

Lee, HJ., Zheng, J.J. PDZ domains and their binding partners: structure, specificity, and modification. *Cell Commun Signal*. 2010;8:8 doi:10.1186/1478-811X-8-8

Li F, Kalyana Sundaram RV, Gatta AT, et al. Vesicle capture by membrane-bound Munc13-1 requires self-assembly into discrete clusters. *FEBS Lett*. 2021;595(17):2185-2196. doi:10.1002/1873-3468.14157.

Li L, Liu H, Hall Q, et al. A Hyperactive Form of unc-13 Enhances Ca²⁺ Sensitivity and Synaptic Vesicle Release Probability in *C. elegans*. *Cell Rep*. 2019;28(11):2979-2995.e4. doi:10.1016/j.celrep.2019.08.018.

Liang M, Jin G, Xie X, et al. Oligomerized liprin- α promotes phase separation of ELKS for compartmentalization of presynaptic active zone proteins. *Cell Rep*. 2021;34(12):108901. doi:10.1016/j.celrep.2021.108901.

Lichter K, Paul MM, Pauli M, et al. Ultrastructural analysis of wild-type and RIM1 α knockout active zones in a large cortical synapse. *Cell Rep*. 2022;40(12):111382. doi:10.1016/j.celrep.2022.111382

Lipton DM, Maeder CI, Shen K. Rapid Assembly of Presynaptic Materials behind the Growth Cone in Dopaminergic Neurons Is Mediated by Precise Regulation of Axonal Transport. *Cell Rep*. 2018;24(10):2709-2722. doi:10.1016/j.celrep.2018.07.096.

Liu H, Li L, Wang W, Gong J, Yang X, Hu Z. Spontaneous Vesicle Fusion Is Differentially Regulated at Cholinergic and GABAergic Synapses. *Cell Rep.* 2018 ;22(9):2334-2345. doi:10.1016/j.celrep.2018.02.023.

Liu H, Li L, Nedelcu D, et al. Heterodimerization of UNC-13/RIM regulates synaptic vesicle release probability but not priming in *C. elegans*. *Elife.* 2019;8:e40585. doi:10.7554/eLife.40585.

Liu KS, Siebert M, Mertel S, et al. RIM-binding protein, a central part of the active zone, is essential for neurotransmitter release. *Science.* 2011 ;16;334(6062):1565-9. doi:10.1126/science.1212991.

Löhner M, Babai N, Müller T, et al. Analysis of RIM Expression and Function at Mouse Photoreceptor Ribbon Synapses. *J Neurosci.* 2017;37(33):7848-7863. doi:10.1523/JNEUROSCI.2795-16.2017.

Ma Q, Song Y, Sun W, et al. Cell-Inspired All-Aqueous Microfluidics: From Intracellular Liquid-Liquid Phase Separation toward Advanced Biomaterials. *Adv Sci (Weinh).* 2020;7(7):1903359. doi:10.1002/advs.201903359.

Maxeiner S, Luo F, Tan A, et al. How to make a synaptic ribbon: RIBEYE deletion abolishes ribbons in retinal synapses and disrupts neurotransmitter release. *EMBO J.* 2016;35(10):1098-1114. doi:10.15252/embj.201592701

McCloskey RJ, Fouad AD, Churgin MA, et al. Food responsiveness regulates episodic behavioral states in *Caenorhabditis elegans*. *J Neurophysiol.* 2017;117(5):1911-1934. doi:10.1152/jn.00555.2016.

McDonald NA, Fetter RD, Shen K. Assembly of synaptic active zones requires phase separation of scaffold molecules. *Nature*. 2020;588(7838):454-458. doi:10.1038/s41586-020-2942-0

Menon KP, Carrillo RA, Zinn K. Development and plasticity of the *Drosophila* larval neuromuscular junction. *Wiley Interdiscip Rev Dev Biol*. 2013;2(5):647-70. doi:10.1002/wdev.108.

Mori I, Ohshima Y. Neural regulation of thermotaxis in *Caenorhabditis elegans*. *Nature*. 1995;376(6538):344-8. doi:10.1038/376344a0.

Morrison LM, Edwards SL, Manning L, et al. Sentryn and SAD Kinase Link the Guided Transport and Capture of Dense Core Vesicles in *Caenorhabditis elegans*. *Genetics*. 2018;210(3):925-946. doi:10.1534/genetics.118.300847.

Moseley-Alldredge M, Sheoran S, Yoo H, et al. A role for the Erk MAPK pathway in modulating SAX-7/L1CAM-dependent locomotion in *Caenorhabditis elegans*. *Genetics*. 2022;220(2):iyab215. doi:10.1093/genetics/iyab215.

Mrestani A, Pauli M, Kollmannsberger P, et al. Active zone compaction correlates with presynaptic homeostatic potentiation. *Cell Rep*. 2021;37(1):109770. doi:10.1016/j.celrep.2021.109770.

Mukherjee K, Yang X, Gerber SH, et al. Piccolo and bassoon maintain synaptic vesicle clustering without directly participating in vesicle exocytosis. *Proc Natl Acad Sci U S A*. 2010;107(14):6504-9. doi:10.1073/pnas.1002307107.

Muniesh MS, Barmaver SN, Huang HY, et al. PTP-3 phosphatase promotes intramolecular folding of SYD-2 to inactivate kinesin-3 UNC-104 in neurons. *Mol Biol Cell*. 2020;31(26):2932-2947. doi:10.1091/mbc.E19-10-0591.

Musser JM, Schippers KJ, Nickel M, et al. Profiling cellular diversity in sponges informs animal cell type and nervous system evolution. *Science*. 2021;374(6568):717-723. doi:10.1126/science.abj2949.

Nelson JC, Colón-Ramos DA. Serotonergic neurosecretory synapse targeting is controlled by netrin-releasing guidepost neurons in *Caenorhabditis elegans*. *J Neurosci*. 2013;33(4):1366-76. doi:10.1523/JNEUROSCI.3471-12.2012.

Nguyen JP, Shipley FB, Linder AN, et al. Whole-brain calcium imaging with cellular resolution in freely behaving *Caenorhabditis elegans*. *Proc Natl Acad Sci U S A*. 2016;113(8):E1074-81. doi:10.1073/pnas.1507110112.

Niacaris T, Avery L. Serotonin regulates repolarization of the *C. elegans* pharyngeal muscle. *J Exp Biol*. 2003;206:223-31. doi:10.1242/jeb.00101.

Nomachi A, Yoshinaga M, Liu J, et al. Moesin controls clathrin-mediated S1PR1 internalization in T cells. *PLoS One*. 2013;8(12):e82590. doi:10.1371/journal.pone.0082590

Nonet ML, Saifee O, Zhao H, et al. Synaptic transmission deficits in *Caenorhabditis elegans* synaptobrevin mutants. *J Neurosci*. 1998;18(1):70-80. doi:10.1523/JNEUROSCI.18-01-00070.1998.

Oh KH, Krout MD, Richmond JE, et al. UNC-2 CaV2 Channel Localization at Presynaptic Active Zones Depends on UNC-10/RIM and SYD-2/Liprin- α in

Caenorhabditis elegans. J Neurosci. 2021;41(22):4782-4794.
doi:10.1523/JNEUROSCI.0076-21.2021.

Ohtsuka T, Takao-Rikitsu E, Inoue E, et al. Cast: a novel protein of the cytomatrix at the active zone of synapses that forms a ternary complex with RIM1 and munc13-1. J Cell Biol. 20025;158(3):577-90. doi:10.1083/jcb.200202083.

Okawa H, Yu WQ, Matti U, et al. Dynamic assembly of ribbon synapses and circuit maintenance in a vertebrate sensory system. Nat Commun. 2019;10(1):2167. doi:10.1038/s41467-019-10123-1.

Oliver D, Ramachandran S, Philbrook A, et al. Kinesin-3 mediated axonal delivery of presynaptic neurexin stabilizes dendritic spines and postsynaptic components. PLoS Genet. 2022;18(1):e1010016. doi:10.1371/journal.pgen.1010016

Oranath A, Schultheis C, Tolstenkov O, et al. Food Sensation Modulates Locomotion by Dopamine and Neuropeptide Signaling in a Distributed Neuronal Network. Neuron. 2018;100(6):1414-1428.e10. doi:10.1016/j.neuron.2018.10.024.

Owald D, Khorramshahi O, Gupta VK, et al. Cooperation of Syd-1 with Neurexin synchronizes pre- with postsynaptic assembly. Nat Neurosci. 2012;15(9):1219-26. doi:10.1038/nn.3183.

Palay SL. Synapses in the central nervous system. J Biophys Biochem Cytol. 1956;2(4 Suppl):193-202. doi:10.1083/jcb.2.4.193.

Parsons SM, Prior C, Marshall IG. Acetylcholine transport, storage, and release. IntRev Neurobiol. 1993;35:279-390. doi:10.1016/s0074-7742(08)60572-3

Patel MR, Lehrman EK, Poon VY, et al. Hierarchical assembly of presynaptic components in defined *C. elegans* synapses. *Nat Neurosci.* 2006;9(12):1488-1498. doi:10.1038/nn1806

Patel MR, Shen K. RSY-1 is a local inhibitor of presynaptic assembly in *C. elegans*. *Science.* 2009;323(5920):1500-1503. doi:10.1126/science.1169025

Pease D.C. Features of the brain stem revealed with electron and phase microscopes. *Anatomical Rec.* 1953; 115: 359

Peters A, Palay SL. The morphology of synapses. *J Neurocytol.* 1996;25(12):687-700. doi:10.1007/BF02284835

Petzoldt AG, Götz TWB, Driller JH, et al. RIM-binding protein couples synaptic vesicle recruitment to release sites. *J Cell Biol.* 2020;219(7):e201902059. doi:10.1083/jcb.201902059.

Pfenninger K, Akert K, Moor H, et al. The fine structure of freeze-fractured presynaptic membranes. *J Neurocytol.* 1972;1:129–149 (1972). doi:10.1007/BF01099180

Philbrook A, Ramachandran S, Lambert CM, et al. Neurexin directs partner-specific synaptic connectivity in *C. elegans*. *Elife.* 2018;7:e35692. doi:10.7554/eLife.35692

Piekut T, Wong YY, Walker SE, et al. Early Metazoan Origin and Multiple Losses of a Novel Clade of RIM Presynaptic Calcium Channel Scaffolding Protein Homologs. *Genome Biol Evol.* 2020;12(8):1217-1239. doi:10.1093/gbe/evaa097.

Poirier MA, Xiao W, Macosko JC, et al. The synaptic SNARE complex is a parallel four-stranded helical bundle. *Nat Struct Biol.* 1998;5(9):765-9. doi:10.1038/1799.

Rahmani A, Chew YL. Investigating the molecular mechanisms of learning and memory using *Caenorhabditis elegans*. *J Neurochem*. 2021;159(3):417-451.doi:10.1111/jnc.15510

Ramakrishnan S, Bera M, Coleman J, et al. Synergistic roles of Synaptotagmin-1 and complexin in calcium-regulated neuronal exocytosis. *Elife*. 2020;9:e54506. doi:10.7554/eLife.54506

Ranganathan R, Ross EM. PDZ domain proteins: scaffolds for signaling complexes. *Curr Biol*. 1997;7(12):R770-3. doi:10.1016/s0960-9822(06)00401-5.

Rao-Mirotznik R, Harkins AB, Buchsbaum G, et al. Mammalian rod terminal: architecture of a binary synapse. *Neuron*. 1995;14(3):561-569. doi:10.1016/0896-6273(95)90312-7

Reddy-Alla S, Böhme MA, Reynolds E, et al. Stable Positioning of Unc13 Restricts Synaptic Vesicle Fusion to Defined Release Sites to Promote Synchronous Neurotransmission. *Neuron*. 2017;95(6):1350-1364.e12.doi:10.1016/j.neuron.2017.08.016

Reiff DF, Thiel PR, and Schuster CM. Differential regulation of active zone density during long-term strengthening of *Drosophila* neuromuscular junctions. *J Neurosci*. 2002;22: 9399–9409. doi:10.1523/JNEUROSCI.22-21-09399.2002.

Ribi WA. The first optic ganglion of the bee. IV. Synaptic fine structure and connectivity patterns of receptor cell axons and first order interneurons. *Cell Tissue Res*. 1981;215(3):443-64. doi:10.1007/BF00233522.

Richmond JE, Davis WS, Jorgensen EM. UNC-13 is required for synaptic vesicle fusion in *C. elegans*. *Nat Neurosci*. 1999;2(11):959-964. doi:10.1038/14755

Richmond JE, Weimer RM, Jorgensen EM. An open form of syntaxin bypasses the requirement for UNC-13 in vesicle priming. *Nature*. 2001;412(6844):338-41. doi:10.1038/35085583.

Rizo J, Südhof TC. C2-domains, structure and function of a universal Ca²⁺-binding domain. *J Biol Chem*. 1998;273(26):15879-82. doi:10.1074/jbc.273.26.15879.

Rizzoli SO, Betz WJ. The structural organization of the readily releasable pool of synaptic vesicles. *Science*. 2004;303(5666):2037-9. doi:10.1126/science.1094682.

Rizzoli SO. Synaptic vesicle recycling: steps and principles. *EMBO J*. 2014;33(8):788-822. doi:10.1002/embj.201386357

Rosenhahn E, O'Brien TJ, Zaki MS, et al. Bi-allelic loss-of-function variants in PPFIBP1 cause a neurodevelopmental disorder with microcephaly, epilepsy, and periventricular calcifications. *Am J Hum Genet*. 2022;109(8):1421-1435. doi:10.1016/j.ajhg.2022.06.008

Rosenmund C, Stevens CF. Definition of the readily releasable pool of vesicles at hippocampal synapses. *Neuron*. 1996;16(6):1197-207. doi:10.1016/s0896-6273(00)80146-4.

Rosner B. *Fundamentals of Biostatistics*, (7th Ed.). Boston, Brooks/Cole; 2010.

Rostaing P, Weimer RM, Jorgensen EM, et al. Preservation of immunoreactivity and fine structure of adult *C. elegans* tissues using high-pressure freezing. *J Histochem Cytochem*. 2004;52(1):1-12. doi:10.1177/002215540405200101.

Ruben GC, Iqbal K, Wisniewski HM, et al. Alzheimer neurofibrillary tangles contain 2.1 nm filaments structurally identical to the microtubule-associated protein tau: a high-resolution transmission electron microscope study of tangles and senile plaque core amyloid. *Brain Res.* 1993;602(2):164-79. doi:10.1016/0006-8993(92)91092-s.

Ryan K, Lu Z, Meinertzhagen IA. The CNS connectome of a tadpole larva of *Ciona intestinalis* (L.) highlights sidedness in the brain of a chordate sibling. *Elife.* 2016;5:e16962. doi:10.7554/eLife.16962.

Saifee O, Wei L, Nonet ML. The *Caenorhabditis elegans* unc-64 locus encodes a syntaxin that interacts genetically with synaptobrevin. *Mol Biol Cell.* 1998;9(6):1235-52. doi:10.1091/mbc.9.6.1235.

Sassa T, Harada S, Ogawa H, et al. Regulation of the UNC-18-*Caenorhabditis elegans* syntaxin complex by UNC-13. *J Neurosci.* 1999;19(12):4772-7. doi:10.1523/JNEUROSCI.19-12-04772.1999.

Sassa T, Harada S, Ogawa H, et al. Regulation of the UNC-18-*Caenorhabditis elegans* syntaxin complex by UNC-13. *J Neurosci.* 1999;19(12):4772-4777. doi:10.1523/JNEUROSCI.19-12-04772.1999

Sauvola CW, Littleton JT. SNARE Regulatory Proteins in Synaptic Vesicle Fusion and Recycling. *Front Mol Neurosci.* 2021;14:733138. doi:10.3389/fnmol.2021.733138.

Sawin ER, Ranganathan R, Horvitz HR. *C. elegans* locomotory rate is modulated by the environment through a dopaminergic pathway and by experience through a serotonergic pathway. *Neuron.* 2000;26(3):619-31. doi:10.1016/s0896-6273(00)81199-x.

Schaffer M, Pfeffer S, Mahamid J, et al. A cryo-FIB lift-out technique enables molecular-resolution cryo-ET within native *Caenorhabditis elegans* tissue. *Nat Methods*. 2019;16(8):757-762. doi:10.1038/s41592-019-0497-5.

Scheer E, Bargmann CI. Sensory neurons couple arousal and foraging decisions in *C. elegans* *eLife*. 2023;12:RP88657. doi:10.7554/eLife.88657.1

Schild LC, Glauser DA. Dynamic switching between escape and avoidance regimes reduces *Caenorhabditis elegans* exposure to noxious heat. *Nat Commun*. 2013;4:2198. doi:10.1038/ncomms3198.

Schoch S, Castillo PE, Jo T, et al. RIM1alpha forms a protein scaffold for regulating neurotransmitter release at the active zone. *Nature*. 2002;415(6869):321-326. doi:10.1038/415321a

Schoenfeld D. The asymptotic properties of nonparametric tests for comparing survival distributions. *Biometrika*. 1981;68(1):316-319. doi: 10.1093/biomet/68.1.316

Schoenfeld DA. Sample-size formula for the proportional-hazards regression model. *Biometrics*. 1983;39(2):499-503. doi:10.2307/2531021

Sejnowski TJ, Yodlowski ML. A freeze-fracture study of the skate electroreceptor. *J Neurocytol*. 1982;11(6):897-912. doi:10.1007/BF01148307

Serra-Pagès C, Medley QG, Tang M, et al. Liprins, a family of LAR transmembrane protein-tyrosine phosphatase-interacting proteins. *J Biol Chem*. 1998;273(25):15611-15620. doi:10.1074/jbc.273.25.15611

Serobyany V, Kontarakis Z, El-Brolosy MA, et al. Transcriptional adaptation in *Caenorhabditis elegans*. *Elife*. 2020;9:e50014. doi:10.7554/eLife.50014.

Shapira M, Zhai RG, Dresbach T, et al. Unitary assembly of presynaptic active zones from Piccolo-Bassoon transport vesicles. *Neuron*. 2003;38(2):237-52. doi:10.1016/s0896-6273(03)00207-1.

Shen K, Fetter RD, Bargmann CI. Synaptic specificity is generated by the synaptic guidepost protein SYG-2 and its receptor, SYG-1. *Cell*. 2004;116(6):869-881. doi:10.1016/s0092-8674(04)00251-x

Shin H, Wyszynski M, Huh KH, et al. Association of the kinesin motor KIF1A with the multimodular protein liprin-alpha. *J Biol Chem*. 2003;278(13):11393-401. doi:10.1074/jbc.M211874200.

Shiple FB, Clark CM, Alkema MJ, et al. Simultaneous optogenetic manipulation and calcium imaging in freely moving *C. elegans*. *Front Neural Circuits*. 2014;8:28. doi:10.3389/fncir.2014.00028.

Siksou L, Rostaing P, Lechère JP, et al. Three-dimensional architecture of presynaptic terminal cytomatrix. *J Neurosci*. 2007;27(26):6868-77. doi:10.1523/JNEUROSCI.1773-07.2007.

Söllner T, Bennett MK, Whiteheart SW, et al. A protein assembly-disassembly pathway in vitro that may correspond to sequential steps of synaptic vesicle docking, activation, and fusion. *Cell*. 1993;75(3):409-18. doi:10.1016/0092-8674(93)90376-2.

Söllner T, Whiteheart S, Brunner M, et al. SNAP receptors implicated in vesicle targeting and fusion. *Nature*. 1993;362, 318–324 (1993). <https://doi.org/10.1038/362318a0>

Sotelo C. The History of the Synapse. *Anat Rec (Hoboken)*. 2020;303(5):1252-1279. doi:10.1002/ar.24392.

Stigloher C, Zhan H, Zhen M, et al. The presynaptic dense projection of the *Caenorhabditis elegans* cholinergic neuromuscular junction localizes synaptic vesicles at the active zone through SYD-2/liprin and UNC-10/RIM-dependent interactions. *J Neurosci*. 2011;31(12):4388-4396. doi:10.1523/JNEUROSCI.6164-10.2011

Sudhof TC. The synaptic vesicle cycle. *Annu Rev Neurosci*. 2004;27:509-547. doi:10.1146/annurev.neuro.26.041002.131412

Suo S, Ishiura S. Dopamine modulates acetylcholine release via octopamine and CREB signaling in *Caenorhabditis elegans*. *PLoS One*. 2013;8(8):e72578. doi:10.1371/journal.pone.0072578.

Szule JA, Harlow ML, Jung JH, et al. Regulation of synaptic vesicle docking by different classes of macromolecules in active zone material. *PLoS One*. 2012;7(3):e33333. doi:10.1371/journal.pone.0033333

Takamori S, Holt M, Stenius K, et al. Molecular anatomy of a trafficking organelle. *Cell*. 2006;127(4):831-46. doi:10.1016/j.cell.2006.10.030.

Takei Y, Harada A, Takeda S, et al. Synapsin I deficiency results in the structural change in the presynaptic terminals in the murine nervous system. *J Cell Biol*. 1995;131(6 Pt 2):1789-1800. doi:10.1083/jcb.131.6.1789

Taru H, Jin Y. The Liprin homology domain is essential for the homomeric interaction of SYD-2/Liprin- α protein in presynaptic assembly. *J Neurosci*. 2011;31(45):16261-8. doi:10.1523/JNEUROSCI.0002-11.2011.

Tatsumi S, Uchihara T, Aiba I, et al. Ultrastructural differences in pretangles between Alzheimer disease and corticobasal degeneration revealed by comparative light and electron microscopy. *Acta Neuropathol Commun*. 2014;2:161. doi:10.1186/s40478-014-0161-3.

Taylor SR, Santpere G, Weinreb A, et al. Molecular topography of an entire nervous system. *Cell*. 2021;184(16):4329-4347.e23. doi:10.1016/j.cell.2021.06.023.

Tolbert LP, Matsumoto SG, Hildebrand JG. Development of synapses in the antennal lobes of the moth *Manduca sexta* during metamorphosis. *J Neurosci*. 1983;3(6):1158-75. doi:10.1523/JNEUROSCI.03-06-01158.1983.

tom Dieck S, Sanmartí-Vila L, Langnaese K, et al. Bassoon, a novel zinc-finger/CAG/glutamine-repeat protein selectively localized at the active zone of presynaptic nerve terminals. *J Cell Biol*. 1998;142(2):499-509. doi:10.1083/jcb.142.2.499.

Trojanowski NF, Raizen DM, Fang-Yen C. Pharyngeal pumping in *Caenorhabditis elegans* depends on tonic and phasic signaling from the nervous system. *Sci Rep*. 2016;15;6:22940. doi:10.1038/srep22940.

Tsalik EL, Niacaris T, Wenick AS, et al. LIM homeobox gene-dependent expression of biogenic amine receptors in restricted regions of the *C. elegans* nervous system. *Dev Biol*. 2003;263(1):81-102. doi:10.1016/s0012-1606(03)00447-0.

Verasztó C, Jasek S, Gühmann M, et al. Whole-animal connectome and cell-type complement of the three-segmented *Platynereis dumerilii* larva. bioRxiv. 2020:260984; doi:<https://doi.org/10.1101/2020.08.21.260984>

Wagh DA, Rasse TM, Asan E, et al. Bruchpilot, a protein with homology to ELKS/CAST, is required for structural integrity and function of synaptic active zones in *Drosophila*. *Neuron*. 2006;49(6):833-844. doi:10.1016/j.neuron.2006.02.008

Wagner OI, Esposito A, Köhler B, et al. Synaptic scaffolding protein SYD-2 clusters and activates kinesin-3 UNC-104 in *C. elegans*. *Proc Natl Acad Sci U S A*. 2009;106(46):19605-19610. doi:10.1073/pnas.0902949106

Wang DY, Wang Y. HLB-1 functions as a new regulator for the organization and function of neuromuscular junctions in nematode *Caenorhabditis elegans*. *Neurosci Bull*. 2009;25(2):75-86. doi:10.1007/s12264-009-0119-9

Wang H, Liu J, Yuet KP, et al. Split cGAL, an intersectional strategy using a split intein for refined spatiotemporal transgene control in *Caenorhabditis elegans*. *Proc Natl Acad Sci U S A*. 2018;115(15):3900-3905. doi:10.1073/pnas.1720063115.

Wang Y, Okamoto M, Schmitz F, et al. Rim is a putative Rab3 effector in regulating synaptic-vesicle fusion. *Nature*. 1997;388(6642):593-8. doi:10.1038/41580.

Wang Y, Sugita S, Sudhof TC. The RIM/NIM family of neuronal C2 domain proteins. Interactions with Rab3 and a new class of Src homology 3 domain proteins. *J Biol Chem*. 2000;275(26):20033-44. doi:10.1074/jbc.M909008199.

Ward A, Liu J, Feng Z, Xu XZ. Light-sensitive neurons and channels mediate phototaxis in *C. elegans*. *Nat Neurosci*. 2008;11(8):916-22. doi:10.1038/nn.2155.

Watanabe S, Boucrot E. Fast and ultrafast endocytosis. *Curr Opin Cell Biol.* 2017;47:64-71. doi:10.1016/j.ceb.2017.02.013

Watanabe S, Davis MW, Kusick GF, et al. SynapseEM: Computer-Assisted Synapse Morphometry. *Front Synaptic Neurosci.* 2020;12:584549. doi:10.3389/fnsyn.2020.584549.

Watanabe S, Rost BR, Camacho-Pérez M, et al. Ultrafast endocytosis at mouse hippocampal synapses. *Nature.* 2013;504(7479):242-247. doi:10.1038/nature12809.

Watanabe S. Flash-and-Freeze: Coordinating Optogenetic Stimulation with Rapid Freezing to Visualize Membrane Dynamics at Synapses with Millisecond Resolution. *Front Synaptic Neurosci.* 2016;8:24. doi:10.3389/fnsyn.2016.00024.

Watanabe S, Boucrot E. Fast and ultrafast endocytosis. *Curr Opin Cell Biol.* 2017;47:64-71. doi:10.1016/j.ceb.2017.02.013.

Wei Z, Zheng S, Spangler SA, et al. Liprin-mediated large signaling complex organization revealed by the liprin- α /CASK and liprin- α /liprin- β complex structures. *Mol Cell.* 2011;43(4):586-598. doi:10.1016/j.molcel.2011.07.021

Weimer RM, Gracheva EO, Meyrignac O, et al. UNC-13 and UNC-10/rim localize synaptic vesicles to specific membrane domains. *JNeurosci.* 2006;26(31):8040-7. doi:10.1523/JNEUROSCI.2350-06.2006.

Weimer RM, Richmond JE, Davis WS, et al. Defects in synaptic vesicle docking in unc-18 mutants. *Nat Neurosci.* 2003;6(10):1023-30. doi:10.1038/nn1118.

White JG, Southgate E, Thomson JN, et al. The structure of the nervous system of the nematode *Caenorhabditis elegans*. *Philos Trans R Soc Lond B Biol Sci.* 1986;314(1165):1-340. doi:10.1098/rstb.1986.0056

White JG, Southgate E, Thomson JN, et al. The structure of the ventral nerve cord of *Caenorhabditis elegans*. *Philos Trans R Soc Lond B Biol Sci.* 1976;275(938):327-48. doi:10.1098/rstb.1976.0086.

Winding M, Pedigo BD, Barnes CL, et al. The connectome of an insect brain. *Science.* 2023;379(6636):eadd9330. doi:10.1126/science.add9330.

Wojcik SM, Brose N. Regulation of membrane fusion in synaptic excitation-secretion coupling: speed and accuracy matter. *Neuron.* 2007;55(1):11-24. doi:10.1016/j.neuron.2007.06.013

Wojtowicz JM, Marin L, Atwood HL. Activity-induced changes in synaptic release sites at the crayfish neuromuscular junction. *J Neurosci.* 1994;14(6):3688-703. doi:10.1523/JNEUROSCI.14-06-03688.1994.

Wu X, Cai Q, Feng Z, et al. Liquid-Liquid Phase Separation in Neuronal Development and Synaptic Signaling. *Dev Cell.* 2020;55(1):18-29. doi:10.1016/j.devcel.2020.06.012.

Wu X, Cai Q, Shen Z, et al. RIM and RIM-BP Form Presynaptic Active-Zone-like Condensates via Phase Separation. *Mol Cell.* 2019;73(5):971-984.e5. doi:10.1016/j.molcel.2018.12.007.

Wu X, Ganzella M, Zhou J, et al. Vesicle Tethering on the Surface of Phase-Separated Active Zone Condensates. *Mol Cell*. 2021;81(1):13-24.e7. doi:10.1016/j.molcel.2020.10.029

Wu X, Qiu H, Zhang M. Interactions between Membraneless Condensates and Membranous Organelles at the Presynapse: A Phase Separation View of Synaptic Vesicle Cycle. *J Mol Biol*. 2023;435(1):167629. doi:10.1016/j.jmb.2022.167629.

Wu YE, Huo L, Maeder CI, et al. The balance between capture and dissociation of presynaptic proteins controls the spatial distribution of synapses. *Neuron*. 2013;78(6):994-1011. doi:10.1016/j.neuron.2013.04.035

Wyszynski M, Kim E, Dunah AW, et al. Interaction between GRIP and liprin-alpha/SYD2 is required for AMPA receptor targeting. *Neuron*. 2002;34(1):39-52. doi:10.1016/s0896-6273(02)00640-2.

Xie X, Liang M, Yu C, et al. Liprin- α -Mediated Assemblies and Their Roles in Synapse Formation. *Front Cell Dev Biol*. 2021;9:653381. doi:10.3389/fcell.2021.653381.

Xu T, Huo J, Shao S, et al. Descending pathway facilitates undulatory wave propagation in *Caenorhabditis elegans* through gap junctions. *Proc Natl Acad Sci U S A*. 2018;115(19):E4493-E4502. doi:10.1073/pnas.1717022115.

Xu Y, Zhang L, Liu Y, et al. Dopamine receptor DOP-1 engages a sleep pathway to modulate swimming in *C. elegans*. *iScience*. 2021;24(4):102247. doi:10.1016/j.isci.2021.102247.

Xuan Z, Manning L, Nelson J, et al. Clarinet (CLA-1), a novel active zone protein required for synaptic vesicle clustering and release. *Elife*. 2017;6:e29276. doi:10.7554/eLife.29276.

Xuan Z, Yang S, Clark B, et al. The active zone protein Clarinet regulates synaptic sorting of ATG-9 and presynaptic autophagy. *PLoS Biol*. 2023;21(4):e3002030. doi:10.1371/journal.pbio.3002030

Yang J, Sui SF, Liu Z. Brain structure and structural basis of neurodegenerative diseases. *Biophys Rep*. 2022;8(3):170-181. doi:10.52601/bpr.2022.220013.

Yang X, Wang S, Sheng Y, et al. Syntaxin opening by the MUN domain underlies the function of Munc13 in synaptic-vesicle priming. *Nat Struct Mol Biol*. 2015;22(7):547-554. doi:10.1038/nsmb.3038

Yeh E, Kawano T, Weimer RM, et al. Identification of genes involved in synaptogenesis using a fluorescent active zone marker in *Caenorhabditis elegans*. *J Neurosci*. 2005;25(15):3833-41. doi:10.1523/JNEUROSCI.4978-04.2005.

Yemini E, Lin A, Nejatbakhsh A, et al. NeuroPAL: A Multicolor Atlas for Whole-Brain Neuronal Identification in *C. elegans*. *Cell*. 2021;184(1):272-288.e11. doi:10.1016/j.cell.2020.12.012.

Yim YS, Kwon Y, Nam J, et al. Slitrks control excitatory and inhibitory synapse formation with LAR receptor protein tyrosine phosphatases. *Proc Natl Acad Sci U S A*. 2013;110(10):4057-62. doi:10.1073/pnas.1209881110.

Yu CJ, Barry NC, Wassie AT, et al. Expansion microscopy of *C. elegans*. *Elife*. 2020;9:e46249. doi:10.7554/eLife.46249.

Zafra F, Piniella D. Proximity labeling methods for proteomic analysis of membrane proteins. *J Proteomics*. 2022;264:104620. doi:10.1016/j.jprot.2022.104620.

Zhai RG, Bellen HJ. The architecture of the active zone in the presynaptic nerve terminal. *Physiology (Bethesda)*. 2004;19:262-270. doi:10.1152/physiol.00014.2004

Zhang M, Augustine GJ. Synapsins and the Synaptic Vesicle Reserve Pool: Floats or Anchors?. *Cells*. 2021;10(3):658. doi:10.3390/cells10030658

Zhang M, Wang W. Organization of signaling complexes by PDZ-domain scaffold proteins. *Acc Chem Res*. 2003;36(7):530-8. doi:10.1021/ar020210b.

Zhen M, Jin Y. The liprin protein SYD-2 regulates the differentiation of presynaptic termini in *C. elegans*. *Nature*. 1999;401(6751):371-5. doi:10.1038/43886.

Zhen M, Samuel AD. *C. elegans* locomotion: small circuits, complex functions. *Curr Opin Neurobiol*. 2015;33:117-126. doi:10.1016/j.conb.2015.03.009

Zhu B, Mak JCH, Morris AP, et al. Functional analysis of epilepsy-associated variants in STXBP1/Munc18-1 using humanized *Caenorhabditis elegans*. *Epilepsia*. 2020;61(4):810-821. doi:10.1111/epi.16464.

Zhu J, McDargh ZA, Li F, et al. Synaptotagmin rings as high-sensitivity regulators of synaptic vesicle docking and fusion. *Proc Natl Acad Sci U S A*. 2022;119(38):e2208337119. doi:10.1073/pnas.2208337119.

Appendix 1

Post-hoc pairwise power calculations

Power analysis values for non-significant results shown in bold. The experiment and figure which the table refers to is shown in the top-left corner. Calculated power ($1-\beta$) is given for all pairwise comparisons performed for all experiments. Effect size (as Cohen's *d*) is also given for all pairwise comparisons except those for aldicarb assays.

1) Confocal imaging

a) UNC-10::GFP imaging data

Puncta Count (Figure 2.3B)	WT Vs <i>cla-1</i> (<i>ok2285</i>)	WT Vs <i>hlb-1</i> (<i>ok725</i>)	WT Vs <i>syd2</i> (<i>ok217</i>)	WT Vs <i>cla-1</i>; <i>hlb-1</i>	WT Vs <i>cla-1</i>; <i>syd-2</i>	WT Vs <i>hlb-1</i> <i>syd-2</i>	WT Vs <i>cla-1</i>; <i>hlb-1 syd-2</i>
Power (1-β)	0.2864402	0.059742	0.003244	0.12969	0.246723237	0.015429	0.59809411
Effect size (d)	0.6479347	0.382315	0.078767	0.485059	0.60013095	0.230701	0.87889966
	<i>cla-1 Vs cla-1</i>; <i>hlb-1</i>	<i>cla-1 Vs cla-1</i>; <i>syd-2</i>	<i>cla-1 Vs cla-1</i>; <i>hlb-1 syd-2</i>				
Power (1-β)	0.00598	0.003166	0.049298				
Effect size (d)	0.1159238	0.068224	0.353044				
	<i>hlb-1 Vs cla-1</i>; <i>hlb-1</i>	<i>hlb-1 Vs hlb-1</i>; <i>syd-2</i>	<i>hlb-1 Vs cla-1</i>; <i>hlb-1 syd-2</i>				
Power (1-β)	0.005154	0.003154	0.161634				
Effect size (d)	0.108964	0.075574	0.533041				
	<i>syd-2 Vs cla-1</i>; <i>syd-2</i>	<i>syd-2 Vs hlb-1</i>; <i>syd-2</i>	<i>syd-2 Vs cla-1</i>; <i>hlb-1 syd-2</i>				
Power (1-β)	0.376963	0.0285585	0.751885				
Effect size (d)	0.709901	0.303086	1.043811784				
	<i>cla-1</i>; <i>hlb-1</i> Vs <i>cla-1</i>; <i>hlb-1</i> <i>syd-2</i>	<i>cla-1</i>; <i>syd-2</i> Vs <i>cla-1</i>; <i>hlb-1</i> <i>syd-2</i>	<i>hlb-1 syd-2</i> Vs <i>cla-1</i>; <i>hlb-1</i> <i>syd-2</i>				
Power (1-β)	0.085434	0.015146817	0.098289				
Effect size (d)	0.413309195	0.214595	0.46664				

Area (Figure 2.3C)	WT Vs <i>cla-1</i> (<i>ok2285</i>)	WT Vs <i>hlb-1</i> (<i>ok725</i>)	WT Vs <i>syd-2</i> (<i>ok217</i>)	WT Vs <i>cla-1; hlb-1</i>	WT Vs <i>cla-1; syd-2</i>	WT Vs <i>hlb-1 syd-2</i>	WT Vs <i>cla-1; hlb-1 syd-2</i>
Power (1-β)	0.059876	0.021108205	0.776816	0.01748407	0.04235209	0.212457	0.00486
Effect size (d)	0.360906	0.255234222	1.013546	0.23012484	0.33463572	0.596865	0.11534
	<i>cla-1 Vs cla-1; hlb-1</i>	<i>cla-1 Vs cla-1; syd-2</i>	<i>cla-1 Vs cla-1; hlb-1 syd-2</i>				
Power (1-β)	0.009041	0.524258558	0.169436				
Effect size (d)	0.148762	0.717746664	0.503103				
	<i>hlb-1 Vs cla-1; hlb-1</i>	<i>hlb-1 Vs hlb-1 syd-2</i>	<i>hlb-1 Vs cla-1; hlb-1 syd-2</i>				
Power (1-β)	0.00217	0.587745298	0.065064				
Effect size (d)	0.038928	0.852307432	0.39331				
	<i>syd-2 Vs cla-1; syd-2</i>	<i>syd-2 Vs hlb-1 syd-2</i>	<i>syd-2 Vs cla-1; hlb-1 syd-2</i>				
Power (1-β)	0.418464	0.028825	0.745241853				
Effect size (d)	0.715435	0.30343783	1.037917				
	<i>cla-1; hlb-1 Vs cla-1; hlb-1 syd-2</i>	<i>cla-1; syd-2 Vs cla-1; hlb-1 syd-2</i>	<i>hlb-1 syd-2 Vs cla-1; hlb-1 syd-2</i>				
Power (1-β)	0.061317	0.018768168	0.146467				
Effect size (d)	0.374022	0.244462	0.538628799				

Intensity (Figure 2.3D)	WT Vs <i>cla-1</i> (<i>ok2285</i>)	WT Vs <i>hlb-1</i> (<i>ok725</i>)	WT Vs <i>syd-2</i> (<i>ok217</i>)	WT Vs <i>cla-1</i>; <i>hlb-1</i>	WT Vs <i>cla-1</i>; <i>syd-2</i>	WT Vs <i>hlb-1</i> <i>syd-2</i>	WT Vs <i>cla-1</i>; <i>hlb-1 syd-2</i>
Power (1-β)	0.125558	0.013309	0.960491	0.026154	0.526038506	0.839186	0.15161918
Effect size (d)	0.452789	0.204953	1.271236616	0.265717	0.80897735	1.07358124	0.535972
	<i>cla-1 Vs cla-1</i> <i>1; hlb-1</i>	<i>cla-1 Vs cla-1</i> ; <i>syd-2</i>	<i>cla-1 Vs cla-1</i> ; <i>hlb-1 syd-2</i>				
Power (1-β)	0.012838	0.991012	0.868329				
Effect size (d)	0.180018	1.231201	0.970387671				
	<i>hlb-1 Vs cla-1</i> <i>1; hlb-1</i>	<i>hlb-1 Vs hlb-1</i> <i>syd-2</i>	<i>hlb-1 Vs cla-1</i> <i>1; hlb-1 syd-2</i>				
Power (1-β)	0.002523	0.941956	0.380364				
Effect size (d)	0.050687	1.170287	0.69362081				
	<i>syd-2 Vs cla-1</i> <i>1; syd-2</i>	<i>syd-2 Vs hlb-1</i> <i>1 syd-2</i>	<i>syd-2 Vs cla-1</i> <i>1; hlb-1 syd-2</i>				
Power (1-β)	0.14858	0.005952	0.518995				
Effect size (d)	0.499772	0.135761	0.864828731				
	<i>cla-1; hlb-1</i> <i>Vs cla-1; hlb-1</i> <i>1 syd-2</i>	<i>cla-1; syd-2</i> <i>Vs cla-1; hlb-1</i> <i>1 syd-2</i>	<i>hlb-1 syd-2</i> <i>Vs cla-1; hlb-1</i> <i>1 syd-2</i>				
Power (1-β)	0.571175	0.032274677	0.236417685				
Effect size (d)	0.773540753	0.307723	0.636022				

1) Confocal imaging

b) SNB-1::GFP imaging data

Puncta Count (Figure 2.4B)	WT Vs <i>cla-1</i> (<i>ok2285</i>)	WT Vs <i>h1b-1</i> (<i>ok725</i>)	WT Vs <i>syd-2</i> (<i>ok217</i>)	WT Vs <i>cla-1</i>; <i>h1b-1</i>	WT Vs <i>cla-1</i> ; <i>syd-2</i>	WT Vs <i>h1b-1</i> <i>syd-2</i>	WT Vs <i>cla-1</i> ; <i>h1b-1 syd-2</i>
Power (1-β)	0.055207	0.081081	0.99824	0.165262065	0.806926	0.99999885	0.99937553
Effect size (d)	0.360356	0.362449	1.476132	0.580448747	1.009096	2.15011017	1.70690804
	<i>cla-1 Vs cla-1</i>; <i>h1b-1</i>	<i>cla-1 Vs cla-1</i>; <i>syd-2</i>	<i>cla-1 Vs cla-1</i> ; <i>h1b-1 syd-2</i>				
Power (1-β)	0.015466	0.0919224	0.757164				
Effect size (d)	0.234816	0.427845	0.957732				
	<i>h1b-1 Vs cla-1</i>; <i>h1b-1</i>	<i>h1b-1 Vs h1b-1</i> <i>syd-2</i>	<i>h1b-1 Vs cla-1</i> ; <i>h1b-1 syd-2</i>				
Power (1-β)	0.020666	0.9990104	0.921876				
Effect size (d)	0.266479	1.503676	1.030002				
	<i>syd-2 Vs cla-1</i>; <i>syd-2</i>	<i>syd-2 Vs h1b-1</i> <i>syd-2</i>	<i>syd-2 Vs cla-1</i>; <i>h1b-1 syd-2</i>				
Power (1-β)	0.160422	0.4295863	0.009381				
Effect size (d)	0.499424	0.761814	0.171229				
	<i>cla-1</i>; <i>h1b-1</i> Vs <i>cla-1</i>; <i>h1b-1</i> <i>syd-2</i>	<i>cla-1</i>; <i>syd-2</i> Vs <i>cla-1</i>; <i>h1b-1</i> <i>syd-2</i>	<i>h1b-1 syd-2</i> Vs <i>cla-1</i>; <i>h1b-1</i> <i>syd-2</i>				
Power (1-β)	0.155356968	0.324637	0.197309				
Effect size (d)	0.564632	0.69265	0.61058				

Area (Figure 2.4C)	WT Vs <i>cla-1</i> (<i>ok2285</i>)	WT Vs <i>hlb-1</i> (<i>ok725</i>)	WT Vs <i>syd-2</i> (<i>ok217</i>)	WT Vs <i>cla-1; hlb-1</i>	WT Vs <i>cla-1; syd-2</i>	WT Vs <i>hlb-1 syd-2</i>	WT Vs <i>cla-1; hlb-1 syd-2</i>
Power (1-β)	0.06668	0.012111	0.007043	0.068871688	0.205809	0.02182601	0.00671148
Effect size (d)	0.392794	0.180518	0.137223	0.420036564	0.569003	0.27558133	0.15006614
	<i>cla-1 Vs cla-1; hlb-1</i>	<i>cla-1 Vs cla-1; syd-2</i>	<i>cla-1 Vs cla-1; hlb-1 syd-2</i>				
Power (1-β)	0.003796	0.799241	0.007468				
Effect size (d)	0.094829	0.991013	0.163326				
	<i>hlb-1 Vs cla-1; hlb-1</i>	<i>hlb-1 Vs hlb-1 syd-2</i>	<i>hlb-1 Vs cla-1; hlb-1 syd-2</i>				
Power (1-β)	0.241318	0.090442	0.031529				
Effect size (d)	0.595174	0.444996	0.312529				
	<i>syd-2 Vs cla-1; syd-2</i>	<i>syd-2 Vs hlb-1 syd-2</i>	<i>syd-2 Vs cla-1; hlb-1 syd-2</i>				
Power (1-β)	0.359379	0.00599	0.001678				
Effect size (d)	0.656344	0.131718	0.020625				
	<i>cla-1; hlb-1 Vs cla-1; hlb-1 syd-2</i>	<i>cla-1; syd-2 Vs cla-1; hlb-1 syd-2</i>	<i>hlb-1 syd-2 Vs cla-1; hlb-1 syd-2</i>				
Power (1-β)	0.012198	0.237967	0.004036393				
Effect size (d)	0.21472	0.633603	0.102103				

Intensity (Figure 2.4D)	WT Vs <i>cla-1</i> (<i>ok2285</i>)	WT Vs <i>hlb-1</i> (<i>ok725</i>)	WT Vs <i>syd-2</i> (<i>ok217</i>)	WT Vs <i>cla-1</i> ; <i>hlb-1</i>	WT Vs <i>cla-1</i> ; <i>syd-2</i>	WT Vs <i>hlb-1</i> <i>syd-2</i>	WT Vs <i>cla-1</i> ; <i>hlb-1 syd-2</i>
Power (1-β)	0.0033	0.608797	0.999840204	0.951674	0.99952193	1	0.999644
Effect size (d)	0.074209	0.74354	1.69280345	1.297535	1.64503084	2.56974031	1.738368
	<i>cla-1 Vs cla-1</i>; <i>hlb-1</i>	<i>cla-1 Vs cla-1</i>; <i>syd-2</i>	<i>cla-1 Vs cla-1</i>; <i>hlb-1 syd-2</i>				
Power (1-β)	0.66101	0.8548538	0.883351				
Effect size (d)	0.872541	1.030131	1.048675313				
	<i>hlb-1 Vs cla-1</i>; <i>hlb-1</i>	<i>hlb-1 Vs hlb-1</i> <i>syd-2</i>	<i>hlb-1 Vs cla-1</i>; <i>hlb-1 syd-2</i>				
Power (1-β)	0.1113	0.9970332	0.470991				
Effect size (d)	0.443988	1.282779	0.673714122				
	<i>syd-2 Vs cla-1</i>; <i>syd-2</i>	<i>syd-2 Vs hlb-1</i> <i>syd-2</i>	<i>syd-2 Vs cla-1</i>; <i>hlb-1 syd-2</i>				
Power (1-β)	0.004691	0.8363067	0.011684				
Effect size (d)	0.10396	1.051235	0.199747855				
	<i>cla-1</i>; <i>hlb-1</i> Vs <i>cla-1</i>; <i>hlb-1</i> <i>syd-2</i>	<i>cla-1</i>; <i>syd-2</i> Vs <i>cla-1</i>; <i>hlb-1</i> <i>syd-2</i>	<i>hlb-1 syd-2</i> Vs <i>cla-1</i>; <i>hlb-1</i> <i>syd-2</i>				
Power (1-β)	0.011153958	0.003528	0.387495				
Effect size (d)	0.20503727	0.085385	0.770505				

2) **Locomotion Assays**

a) Crawling

Motion Mode Paused (Figure 3.1A)	WT Vs <i>cla-1</i> (<i>ok2285</i>)	WT Vs <i>h1b-1</i> (<i>ok725</i>)	WT Vs <i>syd-2</i> (<i>ok217</i>)	WT Vs <i>cla-1</i> ; <i>h1b-1</i>	WT Vs <i>cla-1</i> ; <i>syd-2</i>	WT Vs <i>h1b-1</i> <i>syd-2</i>	WT Vs <i>cla-1</i> ; <i>h1b-1</i> <i>syd-2</i>
Power (1-β)	0.056537	0.999999661	1	0.76916092	0.99999999	0.999969	0.999997
Effect size (d)	0.137166	0.771200974	1.060553	0.36092884	0.82966862	0.676726	0.734805
	<i>cla-1</i> Vs <i>cla-1</i>; <i>h1b-1</i>	<i>cla-1</i> Vs <i>cla-1</i> ; <i>syd-2</i>	<i>cla-1</i> Vs <i>cla-1</i> ; <i>h1b-1</i> <i>syd-2</i>				
Power (1-β)	0.268189	1	1				
Effect size (d)	0.230925	1.069461667	0.94106				
	<i>h1b-1</i> Vs <i>cla-1</i> ; <i>h1b-1</i>	<i>h1b-1</i> Vs <i>h1b-1</i> <i>syd-2</i>	<i>h1b-1</i> Vs <i>cla-1</i> ; <i>h1b-1</i> <i>syd-2</i>				
Power (1-β)	0.995062	1	1				
Effect size (d)	0.547748	1.626893375	1.667254				
	<i>syd-2</i> Vs <i>cla-1</i>; <i>syd-2</i>	<i>syd-2</i> Vs <i>h1b-1</i> <i>syd-2</i>	<i>syd-2</i> Vs <i>cla-1</i>; <i>h1b-1</i> <i>syd-2</i>				
Power (1-β)	0.847491	0.843403	0.503600715				
Effect size (d)	0.401315	0.392329842	0.298198				
	<i>cla-1</i> ; <i>h1b-1</i> Vs <i>cla-1</i> ; <i>h1b-1</i> <i>syd-2</i>	<i>cla-1</i>; <i>syd-2</i> Vs <i>cla-1</i>; <i>h1b-1</i> <i>syd-2</i>	<i>h1b-1</i> <i>syd-2</i> Vs <i>cla-1</i>; <i>h1b-1</i> <i>syd-2</i>				
Power (1-β)	1	0.004372	0.013985				
Effect size (d)	1.294074	0.038166	0.07955239				

Motion Mode Fwd (Figure 3.1B)	WT Vs <i>cla-1</i> (<i>ok2285</i>)	WT Vs <i>h1b-1</i> (<i>ok725</i>)	WT Vs <i>syd-2</i> (<i>ok217</i>)	WT Vs <i>cla-1</i> ; <i>h1b-1</i>	WT Vs <i>cla-1</i>; <i>syd-2</i>	WT Vs <i>h1b-1</i> <i>syd-2</i>	WT Vs <i>cla-1</i>; <i>h1b-1 syd-2</i>
Power (1-β)	0.683317	0.999999	0.987375	0.871917406	0.055122	0.16503161	0.01133947
Effect size (d)	0.335536	0.741615655	0.508613	0.39890804	0.13613587	0.196313	0.070808
	<i>cla-1 Vs cla-1</i>; <i>h1b-1</i>	<i>cla-1 Vs cla-1</i> ; <i>syd-2</i>	<i>cla-1 Vs cla-1</i> ; <i>h1b-1 syd-2</i>				
Power (1-β)	0.003272	0.997823722	0.96266				
Effect size (d)	0.028054	0.565948832	0.466427				
	<i>h1b-1 Vs cla-1</i> ; <i>h1b-1</i>	<i>h1b-1 Vs h1b-1</i> <i>syd-2</i>	<i>h1b-1 Vs cla-1</i> ; <i>h1b-1 syd-2</i>				
Power (1-β)	0.97806	1	1				
Effect size (d)	0.492416	1.083537701	0.961228				
	<i>syd-2 Vs cla-1</i> ; <i>syd-2</i>	<i>syd-2 Vs h1b-1</i> <i>syd-2</i>	<i>syd-2 Vs cla-1</i> ; <i>h1b-1 syd-2</i>				
Power (1-β)	0.999258	0.7228048	0.984386				
Effect size (d)	0.615421	0.352217392	0.510078				
	<i>cla-1</i> ; <i>h1b-1 Vs</i> <i>cla-1</i> ; <i>h1b-1</i> <i>syd-2</i>	<i>cla-1</i>; <i>syd-2</i> Vs <i>cla-1</i>; <i>h1b-1</i> <i>syd-2</i>	<i>h1b-1 syd-2</i> Vs <i>cla-1</i>; <i>h1b-1</i> <i>syd-2</i>				
Power (1-β)	0.997796796	0.01185	0.065534				
Effect size (d)	0.577326	0.073511	0.146618052				

Motion Mode Bwd (Figure 3.1C)	WT Vs <i>cla-1</i> (<i>ok2285</i>)	WT Vs <i>h1b-1</i> (<i>ok725</i>)	WT Vs <i>syd-2</i> (<i>ok217</i>)	WT Vs <i>cla-1</i> ; <i>h1b-1</i>	WT Vs <i>cla-1</i> ; <i>syd-2</i>	WT Vs <i>h1b-1</i> <i>syd-2</i>	WT Vs <i>cla-1</i> ; <i>h1b-1 syd-2</i>
Power (1-β)	1	0.027826	1	0.085376162	1	1	1
Effect size (d)	0.841636	0.106118385	1.739958	0.15844821	2.42891087	1.302709	1.954115
	<i>cla-1 Vs cla-1</i> ; <i>h1b-1</i>	<i>cla-1 Vs cla-1</i> ; <i>syd-2</i>	<i>cla-1 Vs cla-1</i> ; <i>h1b-1 syd-2</i>				
Power (1-β)	1	1	1				
Effect size (d)	0.792625	1.805603654	1.432889				
	<i>h1b-1 Vs cla-1</i> ; <i>h1b-1</i>	<i>h1b-1 Vs h1b-1</i> <i>syd-2</i>	<i>h1b-1 Vs cla-1</i> ; <i>h1b-1 syd-2</i>				
Power (1-β)	0.522023	1	1				
Effect size (d)	0.300271	1.422059271	2.113811				
	<i>syd-2 Vs cla-1</i> ; <i>syd-2</i>	<i>syd-2 Vs h1b-1</i> <i>syd-2</i>	<i>syd-2 Vs cla-1</i> ; <i>h1b-1 syd-2</i>				
Power (1-β)	0.999903	0.011155387	0.958503				
Effect size (d)	0.670193	0.070483435	0.468536				
	<i>cla-1; h1b-1 Vs</i> <i>cla-1; h1b-1</i> <i>syd-2</i>	<i>cla-1; syd-2</i> <i>Vs cla-1; h1b-1</i> <i>syd-2</i>	<i>h1b-1 syd-2 Vs</i> <i>cla-1; h1b-1</i> <i>syd-2</i>				
Power (1-β)	1	0.010644	0.959673				
Effect size (d)	1.960706	0.069742	0.464842946				

Path Coverage (Figure 3.2B)	WT Vs <i>cla-1</i> (<i>ok2285</i>)	WT Vs <i>hlb-1</i> (<i>ok725</i>)	WT Vs <i>syd-2</i> (<i>ok217</i>)	WT Vs <i>cla-1</i>; <i>hlb-1</i>	WT Vs <i>cla-1</i> ; <i>syd-2</i>	WT Vs <i>hlb-1</i> <i>syd-2</i>	WT Vs <i>cla-1</i>; <i>hlb-1 syd-2</i>
Power (1-β)	0.2679541	0.999998	0.90563	0.003037	0.663493068	0.682241	0.0188472
Effect size (d)	0.2300729	0.729402	0.422829	0.025677	0.331999246	0.336426	0.09062251
	<i>cla-1 Vs cla-1</i> ; <i>hlb-1</i>	<i>cla-1 Vs cla-1</i> ; <i>syd-2</i>	<i>cla-1 Vs cla-1</i>; <i>hlb-1 syd-2</i>				
Power (1-β)	0.319451	0.9986468	0.0675				
Effect size (d)	0.2453106	0.581842	0.147668				
	<i>hlb-1 Vs cla-1</i> ; <i>hlb-1</i>	<i>hlb-1 Vs hlb-1</i> <i>syd-2</i>	<i>hlb-1 Vs cla-1</i> ; <i>hlb-1 syd-2</i>				
Power (1-β)	1	1	0.999937				
Effect size (d)	0.9135957	1.140693	0.675781				
	<i>syd-2 Vs cla-1</i>; <i>syd-2</i>	<i>syd-2 Vs hlb-1</i> <i>syd-2</i>	<i>syd-2 Vs cla-1</i> ; <i>hlb-1 syd-2</i>				
Power (1-β)	0.001446	0.0257177	0.989673				
Effect size (d)	0.0029975	0.104135	0.525892				
	<i>cla-1</i>; <i>hlb-1 Vs cla-1</i>; <i>hlb-1 syd-2</i>	<i>cla-1</i> ; <i>syd-2 Vs cla-1</i> ; <i>hlb-1 syd-2</i>	<i>hlb-1 syd-2 Vs cla-1</i> ; <i>hlb-1 syd-2</i>				
Power (1-β)	0.014228933	0.933678	0.936753				
Effect size (d)	0.080732	0.4423368	0.443148				

Speed Forward (Figure 3.3A)	WT Vs <i>cla-1</i> (<i>ok2285</i>)	WT Vs <i>h1b-1</i> (<i>ok725</i>)	WT Vs <i>syd-2</i> (<i>ok217</i>)	WT Vs <i>cla-1</i>; <i>h1b-1</i>	WT Vs <i>cla-1</i> ; <i>syd-2</i>	WT Vs <i>h1b-1</i> <i>syd-2</i>	WT Vs <i>cla-1</i>; <i>h1b-1</i> <i>syd-2</i>
Power (1-β)	0.927863	1	0.999071	0.739120777	0.052446	0.49600172	0.00650697
Effect size (d)	0.4301319	0.811533	0.599652	0.35133	0.13387994	0.289553	0.05098343
	<i>cla-1</i> Vs <i>cla-1</i> ; <i>h1b-1</i>	<i>cla-1</i> Vs <i>cla-1</i> ; <i>syd-2</i>	<i>cla-1</i> Vs <i>cla-1</i> ; <i>h1b-1</i> <i>syd-2</i>				
Power (1-β)	0.09002	0.9998706	0.995276				
Effect size (d)	0.1608423	0.643151	0.543875				
	<i>h1b-1</i> Vs <i>cla-1</i> ; <i>h1b-1</i>	<i>h1b-1</i> Vs <i>h1b-1</i> <i>syd-2</i>	<i>h1b-1</i> Vs <i>cla-1</i> ; <i>h1b-1</i> <i>syd-2</i>				
Power (1-β)	0.999905	1	1				
Effect size (d)	0.6599282	1.234406	1.084956				
	<i>syd-2</i> Vs <i>cla-1</i> ; <i>syd-2</i>	<i>syd-2</i> Vs <i>h1b-1</i> <i>syd-2</i>	<i>syd-2</i> Vs <i>cla-1</i> ; <i>h1b-1</i> <i>syd-2</i>				
Power (1-β)	0.999764	0.720571	0.999329				
Effect size (d)	0.6472959	0.353297	0.614041				
	<i>cla-1</i> ; <i>h1b-1</i> Vs <i>cla-1</i> ; <i>h1b-1</i> <i>syd-2</i>	<i>cla-1</i>; <i>syd-2</i> Vs <i>cla-1</i>; <i>h1b-1</i> <i>syd-2</i>	<i>h1b-1</i> <i>syd-2</i> Vs <i>cla-1</i>; <i>h1b-1</i> <i>syd-2</i>				
Power (1-β)	0.97831974	0.021527	0.42877				
Effect size (d)	0.495699	0.0968537	0.275826				

Speed Backward (Figure 3.3B)	WT Vs <i>cla-1</i> (<i>ok2285</i>)	WT Vs <i>hlb-1</i> (<i>ok725</i>)	WT Vs <i>syd-2</i> (<i>ok217</i>)	WT Vs <i>cla-1</i> ; <i>hlb-1</i>	WT Vs <i>cla-1</i> ; <i>syd-2</i>	WT Vs <i>hlb-1</i> <i>syd-2</i>	WT Vs <i>cla-1</i> ; <i>hlb-1 syd-2</i>
Power (1-β)	0.1689728	0.999699	1	0.998023	0.999997912	0.999998	0.99978142
Effect size (d)	0.197431	0.617330964	0.912146	0.5648235	0.73478829	0.736909	0.634185
	<i>cla-1 Vs cla-1</i> ; <i>hlb-1</i>	<i>cla-1 Vs cla-1</i> ; <i>syd-2</i>	<i>cla-1 Vs cla-1</i> ; <i>hlb-1 syd-2</i>				
Power (1-β)	0.96833	1	1				
Effect size (d)	0.468339	1.128540447	0.978219				
	<i>hlb-1 Vs cla-1</i>; <i>hlb-1</i>	<i>hlb-1 Vs hlb-1</i> <i>syd-2</i>	<i>hlb-1 Vs cla-1</i> ; <i>hlb-1 syd-2</i>				
Power (1-β)	0.027714	1	1				
Effect size (d)	0.107207	1.476606325	1.570608				
	<i>syd-2 Vs cla-1</i>; <i>syd-2</i>	<i>syd-2 Vs hlb-1</i> <i>syd-2</i>	<i>syd-2 Vs cla-1</i>; <i>hlb-1 syd-2</i>				
Power (1-β)	0.827619	0.0989165	0.779992				
Effect size (d)	0.393484	0.168540619	0.373576				
	<i>cla-1</i> ; <i>hlb-1</i> Vs <i>cla-1</i> ; <i>hlb-1</i> <i>syd-2</i>	<i>cla-1</i>; <i>syd-2</i> Vs <i>cla-1</i>; <i>hlb-1</i> <i>syd-2</i>	<i>hlb-1 syd-2</i> Vs <i>cla-1</i>; <i>hlb-1</i> <i>syd-2</i>				
Power (1-β)	1	0.013283	0.136228				
Effect size (d)	1.51997	0.077806	0.186235891				

Hip Curvature Fwd (Figure 3.4Bi)	WT Vs <i>cla-1</i> (<i>ok2285</i>)	WT Vs <i>h1b-1</i> (<i>ok725</i>)	WT Vs <i>syd-2</i> (<i>ok217</i>)	WT Vs <i>cla-1;</i> <i>h1b-1</i>	WT Vs <i>cla-1; syd-2</i>	WT Vs <i>h1b-1</i> <i>syd-2</i>	WT Vs <i>cla-1;</i> <i>h1b-1 syd-2</i>
Power (1-β)	0.999995	0.0327634	1	0.0024	1	1	1
Effect size (d)	0.716182	0.113926	1.905419	0.018407265	1.692626	1.67307866	1.19528583
	<i>cla-1 Vs cla-1;</i> <i>h1b-1</i>	<i>cla-1 Vs cla-</i> <i>1; syd-2</i>	<i>cla-1 Vs cla-</i> <i>1; h1b-1 syd-2</i>				
Power (1-β)	0.999999	1	0.999993				
Effect size (d)	0.757286	1.27154	0.727381				
	<i>h1b-1 Vs cla-</i> <i>1; h1b-1</i>	<i>h1b-1 Vs h1b-1</i> <i>syd-2</i>	<i>h1b-1 Vs cla-1;</i> <i>h1b-1 syd-2</i>				
Power (1-β)	0.024675	1	1				
Effect size (d)	0.102514	1.4969	1.048279				
	<i>syd-2 Vs cla-</i> <i>1; syd-2</i>	<i>syd-2 Vs h1b-</i> <i>1 syd-2</i>	<i>syd-2 Vs cla-1;</i> <i>h1b-1 syd-2</i>				
Power (1-β)	0.343534	0.009717	0.939963				
Effect size (d)	0.260048	0.065938	0.451949				
	<i>cla-1; h1b-1 Vs</i> <i>cla-1; h1b-1</i> <i>syd-2</i>	<i>cla-1; syd-2</i> <i>Vs cla-1; h1b-</i> <i>1 syd-2</i>	<i>h1b-1 syd-2</i> <i>Vs cla-1; h1b-</i> <i>1 syd-2</i>				
Power (1-β)	1	0.499636	0.741981				
Effect size (d)	1.239513	0.297	0.360484				

Hip Curvature Bwd (Figure 3.4Bii)	WT Vs <i>cla-1</i> (<i>ok2285</i>)	WT Vs <i>hlb-1</i> (<i>ok725</i>)	WT Vs <i>syd-2</i> (<i>ok217</i>)	WT Vs <i>cla-1</i> ; <i>hlb-1</i>	WT Vs <i>cla-1</i> ; <i>syd-2</i>	WT Vs <i>hlb-1</i> <i>syd-2</i>	WT Vs <i>cla-1</i> ; <i>hlb-1 syd-2</i>
Power (1-β)	1	0.2045297	1	0.840617	1	1	0.999992
Effect size (d)	0.957634	0.213934	1.750439	0.391214327	1.002908	1.57140285	0.72384387
	<i>cla-1</i> Vs <i>cla-1</i> ; <i>hlb-1</i>	<i>cla-1</i> Vs <i>cla-1</i>; <i>syd-2</i>	<i>cla-1</i> Vs <i>cla-1</i>; <i>hlb-1 syd-2</i>				
Power (1-β)	0.997254	0.0952007	0.00495				
Effect size (d)	0.56473	0.165403	0.042822				
	<i>hlb-1</i> Vs <i>cla-1</i>; <i>hlb-1</i>	<i>hlb-1</i> Vs <i>hlb-1</i> <i>syd-2</i>	<i>hlb-1</i> Vs <i>cla-1</i> ; <i>hlb-1 syd-2</i>				
Power (1-β)	0.097047	1	0.990018				
Effect size (d)	0.168307	1.368665	0.529308				
	<i>syd-2</i> Vs <i>cla-1</i> ; <i>syd-2</i>	<i>syd-2</i> Vs <i>hlb-1</i> <i>syd-2</i>	<i>syd-2</i> Vs <i>cla-1</i> ; <i>hlb-1 syd-2</i>				
Power (1-β)	1	0.0124568	0.999999				
Effect size (d)	1.127732	0.075049	0.771343				
	<i>cla-1</i> ; <i>hlb-1</i> Vs <i>cla-1</i> ; <i>hlb-1</i> <i>syd-2</i>	<i>cla-1</i>; <i>syd-2</i> Vs <i>cla-1</i>; <i>hlb-1</i> <i>syd-2</i>	<i>hlb-1 syd-2</i> Vs <i>cla-1</i> ; <i>hlb-1</i> <i>syd-2</i>				
Power (1-β)	0.841639627	0.094151956	0.999996				
Effect size (d)	0.397729	0.16777	0.739844				

Midbody Curvature Fwd (Figure 3.4Ci)	WT Vs <i>cla-1</i> (<i>ok2285</i>)	WT Vs <i>hlb-1</i> (<i>ok725</i>)	WT Vs <i>syd-2</i> (<i>ok217</i>)	WT Vs <i>cla-1; hlb-1</i>	WT Vs <i>cla-1; syd-2</i>	WT Vs <i>hlb-1 syd-2</i>	WT Vs <i>cla-1; hlb-1 syd-2</i>
Power (1-β)	1	0.521847	1	0.931662	1	1	1
Effect size (d)	1.017439	0.299019	3.250205	0.436321098	2.546011	2.71139005	1.79258662
	<i>cla-1</i> Vs <i>cla-1; hlb-1</i>	<i>cla-1</i> Vs <i>cla-1; syd-2</i>	<i>cla-1</i> Vs <i>cla-1; hlb-1 syd-2</i>				
Power (1-β)	0.99808	1	1				
Effect size (d)	0.574818	1.893867	1.134994				
	<i>hlb-1</i> Vs <i>cla-1; hlb-1</i>	<i>hlb-1</i> Vs <i>hlb-1 syd-2</i>	<i>hlb-1</i> Vs <i>cla-1; hlb-1 syd-2</i>				
Power (1-β)	0.022955	1	1				
Effect size (d)	0.099508	2.257962	1.447571				
	<i>syd-2</i> Vs <i>cla-1; syd-2</i>	<i>syd-2</i> Vs <i>hlb-1 syd-2</i>	<i>syd-2</i> Vs <i>cla-1; hlb-1 syd-2</i>				
Power (1-β)	1	0.3600001	1				
Effect size (d)	1.050327	0.259718	0.80964				
	<i>cla-1; hlb-1</i> Vs <i>cla-1; hlb-1 syd-2</i>	<i>cla-1; syd-2</i> Vs <i>cla-1; hlb-1 syd-2</i>	<i>hlb-1 syd-2</i> Vs <i>cla-1; hlb-1 syd-2</i>				
Power (1-β)	1	0.415254	0.995047				
Effect size (d)	1.478173	0.276503	0.551635				

Midbody Curvature Bwd (Figure 3.4Cii)	WT Vs <i>cla-1</i> (<i>ok2285</i>)	WT Vs <i>hlb-1</i> (<i>ok725</i>)	WT Vs <i>syd-2</i> (<i>ok217</i>)	WT Vs <i>cla-1; hlb-1</i>	WT Vs <i>cla-1; syd-2</i>	WT Vs <i>hlb-1 syd-2</i>	WT Vs <i>cla-1; hlb-1 syd-2</i>
Power (1-β)	1	0.5151539	1	0.927912	1	1	1
Effect size (d)	1.019042	0.298912	3.254751	0.436478025	2.548477	2.71206994	1.79167897
	<i>cla-1</i> Vs <i>cla-1; hlb-1</i>	<i>cla-1</i> Vs <i>cla-1; syd-2</i>	<i>cla-1</i> Vs <i>cla-1; hlb-1 syd-2</i>				
Power (1-β)	0.9980251	1	1				
Effect size (d)	0.574984	1.893867	1.136475				
	<i>hlb-1</i> Vs <i>cla-1; hlb-1</i>	<i>hlb-1</i> Vs <i>hlb-1 syd-2</i>	<i>hlb-1</i> Vs <i>cla-1; hlb-1 syd-2</i>				
Power (1-β)	0.022822	1	1				
Effect size (d)	0.099508	2.258388	1.447799				
	<i>syd-2</i> Vs <i>cla-1; syd-2</i>	<i>syd-2</i> Vs <i>hlb-1 syd-2</i>	<i>syd-2</i> Vs <i>cla-1; hlb-1 syd-2</i>				
Power (1-β)	1	0.3600001	1				
Effect size (d)	1.050327	0.259718	0.810624				
	<i>cla-1; hlb-1</i> Vs <i>cla-1; hlb-1 syd-2</i>	<i>cla-1; syd-2</i> Vs <i>cla-1; hlb-1 syd-2</i>	<i>hlb-1 syd-2</i> Vs <i>cla-1; hlb-1 syd-2</i>				
Power (1-β)	1	0.411438	0.994787				
Effect size (d)	1.478776	0.276787	0.552012				

Neck Curvature Fwd (Figure 3.4Di)	WT Vs <i>cla-1</i> (<i>ok2285</i>)	WT Vs <i>hlb-1</i> (<i>ok725</i>)	WT Vs <i>syd-2</i> (<i>ok217</i>)	WT Vs <i>cla-1; hlb-1</i>	WT Vs <i>cla-1; syd-2</i>	WT Vs <i>hlb-1 syd-2</i>	WT Vs <i>cla-1; hlb-1 syd-2</i>
Power (1-β)	1	0.799514	1	0.981914	1	1	1
Effect size (d)	1.4823156	0.374906	3.437902	0.494092	2.54280553	3.176881	2.02457331
	<i>cla-1 Vs cla-1; hlb-1</i>	<i>cla-1 Vs cla-1; syd-2</i>	<i>cla-1 Vs cla-1; hlb-1 syd-2</i>				
Power (1-β)	1	1	1				
Effect size (d)	1.1361273	1.448486	0.960531				
	<i>hlb-1 Vs cla-1; hlb-1</i>	<i>hlb-1 Vs hlb-1 syd-2</i>	<i>hlb-1 Vs cla-1; hlb-1 syd-2</i>				
Power (1-β)	0.012079	1	1				
Effect size (d)	0.0741663	2.763701	1.660485				
	<i>syd-2 Vs cla-1; syd-2</i>	<i>syd-2 Vs hlb-1 syd-2</i>	<i>syd-2 Vs cla-1; hlb-1 syd-2</i>				
Power (1-β)	1	0.0706618	1				
Effect size (d)	1.3395174	0.151042	0.967855				
	<i>cla-1; hlb-1 Vs cla-1; hlb-1 syd-2</i>	<i>cla-1; syd-2 Vs cla-1; hlb-1 syd-2</i>	<i>hlb-1 syd-2 Vs cla-1; hlb-1 syd-2</i>				
Power (1-β)	1	0.24433006	1				
Effect size (d)	1.777319	0.2287305	0.812687				

Neck Curvature Bwd (Figure 3.4Dii)	WT Vs <i>cla-1</i> (<i>ok2285</i>)	WT Vs <i>h1b-1</i> (<i>ok725</i>)	WT Vs <i>syd-2</i> (<i>ok217</i>)	WT Vs <i>cla-1; h1b-1</i>	WT Vs <i>cla-1; syd-2</i>	WT Vs <i>h1b-1 syd-2</i>	WT Vs <i>cla-1; h1b-1 syd-2</i>
Power (1-β)	0.995864	0.0680202	1	0.022202	0.384249	1	0.247687
Effect size (d)	0.549537	0.148841	1.541461	0.097584538	0.264689	1.06971975	0.22989809
	<i>cla-1</i> Vs <i>cla-1; h1b-1</i>	<i>cla-1</i> Vs <i>cla-1; syd-2</i>	<i>cla-1</i> Vs <i>cla-1; h1b-1 syd-2</i>				
Power (1-β)	0.975277	0.3096894	0.246451				
Effect size (d)	0.485783	0.244858	0.23146				
	<i>h1b-1</i> Vs <i>cla-1; h1b-1</i>	<i>h1b-1</i> Vs <i>h1b-1 syd-2</i>	<i>h1b-1</i> Vs <i>cla-1; h1b-1 syd-2</i>				
Power (1-β)	0.008711	1	0.017778				
Effect size (d)	0.062202	0.922836	0.090025				
	<i>syd-2</i> Vs <i>cla-1; syd-2</i>	<i>syd-2</i> Vs <i>h1b-1 syd-2</i>	<i>syd-2</i> Vs <i>cla-1; h1b-1 syd-2</i>				
Power (1-β)	1	0.3264714	1				
Effect size (d)	2.02687	0.250433	1.159145				
	<i>cla-1; h1b-1</i> Vs <i>cla-1; h1b-1 syd-2</i>	<i>cla-1; syd-2</i> Vs <i>cla-1; h1b-1 syd-2</i>	<i>h1b-1 syd-2</i> Vs <i>cla-1; h1b-1 syd-2</i>				
Power (1-β)	0.072120275	0.001950098	1				
Effect size (d)	0.153726	0.012249	0.784397				

Minor Axis Forward (Figure 3.5B)	WT Vs <i>cla-1</i> (<i>ok2285</i>)	WT Vs <i>hlb-1</i> (<i>ok725</i>)	WT Vs <i>syd-2</i> (<i>ok217</i>)	WT Vs <i>cla-1</i> ; <i>hlb-1</i>	WT Vs <i>cla-1</i> ; <i>syd-2</i>	WT Vs <i>hlb-1</i> <i>syd-2</i>	WT Vs <i>cla-1</i> ; <i>hlb-1</i> <i>syd-2</i>
Power (1-β)	0.564062	0.660381	0.999999	0.963718	1	1	1
Effect size (d)	0.30554	0.333286	0.763234	0.465969494	2.245514	1.31504672	1.99831028
	<i>cla-1</i> Vs <i>cla-1</i>; <i>hlb-1</i>	<i>cla-1</i> Vs <i>cla-1</i> ; <i>syd-2</i>	<i>cla-1</i> Vs <i>cla-1</i> ; <i>hlb-1</i> <i>syd-2</i>				
Power (1-β)	0.074843	1	1				
Effect size (d)	0.152057	1.999905	1.782098				
	<i>hlb-1</i> Vs <i>cla-1</i>; <i>hlb-1</i>	<i>hlb-1</i> Vs <i>hlb-1</i> <i>syd-2</i>	<i>hlb-1</i> Vs <i>cla-1</i> ; <i>hlb-1</i> <i>syd-2</i>				
Power (1-β)	0.03362	1	1				
Effect size (d)	0.115767	1.020995	1.733039				
	<i>syd-2</i> Vs <i>cla-1</i> ; <i>syd-2</i>	<i>syd-2</i> Vs <i>hlb-1</i> <i>syd-2</i>	<i>syd-2</i> Vs <i>cla-1</i> ; <i>hlb-1</i> <i>syd-2</i>				
Power (1-β)	1	0.9953516	1				
Effect size (d)	1.389546	0.551012	1.278058				
	<i>cla-1</i> ; <i>hlb-1</i> Vs <i>cla-1</i> ; <i>hlb-1</i> <i>syd-2</i>	<i>cla-1</i>; <i>syd-2</i> Vs <i>cla-1</i>; <i>hlb-1</i> <i>syd-2</i>	<i>hlb-1</i> <i>syd-2</i> Vs <i>cla-1</i> ; <i>hlb-1</i> <i>syd-2</i>				
Power (1-β)	1	0.013437952	0.999999				
Effect size (d)	1.70391	0.078611	0.75974				

Minor Axis Bwd (Figure 3.5C)	WT Vs <i>cla-1</i> (<i>ok2285</i>)	WT Vs <i>hlb-1</i> (<i>ok725</i>)	WT Vs <i>syd-2</i> (<i>ok217</i>)	WT Vs <i>cla-1</i>; <i>hlb-1</i>	WT Vs <i>cla-1</i> ; <i>syd-2</i>	WT Vs <i>hlb-1</i> <i>syd-2</i>	WT Vs <i>cla-1</i> ; <i>hlb-1 syd-2</i>
Power (1-β)	0.062151	0.0558761	1	0.006966	1	1	1
Effect size (d)	0.143203	0.138862	0.969727	0.053753734	1.845296	1.1577131	1.52528341
	<i>cla-1 Vs cla-1</i>; <i>hlb-1</i>	<i>cla-1 Vs cla-1</i>; <i>syd-2</i>	<i>cla-1 Vs cla-1</i>; <i>hlb-1 syd-2</i>				
Power (1-β)	0.258657	1	1				
Effect size (d)	0.230248	2.04565	1.585217				
	<i>hlb-1 Vs cla-1</i>; <i>hlb-1</i>	<i>hlb-1 Vs hlb-1</i> <i>syd-2</i>	<i>hlb-1 Vs cla-1</i>; <i>hlb-1 syd-2</i>				
Power (1-β)	0.021842	1	1				
Effect size (d)	0.097646	1.351805	1.688018				
	<i>syd-2 Vs cla-1</i>; <i>syd-2</i>	<i>syd-2 Vs hlb-1</i> <i>syd-2</i>	<i>syd-2 Vs cla-1</i>; <i>hlb-1 syd-2</i>				
Power (1-β)	1	0.3485313	0.999999				
Effect size (d)	1.315486	0.257141	0.780918				
	<i>cla-1; hlb-1 Vs</i> <i>cla-1; hlb-1</i> <i>syd-2</i>	<i>cla-1; syd-2</i> <i>Vs cla-1; hlb-1</i> <i>syd-2</i>	<i>hlb-1 syd-2 Vs</i> <i>cla-1; hlb-1</i> <i>syd-2</i>				
Power (1-β)	1	0.010434119	0.993707				
Effect size (d)	1.666395	0.069488	0.545659				

2) Locomotion Assays

b) Swimming/thrashing

Bend Count (Figure 3.6B)	WT Vs <i>cla-1</i> (<i>ok2285</i>)	WT Vs <i>hlb-1</i> (<i>ok725</i>)	WT Vs <i>syd-2</i> (<i>ok217</i>)	WT Vs <i>cla-1</i>; <i>hlb-1</i>	WT Vs <i>cla-1</i> ; <i>syd-2</i>	WT Vs <i>hlb-1</i> <i>syd-2</i>	WT Vs <i>cla-1</i> ; <i>hlb-1 syd-2</i>
Power (1-β)	0.1384247	0.002389	1	0.095338	1	1	1
Effect size (d)	0.422185	0.042124586	3.97437	0.37607748	3.97656239	3.899781	4.64004
	<i>cla-1 Vs cla-1</i> <i>1; hlb-1</i>	<i>cla-1 Vs cla-1</i> ; <i>syd-2</i>	<i>cla-1 Vs cla-1</i> ; <i>hlb-1 syd-2</i>				
Power (1-β)	0.0020374	1	1				
Effect size (d)	0.029762	3.773414914	4.454754				
	<i>hlb-1 Vs cla-1</i> <i>1; hlb-1</i>	<i>hlb-1 Vs hlb-1</i> <i>syd-2</i>	<i>hlb-1 Vs cla-1</i> ; <i>hlb-1 syd-2</i>				
Power (1-β)	0.176942	1	1				
Effect size (d)	0.457884	4.47698822	5.37873				
	<i>syd-2 Vs cla-1</i> <i>1; syd-2</i>	<i>syd-2 Vs hlb-1</i> <i>1 syd-2</i>	<i>syd-2 Vs cla-1</i> <i>1; hlb-1 syd-2</i>				
Power (1-β)	0.001956	0.0403749	0.178013				
Effect size (d)	0.028445	0.273789928	0.457573				
	<i>cla-1; hlb-1 Vs</i> <i>cla-1; hlb-1</i> <i>syd-2</i>	<i>cla-1; syd-2</i> <i>Vs cla-1; hlb-1</i> <i>1 syd-2</i>	<i>hlb-1 syd-2</i> <i>Vs cla-1; hlb-1</i> <i>1 syd-2</i>				
Power (1-β)	1	0.002632	0.70451				
Effect size (d)	4.252516	0.049211	0.786904422				

Bend Curvature (Figure 3.7Ai)	WT Vs <i>cla-1</i> (<i>ok2285</i>)	WT Vs <i>hlb-1</i> (<i>ok725</i>)	WT Vs <i>syd-2</i> (<i>ok217</i>)	WT Vs <i>cla-1; hlb-1</i>	WT Vs <i>cla-1; syd-2</i>	WT Vs <i>hlb-1 syd-2</i>	WT Vs <i>cla-1; hlb-1 syd-2</i>
Power (1-β)	0.1113312	0.010169	0.004304	0.466411	0.067943221	0.08739	0.0927717
Effect size (d)	0.653806	0.251939	0.139761	1.068316583	0.554556	0.60358792	0.61568453
	<i>cla-1 Vs cla-1; hlb-1</i>	<i>cla-1 Vs cla-1; syd-2</i>	<i>cla-1 Vs cla-1; hlb-1 syd-2</i>				
Power (1-β)	0.141813	0.0054537	0.001306				
Effect size (d)	0.707581	0.169557	0				
	<i>hlb-1 Vs cla-1; hlb-1</i>	<i>hlb-1 Vs hlb-1 syd-2</i>	<i>hlb-1 Vs cla-1; hlb-1 syd-2</i>				
Power (1-β)	0.022522	0.0287808	0.02946				
Effect size (d)	0.367253	0.405672	0.40941				
	<i>syd-2 Vs cla-1; syd-2</i>	<i>syd-2 Vs hlb-1 syd-2</i>	<i>syd-2 Vs cla-1; hlb-1 syd-2</i>				
Power (1-β)	0.008027	0.1196522	0.124448				
Effect size (d)	0.219942	0.669417	0.678068				
	<i>cla-1; hlb-1 Vs cla-1; hlb-1 syd-2</i>	<i>cla-1; syd-2 Vs cla-1; hlb-1 syd-2</i>	<i>hlb-1 syd-2 Vs cla-1; hlb-1 syd-2</i>				
Power (1-β)	0.124448338	0.005252039	0.001692				
Effect size (d)	0.678068	0.164763	0.029				

Bend Curvature CV (Figure 3.7Aii)	WT Vs <i>cla-1</i> (<i>ok2285</i>)	WT Vs <i>hlb-1</i> (<i>ok725</i>)	WT Vs <i>syd-2</i> (<i>ok217</i>)	WT Vs <i>cla-1; hlb-1</i>	WT Vs <i>cla-1; syd-2</i>	WT Vs <i>hlb-1 syd-2</i>	WT Vs <i>cla-1; hlb-1 syd-2</i>
Power (1-β)	0.031895	0.0862476	0.999962	0.05833	0.991418	0.999584059	1
Effect size (d)	0.4222426	0.60095	2.544238	0.526199	1.969306976	2.319409	2.9318228
	<i>cla-1 Vs cla-1; hlb-1</i>	<i>cla-1 Vs cla-1; syd-2</i>	<i>cla-1 Vs cla-1; hlb-1 syd-2</i>				
Power (1-β)	0.003503	0.9994533	1				
Effect size (d)	0.1144535	2.291429	3.26235				
	<i>hlb-1 Vs cla-1; hlb-1</i>	<i>hlb-1 Vs hlb-1 syd-2</i>	<i>hlb-1 Vs cla-1; hlb-1 syd-2</i>				
Power (1-β)	0.504556	0.9696724	0.999874				
Effect size (d)	1.1032671	1.784115	2.435949				
	<i>syd-2 Vs cla-1; syd-2</i>	<i>syd-2 Vs hlb-1 syd-2</i>	<i>syd-2 Vs cla-1; hlb-1 syd-2</i>				
Power (1-β)	0.001503	0.0056191	0.075266				
Effect size (d)	0.0156483	0.173371	0.574141				
	<i>cla-1; hlb-1 Vs cla-1; hlb-1 syd-2</i>	<i>cla-1; syd-2 Vs cla-1; hlb-1 syd-2</i>	<i>hlb-1 syd-2 Vs cla-1; hlb-1 syd-2</i>				
Power (1-β)	0.999999999	0.066412	0.150308				
Effect size (d)	3.270932	0.5502575	0.721127				

Swim Peak Time (Figure 3.7Bi)	WT Vs <i>cla-1</i> (<i>ok2285</i>)	WT Vs <i>hlb-1</i> (<i>ok725</i>)	WT Vs <i>syd-2</i> (<i>ok217</i>)	WT Vs <i>cla-1; hlb-1</i>	WT Vs <i>cla-1; syd-2</i>	WT Vs <i>hlb-1 syd-2</i>	WT Vs <i>cla-1; hlb-1 syd-2</i>
Power (1-β)	0.054102	0.0035488	1	0.023787	0.990805	1	1
Effect size (d)	0.512551	0.116034	3.425144339	0.375682	1.95999403	3.8451822	3.157751
	<i>cla-1 Vs cla-1; hlb-1</i>	<i>cla-1 Vs cla-1; syd-2</i>	<i>cla-1 Vs cla-1; hlb-1 syd-2</i>				
Power (1-β)	0.001416	0.9862837	1				
Effect size (d)	0.008997	1.90436	3.054589232				
	<i>hlb-1 Vs cla-1; hlb-1</i>	<i>hlb-1 Vs hlb-1 syd-2</i>	<i>hlb-1 Vs cla-1; hlb-1 syd-2</i>				
Power (1-β)	0.011881	1	1				
Effect size (d)	0.273516	3.761075	3.122741216				
	<i>syd-2 Vs cla-1; syd-2</i>	<i>syd-2 Vs hlb-1 syd-2</i>	<i>syd-2 Vs cla-1; hlb-1 syd-2</i>				
Power (1-β)	0.733926	0.0018329	0.227734				
Effect size (d)	1.327216	0.038132	0.82657517				
	<i>cla-1; hlb-1 Vs cla-1; hlb-1 syd-2</i>	<i>cla-1; syd-2 Vs cla-1; hlb-1 syd-2</i>	<i>hlb-1 syd-2 Vs cla-1; hlb-1 syd-2</i>				
Power (1-β)	1	0.004571	0.223752				
Effect size (d)	3.003138445	0.147261	0.821737				

Swim Peak Time CV (Figure 3.7Bii)	WT Vs <i>cla-1</i> (<i>ok2285</i>)	WT Vs <i>hlb-1</i> (<i>ok725</i>)	WT Vs <i>syd-2</i> (<i>ok217</i>)	WT Vs <i>cla-1</i>; <i>hlb-1</i>	WT Vs <i>cla-1</i> ; <i>syd-2</i>	WT Vs <i>hlb-1</i> <i>syd-2</i>	WT Vs <i>cla-1</i> ; <i>hlb-1</i> <i>syd-2</i>
Power (1-β)	0.0183651	0.002641	0.997054	0.005263	0.985651548	0.999575	1
Effect size (d)	0.336392	0.080584	2.104631	0.165029511	1.897904	2.31724136	3.79078787
	<i>cla-1</i> Vs <i>cla-1</i>; <i>hlb-1</i>	<i>cla-1</i> Vs <i>cla-1</i> ; <i>syd-2</i>	<i>cla-1</i> Vs <i>cla-1</i> ; <i>hlb-1</i> <i>syd-2</i>				
Power (1-β)	0.0066751	0.99619	1				
Effect size (d)	0.195614	2.073468	4.111744				
	<i>hlb-1</i> Vs <i>cla-1</i>; <i>hlb-1</i>	<i>hlb-1</i> Vs <i>hlb-1</i> <i>syd-2</i>	<i>hlb-1</i> Vs <i>cla-1</i> ; <i>hlb-1</i> <i>syd-2</i>				
Power (1-β)	0.010257	0.9992835	1				
Effect size (d)	0.253119	2.263164	3.750301				
	<i>syd-2</i> Vs <i>cla-1</i>; <i>syd-2</i>	<i>syd-2</i> Vs <i>hlb-1</i> <i>syd-2</i>	<i>syd-2</i> Vs <i>cla-1</i>; <i>hlb-1</i> <i>syd-2</i>				
Power (1-β)	0.001352	0.052807	0.001772				
Effect size (d)	0.00384	0.508204	0.034273				
	<i>cla-1</i> ; <i>hlb-1</i> Vs <i>cla-1</i> ; <i>hlb-1</i> <i>syd-2</i>	<i>cla-1</i>; <i>syd-2</i> Vs <i>cla-1</i>; <i>hlb-1</i> <i>syd-2</i>	<i>hlb-1</i> <i>syd-2</i> Vs <i>cla-1</i>; <i>hlb-1</i> <i>syd-2</i>				
Power (1-β)	1	0.003119	0.297423				
Effect size (d)	4.316232	0.100433	0.904901				

3) Aldicarb Assays

Aldicarb (Figure 3.10)	WT Vs <i>cla-1</i> (<i>ok2285</i>)	WT Vs <i>hlb-1</i> (<i>ok725</i>)	WT Vs <i>syd-2</i> (<i>ok217</i>)	WT Vs <i>cla-1</i> ; <i>hlb-1</i>	WT Vs <i>cla-1</i> ; <i>syd-2</i>	WT Vs <i>hlb-1</i> <i>syd-2</i>	WT Vs <i>cla-1</i> ; <i>hlb-1 syd-2</i>
Power (1-β)	0.9979	0.00393	0.0273	1	0.9335	0.6268	1
	<i>cla-1</i> Vs <i>cla-1</i> ; <i>hlb-1</i>	<i>cla-1</i> Vs <i>cla-1</i> ; <i>syd-2</i>	<i>cla-1</i> Vs <i>cla-1</i> ; <i>hlb-1 syd-2</i>				
Power (1-β)	0.5033	0.5073	0.5067				
	<i>hlb-1</i> Vs <i>cla-1</i> ; <i>hlb-1</i>	<i>hlb-1</i> Vs <i>hlb-1</i> <i>syd-2</i>	<i>hlb-1</i> Vs <i>cla-1</i> ; <i>hlb-1 syd-2</i>				
Power (1-β)	1	0.2268	1				
	<i>syd-2</i> Vs <i>cla-1</i> ; <i>syd-2</i>	<i>syd-2</i> Vs <i>hlb-1</i> <i>syd-2</i>	<i>syd-2</i> Vs <i>cla-1</i> ; <i>hlb-1 syd-2</i>				
Power (1-β)	0.9277	0.4737	1				
	<i>cla-1</i>; <i>hlb-1</i> Vs <i>cla-1</i>; <i>hlb-1</i> <i>syd-2</i>	<i>cla-1</i> ; <i>syd-2</i> Vs <i>cla-1</i> ; <i>hlb-1</i> <i>syd-2</i>	<i>hlb-1 syd-2</i> Vs <i>cla-1</i> ; <i>hlb-1</i> <i>syd-2</i>				
Power (1-β)	0.0402	0.9873	1				

4) Electron Microscopy

Cumulative DP area (Figure 4.5B)	WT Vs <i>cla-1</i> (<i>ok2285</i>)	WT Vs <i>h1b-1</i> (<i>ok725</i>)	WT Vs <i>syd-2</i> (<i>ok217</i>)	WT Vs <i>cla-1; syd-2</i>	WT Vs <i>h1b-1 syd-2</i>	WT Vs <i>cla-1; h1b-1 syd-2</i>
Power (1-β)	0.9983169	0.056598	0.963986	0.875514	0.146971513	0.999516
Effect size (d)	1.119697	0.295905	0.975290039	0.855974	0.46490264	1.1715082
	<i>cla-1 Vs cla-1; syd-2</i>	<i>cla-1 Vs cla-1; h1b-1 syd-2</i>				
Power (1-β)	0.036446967	0.058968				
Effect size (d)	0.406761	0.155635				
	<i>h1b-1 Vs h1b-1 syd-2</i>	<i>h1b-1 Vs cla-1; h1b-1 syd-2</i>				
Power (1-β)	0.011359377	0.020274				
Effect size (d)	0.176886	0.928954				
	<i>syd-2 Vs cla-1; syd-2</i>	<i>syd-2 Vs h1b-1 syd-2</i>	<i>syd-2 Vs cla-1; h1b-1 syd-2</i>			
Power (1-β)	0.010431	0.132225	0.041344			
Effect size (d)	0.146605	0.548967	0.322322508			
	<i>cla-1; syd-2 Vs cla-1; h1b-1 syd-2</i>	<i>h1b-1 syd-2 Vs cla-1; h1b-1 syd-2</i>				
Power (1-β)	0.078503219	0.11796688				
Effect size (d)	0.551429	0.820652				

SVs (Figure 4.6)	WT Vs <i>cla-1</i> (<i>ok2285</i>)	WT Vs <i>hlb-1</i> (<i>ok725</i>)	WT Vs <i>syd-2</i> (<i>ok217</i>)	WT Vs <i>cla-1; syd-2</i>	WT Vs <i>hlb-1 syd-2</i>	WT Vs <i>cla-1; hlb-1 syd-2</i>
Power (1-β)	0.246473	0.014201	0.901791236	0.956765	0.12564447	0.99449315
Effect size (d)	0.536187	0.169885	0.87665983	0.980547	0.38396349	1.07108577
	<i>cla-1 Vs cla-1; syd-2</i>	<i>cla-1 Vs cla-1; hlb-1 syd-2</i>				
Power (1-β)	0.10941	0.180384426				
Effect size (d)	0.485922	0.569264				
	<i>hlb-1 Vs hlb-1 syd-2</i>	<i>hlb-1 Vs cla-1; hlb-1 syd-2</i>				
Power (1-β)	0.232511	0.979813				
Effect size (d)	0.512348	1.111085				
	<i>syd-2 Vs cla-1; syd-2</i>	<i>syd-2 Vs hlb-1 syd-2</i>	<i>syd-2 Vs cla-1; hlb-1 syd-2</i>			
Power (1-β)	0.042566	0.340065	0.036957			
Effect size (d)	0.283727	0.723749	0.314213427			
	<i>cla-1; syd-2 Vs cla-1; hlb-1 syd-2</i>	<i>hlb-1 syd-2 Vs cla-1; hlb-1 syd-2</i>				
Power (1-β)	0.002874	0.80237518				
Effect size (d)	0.061446	1.139466				

Terminal area (Figure 4.7)	WT Vs <i>cla-1</i> (<i>ok2285</i>)	WT Vs <i>h1b-1</i> (<i>ok725</i>)	WT Vs <i>syd-2</i> (<i>ok217</i>)	WT Vs <i>cla-1; syd-2</i>	WT Vs <i>h1b-1</i> <i>syd-2</i>	WT Vs <i>cla-1;</i> <i>h1b-1 syd-2</i>
Power (1-β)	0.842058	0.0620152	0.297654	0.873697	0.031011	0.981678375
Effect size (d)	0.882018	0.306026	0.543432625	0.983518	0.25790016	1.0168617
	<i>cla-1 Vs cla-1; syd-2</i>	<i>cla-1 Vs cla-1; h1b-1 syd-2</i>				
Power (1-β)	0.0070474	0.005836				
Effect size (d)	0.154947	0.118776				
	<i>h1b-1 Vs h1b-1 syd-2</i>	<i>h1b-1 Vs cla-1; h1b-1 syd-2</i>				
Power (1-β)	0.000783	0.590119				
Effect size (d)	0.058373	0.741856				
	<i>syd-2 Vs cla-1; syd-2</i>	<i>syd-2 Vs h1b-1 syd-2</i>	<i>syd-2 Vs cla-1; h1b-1 syd-2</i>			
Power (1-β)	0.3841163	2.4E-05	0.180805			
Effect size (d)	0.616039	0.321186	0.543391814			
	<i>cla-1; syd-2 Vs cla-1; h1b-1 syd-2</i>	<i>h1b-1 syd-2 Vs cla-1; h1b-1 syd-2</i>				
Power (1-β)	0.000907601	0.001932887				
Effect size (d)	0.063653	0.94704				

Undocked SVs (Figure 4.8A)	WT Vs <i>cla-1</i> (<i>ok2285</i>)	WT Vs <i>hlb-1</i> (<i>ok725</i>)	WT Vs <i>syd-2</i> (<i>ok217</i>)	WT Vs <i>cla-1; syd-2</i>	WT Vs <i>hlb-1</i> <i>syd-2</i>	WT Vs <i>cla-1</i>; <i>hlb-1 syd-2</i>
Power (1-β)	0.265204	0.0002591	0.916346	0.948408	0.131477	0.993573399
Effect size (d)	0.547866	0.120417	0.891215	0.957463158	0.386706	1.05916973
	<i>cla-1 Vs cla-1; syd-2</i>	<i>cla-1 Vs cla-1; hlb-1 syd-2</i>				
Power (1-β)	0.088273	0.1603572				
Effect size (d)	0.451113	0.547123				
	<i>hlb-1 Vs hlb-1 syd-2</i>	<i>hlb-1 Vs cla-1; hlb-1 syd-2</i>				
Power (1-β)	0.177403	0.96401867				
Effect size (d)	0.46596	1.055647				
	<i>syd-2 Vs cla-1; syd-2</i>	<i>syd-2 Vs hlb-1 syd-2</i>	<i>syd-2 Vs cla-1; hlb-1 syd-2</i>			
Power (1-β)	0.022825	0.3852759	0.02729			
Effect size (d)	0.219231	0.757731	0.277791			
	<i>cla-1; syd-2 Vs cla-1; hlb-1 syd-2</i>	<i>hlb-1 syd-2 Vs cla-1; hlb-1 syd-2</i>				
Power (1-β)	0.003627	0.802967				
Effect size (d)	0.087835	1.139613				

Docked SVs (Figure 4.8B)	WT Vs <i>cla-1</i> (<i>ok2285</i>)	WT Vs <i>h1b-1</i> (<i>ok725</i>)	WT Vs <i>syd-2</i> (<i>ok217</i>)	WT Vs <i>cla-1</i>; <i>syd-2</i>	WT Vs <i>h1b-1</i> <i>syd-2</i>	WT Vs <i>cla-1</i>; <i>h1b-1 syd-2</i>
Power (1-β)	0.028603	0.319865	0.015416785	0.946998	0.23275424	0.47548865
Effect size (d)	0.2347621	0.537411	0.177199	0.839295	0.462942	0.595426
	<i>cla-1 Vs cla-1</i> <i>; syd-2</i>	<i>cla-1 Vs cla-1</i> <i>; h1b-1 syd-2</i>				
Power (1-β)	0.568684	0.0953667				
Effect size (d)	0.8424028	0.464527				
	<i>h1b-1 Vs h1b-1</i> <i>syd-2</i>	<i>h1b-1 Vs cla-1</i>; <i>h1b-1 syd-2</i>				
Power (1-β)	0.972361	0.9955619				
Effect size (d)	1.1709024	1.327413				
	<i>syd-2 Vs cla-1</i> <i>; syd-2</i>	<i>syd-2 Vs h1b-1</i> <i>syd-2</i>	<i>syd-2 Vs cla-1</i> <i>; h1b-1 syd-2</i>			
Power (1-β)	0.763652	0.043975	0.136081			
Effect size (d)	0.8518956	0.334477	0.496422			
	<i>cla-1; syd-2</i> <i>Vs cla-1; h1b-1</i> <i>syd-2</i>	<i>h1b-1 syd-2</i> <i>Vs cla-1; h1b-1</i> <i>syd-2</i>				
Power (1-β)	0.10104	0.012699				
Effect size (d)	0.4944964	0.21031				

Undocked 0-99nm (Figure 4.9B)	WT Vs <i>cla-1</i> (<i>ok2285</i>)	WT Vs <i>h1b-1</i> (<i>ok725</i>)	WT Vs <i>syd-2</i> (<i>ok217</i>)	WT Vs <i>cla-1; syd-2</i>	WT Vs <i>h1b-1</i> <i>syd-2</i>	WT Vs <i>cla-1;</i> <i>h1b-1 syd-2</i>
Power (1-β)	0.9355322	0.024679	0.251461	0.98695	0.238794803	0.801149
Effect size (d)	0.889017	0.224283	0.490231	0.957278	0.419553425	0.834605
	<i>cla-1 Vs cla-1; syd-2</i>	<i>cla-1 Vs cla-1; h1b-1 syd-2</i>				
Power (1-β)	0.014522	0.0015086				
Effect size (d)	0.2250845	0.007624				
	<i>h1b-1 Vs h1b-1 syd-2</i>	<i>h1b-1 Vs cla-1; h1b-1 syd-2</i>				
Power (1-β)	0.372202	0.815859				
Effect size (d)	0.5666353	0.892353				
	<i>syd-2 Vs cla-1; syd-2</i>	<i>syd-2 Vs h1b-1 syd-2</i>	<i>syd-2 Vs cla-1; h1b-1 syd-2</i>			
Power (1-β)	0.594744	0.0002261	0.101808			
Effect size (d)	0.740502	0.14962	0.467972			
	<i>cla-1; syd-2 Vs cla-1; h1b-1 syd-2</i>	<i>h1b-1 syd-2 Vs cla-1; h1b-1 syd-2</i>				
Power (1-β)	0.000199	0.36138				
Effect size (d)	0.1736651	0.760292				

Undocked 99-198nm (Figure 4.9C)	WT Vs <i>cla-1</i> (<i>ok2285</i>)	WT Vs <i>hlb-1</i> (<i>ok725</i>)	WT Vs <i>syd-2</i> (<i>ok217</i>)	WT Vs <i>cla-1; syd-2</i>	WT Vs <i>hlb-1 syd-2</i>	WT Vs <i>cla-1; hlb-1 syd-2</i>
Power (1-β)	0.461977	0.055044	0.587529	0.915836004	0.590778	0.78992455
Effect size (d)	0.618838	0.317574	0.662214	0.86976906	0.616457	0.8072022
	<i>cla-1 Vs cla-1; syd-2</i>	<i>cla-1 Vs cla-1; hlb-1 syd-2</i>				
Power (1-β)	0.05249	0.0206786				
Effect size (d)	0.387431	0.259225				
	<i>hlb-1 Vs hlb-1 syd-2</i>	<i>hlb-1 Vs cla-1; hlb-1 syd-2</i>				
Power (1-β)	0.615589	0.7746089				
Effect size (d)	0.700091	0.828709				
	<i>syd-2 Vs cla-1; syd-2</i>	<i>syd-2 Vs hlb-1 syd-2</i>	<i>syd-2 Vs cla-1; hlb-1 syd-2</i>			
Power (1-β)	0.129347	0.0005036	0.017808			
Effect size (d)	0.421632	0.094673	0.236645			
	<i>cla-1; syd-2 Vs cla-1; hlb-1 syd-2</i>	<i>hlb-1 syd-2 Vs cla-1; hlb-1 syd-2</i>				
Power (1-β)	0.000477	0.045903				
Effect size (d)	0.111902	0.370506				

Undocked 198-297nm (Figure 4.9D)	WT Vs <i>cla-1</i> (<i>ok2285</i>)	WT Vs <i>hlb-1</i> (<i>ok725</i>)	WT Vs <i>syd-2</i> (<i>ok217</i>)	WT Vs <i>cla-1; syd-2</i>	WT Vs <i>hlb-1</i> <i>syd-2</i>	WT Vs <i>cla-1</i>; <i>hlb-1 syd-2</i>
Power (1-β)	0.057698	0.05517	0.654454	0.429654987	0.036903	0.30165555
Effect size (d)	0.314988	0.320073	0.713037	0.579594	0.239481931	0.535523
	<i>cla-1 Vs cla-1; syd-2</i>	<i>cla-1 Vs cla-1; hlb-1 syd-2</i>				
Power (1-β)	0.035026	0.0201991				
Effect size (d)	0.3259873	0.255221				
	<i>hlb-1 Vs hlb-1 syd-2</i>	<i>hlb-1 Vs cla-1; hlb-1 syd-2</i>				
Power (1-β)	0.1861055	0.447938				
Effect size (d)	0.4494399	0.631567				
	<i>syd-2 Vs cla-1; syd-2</i>	<i>syd-2 Vs hlb-1 syd-2</i>	<i>syd-2 Vs cla-1; hlb-1 syd-2</i>			
Power (1-β)	0.0195084	0.339195	0.015924			
Effect size (d)	0.2040002	0.70144	0.223887			
	<i>cla-1; syd-2 Vs cla-1; hlb-1 syd-2</i>	<i>hlb-1 syd-2 Vs cla-1; hlb-1 syd-2</i>				
Power (1-β)	0.000808639	0.001734649				
Effect size (d)	0.0658894	0.453915				

Undocked 297-396nm (Figure 4.9E)	WT Vs <i>cla-1</i> (<i>ok2285</i>)	WT Vs <i>hlb-1</i> (<i>ok725</i>)	WT Vs <i>syd-2</i> (<i>ok217</i>)	WT Vs <i>cla-1; syd-2</i>	WT Vs <i>hlb-1</i> <i>syd-2</i>	WT Vs <i>cla-1;</i> <i>hlb-1 syd-2</i>
Power (1-β)	0.013743	0.019025	0.205919	0.329152876	0.010379	0.39027761
Effect size (d)	0.16846	0.206392	0.463153277	0.473627	0.1302363	0.50810326
	<i>cla-1 Vs cla-1; syd-2</i>	<i>cla-1 Vs cla-1; hlb-1 syd-2</i>				
Power (1-β)	0.070257	0.106771				
Effect size (d)	0.401464	0.441365				
	<i>hlb-1 Vs hlb-1 syd-2</i>	<i>hlb-1 Vs cla-1; hlb-1 syd-2</i>				
Power (1-β)	0.045735	0.072462				
Effect size (d)	0.274621	0.499124				
	<i>syd-2 Vs cla-1; syd-2</i>	<i>syd-2 Vs hlb-1 syd-2</i>	<i>syd-2 Vs cla-1; hlb-1 syd-2</i>			
Power (1-β)	0.0017355	0.113547	0.002054			
Effect size (d)	0.004047	0.475484	0.018603674			
	<i>cla-1; syd-2 Vs cla-1; hlb-1 syd-2</i>	<i>hlb-1 syd-2 Vs cla-1; hlb-1 syd-2</i>				
Power (1-β)	0.002078	0.279595				
Effect size (d)	0.024359	0.708646				

Undocked 396-495nm (Figure 4.9F)	WT Vs <i>cla-1</i> (<i>ok2285</i>)	WT Vs <i>h1b-1</i> (<i>ok725</i>)	WT Vs <i>syd-2</i> (<i>ok217</i>)	WT Vs <i>cla-1; syd-2</i>	WT Vs <i>h1b-1</i> <i>syd-2</i>	WT Vs <i>cla-1</i>; <i>h1b-1 syd-2</i>
Power (1-β)	0.07222	0.002089	0.211964	0.467359076	0.038961	0.81382167
Effect size (d)	0.302597	0.017934	0.442028	0.515514554	0.254058	0.67342423
	<i>cla-1 Vs cla-1; syd-2</i>	<i>cla-1 Vs cla-1; h1b-1 syd-2</i>				
Power (1-β)	0.086392	0.128542				
Effect size (d)	0.444308	0.785699				
	<i>h1b-1 Vs h1b-1 syd-2</i>	<i>h1b-1 Vs cla-1; h1b-1 syd-2</i>				
Power (1-β)	0.010729	0.1335727				
Effect size (d)	0.142608	0.389661				
	<i>syd-2 Vs cla-1; syd-2</i>	<i>syd-2 Vs h1b-1 syd-2</i>	<i>syd-2 Vs cla-1; h1b-1 syd-2</i>			
Power (1-β)	0.012921	0.0221404	0.09597			
Effect size (d)	0.165679	0.26722	0.417883			
	<i>cla-1; syd-2 Vs cla-1; h1b-1 syd-2</i>	<i>h1b-1 syd-2 Vs cla-1; h1b-1 syd-2</i>				
Power (1-β)	0.061766	0.340867				
Effect size (d)	0.559446	0.771252				

Undocked 495-1001nm (Figure 4.9G)	WT Vs <i>cla-1</i> (<i>ok2285</i>)	WT Vs <i>h1b-1</i> (<i>ok725</i>)	WT Vs <i>syd-2</i> (<i>ok217</i>)	WT Vs <i>cla-1; syd-2</i>	WT Vs <i>h1b-1</i> <i>syd-2</i>	WT Vs <i>cla-1;</i> <i>h1b-1 syd-2</i>
Power (1-β)	0.121298	0.0040063	0.219561	0.024564	0.3221	0.121298
Effect size (d)	0.328781	0.069126	0.307763	0.364228974	0.19057	0.43339632
	<i>cla-1 Vs cla-1; syd-2</i>	<i>cla-1 Vs cla-1; h1b-1 syd-2</i>				
Power (1-β)	0.015389	0.0937635				
Effect size (d)	0.216556	0.449131				
	<i>h1b-1 Vs h1b-1 syd-2</i>	<i>h1b-1 Vs cla-1; h1b-1 syd-2</i>				
Power (1-β)	0.016161	0.0658238				
Effect size (d)	0.172428	0.304653				
	<i>syd-2 Vs cla-1; syd-2</i>	<i>syd-2 Vs h1b-1 syd-2</i>	<i>syd-2 Vs cla-1; h1b-1 syd-2</i>			
Power (1-β)	0.013631	0.015272	0.0387661			
Effect size (d)	0.170526	0.219299	0.299092			
	<i>cla-1; syd-2 Vs cla-1; h1b-1 syd-2</i>	<i>h1b-1 syd-2 Vs cla-1; h1b-1 syd-2</i>				
Power (1-β)	0.036670955	0.059297613				
Effect size (d)	0.475857	0.671365				

DCVs (Figure 4.11)	WT Vs <i>cla-1</i> (<i>ok2285</i>)	WT Vs <i>h1b-1</i> (<i>ok725</i>)	WT Vs <i>syd-2</i> (<i>ok217</i>)	WT Vs <i>cla-1; syd-2</i>	WT Vs <i>h1b-1 syd-2</i>	WT Vs <i>cla-1; h1b-1 syd-2</i>
Power (1-β)	0.003934	0.003064	0.96566041	0.999948	0.88791117	0.99931774
Effect size (d)	0.077796	0.043704	0.97494	1.265616937	0.893847	1.19585183
	<i>cla-1 Vs cla-1; syd-2</i>	<i>cla-1 Vs cla-1; h1b-1 syd-2</i>				
Power (1-β)	0.875202	0.7861433				
Effect size (d)	1.055001	1.039996				
	<i>h1b-1 Vs h1b-1 syd-2</i>	<i>h1b-1 Vs cla-1; h1b-1 syd-2</i>				
Power (1-β)	0.87773	0.9983511				
Effect size (d)	0.994842	1.337177				
	<i>syd-2 Vs cla-1; syd-2</i>	<i>syd-2 Vs h1b-1 syd-2</i>	<i>syd-2 Vs cla-1; h1b-1 syd-2</i>			
Power (1-β)	0.470393	0.0033882	0.063726			
Effect size (d)	0.667366	0.067133	0.38729			
	<i>cla-1; syd-2 Vs cla-1; h1b-1 syd-2</i>	<i>h1b-1 syd-2 Vs cla-1; h1b-1 syd-2</i>				
Power (1-β)	0.020572	0.0698819				
Effect size (d)	0.282846	0.440224				